Mathematical models for cell-substrate interaction

Gordon Robert McNicol

Submitted in fulfilment of the requirements for the
Degree of Doctor of Philosophy

School of Mathematics and Statistics
College of Science and Engineering
University of Glasgow

July 2024

Abstract To function and survive cells need to be able to sense and respond to their local environment through mechanotransduction. Crucially, mechanical and biochemical perturbations initiate cell signaling cascades, which can induce responses such as growth, apoptosis, proliferation and differentiation. At the heart of this process are actomyosin stress fibres (SFs), which form part of the cell cytoskeleton, and focal adhesions (FAs), which bind this cytoskeleton to the extra-cellular matrix (ECM). In addition to their structural role, FAs additionally serve as signaling hubs for changes in cell function. It follows that understanding the formation of these structures is a prerequisite for any attempt to elucidate how mechanical and biochemical cues influence cell behaviour.

The focus of this thesis is on the development of mathematical models to describe the coupled formation and maturation of cell-substrate adhesions and cell cytoskeleton in non-motile cells. In particular, we formulate a zero-dimensional bio-chemical model and one- and two-dimensional bio-chemo-mechanical models to describe the development of SFs and FAs and activation of ROCK signaling. We use a large family of PDEs (or ODEs) to describe three sets of biochemical events: the polymerisation of actin and subsequent bundling into contractile SFs; the formation and maturation of cell-substrate adhesions; and the activation of signaling proteins in response to FA and SF formation. In our one- and two-dimensional models, the evolution of these key proteins is coupled to a Kelvin-Voigt viscoelastic description of the cell cytoplasm and the ECM. We employ these various models to understand how cells respond to external and intracellular cues *in vitro* and are able to reproduce, and elucidate the mechanism of, a range of experimentally observed phenomena. This includes non-uniform cell striation and cells forming weaker SFs and FAs on softer substrates. It follows that the developed models provide a platform for systematic investigation into how the cell biochemistry and mechanics influence cell development and facilitates prediction of internal cell measurements that are difficult to ascertain experimentally.

Contents

List of Tables

List of Figures

Acknowledgements

Firstly, I would like to express my appreciation to my PhD supervisors, Prof. Peter Stewart and Prof. Matt Dalby. Thank you for your support, guidance and generosity with your time throughout my PhD. I have thoroughly enjoyed our time working together. I would also like to thank Peter for introducing me to research as far back as 2018.

I would like to thank my thesis examiners, Dr. Carina Dunlop and Dr. Raimondo Penta, for their careful reading of my thesis. I greatly enjoyed discussing this research with you both and I am grateful for the helpful comments and suggestions you provided.

I would also like to thank Dr. Jakub Köry, who sadly recently passed away. You too were always generous with your time, provided many insightful suggestions and were excellent company on our research trips to Boston and Switzerland.

To the staff and students in the Department of Mathematics and Statistics at the University of Glasgow generally, thank you for providing such a welcoming and healthy working atmosphere. My past nine years in the department have been a pleasure and I will remember fondly my time at this University.

I also appreciate the generous financial support provided by the University of Glasgow through a Lord Kelvin Adam Smith scholarship. This has been invaluable in supporting this interdisciplinary collaboration and has facilitated many opportunities throughout my PhD.

I am grateful to my high school maths teachers Mrs. Baxter and Mrs. Ferguson. Thank you for providing me with the knowledge, confidence and encouragement to pursue a degree in mathematics in the first place.

I would not be where I am today without the support of all of my friends and family. I would particularly like to thank my parents, Louise and Gordon McNicol. You have both given me so much love, support and encouragement throughout my life, but particularly during the stressful periods of this PhD. I am proud to call you my mum and dad.

Finally, to my partner, Riley Tilson: thank you for everything, particularly for your patience in enduring my rants about code and small mathematical details. You have been a constant source of love, support and motivation, even during the periods when we have been separated by an ocean.

Declaration

With the exception of Ch. 1, which contains introductory material, all work in this thesis was carried out by the author unless otherwise explicitly stated. The work in Ch. 3 is currently under revision for publication in the Journal of Theoretical Biology; the work in Chs. 2, 4-5 is currently being prepared for publication. Moreover, the work in this thesis has not been submitted for another degree in any other department or university.

Chapter 1

Introduction

In order to function and survive, eukaryotic cells need to be able to sense and respond to their surrounding environment in a process called mechanotransduction, mediated by both mechanical and biochemical cues. Mechanotransduction is ubiquitous across eukaryotic cells, which are exposed to a variety of micro- and nano-scale stimuli which initiate signaling cascades inside the cell inducing, among other things, cell growth, apoptosis, motility, proliferation, quiescence or, in the case of stem cells, differentiation (Orr et al., 2006). In particular, cells are exposed to a variety of forces *in vivo*, including gravity, blood-flow induced shear stress on endothelial cells, cyclic stretching of vessels due to blood pressure, and microscopic forces that arise from interactions between contracting cells (Chen, 2008, Li et al., 2005). The corresponding changes at the cellular level can propagate and influence behaviour on the tissue scale. Indeed, it is through this process that many familiar senses originate, including touch, hearing and balance (Chalfie, 2009). However, as well as contributing to essential functions in the body, mechanotransduction is implicated in contributing to various diseases, including atherosclerosis and cancer (DuFort et al., 2011, Hahn and Schwartz, 2009, Jaalouk and Lammerding, 2009, Nigro et al., 2011).

Before proceeding, we briefly introduce a number of terms that are key and appear throughout this thesis. These are listed in bold in this paragraph and we explore these proteins and structures in more detail throughout this Chapter. The **cell cytoskeleton** is composed of a complex and evolving network of proteins (mainly actin filaments) that together give the cell shape, structure and stability. This structure is bathed in the cell cytoplasm, a viscous liquid with suspended ions and proteins. The cytoskeleton is composed of three key components: **actin microfilaments**, intermediate filaments and microtubules, all of which can rapidly grow and disassemble in response to the needs of the cell. Moreover, through the cytoskeleton, forces due to **myosin II** (which cross-links actin filaments) based contraction of **stress fibres** (which are composed of actin and a variety of cross-linkers) can be communicated to the **extra-cellular matrix** allowing the cell to remodel, amongst others, **collagen** and **fibronectin fibres** in its surrounding

environment. These forces pass from the cell to the substrate through a link formed at **focal adhesions**; these adhesions are composed of **integrins** (proteins which can hook onto collagen and fibronectin fibres in the underlying substrate), **substrate ligands** and numerous focal adhesion associated proteins including **talin** and **vinculin**. These structures are illustrated in Fig. 1.1 (below).

1.1 Mesenchymal stem cells

Our primary interest in this thesis is to model stem cells; these are unspecialised cells that can undergo differentiation, specialising to a particular cell type, expressing only certain genes and producing related proteins. This process is critical in complex organisms, allowing for growth and repair through the production of specialised cell types to renew damaged tissue (Biehl and Russell, 2009). Such cells can be broadly divided into two types: embryonic stem cells (removed from embryos), which can differentiate and specialise into a wide variety of different cell types (i.e. they are pluripotent), and adult stem cells, which are found in a number of locations in the body but can generally differentiate into only certain cell types, usually related to the location in which they are found (Hu et al., 2018, Zakrzewski et al., 2019). Indeed, the seminal work of Engler et al. (2006) demonstrated that the elasticity of the surrounding ECM directs stem cell fate, generally in a way to promote tissue-specific healing (e.g. cells cultured on matrix with a stiffness similar to that of pre-calcified bone undergo osteogenesis); this requires myosin II contractility of the cell.

One example of adult stem cells are human mesenchymal stem cells (hMSCs), contained in bone marrow, which have the ability to differentiate into a number of important cell types associated with the musculoskeletal system such as osteoblasts (bone cells), adipocytes (fat cells), chrondrocytes (cartilage cells) and fibroblasts (a key component of connective tissue) (Hu et al., 2018, Robertson et al., 2018, Ullah et al., 2015). Given the wide array of specialised cell types that can be derived from hMSCs, it is desirable to be able to direct the differentiation process along a desired lineage, with applications in tissue engineering, particularly for orthopedic surgery. For example, every year an estimated 11,000,000 cm^3 of bone grafts are required during an estimated 2,000,000 procedures (Fernandez de Grado et al., 2018, Robertson et al., 2018). However, despite this being a standard and widespread technique, there remain many potential complications during treatment, including chronic pain, dysesthesia and infection. These problems could be circumvented through control over stem cell differentiation, allowing a patient's own stem cells to be used to grow the necessary tissue and hence cutting the risk of tissue rejection.

A variety of techniques exist to direct differentiation (and other types of cell function) *in vitro*. These techniques include passive methods, for example topographical control

or altering environmental stiffness (Dalby et al., 2014, Urbanczyk et al., 2020). These methods focus on the generation of internal tension within the cell by altering the environment to which the cell is adhered (Kilian et al., 2010). Meanwhile, active techniques, such as using shear flow, can promote osteogenesis (Kim et al., 2014, Yourek et al., 2010). A more recent active technique has been inspired by the nanoscale vibrations that occur on the cell membrane when interacting with a substrate (these are specific to the cell type, e.g. Rappaz et al., 2009, report that the membranes of red blood cells oscillate with an amplitude of 36 nm, with a frequency range of 0.2-12 Hz). In particular, high-frequency vibrational stimulation of nanoscale amplitude (*'nanokicking'*) has been applied to hMSCs as a means to direct differentiation. For example, nanoscale vibrations with a frequency range of approximately 1000 Hz have been shown to induce osteogenesis in hMSCs (Nikukar et al., 2013, Robertson et al., 2018). Similar to the passive methods, each of these techniques achieves changes in function through the generation of tension in the cell cytoskeleton, which affects the development of cytoskeleton and adhesion between the cell and surrounding extra-cellular matrix (ECM) (Fletcher and Mullins, 2010, Martino et al., 2018). Changes in adhesion consequently activate key biochemical signaling pathways inside the cell, such as those related to focal adhesion kinase (FAK), extra-cellular signal related kinase (ERK) and Rho-kinase (ROCK) (Hastings et al., 2019, Provenzano and Keely, 2011). These cascades are linked to transcription changes in the cell nucleus, which then leads to changes in cell function. Hence, in order to understand how changes in cell function occur in response to mechanotransductive cues, it is first crucial to understand the coupled development of cell cytoskeleton and cell-substrate adhesions; this shall be the focus of this thesis.

1.2 Mechanosensing structures

The forces experienced by cells and their subcellular components can be classified as intracellular or extracellular. In non-muscle cells, intracellular forces are dominated by contraction due to myosin II motors, though other components of the cytoskeleton may contribute, e.g. microtubules (Dogterom and Yurke, 1997) or (the polymerisation of) actin filaments in lamellipodia (Prass et al., 2006). External forces (which can be compressive, tensile or shearing) can be exerted both naturally (e.g. by other cells) or artificially (e.g. optical or magnetic tweezers). In any case, a force threshold on the order of the pN to nN range is generally required to prompt a cellular response, with the applied forces usually sensed through increased stress on, and deformation of, a mechanosenser (Chen, 2008, Choquet et al., 1997, Jiang et al., 2003).

Mechanosensing occurs at a variety of locations in the cell, including the nucleus, the cytoskeleton, the cortex and stretch-activated ion channels (Chen, 2008, Enyedi and Niethammer, 2017, Isermann and Lammerding, 2013, Martino et al., 2018), but particularly

at focal adhesions (FAs) (Katsumi et al., 2004). At FAs cytoskeletally generated forces lead to stress due to an opposite and equal reaction force arising in the ECM. We detail the components and formation of FAs in Sec. 1.2.1 and of stress fibres (SFs), a key component of the actin cytoskeleton in non-motile cells, in Sec. 1.2.2.

1.2.1 Focal adhesions

Focal adhesions form a link across the cell membrane between cell cytoskeleton, particularly SFs, and the ECM, allowing cells to exert traction on the substrate to which they are adhered (Endlich et al., 2007). Adhesions are regulated by a plethora of proteins which can be divided into scaffolding proteins (e.g. vinculin and talin) and signaling proteins (e.g. FAK, specific phosphatases and Rho-family proteins) (Maziveyi and Alahari, 2017, Parsons et al., 2010, Wozniak et al., 2004). Scaffolding proteins, as indicated in Fig. 1.1, help form and maintain a stable structural scaffold, linking the SFs to the ECM through integrins and contributing to maturation of the adhesion. Meanwhile, signaling proteins are recruited to adhesions, where they generate and influence adhesion-dependent signals that act to control the development and sustainability of FAs whilst simultaneously regulating key cell processes.

The formation of these structures is initiated through integrins, transmembrane receptors which cluster at adhesions (Endlich et al., 2007, Gilmore and Burridge, 1996). These proteins can freely diffuse on the membrane but can become bound to the cytoskeleton by the scaffolding protein talin in a force-independent manner. This coupling not only impedes motion but activates the integrin so that it develops a high affinity for binding to ECM ligands (Calderwood, 2004, Klapholz and Brown, 2017, Wegener et al., 2007). When a high-affinity integrin and ligand bind, a nascent adhesion forms. These immature structures are weak and susceptible to disassembly but can mature (in a myosin-dependent process) to form more stable (less prone to disassembly) FAs through recruitment of vinculin (Atherton et al., 2016, Ciobanasu et al., 2014). Indeed, force induced stretching of nascent adhesions exposes cryptic vinculin binding sites (VBSs) on talin, with vinculin recruited (see Fig. 1.1) to reinforce the cytoskeleton-talin-integrin connections (Bays and DeMali, 2017, Carisey et al., 2013). In particular, these links strengthen and mature (through intracellular signaling) in response to loading, allowing the cell cytoskeleton to respond to externally applied forces and to communicate intracellular contractile forces to the surrounding environment (Gardel et al., 2008, Parsons et al., 2010, Wozniak et al., 2004). This also enables cells to sense matrix stiffness, facilitating durotaxis (Rens and Merks, 2020) and directing the lineage fates of hMSCs (Engler et al., 2006).

Adhesions also serve as sites for the polymerisation of actin filaments, as shown in Fig. 1.1, which elongate towards the cell centre. In turn, these filaments provide a structural template for adhesion growth (Hirata et al., 2014b). The resultant actin bundles form

connections with the actin cytoskeleton, allowing myosin II-generated contraction forces to be transmitted to the ECM and causing maturation of adhesion complexes through changes to their structural properties and signaling activity (Legerstee et al., 2019, Schwarz and Gardel, 2012). It follows that adhesions serve as a physical link between the cytoskeleton and ECM in addition to their role as signaling hubs to regulate pathways for growth, apoptosis and differentiation (Lukashev and Werb, 1998).

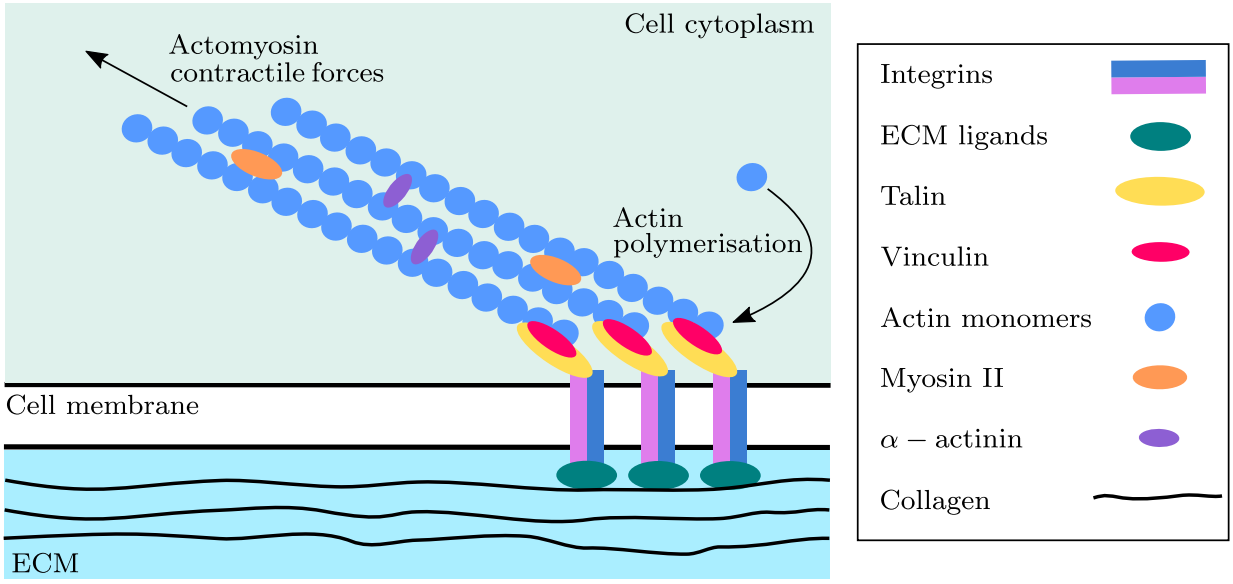

Figure 1.1: Adhesion structure and SF formation. Key proteins in adhesion formation (talin, integrins and ligands) and maturation (vinculin). Actin polymerisation occurs at adhesion sites, with the resultant filaments cross-linked by $\alpha-$actinin and myosin II.

1.2.2 Stress fibres

Cells continuously react to mechanical stimuli by pushing and pulling on their immediate surroundings, changing their orientation and morphology to adapt to external mechanical constraints and by migrating and dividing. The actin cytoskeleton is critical for giving a cell shape and structure and is involved in many cellular processes including morphogenesis, cytokenesis and phagocytosis (Lawrence et al., 2016, Lee and Dominguez, 2010, May and Machesky, 2001); it is also key to transmitting forces from the cell to its surroundings.

Stress fibres are a key component of the cell cytoskeleton that form in non-muscle cells in response to loading (Kassianidou and Kumar, 2015, Tojkander et al., 2012). These dynamic contractile actomyosin bundles are composed of actin filaments (around 10-30 actin filaments), cross-linked by myosin II motors (as shown in Fig. 1.2 below), together with a large family of other bundling and cross-linking proteins that display constant association and dissociation (Kassianidou and Kumar, 2015, Svitkina, 2018). They feature prominently in non-motile cells, which are the focus of this thesis, but also allow highly

motile cells to constrict and deform their surrounding ECM (even though SFs are much weaker in these cells) (Kemp and Brieher, 2018). Such fibres can be broadly categorised into four types which have different functions and dominant locations in the cell: dorsal SFs, transverse arcs, ventral SFs (VSFs) and the perinuclear actin cap (Hotulainen and Lappalainen, 2006, Tojkander et al., 2012); the properties of each of these are explored in more detail below.

Ventral SFs, shown in Fig. 1.3 (below), are the dominant type in non-motile cells, extending across the length of the cell, connecting two FAs and generating a nearly isometric tension (Burridge and Wittchen, 2013, Livne and Geiger, 2016). Such fibres are crucial to mechanotransduction as the contractile forces they generate (through myosin motor action) are exerted on, and promote the formation and maturation of, mechanosensing FAs. Their density is highly dependent on the cellular microenvironment (Doss et al., 2020, Tojkander et al., 2012). In particular, animal cells cultured on rigid surfaces often displaying thicker fibres aligned (with adhesions) along the major cell axis compared to the very thin and poorly aligned fibres in cells cultured on compliant substrates (Burridge and Wittchen, 2013, Discher et al., 2005).

Actin filaments

The primary function of actin filaments in cells is to produce force. This can occur by two mechanisms:

- Polymerisation of actin filaments against the cell membrane, exerting a pushing force on the membrane (Alexandrova et al., 2020). This is regulated by a large family of actin-binding proteins which control nucleation, elongation, disassembly, branching, cross-linking and bundling of filaments (Pollard, 2016, Svitkina, 2018).

- Actin filaments can be cross-linked by myosin II to form contractile actomyosin SFs with force generated by ATP-driven movement of myosin II motors (Cooper and Adams, 2022).

The formation of SFs is initiated through polymerisation of (G-)actin monomers into long (F-)actin filaments. Filament growth is initiated with the nucleation of three associating monomers (Cooper and Adams, 2022). The filament then evolves through a combination of branching from, and severing of, existing filaments. Branching is regulated by the Arp2/3 complex and is crucial in motile cells (Insall and Machesky, 2009, Kelleher et al., 1995, Schwob and Martin, 1992). Moreover, capping proteins can regulate filament growth by blocking the addition of new monomers (or severing filaments) to increase actin dynamics (Dufort and Lumsden, 1996, Mogilner and Edelstein-Keshet, 2002). The actin polymerisation process is polarised, with a rapidly-growing barbed end and slow-growing pointed end on each filament (Mogilner and Edelstein-Keshet, 2002, Winder and Ayscough, 2005),

leading to actin treadmilling (Pollard and Borisy, 2003, Wilson et al., 2010). The filament grows when ATP-actin monomers are recruited to the barbed end (Dominguez and Holmes, 2011, Pollard et al., 2000), as indicated in Fig. 1.2. Over time, ATP bound in actin monomers is hydrolysed, releasing phosphate. The resultant ADP-actin filament disassembles through monomer loss at the pointed end (Blanchoin et al., 2014, Fujiwara et al., 2007, Winder and Ayscough, 2005). Newly freed monomers undergo nucleotide exchange, replenishing the pool of ATP-actin monomers available for polymerisation at the barbed end (Winder and Ayscough, 2005). The resultant actin filaments can then be bundled and cross-linked by filamin, $\alpha-$actinin and particularly myosin II to form SFs (Hotulainen and Lappalainen, 2006, Kassianidou and Kumar, 2015, Svitkina, 2018), as indicated in Figs. 1.1, 1.2.

In highly motile cells, where mechanotransductive reorganisation of the cytoskeleton requires a plentiful supply of actin monomer, rapid filament growth is observed. This is regulated through a large family of actin binding proteins which promote the conversion of ADP-actin to ATP-actin and which deliver monomers to barbed ends allowing for new polymerisation. Sequestering proteins ensure that their a constant large pool of monomer available in such cells (Pollard, 2016).

Myosin recruitment and movement

Myosin serves as a molecular motor, through hydrolysis of ATP, to provide energy to drive actin filament sliding and hence generate force and movement (Alberts et al., 2015, Cooper and Adams, 2022, Kolega, 2006). The interaction between myosin and actin is pivotal to muscle action but is also responsible in non-muscle cells for cytokinesis, movement and contraction (Vicente-Manzanares et al., 2009, Zang et al., 1997). This thesis is focused on non-muscle cells that are non-motile, where actomyosin SFs display many similarities to muscle fibres, particularly exhibiting a sarcomeric-like structure similar to myofibrils (Kassianidou and Kumar, 2015, Thoresen et al., 2013).

In striated muscle cells, actomyosin contraction is mediated directly by Ca^{2+} ions (Szent-Györgyi, 1975, Webb, 2003). However, in non-muscle cells (and smooth muscle), contraction is regulated primarily by phosphorylation of myosin light chain (MLC), which itself is regulated by the competing effects of myosin light chain kinase (MLCK) and myosin light chain phosphatase (MLCP) (Johnson, 2006, Kamm and Stull, 1989). The phosphorylation of MLCK is partly regulated by Ca^{2+} ions, whilst MLCP phosphorlaytion is independent of Ca^{2+} concentration (Kitazawa et al., 2003, Somlyo and Somlyo, 1994). Consequently, Ca^{2+} indirectly contributes to myosin II activation in non-muscle cells. The subsequent phosphorylation of MLC promotes the assembly of myosin into filaments and increases the enzymatic ability of myosin to facilitate contraction (Cooper and Adams, 2022, Kitazawa et al., 2003).

Once bound to actin filaments, as illustrated in Fig. 1.2, myosin motors can facilitate contraction of sarcomeres (without affecting overall filament length) by sliding actin filaments towards the sarcomere centre (Squire, 2016). The conversion of chemical to kinetic energy is controlled by changes in myosin conformation due to ATP hydrolysis (Bagshaw, 1993, Cooper and Adams, 2022, Huxley, 1957). This reaction facilitates repeated cycles of interaction between myosin and actin, causing continual movement of myosin heads along actin filaments (Cooper and Adams, 2022).

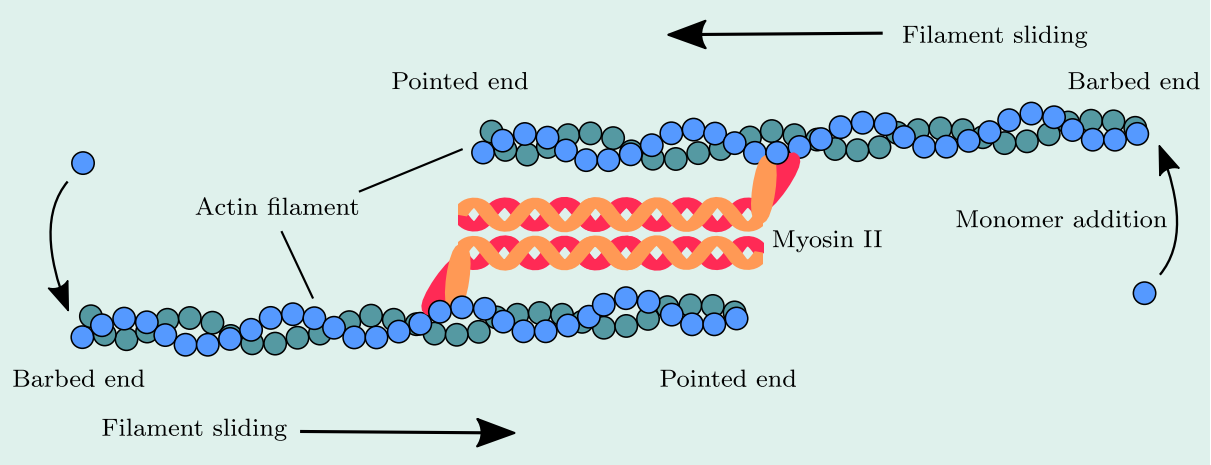

Figure 1.2: Actomyosin SF structure. Myosin II binds to actin filaments, sliding the filaments towards each other, facilitating contraction.

Despite the similarities between muscle fibres and SFs in non-motile non-muscle cells (e.g. structural periodicity), SFs are less well ordered (Gordon III, 1978). Moreover, unlike muscle fibres, SFs exhibit non-uniform striation, with sarcomeres near adhesions tending to shorten, whilst those further away elongate (Peterson et al., 2004).

Stress fibre types

In both motile and non-motile cells, reflecting their wide range of responsibilities, there are a variety of SF types, with different shapes, composition and relationships with FAs. Each type predominantly contains actin, but contractile SFs additionally contain myosin (Hotulainen and Lappalainen, 2006). When anchored to FAs, these structures provide a connection between the ECM and the actin cytoskeleton and are highly dynamic, even in stationary cells, with rapid reaction kinetics that are essential for their formation and contractility (Deguchi and Sato, 2009, Katoh et al., 2001, Kaunas et al., 2005). As already mentioned, they can be broadly divided into four categories: dorsal SFs, transverse arcs, ventral SFs and the perinuclear actin cap (Small et al., 1998); these are shown in Fig. 1.3 and any of these types may become dominant in response to the needs of the cell (Tojkander et al., 2012).

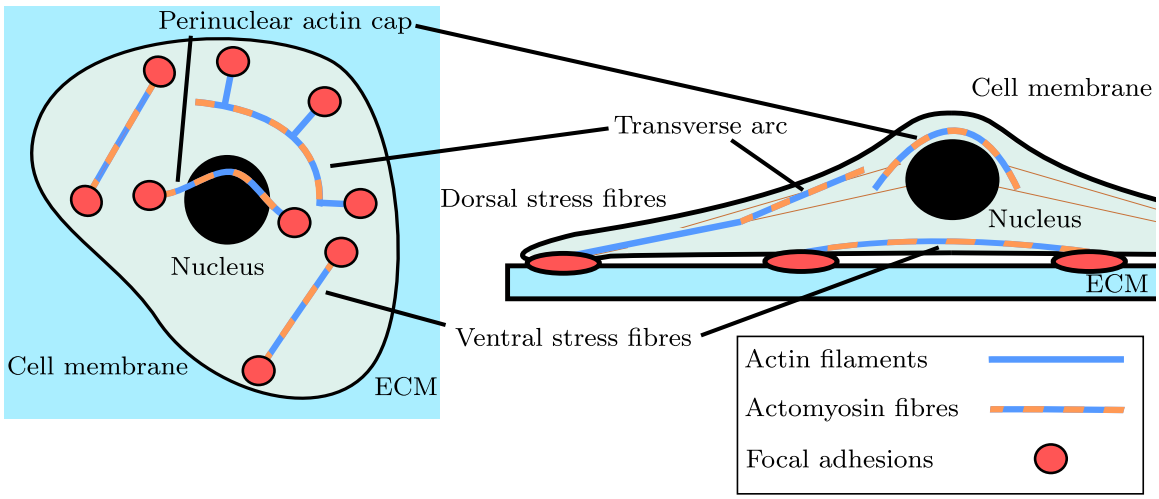

Figure 1.3: Stress fibre types. Illustration of the structure of dorsal SFs, transverse arcs, ventral SFs and perinuclear actin cap and their location relative to the cell nucleus and FAs.

Dorsal stress fibres: Dorsal SFs are long, linear bundles of actin, cross-linked by $\alpha-$actinin, that are particularly prominent in migrating cells (Livne and Geiger, 2016). They generally do not contain myosin II and so are non-contractile (Tojkander et al., 2011). Elongating from new adhesions (usually near the cell front) as the cell moves forward, they have rapidly growing barbed ends facing the cell membrane and grow towards the cell centre (see Fig. 1.3), providing tracks for the sliding of transverse arcs and connecting these to FAs (Hotulainen and Lappalainen, 2006, Livne and Geiger, 2016, Pellegrin and Mellor, 2007, Tojkander et al., 2015).

Transverse arcs: Transverse arcs are long, curved actomyosin bundles, with periodic cross-linking by $\alpha-$actinin and myosin (Livne and Geiger, 2016), which form particularly in motile cells. They form in the lamellipodia (Hotulainen and Lappalainen, 2006, Tojkander et al., 2011, Winder and Ayscough, 2005) and undergo retrograde flow, sliding centripetally towards the cell centre along dorsal SFs due to myosin II motor action (Tee et al., 2015). The arcs are not directly attached to FAs, but transmit myosin II generated contractile forces to the surrounding microenvironment through their connection with dorsal SFs (see Fig. 1.3). The arcs continue to flow towards the cell centre with the elongating dorsal SF in a myosin II dependent manner, coalescing in the cell centre to form strong contractile actomyosin bundles (Livne and Geiger, 2016, Small et al., 1998).

Ventral stress fibres: These long, linear actomyosin bundles are particularly prevalent in non-motile cells, running along the cell periphery (Prager-Khoutorsky et al., 2011). Such fibres can form through fusion (and exhibit properties) of a transverse arc with (two) dorsal SFs at its edges in a tension-dependent manner (Hotulainen and Lappalainen, 2006, Livne

and Geiger, 2016, Tojkander et al., 2015). Anchored to FAs at both ends (see Fig. 1.3), VSFs usually extend from one side of the cell to another and can generate isometric tension through actomyosin contraction (Deguchi and Sato, 2009, Small et al., 1998); they also promote constriction and facilitate cell movement. Towards their centre they are composed of alternating bands of $\alpha-$actinin and myosin II with a periodic polarity pattern similar to that observed in muscle cells. In contrast to driving centripetal motion in transverse arcs, myosin II in VSFs functions to transmit contractile forces to the ECM through their attachment to FAs, facilitating communication with the cellular microenvironment (Balaban et al., 2001, Grashoff et al., 2010, Livne and Geiger, 2016). Hence, VSFs are typically found in mature cells, where they play a significant role in mechanosensing (Livne and Geiger, 2016, Pellegrin and Mellor, 2007).

Perinuclear actin cap: These SFs are similar to VSFs, however (as indicated in Fig. 1.3) these are positioned over the cell nucleus (Kim and Wirtz, 2014). The role of the perinuclear actin cap is to both regulate the shape of the nucleus in cells and to act as mechanotransducers to convey force from the microenvironment to the nucleus (Khatau et al., 2009, Luxton et al., 2010).

1.2.3 Comparison between non-motile and motile cells

Non-motile cells typically have thick and relatively stable SFs compared with the thinner, transient SFs found in highly motile cells (Pellegrin and Mellor, 2007, Tojkander et al., 2012). Moreover, the spatial orientation of individual actin filaments within the SF differ between motile and non-motile cells. In particular, SFs in the ventral region of motile cells show a preference in actin filament orientation along the longitudinal axis of the SF, such that the barbed ends of filaments are predominantly directed towards FAs. In non-motile cells, VSFs show a periodic polarity with a similar organisation to that of muscle cell sarcomeres (Cramer et al., 1997, Patla et al., 2010, Rigort et al., 2012).

1.2.4 Coupling of stress fibres and focal adhesions

Stress fibres and FAs are highly interdependent. For example, disruption of SFs (e.g. by inhibiting myosin II) is accompanied by rapid disassembly of the attached FAs (Livne and Geiger, 2016). Moreover, SFs diminish when their anchorage sites disassemble during cell migration (Laukaitis et al., 2001). Actin polymerisation at adhesions also appears to be force-dependent (Hirata et al., 2008) and inhibition of SF generated forces by myosin II prevents actin treadmilling (Endlich et al., 2007, Livne and Geiger, 2016).

Ventral SFs and FAs, through their direct attachment, are particularly strongly coupled and play a key role in cellular mechanics and force sensing. The assembly, growth and

maintenance of FAs depends on mechanical stress and the mechanical force transmitted to FAs by SFs can alter the conformation of mechanosensetive FA proteins including integrins and talin (Martino et al., 2018). It follows that SF tension or contractility can convert mechanical signals into biochemical cues (Burridge and Guilluy, 2016). Moreover, VSFs that are in a state of isometric tension can displace the attached FAs towards the cell centre (Badley et al., 1980). It has also been observed that FA proteins are organized in elongated patches of similar width to the SFs connected to them, with the cross-sectional area of SFs near FAs found to have a linear relationship with the area of the adhesion (Hu et al., 2015, Livne and Geiger, 2016).

1.2.5 Signaling proteins

In response to adhesion formation and maturation, signaling proteins (particularly Rho signaling in non-motile cells) become activated, regulating actin polymerisation and myosin II activation (Deguchi and Sato, 2009, Pellegrin and Mellor, 2007). In particular, activation of mDia1, ROCK and downstream effectors promotes cytoskeleton development through increased formation of contractile actomyosin SFs (Feng et al., 1999, Maekawa et al., 1999). In turn, these SFs exert forces on their attached adhesions, precipitating vinculin recruitment to adhesions, increasing Rho signaling and closing a positive feedback loop.

The application of force, intracellular or external, has been shown to trigger the growth of adhesions in a Rho-dependent manner (Ridley and Hall, 1992, Riveline et al., 2001). Downstream, Rho activates the formin mDia1, leading to increased actin polymerisation through binding of mDia1 to the actin binding protein profilin (Satoh and Tominaga, 2001, Wasserman, 1998, Watanabe et al., 1999, Yamana et al., 2006). In motile cells, it is instead Rac that regulates assembly of an actin network; this occurs at the cell periphery, inducing lamellipodia (Ridley et al., 1992).

Additionally, Rho signaling activates the enzyme Rho-associated kinase (ROCK), leading to increased phosphorylation of MLC on myosin II motors and increasing motor activity (Liu et al., 2015, Totsukawa et al., 2000). This can occur through phosphorylation of MLCP at its myosin binding site (Wang et al., 2009). Depending on the respective activities of MLCP and MLCK, MLC either can be phosphorylated or dephosphorylated and this controls myosin binding to actin filaments. MLC needs to be phosphorylated (i.e. myosin activated) to allow myosin to bind to actin and facilitate contraction of SFs (Amano et al., 1996). Phosphorylation of MLCK can occur through ROCK activation (Dalby et al., 2018), or through an influx in calcium signaling (Kamm and Stull, 1985, Somlyo and Somlyo, 2003, Tansey et al., 1992, 1994). When phosphorylated, MLCP is inhibited in its ability to inactivate (dephosphorylate) myosin II, whilst phosphorylation of MLCK leads to myosin II activation. Activated ROCK can also phosphorylate MLC directly, though this effect is significantly weaker than phosphorylation by MLCK (Amano

et al., 1996, Feng et al., 1999, Totsukawa et al., 2004).

Rho signaling also regulates the activity of cofilin, a key actin binding protein that severs actin filaments and enhances actin dynamics (Sumi et al., 1999). This occurs through targeting of LIM kinase (LIMK) by activated ROCK (Maekawa et al., 1999). The subsequent phosphorylation of cofilin inhibits its severing ability, stabilising actin structures (Bamburg et al., 1999, Bishop and Hall, 2000).

1.2.6 Molecular clutch

The cytoplasmic portion of FAs contains multiple layers, parallel to the substrate, with distinct proteins, ranging from integrins adjacent to the substrate to actin deeper into the cell (Hirata et al., 2014b, Legerstee and Houtsmuller, 2021). The link formed between the cytoskeleton and ECM at FAs is highly dynamic and is governed by the accumulation of transient behaviour of the constituent proteins. In particular, these proteins display rapid reaction kinetics, with individual molecules residing at FAs for much shorter times than the lifetime of the adhesion (Hoffman et al., 2011). In motile or deforming cells, it follows that the cytoskeleton-integrin-ECM linkage at FAs is in a dynamic steady state between the moving actin cytoskeleton and stationary ECM (Hirata et al., 2014b).

When forces are applied to FAs, they influence the mechanical strength of the linkage by changing the reaction kinetics of molecular interactions at the FA (Geiger et al., 2009, Hirata et al., 2014b). This dynamic linkage behaves like a molecular clutch. When disengaged, the actin cytoskeleton moves freely (without connection to the ECM) and contractile forces generated by myosin II are not transmitted to the cellular microenvironment. When partially engaged, the actin cytoskeleton links to the ECM via transient connections between protein layers, leading to partial transmission of myosin II generated forces to the ECM. Finally, if the clutch is fully engaged (i.e. if the adhesion is fully matured) then actin movement is significantly hindered and contractile forces from the cell cytoskeleton are easily transmitted to the microenvironment (Brown et al., 2006, Guo and Wang, 2007, Hu et al., 2007b).

1.2.7 The extra-cellular matrix

The ECM consists of a complex network of proteins and macromolecules which provides scaffolding for cellular components and bio-chemo-mechanical cues to allow cells to sense and interact with their extracellular environment, facilitating, for example, tissue morphogenesis, cell differentiation and homeostasis (Frantz et al., 2010, Lu et al., 2011, Yamada et al., 2019). Present in all tissues and organs, the constituents of the ECM cooperate to form a structurally stable composite, influencing the mechanical properties of tissues (Yue, 2014).

Their constituents include macromolecules such as glycosaminoglycans (GAGs) (e.g. hyaluronan). These large, highly negatively charged polysaccharides can additionally form covalent bonds with proteins to form volume-filling proteoglycans (Frantz et al., 2010, Mouw et al., 2014). Moreover, their negative charge facilitates recruitment of water into the ECM, enabling the matrix to withstand compression whilst also facilitating rapid diffusion of proteins (Alberts et al., 2015, Karamanos et al., 2021).

Fibrous proteins (e.g. collagen and elastin) are another key component of the ECM. There are many collagen types but common to all is their arrangement in a triple helix, with the capacity to bind to cell surface receptors (e.g. integrins) (Ricard-Blum, 2011, Shoulders and Raines, 2009). Collagen fibres strengthen and organise the matrix and they can, depending on their type, organise into fibrillar structures capable of resisting tensile stress (Alberts et al., 2015, Gosline et al., 2002, Muiznieks and Keeley, 2013). Meanwhile, the highly flexible protein elastin is commonly found in blood vessels and skin, providing elasticity to the ECM (Baumann et al., 2021, Gosline et al., 2002, Muiznieks and Keeley, 2013).

Additionally, glycoproteins (e.g. laminin, fibronectin) promote cell migration and differentiation (Singh and Schwarzbauer, 2012). For example, fibronectin cross-links with ECM proteins and interacts with integrins to facilitate the formation of cell-substrate adhesions (Burridge et al., 1988, Hsiao et al., 2017, Jockusch et al., 1995, Mosher et al., 1979, Singh et al., 2010). Fibronectin can also coalesce to form fibrils (Mao and Schwarzbauer, 2005). On the other hand, laminin facilitates cell-substrate adhesion and cell motility through the formation of mesh-like networks (Crossley et al., 2024, Hamill et al., 2009).

The ECM undergoes constant remodeling whereby its components are continually created, destroyed or modified. For example, fibroblasts synthesise collagen to maintain a stable structural framework in the ECM of connective tissue (Leblond, 1989). Meanwhile, chondrocytes synthesise collagen for cartilage (Sandell and Aigner, 2001), endothelial cells synthesise fibronectin (Jaffe and Mosher, 1978) and osteoblasts and osteoclasts compete to synthesise and degrade bone (Florencio-Silva et al., 2015, Lu et al., 2011, Zelzer and Olsen, 2003). Moreover, proteases can be stored by the ECM to selectively target components of the ECM (Goetzl et al., 1996, Parsons et al., 1997). These proteases (e.g. matrix metalloproteinases) are crucial, for example, in enhancing cell motility, through degradation of damaged collagen fibres, during wound healing (Cawston and Young, 2010, Crossley et al., 2024, Lu et al., 2011).

The ECM performs a diverse range of functions. For example, it can serve as a physical barrier, an anchorage site, or a track to direct the motion of motile cells (Yue, 2014). The ECM can also provide mechanical cues to cells, which can sense the physical properties of the ECM (e.g. stiffness, porosity and orientation) through cell-substrate adhesions. For example, stiff matrices promote integrin clustering, mature FAs and ROCK activation,

leading to increased proliferation, contractility and, in the case of hMSCs, osteogenesis (Choquet et al., 1997, Paszek et al., 2005, Sun et al., 2018). Beyond its structural function, the ECM influences cell behaviour through biochemical signaling (Muncie and Weaver, 2018) and different cellular responses can be induced by different types of matrix (Frantz et al., 2010).

1.2.8 Summary of key proteins

To serve as a reference point, we summarise in Table 1.1 the key structural and signaling proteins involved in cell-substrate adhesion and cytoskeleton development, many of which have been explored in detail in this Chapter.

Protein	**Type**	**Role**
Actin	Structural	G-actin monomers polymerise to form F-actin microfilaments, the basis for SFs. During cell motility, polymerisation of actin filaments pushes the cell membrane.
Arp2/3	Structural	Nucleates new branches from existing filaments, particularly in motile cells.
Cofilin	Structural	Severs actin filaments (when unphosphorylated), replenishing pool of actin monomers. Phosphorylation inhibits this ability.
Collagen	Structural	Strengthens and organises the ECM, allowing it to resist tensile forces.
Elastin	Structural	Highly flexible, provides elasticity to the ECM.
Fibronectin	Structural	Cross-links with ECM proteins, connects ECM to integrins and can forms fibrils in a force-dependent manner.
Filamin	Structural	Actin cross-linker, accumulates at adhesions to remodel filaments into bundles.
FAK	Signaling	Activates Rho activity in response to adhesion formation and maturation.
Integrins	Structural	Transmembrane receptors that, when activated by talin binding, can bind to ECM ligands to form nascent adhesions. Clustering through diffusion leads to FA formation.
LIMK	Signaling	Phosphorylates cofilin (when activated by ROCK), inhibiting its severing ability.

Continued on the next page

Table 1.1 – continued from previous page

Protein	**Type**	**Role**
mDia1	Structural	Activated in response to adhesion formation, binds to the actin binding protein profilin, promoting actin polymerisation.
MLCK	Signaling	When phosphorylated (in response to ROCK activation), MLCK can phosphorylate (activate) myosin II, facilitating its interaction with actin.
MLCP	Signaling	When unphosphorylated, MLCP dephosphorylates (inactivates) activated myosin II; this ability is inhibited when phosphorylated by activated ROCK.
Myosin II	Structural	Cross-links actin filaments; facilitates contraction of SFs through motor action when activated (by phosphorylation).
Profilin	Structural	Binds with mDia1, facilitating actin polymerisation through conversion of ADP-actin monomers to ATP-actin monomers.
Rac	Signaling	Regulates the actin cytoskeleton in motile cells.
Rho	Signaling	In response to adhesion formation and maturation, activates the enzyme ROCK and formin mDia1, facilitating myosin II activation, actin filament elongation and, consequently, SF formation.
ROCK	Signaling	By phosphorylating downstream effectors, induces the formation of SFs and FAs by inhibiting actin filament depolymerisation and promoting myosin II activation.
Talin	Structural	Connects the cell cytoskeleton to integrins, causing activation of integrins, facilitating nascent adhesion formation.
Vinculin	Structural	Recruited to nascent adhesions in a force-dependent manner to strengthen the talin-actin bonds and prompt maturation into FAs.
$\alpha-$actinin	Structural	Bundles actin filaments to form short bundles, providing a template for adhesion elongation.

Table 1.1: Summary of important structural and signaling proteins involved in FA and SF formation and maturation.

1.3 Overview of our modelling approach

There are some common underlying principles to our modelling approaches in Chs. 2-5 to describe the coupled development and maturation of cell-substrate adhesions and cell cytoskeleton. We outline these principles here.

1.3.1 Biochemistry

Throughout this thesis we shall assume that integrins can exist in four states. As indicated in the blue section of Fig. 1.4 these states are low-affinity (for ECM ligand binding), high-affinity (for ECM ligand binding), bound (to an ECM ligand) or recruited into a mature FA. Moreover, as indicated in the red region of Fig. 1.4, we assume myosin II is either inactivated or activated, and that actin can exist in three states, namely in monomeric (G-actin) form, as part of a filament (F-actin) or recruited into a SF that has been cross-linked by activated myosin II. The development of SFs and FAs is assumed to be coupled, as indicated with green arrows in Fig. 1.4, through intracellular signaling. The intracellular signaling cascades we consider are indicated in Fig. 1.5. In particular, maturating adhesions are assumed to activate mDia1 and Rho signaling, leading to changes in the dynamics of actin polymerisation and myosin II activation through downstream effectors cofilin, MLCP and MLCK. Stress fibre formation is then linked to increased adhesion maturation.

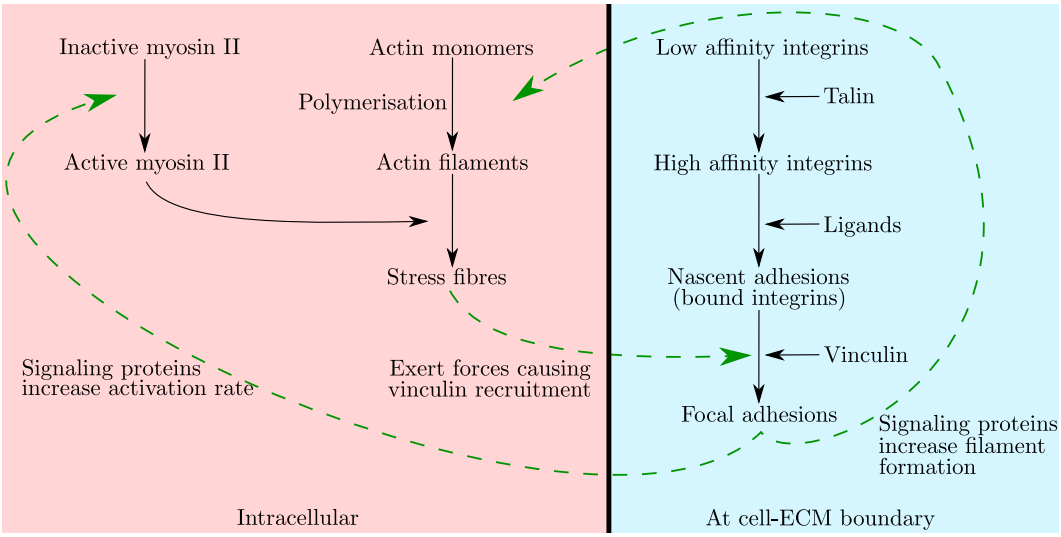

Figure 1.4: Overview of important biochemistry in the formation of FAs and VSFs. Key proteins involved in adhesion formation and maturation (blue region) and SF assembly (red region). Feedback loop indicated by dashed lines, a thick line is used to separate reactions that occur on the cell membrane and reactions that occur deeper in the cytoplasm.

To summarise, we consider three key coupled biochemical events:

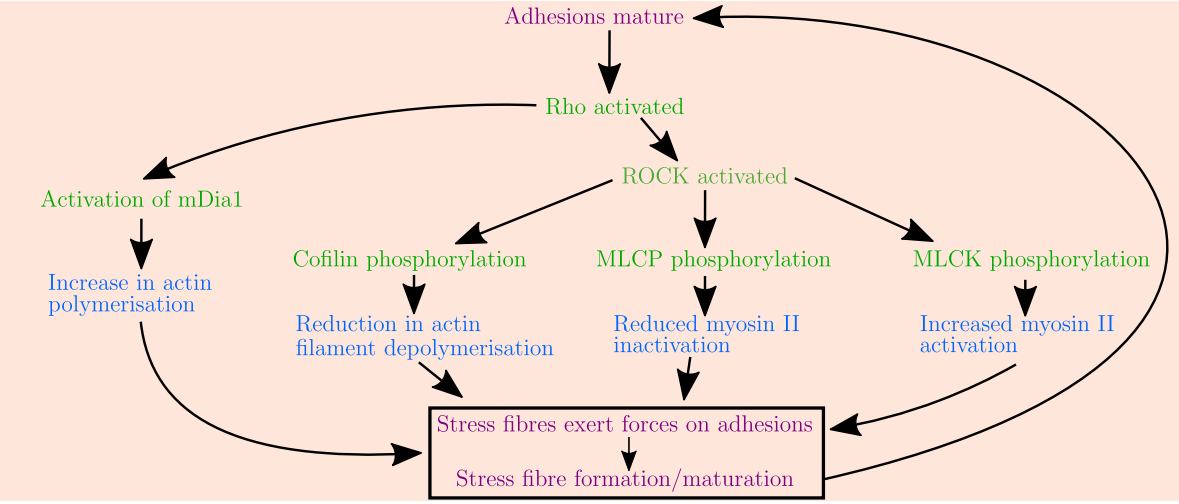

Figure 1.5: Intracellular signaling feedback loop. Adhesion maturation leads to Rho activation, promoting actin polymerisation and ROCK activation. Activation of ROCK leads to phosphorylation of downstream effectors (cofilin, MLCP and MLCK) and, consequently, SF development and further adhesion maturation.

- Adhesion formation: As shown in the blue section of Fig. 1.4, we describe the activation (by talin binding) of integrins and subsequent binding of these integrins with ECM ligands to form bound integrins (nascent adhesions). Subsequently, these adhesions can mature (through recruitment of vinculin) in a stretch-dependent manner into FAs.

- Intracellular signaling: As indicated in green in Fig. 1.4, the formation and maturation of cell-substrate adhesions leads to increased actin filament formation and myosin II activation, facilitating increased SF formation. Fig. 1.5 provides more detail on the signaling pathways we consider, illustrating how adhesion maturation leads to ROCK and mDia1 activation. In turn, mDia1 activation leads to increased actin polymerisation, whilst ROCK activation precipitates phosphorylation of cofilin, MLCP and MLCK leading to changes in actin and myosin dynamics.

- Stress fibre formation: As shown in the red section of Fig. 1.4, we incorporate the polymerisation of actin monomers to form actin filaments, activation of myosin II, and cross-linking of actin by myosin II to form SFs. The myosin II generated contractile forces stretch adhesions, leading to maturation into FAs, as indicated in Fig. 1.5.

In Chs. 3-5 we describe the evolution of each of these (structural and signaling) proteins using a set of reaction-diffusion-advection equations. Hence, the concentration, $c(\boldsymbol{x}, t)$, of a generic protein, C, at position $\boldsymbol{x}$ and time t is described by

$$\frac{\partial c}{\partial t} = f\left(c, c_1, ..., c_j\right) + D\nabla^2 c - \nabla \cdot (\boldsymbol{v}c)\,, \tag{1.1}$$

where f captures the reactions, involving other proteins with concentrations $c_1, ..., c_j$, that lead to the formation or depletion of the protein C, D is the diffusivity of C, and where C is advected with velocity $\boldsymbol{v}$. In Ch. 2 we neglect spatial variations in protein concentration, instead specifying a large family of ODEs to describe the evolution of the average concentration or density of each protein.

1.3.2 Mechanics

In Chs. 3-5, in order to calculate the stress and deformation of the cell, ECM and adhesions, we must impose constitutive assumptions on each of these structures. In line with existing modelling approaches (e.g. Byrne and Chaplain, 1996, Gracheva and Othmer, 2004, Jamali et al., 2010), we model each of these structures as a Kelvin-Voigt viscoelastic material. Such a system consists of a viscous damper and elastic spring connected in parallel and is appropriate to describe the rheology of long-time solid-like viscoelastic materials; contrast this with the Maxwell model, which consists of a damper and spring connected in series and is applicable to long-time fluid-like viscoelastic materials. In general, for such a material, the Cauchy stress, $\boldsymbol{\sigma}$, is related to both the strain, $\boldsymbol{\epsilon}$, and strain rate, $\dot{\boldsymbol{\epsilon}}$, so that

$$\boldsymbol{\sigma} = f\left(\boldsymbol{\epsilon}\right) + g\left(\dot{\boldsymbol{\epsilon}}\right), \tag{1.2}$$

for functions f, g. Throughout this thesis we assume displacements in both the cell and ECM are small, allowing us to assume linear viscoelasticity. In this case, the stress is given by

$$\boldsymbol{\sigma} = E\boldsymbol{\epsilon} + \mu\dot{\boldsymbol{\epsilon}}, \tag{1.3}$$

where E is the Young's modulus of the material and μ is the material viscosity (Lai et al., 1976). Of-course these are simple rheological assumptions for each of these structures, and future developments of the model could consider more sophisticated mechanical features. For example, the ECM is a complex porous structure, percolated by interstitial fluid. Consequently, a poroviscoelastic model (e.g. in a similar manner to Cowin, 1999, Taffetani et al., 2014) could better capture ECM rheology; in our model the ECM behaves akin to a manufactured hydrogel (Saldin et al., 2017). Moreover, the ECM is an intrinsically three-dimensional structure, whilst we restrict our modelling to one- and two-dimensions. Despite these simplifications, our models are still able to capture ECM deformation in response to cell contractility, viscous resistance, energy dissipation, and serve as a platform that is readily adaptable to capture remodelling of ECM mechanical properties (e.g. strain stiffening).

1.3.3 Constitutive assumptions

Throughout this thesis, in order to close the positive feedback loop connecting FA and SF formation and to connect the cell biochemistry to the underlying mechanical properties, we make several constitutive assumptions. In particular, certain reaction rates (e.g. that of actin polymerisation) are assumed to depend on the concentration of signaling proteins. Moreover, in Chs. 3-5 we link the rate of adhesion maturation to adhesion stretch (in Ch. 2 we simply assume that the rate of adhesion maturation depends on SF concentration). Furthermore, in a similar manner to Gracheva and Othmer (2004), Larripa and Mogilner (2006), we couple the mechanical properties of the cytoskeleton and adhesions to the biochemistry (e.g. assuming a linear dependence of adhesion stiffness on adhesion density).

1.4 Existing modelling approaches

At the molecular level, several models have been developed to describe the interaction between ligands and their receptors. For example, the model of Bell (1978) is often applied to describe the dissociation of slip bonds (those which exhibit increasing dissociation as force is loaded on them), assuming the bond dissociation increases exponentially with the applied force; this model, however, assumes a bond rupture is reversible. To account for the possibility of rebinding, Li and Ji (2014) have employed Brownian dynamics simulations. Their model predicts that stronger ligand-receptor bonds form on stiffer substrates, suggesting an ability of cell-substrate adhesions to respond to mechanical cues at the molecular level (Chen et al., 2015). Separately, Erdmann and Schwarz (2006, 2007) formulate a model connecting the rebinding rate of ligand-receptor pairs to their separation, an approach that has been able to demonstrate the strong influence of substrate stiffness on the lifetime and strength of a cluster of receptor–ligand bonds (Gao et al., 2011, Qian et al., 2008, 2009). On the other hand, to describe catch ligand-receptor bonds, where the dissociation rate decreases with the applied force, several theoretical models (e.g. Pereverzev et al., 2005, Thomas et al., 2006, Zhu et al., 2005) have been developed and are reviewed by Thomas (2008). These bonds, first proposed by Dembo et al. (1988), have been reported between certain integrins and fibronectin (Kong et al., 2009).

Focal adhesions form due to the clustering of integrin-ligand connections. To describe this process, Peng et al. (2012) have formulated a model that accounts for integrin diffusion, activation and binding and predict that FA nucleation is enhanced on stiff substrates. A similar study by Bihr et al. (2012) predicts the critical number of receptor-ligand bonds needed for adhesion nucleation. A separate approach by Shemesh et al. (2005) employs a thermodynamic model to describe the aggregation of integrins to form adhesions, predicting conditions that can lead to FA growth or disassembly. Meanwhile, Welf et al. (2012) have used a coupled set of reaction-diffusion equations to predict the clustering

of integrins through localised activation and binding of integrins to ECM ligands. More recently, a coarse-grained approach has been applied by Bidone et al. (2019) to predict the formation of adhesions. Accounting for the different properties of different integrin types (e.g. diffusion, affinity to the ECM etc.), they predict the effect of ligand binding affinity of integrins and interaction strength on adhesion morphology and distribution.

Focal adhesions mature and grow under relatively small forces, but can disassemble when the applied force becomes sufficiently large (with the kinetics of bond breaking often described using Bell, 1978). To describe these two modes of behaviour, Kong et al. (2008, 2010) have employed a model at the molecular level to account for force-dependent integrin clustering and integrin–ligand binding. They demonstrate that small forces promote clustering of integrins and other adhesion molecules whilst adhesions disassemble when subjected to large forces, governed by the reaction kinetics of integrin–ligand bonds.

In this thesis we describe the coupled formation and maturation of FAs and VSFs using a theoretical model. Our approach builds on several key studies which have each considered a smaller portion of the overall process. Firstly, we model the formation of SFs in a manner similar to Deshpande et al. (2006, 2007), who developed a continuum model for SF concentration that incorporates three key biochemical processes: activation of (calcium) signaling for actin polymerisation and myosin phosphorylation, tension dependent formation of actomyosin SFs, and the generation of tension from actin-myosin interactions. Their approach predicts that SFs and FAs form near sites of applied tension (and can be extended to consider cyclic stretch, see Wei et al., 2008). Their model further predicts that cells generate lower forces on more compliant surfaces, that cell shape and boundary conditions influence the development of structural anisotropy and that SFs exhibit a high concentration local to FAs (with adhesions orienting themselves preferentially along the direction of fibres). Secondly, we model integrin activation, adhesion formation and positive feedback (connecting FA and SF development) following refinements of these SF models (Deshpande et al., 2008, Keshavanarayana et al., 2017, Vernerey and Farsad, 2014), who use a thermodynamic approach, incorporating suitable chemical potentials of low- and high-affinity integrins and the stretch energy stored in adhesions. This approach demonstrated that FAs concentrate around the cell periphery, that the fraction of the cell area covered with FAs increases with decreasing cell size and facilitated prediction of FA and SF formation on various patterned surfaces (McMeeking and Deshpande, 2017, Pathak et al., 2008). Moreover, they were able to demonstrate the formation of highly aligned SFs along the non-adhered edges of cells on concave ligand patterns. Similar analysis by Ronan et al. (2012, 2014) illustrates the effect of substrate stiffness on FA and SF formation.

Our approach is similar in spirit to the bio-chemo-mechanical model developed by Besser and Schwarz (2007) to study the deformation of SFs alone by linking the activation

of the Rho-pathway to mechanical forces at adhesions. By modelling the consequent phosphorylation of certain downstream effectors (and increased activation of myosin II), they replicated experimentally observed non-uniform striation of SFs (Peterson et al., 2004). Moreover, by considering a steady state analysis for biologically relevant parameter values, they were able to demonstrate bistability (i.e. the cell exhibits two stable steady states), characteristic of a positive feedback loop (Tyson et al., 2003). In particular, they showed one steady state corresponded to cells failing to establish mechanical stress, exhibiting low myosin II activation; the other steady state, corresponding to well adhered cells, exhibited significant intracellular stress due to the non-uniform activation of myosin motors. This was further developed by Besser et al. (2011) who, neglecting the cell biochemistry, were able to provide analytical solutions to describe cell deformation. In Ch. 3 our model similarly connects the cytoskeletal mesh scale to the microscale using discrete-to-continuum upscaling, but our model predicts FA and SF localisation without presupposing where this will occur, provides a detailed analysis of the Rho-signaling feedback loop (which is linked to changes in cell function) and incorporates ECM deformation.

Another similar modelling approach is taken by Edwards and Schwarz (2011) and Dunlop (2019), who also connect the cell (assumed to be an elastic material subjected to contractile pressures) to a substrate through a set of elastic springs to mimic FAs. This purely mechanical model has been able to predict the experimentally observed localisation of traction forces around the cell edge (and particularly to regions adhered to stiffer ECM), and non-uniform cell striation and stretch (in response to non-uniform cellular contractility). A similar approach, employed by Banerjee and Marchetti (2013), demonstrates that adhesion patterning can be used to control stress distribution in the cell. Moreover, using this framework, Solowiej-Wedderburn and Dunlop (2022, 2023) predict the effect of adhesion patterning on cell morphology, demonstrating that patterning changes the effective substrate stiffness experienced by an adhered cell. He et al. (2014) similarly consider the deformation of a cell (treated as a contracting-disk), connected to a substrate via elastic adhesions. They predict that the cell traction increases with increasing substrate stiffness before plateauing, suggesting that cells cannot sense changes in substrate stiffness at sufficiently high levels. This work has also demonstrated that displacement and stress in the substrate decay exponentially with distance from the adhering cell, with a characteristic decay length (the mechanosensing length of the cell) on the order of that of the cell radius, consistent with experimental observations (Merkel et al., 2007). This mechanosensing length has been shown to be insensitive to substrate stiffness for a wide range of stiffnesses (Chen et al., 2015).

Our model also incorporates the dynamics of actin polymerisation, building on a previous study by Mogilner and Edelstein-Keshet (2002), who considered the dynamics of actin polymerisation in the cortex of rapidly moving cells. Using a large family of PDEs they

were able to describe the dynamics of actin sequestering, nucleation of filament branches and changes in filament length due to polymerisation, capping and depolymerisation. Hu et al. (2007a) also considered actin dynamics, predicting the time taken for actin filament formation to equilibrate. Moreover, stochastic approaches by Hu and Othmer (2011), Matzavinos and Othmer (2007) predict filament growth and decay in the presence of actin binding proteins and fluctuations in actin filament length. We use a relatively simplistic (continuum) model to describe polymerisation dynamics.

In this thesis we focus on non-motile cells and consequently the formation of VSFs. The model developed couples local variations in mechanical properties induced by the signaling and scaffolding proteins to the macroscale deformation of the cell using an approach similar to Gracheva and Othmer (2004). In particular (building on earlier work by DiMilla et al., 1991, who developed a discrete model for the cell consisting of both Kelvin-Voigt and Maxwell units), they coupled the mechanical properties of the cell (treated as a Kelvin-Voigt viscoelastic material with additional active stresses) and adhesions to the cell biochemistry in motile cells (see also Larripa and Mogilner, 2006, which focuses on the formation of actin cytoskeleton). Most other models for the development of cell-substrate adhesion and cytoskeleton are focused on motile cells, where other SF types become crucial (e.g. transverse arcs or dorsal SFs); the reader is directed to detailed reviews elsewhere (e.g. Chen et al., 2020, Flaherty et al., 2007, Holmes and Edelstein-Keshet, 2012, Mak et al., 2016a, Mogilner, 2009).

Many of the aforementioned models have focused on mechanosensing through adhesions. However it is worth noting that, on short time scales, before adhesions have had an opportunity to mature, myosin motors can play a significant role in mechanosensing. For example, computational modelling by Åström et al. (2008) demonstrates that actin networks can adjust to mechanical environments by modulating cross-links within the networks. Meanwhile, modelling by Walcott and Sun (2010) demonstrates that the application of force to the cytoskeleton can cause actin filament aggregation and re-orientation to a direction parallel to the force. The filament aggregation rate is shown to be force-dependent, suggesting a mechanism for stress fibre formation and stiffness sensing for cells adhered to soft substrates. Separately, Borau et al. (2012), Kim et al. (2009a,b) use Brownian dynamics simulations to investigate the large-scale contractile responses of a cross-linked actomyosin network (on timescales of hundreds of seconds) to investigate stiffness sensing of actomyosin networks. They identify distinct mechanisms to limit the amount of internal stress depending on the mechanical properties of the substrate. Further developments by Mak et al. (2016b) incorporate actin turnover and cross-linking protein binding and unbinding, demonstrating the significant role that actin turnover has on adjusting stress and stabilising the network. Continuing with this approach, Bidone et al. (2017) have demonstrated how myosin motor and actin cross-linker density, and the ori-

entation, mechanical properties and turnover of actin filaments can influence the bundling of a cross-linked actomyosin network.

1.5 Thesis structure

The remainder of this thesis is structured as follows. In Ch. 2 we provide a simple spatially-averaged description for cell-substrate interactions. In particular, we use a large family of ODEs to describe the formation and maturation of FAs, the polymerisation of actin, activation of intracellular signaling and formation of VSFs. This approach neglects spatial variations in the biochemical properties of the cell, adhesions and the ECM, requires a high-degree of empiricism, and does not incorporate a mechanical description of cell-substrate interaction. Nonetheless, this simplistic modelling approach provides intuition, allows for rapid calculation of possible steady states and is shown to reproduce remarkably well qualitatively the global biochemical dynamics of cell-substrate adhesion and cytoskeleton development predicted by higher-dimensional models. Ch. 3 then provides a basis for the remaining work in this thesis. In Ch. 3 we develop, via discrete-continuum upscaling, a one-dimensional bio-chemo-mechanical continuum model to describe the deformation and stress of a cell adhering to a substrate, including the ECM and adhesions. We use a large family of PDEs to describe the evolution of key proteins involved in cell-substrate adhesion and cytoskeleton formation and maturation. We couple the mechanical properties of the cell, adhesions and the ECM to the concentrations and densities of these proteins. By linking the rate of adhesion maturation to adhesion stretch and of ROCK activation to adhesion density we are able to predict changes in signaling during cell-substrate interaction. We illustrate a baseline case, making predictions of both global and local behaviour of the cell. In Ch. 4, employing the model developed in Ch. 3, we perform sweeps of the parameter space, investigating the effect of various mechanotransductive and chemotransductive cues applied to the cell. In particular, we are able to elucidate the mechanism through which cells sense ECM stiffness and viscosity through adhesion maturation, how ROCK inhibition facilitates stress relaxation inside the cell and how integrin clustering to form adhesions is affected by ECM ligand density. In Ch. 5 we introduce a two-dimensional analogue to the model introduced in Ch. 3. This approach is more realistic than our one-dimensional model, facilitating the explicit inclusion of the cell nucleus (which we treat as a rigid body) and of the cell membrane, which can resist deformation. To understand the mechanism by which adhering cells adopt their characteristic non-uniform lobed shape during the cell-substrate adhesion and cytoskeleton development, we test the (linear) stability of the axisymmetric deformation to perturbation normal modes of varying azimuthal wavenumber. To conclude this thesis, in Ch. 6 we summarise and contextualise our findings and provide an outlook for future research.

Chapter 2

A spatially-averaged model

In this short Chapter, we develop a spatially-averaged framework to describe the development of cell-substrate adhesions and cell cytoskeleton, in order to develop an intuition for the cell biochemistry. In contrast with Chs. 3-5 (below), we neglect spatial variations and describe the evolution of spatially averaged concentrations of the relevant proteins (those outlined in Sec. 1.3.1 and summarised in Figs. 1.4-1.5). In particular, we use a large system of coupled ODEs to describe the formation and maturation of adhesions, the polymerisation and cross-linking of actin by myosin II to form SFs, and the activation of ROCK signaling and phosphorylation of its downstream effectors. Our approach here is significantly oversimplified as the mechanical properties of the cell and ECM do not play a role (as discussed in Ch. 3, spatial variations in myosin II generated contractility are required for cell contraction and hence adhesion stretching). Consequently, to capture the effect SFs have on FA development (through inducing adhesion stretch), we introduce an empirical relation connecting the rate of adhesion maturation to the concentration of VSFs. Despite its simplicity, this reduced approach still consistently predicts the global behaviour of a cell as it interacts with a substrate by forming FAs and developing SFs.

This Chapter is structured as follows. In Sec. 2.1 we construct our biochemical model, specifying a large family of ODEs to describe the formation of SFs (Sec. 2.1.1), the development of cell-substrate adhesions (Sec. 2.1.2), and the activation of signaling proteins and phosphorylation of their downstream effectors (Sec. 2.1.3) before specifying appropriate initial conditions (Sec. 2.1.4). To simplify our analysis, we non-dimensionalise the governing ODEs in Sec. 2.2. Thereafter, we introduce our constitutive modelling assumptions in Sec. 2.3. Particularly, we specify how adhesion formation and maturation leads to ROCK activation and increased signaling (Sec. 2.3.1) and introduce an empirical law linking the adhesion maturation rate to SF formation (Sec. 2.3.2). We specify our assumed model parameters in Sec. 2.4 and briefly describe our computational method in Sec. 2.5 before illustrating results from this model in Sec. 2.6. In particular, to investigate the temporal dynamics of a cell binding to an ECM, we present a baseline output from our model,

illustrating the evolution of the average concentration and density of key cytoskeleton, adhesion and signaling proteins with time (Sec. 2.6.1). Subsequently, we consider sweeps of the parameter space to investigate how changes in our constitutive assumptions can impact model predictions (Secs. 2.6.2-2.6.3). Finally, we apply the model to investigate how changes in the ECM ligand density (Sec. 2.6.4) and the introduction of a ROCK inhibitor (Sec. 2.6.5) can influence the development of adhesions and cytoskeleton. We conclude the Chapter with a brief summary in Sec. 2.7.

2.1 Spatially-averaged biochemical equations

In this Section we develop a spatially-averaged modelling framework to describe FA and SF formation. We formulate a set of ODEs to describe the evolution of the average concentration or density of various proteins in the cell. This formulation neglects localisation of the key cytoskeleton, adhesion and signaling proteins in the cell, which is the subject of work in Chs. 3-5. Note that several of the reactions rates describing the dynamics of scaffolding proteins are non-constant and are coupled to the concentration of signaling proteins or other scaffolding proteins; constitutive assumptions to describe these reaction kinetics are detailed in Sec. 2.3 (below). Such a dependence prevents simple decoupled solutions of the system, which must be solved numerically.

2.1.1 Cytoskeleton proteins

Based on our discussion in Ch. 1, we suppose that actin monomers, average concentration $\bar{c}_G$, are polymerised into actin filaments, average concentration $\bar{c}_F$. In practice this process occurs at adhesions (see Fig. 1.1). Hence, in this spatially-averaged model, we assume the rate of polymerisation is catalysed by bound integrins, average density $\bar{n}_b$, and FAs, average density $\bar{n}_A$. Subsequently, actin filaments can be cross-linked by activated myosin II, average concentration $\bar{c}_m^+$, to form contractile VSFs, with average concentration $\bar{c}_S^+$; the dynamics of myosin II activation are described below. We describe the average concentration of actin monomers by

$$\frac{d\bar{c}_G}{dt} = -k_p^+ \bar{c}_G \left(\bar{n}_b + \bar{n}_A\right) + k_p^- \bar{c}_F + k_m^- \bar{c}_S^+, \tag{2.1a}$$

where k_p^+ represents the rate per adhesion of actin polymerisation, k_p^- is the dissociation rate of actin filaments and k_m^- is the dissociation rate of SFs; note that in this model the rates of actin polymerisation and depolymerisation depend on the concentration of signaling proteins, as detailed in Sec. 2.3.1 (below). In particular, we assume that SFs decompose directly into their constituent actin monomers (and myosin cross-linkers). We

describe the corresponding dynamics of the actin filaments by

$$\frac{d\bar{c}_F}{dt} = k_p^+ \bar{c}_G \left(\bar{n}_b + \bar{n}_A\right) - k_p^- \bar{c}_F - k_m^+ \bar{c}_F \left(\bar{c}_F + \bar{c}_S^+\right) \bar{c}_m^+, \tag{2.1b}$$

where cross-linking of actin filaments by myosin II occurs at a rate proportional to k_m^+. In turn, the corresponding dynamics of SFs satisfy

$$\frac{d\bar{c}_S^+}{dt} = k_m^+ \left(\bar{c}_F + \bar{c}_S^+\right) \bar{c}_m^+ - k_m^- \bar{c}_S^+. \tag{2.1c}$$

Notice that we satisfy the conservation law

$$\frac{d}{dt}\left(\bar{c}_G + \bar{c}_F + \bar{c}_S^+\right) = 0, \tag{2.1d}$$

i.e. the total actin in the cell, $\bar{c}_G + \bar{c}_F + \bar{c}_S^+$, is a constant, K_A.

Inactive myosin II, average concentration $\bar{c}_m$, is activated in response to signaling proteins which, in turn, are regulated by ROCK. The concentration of inactive myosin II and activated myosin II are described, respectively, by

$$\frac{d\bar{c}_m}{dt} = -k_a^+ \bar{c}_m + k_a^- \bar{c}_m^+, \tag{2.1e}$$

$$\frac{d\bar{c}_m^+}{dt} = k_a^+ \bar{c}_m - k_a^- \bar{c}_m^+ - k_m^+ \bar{c}_F \left(\bar{c}_F + \bar{c}_S^+\right) \bar{c}_m^+ + k_m^- \bar{c}_S^+, \tag{2.1f}$$

where k_a^+ is the rate at which myosin II is activated and k_a^- is the rate at which active myosin II is inactivated (these rates are non-constant, depending on the concentration of signaling proteins, as detailed below in Sec. 2.3.1); free active myosin II is lost due to its recruitment into SFs.

2.1.2 Adhesion proteins

Interaction between the cell and substrate occurs primarily via adhesions. The formation of these structures is initiated by the binding of talin to free integrins, average density $\bar{n}_f$, to form high-affinity integrins, average density $\bar{n}_h$. We describe the dynamics of free integrins by

$$\frac{d\bar{n}_f}{dt} = -k_h^+ \bar{n}_f + k_h^- \bar{n}_h, \tag{2.1g}$$

where k_h^+ is the rate of integrin activation and k_h^- is the rate of integrin inactivation. High-affinity integrins then bind to ECM ligands, average density $\bar{n}_s$, to form bound integrins, $\bar{n}_b$. The dynamics of high-affinity integrins and ECM ligands are described by

$$\frac{d\bar{n}_h}{dt} = k_h^+ \bar{n}_f - k_h^- \bar{n}_h - k_b^+ \bar{n}_h \bar{n}_s + k_b^- \bar{n}_b, \tag{2.1h}$$

$$\frac{d\bar{n}_s}{dt} = -k_b^+ \bar{n}_h \bar{n}_s + k_b^- \bar{n}_b, \tag{2.1i}$$

where binding occurs at a rate proportional to k_b^+ and integrin-ligand connections break at a rate k_b^-. We describe the dynamics of bound integrins by the simple reaction equation

$$\frac{d\bar{n}_b}{dt} = k_b^+ \bar{n}_h \bar{n}_s - k_b^- \bar{n}_b - k_F^+ \bar{n}_b + k_F^- \bar{n}_A, \tag{2.1j}$$

where bound integrins mature into FAs, $\bar{n}_A$, at rate k_F^+, and FAs dissociate into weaker bound integrins at rate k_F^-. We describe the dynamics of FA formation by

$$\frac{d\bar{n}_A}{dt} = k_F^+ \bar{n}_b - k_F^- \bar{n}_A. \tag{2.1k}$$

Note that the adhesion maturation rate is linked to the concentration of SFs in the cell, this is discussed in Sec. 2.3.2 (below).

2.1.3 Signaling proteins

We focus on Rho signaling, which becomes activated in response to the formation of cell-substrate adhesions, regulating actin polymerisation rates and myosin II activation (Deguchi and Sato, 2009) through a variety of mechanisms including upregulation of mDia1 and ROCK (Feng et al., 1999, Maekawa et al., 1999), as shown in Fig. 1.5. For modelling simplicity, we assume that increases in mDia1 activity occurs in tandem with ROCK activation. Therefore, we use activated ROCK as a proxy measure for mDia1 activity and hence the actin polymerisation rate. Activation or phosphorylation of each of these species is described by very simple reaction kinetics, however several of the subsequent rate constants are not constant, complicating dynamics.

We let $\bar{c}_R$ denote the average concentration of inactive ROCK and $\bar{c}_R^+$ denote the average concentration of activated ROCK inside the cell. We describe the dynamics of ROCK activation by

$$\frac{d\bar{c}_R}{dt} = -k_R^+ \bar{c}_R + k_R^- \bar{c}_R^+, \tag{2.1l}$$

$$\frac{d\bar{c}_R^+}{dt} = k_R^+ \bar{c}_R - k_R^- \bar{c}_R^+, \tag{2.1m}$$

where k_R^+ is the activation rate of inactive ROCK and k_R^- is the rate at which activated ROCK becomes inactivated.

In response to ROCK activation, MLCP, average concentration $\bar{c}_P$, is phosphorylated at rate k_1^+ to form phosphorylated MLCP, average concentration $\bar{c}_{P-P}$. Phosphorylated MLCP is dephosphorylated at rate k_1^-. The reaction dynamics for MLCP are hence de-

scribed by

$$\frac{d\bar{c}_P}{dt} = -k_1^+ \bar{c}_P + k_1^- \bar{c}_{P-P}, \tag{2.1n}$$

$$\frac{d\bar{c}_{P-P}}{dt} = k_1^+ \bar{c}_P - k_1^- \bar{c}_{P-P}. \tag{2.1o}$$

A further consequence of ROCK activation is phosphorylation of MLCK, average concentration $\bar{c}_K$, at rate k_2^+ to form phosphorylated MLCK, average concentration $\bar{c}_{K-P}$. Phosphorylated MLCK is dephosphorylated at rate k_2^-. The reaction dynamics for MLCK are hence described by

$$\frac{d\bar{c}_K}{dt} = -k_2^+ \bar{c}_K + k_2^- \bar{c}_{K-P}, \tag{2.1p}$$

$$\frac{d\bar{c}_{K-P}}{dt} = k_2^+ \bar{c}_K - k_2^- \bar{c}_{K-P}. \tag{2.1q}$$

Finally, ROCK activation also precipitates phosphorylation of cofilin, average concentration $\bar{c}_C$. Phosphorylation occurs at rate k_3^+ to form phosphorylated cofilin, average concentration $\bar{c}_{C-P}$. Phosphorylated cofilin is dephosphorylated at rate k_3^-. The reaction dynamics for cofilin are described by

$$\frac{d\bar{c}_C}{dt} = -k_3^+ \bar{c}_C + k_3^- \bar{c}_{C-P}, \tag{2.1r}$$

$$\frac{d\bar{c}_{C-P}}{dt} = k_3^+ \bar{c}_C - k_3^- \bar{c}_{C-P}. \tag{2.1s}$$

Despite their relatively simple appearance, the dynamics of signaling proteins are coupled to the dynamics of the wider system. Indeed several of the reaction rates are non-constant functions of other variables (as detailed below in Sec. 2.3).

2.1.4 Initial conditions

We assume that the cell is newly introduced to the substrate so that no adhesions have formed and all integrins are in their low-affinity state for ECM ligand binding. Moreover, we assume that no SFs or actin filaments have formed so that all actin is monomeric. We additionally assume that ROCK is initially wholly inactive and consequently, MLCP, MLCK and cofilin are all initially unphosphorylated, with myosin II found entirely in its inactive state. The full details of the initial conditions are presented in Table 2.1 in Sec. 2.4 (below).

2.2 Non-dimensionalisation

To simplify our analysis, we non-dimensionalise our biochemical and mechanical equations. We scale actin concentrations on C_A, the initial average concentration of actin (in all its forms), scale myosin concentrations on C_M, the initial average concentration of myosin (in its inactive and active forms). We scale integrin and adhesion density on the average initial integrin (in all its forms) density, N_I, and scale ligand density on N_S, the initial average free ligand density. A similar treatment is given to signaling proteins with ROCK concentration scaled on C_R, the average initial ROCK concentration (in its active and inactive forms), MLCP concentration scaled on C_P, the average concentration of MLCP (in its phosphorylated and unphosphorylated forms), MLCK concentration is scaled on C_K, the average total concentration of MLCK (in its phosphorylated and unphosphorylated forms) and cofilin concentration is scaled on C_C, the average total concentration of cofilin (in its phosphorylated and unphosphorylated forms). In particular, we set

$$\begin{gathered} C_A = \bar{c}_G(0) + \bar{c}_F(0) + \bar{c}_S^+(0), \quad C_M = \bar{c}_m(0) + \bar{c}_m^+(0), \\ N_I = \bar{n}_f(0) + \bar{n}_h(0) + \bar{n}_b(0) + \bar{n}_A(0), \quad N_S = \bar{n}_s(0), \\ C_R = \bar{c}_R(0) + \bar{c}_R^+(0), \quad C_P = \bar{c}_P(0) + \bar{c}_{P-P}(0), \\ C_K = \bar{c}_K(0) + \bar{c}_{K-P}(0), \quad C_C = \bar{c}_C(0) + \bar{c}_{C-P}(0). \end{gathered} \tag{2.2}$$

Moreover, given that our primary interest is in the microscale patterning of adhesion, we scale time on $\langle t \rangle = 1/\left(k_b^+ N_S\right)$, the characteristic timescale for the formation of nascent adhesions (due to the binding of high-affinity integrins with ECM ligands). Note that this process is rapid compared to adhesion maturation into focal structures, and so we consider the dynamics of the model over a large number of dimensionless time units. Although we do not explore in detail here, this sets up a fascinating problem that is amenable to a multiple scales analysis, which may in future allow for simplification of the model as certain reactions happen on very short timescales. Such an analysis requires a large separation of timescales. As evidenced in Sec. 2.4 and Table 2.4 (below), we expect such a separation in our system, with at least three important timescales: integrin activation (which happens on very short timescales); integrin-ligand binding (the timescale on which we have non-dimensionalised the system); and adhesion maturation (which happens on longer timescales). This is further evidenced in Fig. 2.1 (see Sec. 2.6, below).

By introducing the following dimensionless groups

$$\begin{gathered}
\tilde{k}_p^+ = k_p^+ N_I \langle t \rangle, \quad \tilde{k}_p^- = k_p^- \langle t \rangle, \quad \tilde{k}_m^+ = k_m^+ C_A C_M \langle t \rangle, \quad \check{k}_m^+ = k_m^+ C_A^2 \langle t \rangle, \\
\tilde{k}_m^- = k_m^- \langle t \rangle, \quad \check{k}_m^- = k_m^- \langle t \rangle C_A / C_M, \quad \tilde{k}_a^+ = k_a^+ \langle t \rangle, \quad \tilde{k}_a^- = k_a^- \langle t \rangle, \\
\tilde{k}_h^+ = k_h^+ \langle t \rangle, \quad \tilde{k}_h^- = k_h^- \langle t \rangle, \quad \tilde{k}_b^+ = k_b^+ N_S \langle t \rangle (= 1), \quad \check{k}_b^+ = k_b^+ N_I \langle t \rangle, \\
\tilde{k}_b^- = k_b^- \langle t \rangle, \quad \check{k}_b^- = k_b^- \langle t \rangle N_I / N_S, \quad \tilde{k}_F^+ = k_F^+ \langle t \rangle, \quad \tilde{k}_F^- = k_F^- \langle t \rangle, \\
\tilde{k}_R^+ = k_R^+ \langle t \rangle, \quad \tilde{k}_R^- = k_R^- \langle t \rangle, \quad \tilde{k}_1^+ = k_1^+ \langle t \rangle, \quad \tilde{k}_1^- = k_1^- \langle t \rangle, \\
\tilde{k}_2^+ = k_2^+ \langle t \rangle, \quad \tilde{k}_2^- = k_2^- \langle t \rangle, \quad \tilde{k}_3^+ = k_3^+ \langle t \rangle, \quad \tilde{k}_3^- = k_3^- \langle t \rangle,
\end{gathered} \tag{2.3}$$

we can write the dimensional governing ODEs, described by Eq. (2.1) in Sec. 2.1, in the following dimensionless form

$$\frac{d\bar{c}_G}{dt} = -\tilde{k}_p^+ \bar{c}_G \left(\bar{n}_B + \bar{n}_A\right) + \tilde{k}_p^- \bar{c}_F + \tilde{k}_m^- \bar{c}_S^+, \tag{2.4a}$$

$$\frac{d\bar{c}_F}{dt} = \tilde{k}_p^+ \bar{c}_G \left(\bar{n}_B + \bar{n}_A\right) - \tilde{k}_p^- \bar{c}_F - \tilde{k}_m^+ \bar{c}_F \left(\bar{c}_F + \bar{c}_S^+\right) \bar{c}_m^+, \tag{2.4b}$$

$$\frac{d\bar{c}_S^+}{dt} = \tilde{k}_m^+ \bar{c}_F \left(\bar{c}_F + \bar{c}_S^+\right) \bar{c}_m^+ - \tilde{k}_m^- \bar{c}_S^+, \tag{2.4c}$$

$$\frac{d\bar{c}_m}{dt} = -\tilde{k}_a^+ \bar{c}_m + \tilde{k}_a^- \bar{c}_m^+, \tag{2.4d}$$

$$\frac{d\bar{c}_m^+}{dt} = \tilde{k}_a^+ \bar{c}_m - \tilde{k}_a^- \bar{c}_m^+ - \check{k}_m^+ \bar{c}_F \left(\bar{c}_F + \bar{c}_S^+\right) \bar{c}_m^+ + \check{k}_m^- \bar{c}_S^+, \tag{2.4e}$$

$$\frac{d\bar{n}_f}{dt} = -\tilde{k}_h^+ \bar{n}_f + \tilde{k}_h^- \bar{n}_h, \tag{2.4f}$$

$$\frac{d\bar{n}_h}{dt} = \tilde{k}_h^+ \bar{n}_f - \tilde{k}_h^- \bar{n}_h - \tilde{k}_b^+ \bar{n}_h \bar{n}_s + \tilde{k}_b^- \bar{n}_b, \tag{2.4g}$$

$$\frac{d\bar{n}_b}{dt} = \tilde{k}_b^+ \bar{n}_h \bar{n}_s - \tilde{k}_b^- \bar{n}_b - \tilde{k}_F^+ \bar{n}_b + \tilde{k}_F^- \bar{n}_A, \tag{2.4h}$$

$$\frac{d\bar{n}_A}{dt} = \tilde{k}_F^+ \bar{n}_b - \tilde{k}_F^- \bar{n}_A, \tag{2.4i}$$

$$\frac{d\bar{n}_s}{dt} = -\check{k}_b^+ \bar{n}_h \bar{n}_s + \check{k}_b^- \bar{n}_b, \tag{2.4j}$$

$$\frac{d\bar{c}_R}{dt} = -k_R^+ \bar{c}_R + k_R^- \bar{c}_R^+, \tag{2.4k}$$

$$\frac{d\bar{c}_R^+}{dt} = k_R^+ \bar{c}_R - k_R^- \bar{c}_R^+, \tag{2.4l}$$

$$\frac{d\bar{c}_P}{dt} = -\tilde{k}_1^+ \bar{c}_P + \tilde{k}_1^- \bar{c}_{P-P}, \tag{2.4m}$$

$$\frac{d\bar{c}_{P-P}}{dt} = \tilde{k}_1^+ \bar{c}_P - \tilde{k}_1^- \bar{c}_{P-P}, \tag{2.4n}$$

$$\frac{d\bar{c}_K}{dt} = -\tilde{k}_2^+ \bar{c}_K + \tilde{k}_2^- \bar{c}_{K-P}, \tag{2.4o}$$

$$\frac{d\bar{c}_{K-P}}{dt} = \tilde{k}_2^+ \bar{c}_K - \tilde{k}_2^- \bar{c}_{K-P}, \tag{2.4p}$$

$$\frac{d\bar{c}_C}{dt} = -\tilde{k}_3^+ \bar{c}_C + \tilde{k}_3^- \bar{c}_{C-P}, \tag{2.4q}$$

$$\frac{d\bar{c}_{C-P}}{dt} = \tilde{k}_3^+ \bar{c}_C - \tilde{k}_3^- \bar{c}_{C-P}. \tag{2.4r}$$

2.3 Constitutive assumptions

As discussed in Ch. 1 and indicated in Fig. 1.5, a positive feedback loop connects FA and SF development. To capture this we make several modelling assumptions, we outline these here.

2.3.1 Signaling proteins effect on reaction rates

To capture the effect adhesion formation and maturation has on intracellular signaling (Bhadriraju et al., 2007), we describe the rate of ROCK activation by

$$k_R^+ = K_R^+ \left(\bar{n}_b + \delta \bar{n}_A\right)/N_I, \tag{2.5}$$

where K_R^+ is a dimensional rate constant. This form is chosen so that the relative strength of signaling due to FAs compared to nascent adhesions is increased by a factor of $\delta = O(1)$.

To incorporate the effects of ROCK activation on MLCP, MLCK and cofilin phosphorylation (Dalby et al., 2018, Deguchi and Sato, 2009, Maekawa et al., 1999), we set $k_j^+ = K_j^+ g_j\left(\bar{c}_R^+/C_R\right)$, $j = 1, 2, 3$, where K_j^+ are dimensional rate constants and g_j are dimensionless functions of activated ROCK concentration.

To capture the effect that MLCK phosphorylation has on myosin II activation and that MLCP phosphorylation has on myosin II inactivation (as discussed in Sec. 1.2.5) we set

$$k_a^+ = K_a^+ g_a^+\left(\bar{c}_{K-P}/C_K\right), \quad g_a^+\left(\bar{c}_{K-P}/C_K\right) = \bar{c}_{K-P}/C_K, \tag{2.6a}$$

$$k_a^- = K_a^- g_a^-\left(\bar{c}_P/C_P\right), \quad g_a^-\left(\bar{c}_P/C_P\right) = \bar{c}_P/C_P, \tag{2.6b}$$

where K_a^+, K_a^- are dimensional constants and g_a^+, g_a^- are dimensionless functions of phosphorylated MLCK and unphosphorylated MLCP concentration, respectively.

Finally, to capture the effects increased Rho and ROCK activation has on actin polymerisation and that cofilin phosphorylation has on actin depolymerisation (as discussed in Sec. 1.2.5), we set

$$k_p^+ = K_p^+ g_p^+\left(\bar{c}_R^+/C_R\right), \quad g_p^+\left(\bar{c}_R^+/C_R\right) = \bar{c}_R^+/C_R, \tag{2.6c}$$

$$k_p^- = K_p^- g_p^-\left(\bar{c}_C/C_C\right), \quad g_p^-\left(\bar{c}_C/C_C\right) = \bar{c}_C/C_C, \tag{2.6d}$$

where K_p^+, K_p^- are dimensional constants and g_p^+, g_p^- are dimensionless functions of the concentration of ROCK and unphosphorylated cofilin.

2.3.2 The effect of stress fibre formation

In response to contractile forces generated by SFs, nascent adhesions mature into FAs. In Chs. 3-5 (below) the rate of formation of FAs is assumed to depend on the length (or stretch) of integrin-ligand connections, facilitating mechanical feedback into the cell biochemistry. However, our spatially-averaged modelling approach does not incorporate mechanical deformation. Consequently, we develop an empirical relation to link the rate of adhesion maturation to SF concentration, setting

$$k_F^+ = K_F^+ g_s^+ \left(\bar{c}_S^+/C_A\right), \quad g_s^+ \left(\bar{c}_S^+/C_A\right) = \frac{\left(\bar{c}_S^+/C_A\right)^\alpha}{\left(\bar{c}_S^+/C_A\right)^\alpha + \beta^\alpha}, \tag{2.7}$$

where K_F^+ is a dimensionless constant and g_s^+ is a dimensionless function of SF concentration; α describes the strength of coupling between SFs and FA formation and β is the fraction of actin recruited into SFs that precipitates a half-maximal response. The assumed form of g_s^+ (a Hill type equation) is used to capture increased FA formation with SF formation; this rate saturates when SFs become sufficiently dense (and adhesions stretched), reflecting resistance to continued adhesion stretch as adhesions mature.

2.4 Parameter estimation

In this Section we briefly outline the (baseline) parameter values we employ in our model. Unless otherwise stated, in Sec. 2.6 these constitute the initial value used for each protein species (Table 2.1), and the assumed rates used for scaffolding proteins (Table 2.2) and for signaling proteins (Table 2.3). Note that we assume the cell has a volume of $V = 1000\ \mu\text{m}^3$.

Protein	Value	Justification/interpretation
$\bar{c}_G(0)$	$(100/V)\ \mu\text{M}\ \mu\text{m}^{-3}$	All actin is initially sequestered. In line with Kiuchi et al. (2011) who suggest that most living cells contain roughly 100 μM of G-actin.
$\bar{c}_F(0)$	$0\ \mu\text{M}\ \mu\text{m}^{-3}$	All actin is initially sequestered.
$\bar{c}_S^+(0)$	$0\ \mu\text{M}\ \mu\text{m}^{-3}$	All actin is initially sequestered.
$\bar{c}_m(0)$	$(30/V)\ \mu\text{M}\ \mu\text{m}^{-3}$	All myosin II initially inactive. Estimated based on Besser and Schwarz (2007), who use a total amount of myosin II of 30 μM (based on Butler et al. (1994)); and on Gracheva and Othmer (2004) who assume a total amount of myosin II of 20 μM.
$\bar{c}_m^+(0)$	$0\ \mu\text{M}\ \mu\text{m}^{-3}$	All myosin II initially inactive.

Continued on the next page

Table 2.1 – continued from previous page

Protein	Value	Justification/Interpretation
$\bar{n}_f(0)$	$100\ \mu\text{m}^{-2}$	Initially no adhesions have formed. The same value has been used by Bidone et al. (2019) (based on Oakes et al., 2018) and by Paszek et al. (2009).
$\bar{n}_h(0)$	$0\ \mu\text{m}^{-2}$	Initially no adhesions have formed.
$\bar{n}_b(0)$	$0\ \mu\text{m}^{-2}$	Initially no adhesions have formed.
$\bar{n}_A(0)$	$0\ \mu\text{m}^{-2}$	Initially no adhesions have formed.
$\bar{n}_s(0)$	$1000\ \mu\text{m}^{-2}$	The same value has been used by Bidone et al. (2019) and is consistent with Paszek et al. (2009).
$\bar{c}_R(0)$	$(1/V)$ nM μm^{-3}	Assume all ROCK is initially inactive. Besser and Schwarz (2007) use values for the total amount of ROCK of 0-5 nM based on Feng et al. (1999).
$\bar{c}_R^+(0)$	0 nM μm^{-3}	Assume all ROCK is initially inactive.
$\bar{c}_K(0)$	$(0.1/V)\ \mu$M μm^{-3}	All MLCK is initially unphosphorylated. Besser and Schwarz (2007) use a value for the total amount of MLCK of 0.1 μM based on Nagamoto and Yagi (1984).
$\bar{c}_{K-P}(0)$	$0\ \mu$M μm^{-3}	Assume all MLCK is initially unphosphorylated.
$\bar{c}_P(0)$	$(1/V)\ \mu$M μm^{-3}	All MLCP is initially unphosphorylated. Besser and Schwarz (2007) use values for the total amount of MLCP of 0-1.2 μM based on Hartshorne et al. (1998).
$\bar{c}_{P-P}(0)$	$0\ \mu$M μm^{-3}	Assume all MLCP is initially unphosphorylated.
$\bar{c}_C(0)$	$(1/V)\ \mu$M μm^{-3}	Assume all cofilin is initially unphosphorylated.
$\bar{c}_{C-P}(0)$	$0\ \mu$M μm^{-3}	Assume all cofilin is initially unphosphorylated.

Table 2.1: Baseline initial conditions imposed on protein concentrations in spatially-averaged model.

Parameter	Value	Justification/Interpretation
K_p^+	$2 \times 10^{-3}\,\text{adhesion}^{-1}\,\text{s}^{-1}$	Typical actin polymerisation rate. Order of magnitude estimate based on Larripa and Mogilner (2006), Svitkina et al. (1997) (and the noted difference in filament density between the cell centre and edge).
k_p^-	$1 \times 10^{-2}\,\text{s}^{-2}$	Actin filament sequestering rate. Estimate inferred from Larripa and Mogilner (2006) based on Svitkina et al. (1997).
K_a^+	$1 \times 10^{-2}\,\text{s}^{-1}$	Typical myosin II activation rate. Estimated (chosen so that activation occurs on the order of minutes).
K_a^-	$1 \times 10^{-2}\,\text{s}^{-1}$	Typical rate of myosin II inactivation. (chosen so that inactivation occurs on the order of minutes).
k_m^+	$1 \times 10^{2}\,\mu\text{M}^{-2}\,\text{s}^{-1}$	Rate of cross-linking of actin bundles by myosin II. Order of magnitude inferred from Larripa and Mogilner (2006).
k_m^-	$1 \times 10^{-2}\,\text{s}^{-1}$	Rate of SF disassembly into constituent actin monomers and myosin II. Estimate inferred from Larripa and Mogilner (2006).
k_h^+	$0.5\,\text{s}^{-1}$	Rate of conversion of free integrins to high-affinity. The same value is used by Paszek et al. (2009) based on Iber and Campbell (2006), Tadokoro et al. (2003).
k_h^-	$5\,\text{s}^{-1}$	Rate of conversion of integrins from high-affinity to low-affinity. The same value is used by Paszek et al. (2009) based on Iber and Campbell (2006), Tadokoro et al. (2003).
k_b^+	$1 \times 10^{-4}\,\text{ligand}^{-1}\,\text{s}^{-1}$	Rate of integrin-ligand binding (nascent adhesion formation). Estimated based on rapid formation of bound integrins (on the order of tens of seconds).
k_b^-	$1 \times 10^{-2}\,\text{s}^{-1}$	Rate of nascent adhesion disassembly. Estimated based on expected short lifetime (compared to FAs) on the order of tens of seconds to minutes.

Continued on the next page

Table 2.2 – continued from previous page

Parameter	Value	Justification/Interpretation
K_F^+	$1 \times 10^{-2}\ \mathrm{s}^{-1}$	Rate of FA formation. Order of magnitude estimate chosen so that reverse reaction dominates when there is little SF formation but forward reaction dominates when SF concentration is large.
k_F^-	$1 \times 10^{-3}\ \mathrm{s}^{-1}$	Rate of FA disassembly. Estimated based on expected long lifetime (compared to nascent adhesions) on the order of tens of minutes.

Table 2.2: Baseline parameters for scaffolding protein dynamics in spatially-averaged model.

Parameter	Value	Justification/Interpretation
K_R^+	$1 \times 10^{-2}\ \mathrm{s}^{-1}$	Typical activation rate of phosphorylation of ROCK. Estimated (chosen to ensure little ROCK activation when adhesions have not matured).
k_R^-	$1 \times 10^{-1}\ \mathrm{s}^{-1}$	Typical inactivation rate of activated ROCK. Estimated (chosen to ensure little ROCK activation without adhesion maturation).
δ	4	Increase in ROCK activation rate due to adhesion maturation. Based on parameter sweep outlined in Sec. 2.6.2.
α	2	Hill coefficient (strength of coupling between SF formation and adhesion maturation rate). Based on parameter sweep outlined in Sec. 2.6.2.
β	0.25	Fraction of actin recruited into SFs that precipitates a half-maximal adhesion maturation rate. Based on parameter sweep outlined in Sec. 2.6.2.
K_1^+	$1 \times 10^{-2}\ \mathrm{s}^{-1}$	Typical rate of phosphorylation of MLCP. Estimated (chosen to ensure little phosphorylation without adhesion maturation).
k_1^-	$1 \times 10^{-2}\ \mathrm{s}^{-1}$	Rate of dephosphorylation of MLCP-P. Estimated (chosen to ensure little phosphorylation without adhesion maturation).

Continued on the next page

Table 2.3 – continued from previous page

Parameter	Value	Justification/Interpretation
K_2^+	$1 \times 10^{-2}\ \mathrm{s}^{-1}$	Rate of phosphorylation of MLCK. Estimated (chosen to ensure little phosphorylation without adhesion maturation).
k_2^-	$1 \times 10^{-2}\ \mathrm{s}^{-1}$	Rate of dephosphorylation of MLCK-P. Estimated (chosen to ensure little phosphorylation without adhesion maturation).
K_3^+	$5 \times 10^{-2}\ \mathrm{s}^{-1}$	Rate of phosphorylation of cofilin. Estimated based on 10-30% phosphorylation of cofilin (Prudent et al., 2018).
k_3^-	$1 \times 10^{-2}\ \mathrm{s}^{-1}$	Rate of dephosphorylation of phosphorylated cofilin. Estimated based on 10-30% phosphorylation of cofilin (Prudent et al., 2018).

Table 2.3: Baseline parameters for signaling protein dynamics in spatially-averaged model.

2.5 Computational method

We solve the large system of dimensionless governing biochemical ODEs numerically using the Matlab solver ode15s, employing Matlab's default error tolerances. The results are well converged (even for long times), and an in-depth analysis on a similar system is presented in Sec. 3.8.1 in Ch. 3 (below).

2.6 Results

In this Section we present results from this spatially-averaged model. We begin in Sec. 2.6.1 by illustrating a baseline output from this model, using parameter values as outlined in Sec. 2.4. This summarises the global response of the cell, including the formation of FAs and SFs, when interacting with ECM. We then proceed to investigate the effect of changes to our baseline parameter values on model predictions (Secs. 2.6.2-2.6.3), and explore the effect of environmental and chemotransductive cues on the development and sustainability of cell-substrate adhesions and cell cytoskeleton (Secs. 2.6.4-2.6.5). Note that in Secs. 2.6.2-2.6.5 we consider the dynamics of the system at $t = 10000$ s, where the system is generally at a steady state. For the sake of consistency with Chs. 3-5 we do not consider a formal steady state analysis (where such a computation is significantly more computationally costly given the large system of coupled equations). However, this simple

ODE model is readily amenable to such an analysis, and would assist in understanding bifurcations in the system. We suspend simulations at $t = 10000$ s, not only because our simulations are at steady state, but also because beyond this time other effects (e.g. cell remodelling of its microenvironment and growth) likely become important, reducing the applicability of the model.

2.6.1 Baseline

In order to elucidate the overall temporal dynamics of cell-substrate binding, Fig. 2.1 illustrates a number of global measures of the system, which summarise the adhesion strength and cytoskeleton development over time. We solve the dimensionless governing equations, with dimensionless parameters (based on our parameter estimation in Sec. 2.4) detailed in Table 2.4. As a function of time, we plot the partition of integrins across their different forms (Fig. 2.1a), the fraction of signaling proteins activated or phosphorylated (Fig. 2.1b), the partition of actin into its different forms (Fig. 2.1c) and the partition of myosin into its inactivated or activated forms as a function of time (Fig. 2.1d). Note that, to more easily facilitate comparison with results presented in Chs. 3-5 (see Figs. 3.7, 5.3 below), we highlight in Fig. 2.1 certain times using open circles. In particular, we highlight $t = 250$ s (grey), $t = 500$ s (dark blue), $t = 1000$ s (orange), $t = 1500$ s (yellow), $t = 2000$ s (purple), $t = 2500$ s (green), $t = 5000$ s (maroon) and $t = 10000$ s (black) after the cell has been introduced to the substrate.

Dimensionless parameter	**Value**	**Dimensionless parameter**	**Value**
$\tilde{K}_p^+$	2	$\tilde{K}_p^-$	0.1
$\tilde{K}_a^+$	0.1	$\tilde{K}_a^-$	0.1
$\tilde{k}_m^+$	3	$\tilde{k}_m^-$	0.1
$\check{k}_m^+$	10	$\check{k}_m^-$	$0.\bar{3}$
$\tilde{k}_h^+$	5	$\tilde{k}_h^-$	50
$\tilde{k}_b^+$	1	$\tilde{k}_b^-$	0.1
$\check{k}_b^+$	0.1	$\check{k}_b^-$	0.01
$\tilde{K}_F^+$	0.1	$\tilde{k}_F^-$	0.01
$\tilde{K}_R^+$	0.1	$\tilde{K}_R^+$	1
$\tilde{K}_1^+$	0.1	$\tilde{K}_1^-$	0.1
$\tilde{K}_2^+$	0.1	$\tilde{K}_2^-$	0.1
$\tilde{K}_3^+$	0.5	$\tilde{K}_3^-$	0.1

Table 2.4: Dimensionless parameters employed in baseline simulations of spatially-averaged model.

In the early stages after the cell is introduced to the substrate the cell, free (low-affinity) integrins are rapidly activated to form high-affinity integrins (Fig. 2.1a). High-affinity integrins subsequently bind to ECM ligands to form bound integrins (i.e. nascent adhesions) in line with Eqs. (2.1h)-(2.1j), as shown in Fig. 2.1(a). The formation of nascent adhesions leads to weak activation of ROCK and phosphorylation of its downstream effectors MLCP, MLCK and cofilin (Fig. 2.1b). In response, actin is polymerised (Fig. 2.1c) and a small amount of myosin II is activated (Fig. 2.1d), leading to an increase in actin filament concentration and a small increase in VSF concentration (Fig. 2.1c). In response to the formation of VSFs, the adhesion maturation rate increases in line with Eq. (2.7), leading to the formation of mature FAs (Fig. 2.1a); this process begins several minutes after the cell is introduced to the substrate, consistent with experimental observations (e.g. see Mavrakis and Juanes, 2023). Adhesion maturation precipitates a commensurate increase in ROCK activation (in line with Eq. 2.5), and, consequently, enhanced MLCP, MLCK and cofilin phosphorylation (Fig. 2.1b). This initiates positive feedback, with the activation of signaling proteins leading to an increase (decrease) in actin polymerisation (depolymerisation), as observed in Fig. 2.1(c), and in myosin II activation (inactivation), as observed in Fig. 2.1(d). In particular, there are significant increases in actin filament and VSF formation (Fig. 2.1c), leading to further strengthening of adhesions. After approximately 2500 s, the cell settles to a steady state (Fig. 2.1a-d). However, this final steady state is a consequence of our modelling approach, whereas the cell would continue to grow, interact with neighbouring cells and remodel its environment.

We note that the results presented in Fig. 2.1 are similar to the predictions for the global dynamics of cell-substrate adhesion made by the one- and two-dimensional models we subsequently develop in Chs. 3-5 (below). Given that this simple zero-dimensional system is readily amenable to a multiple scales analysis, this spatially-averaged model could be employed to reduce the complexity (through a reduction in the number of parameters and equations) of higher-dimensional models.

2.6.2 Varying feedback strength

In forming the model we have introduced empirical parameters δ, α and β. Recall from Eq. (2.5) that δ measures the relative increase in the rate of ROCK activation when adhesions mature into FAs compared to when they are immature (i.e. bound integrins). Meanwhile, from Eq. (2.7), α is a Hill coefficient, measuring the strength of coupling between SF concentration and the adhesion maturation rate, and β is the fraction of actin that must be recruited into SFs to produce a half-maximal rate of adhesion maturation. These parameters essentially govern the strength of the positive feedback loop, with δ ensuring that maturation of adhesions leads to increased phosphorylation of MLCP, MLCK and cofilin and consequently increased VSF formation, whilst α and β ensure that SF for-

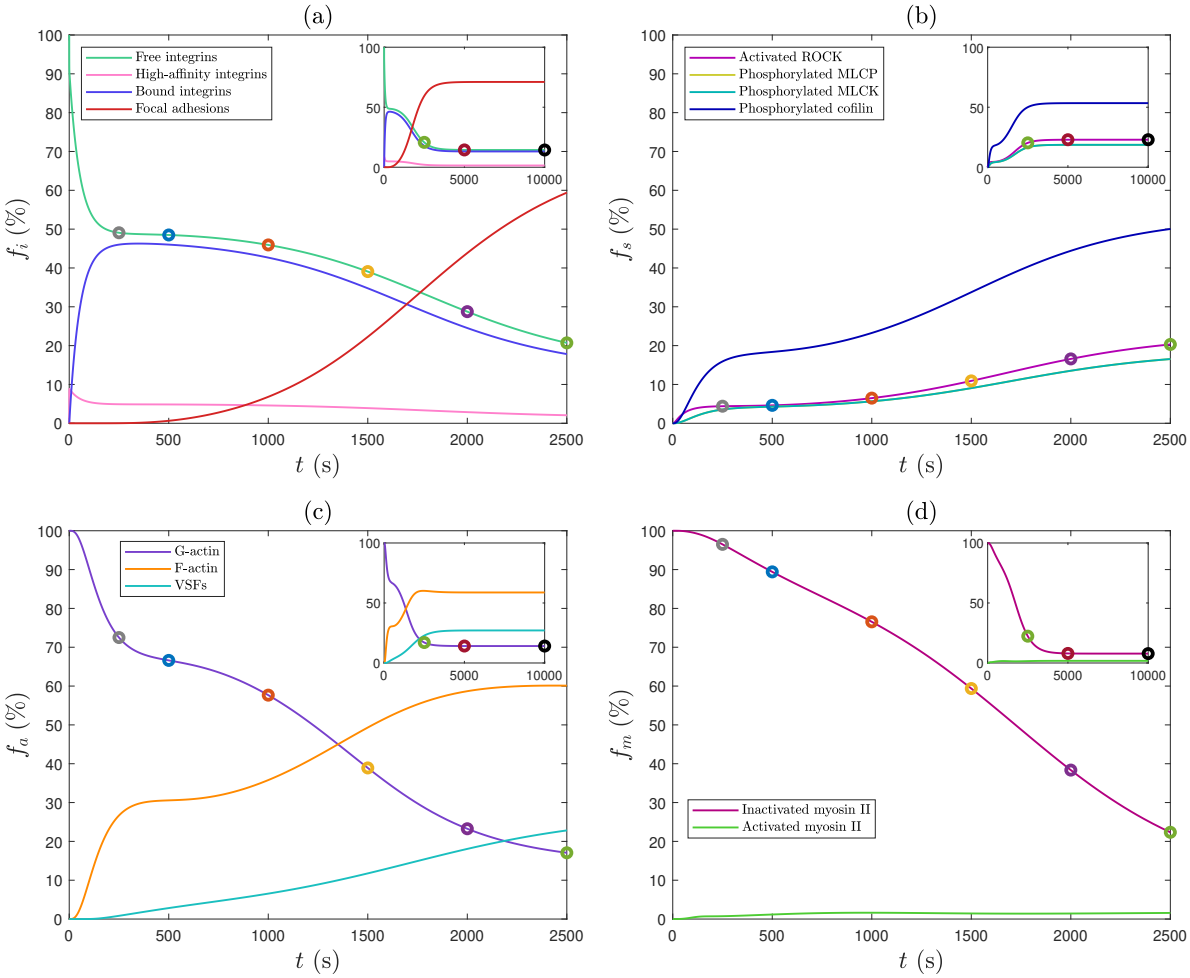

Figure 2.1: Time-dependent evolution of percentage of total: (a) integrins in their various forms (free low-affinity integrins, high-affinity integrins, bound integrins and recruited into FAs), (b) ROCK activated and MLCP, MLCK and cofilin phosphorylated, (c) actin in its different forms (monomeric, polymerised into filaments or recruited into SFs), (d) myosin II in its inactive and active forms. Insets show large time dynamics for each property, open circles indicate times of interest explored in Chs. 3-5. Parameter values are given in Table 2.4.

mation leads to adhesion maturation. We explore the effect of changes to these parameters below. Note that δ also features in our higher-dimensional models formulated in Chs. 3-5 (below); α and β do not feature in these models as we link the adhesion maturation directly to the relative deformation of the cell, rather than employing the empirical relation Eq. (2.7).

Changes in δ

We investigate the effect of changes to the empirical parameter δ by considering the range $0 \leq \delta \leq 10$ whilst fixing all other parameters to their baseline values (those outlined in Sec. 2.4). To quantify changes in the cell with increasing δ, we consider the partition of

integrins (Fig. 2.2a) and the partition of actin (Fig. 2.2b) 10000 s after the cell has been introduced to the substrate. As would be expected, an increase in δ leads to an increase in both FA density (Fig. 2.2a) and VSF (and actin filament) concentration (Fig. 2.2b), as ROCK signaling is enhanced through Eq. (2.5). However, this effect becomes significantly less pronounced when $\delta \gtrsim 2$, particularly for FA formation. In all other results presented in this Chapter we use $\delta = 4$, which is sufficient to capture the positive feedback loop. Note also that the influence of δ saturates beyond this value (Fig. 2.2); this is to be expected as myosin II becomes a limiting factor with increasing δ.

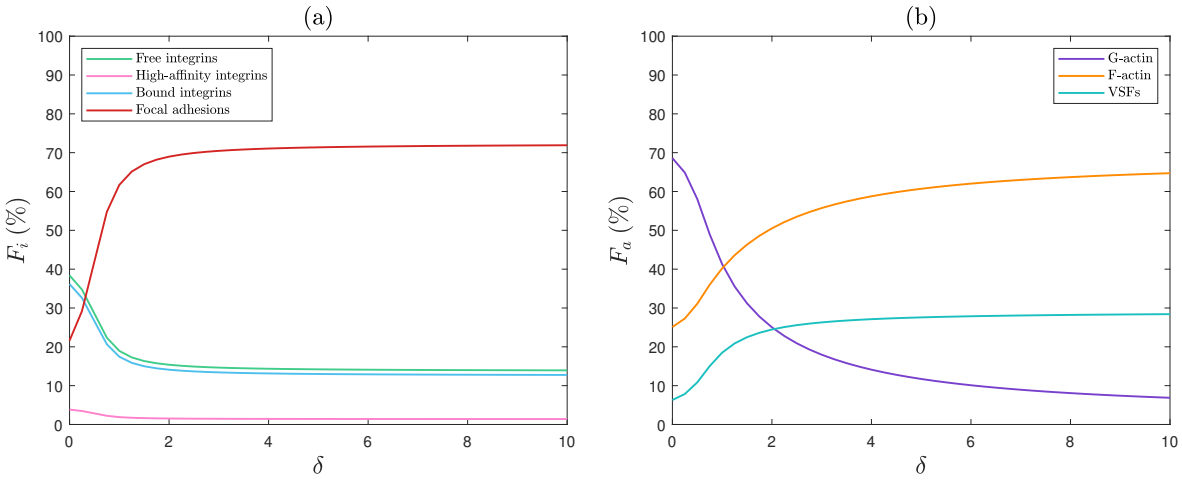

Figure 2.2: Effect of changing δ on FA and VSF formation. As a function of δ, at $t = 10000$ s: (a) fraction, F_i, of integrins that are free, high-affinity, bound or recruited into FAs; (b) fraction, F_a, of monomeric and filamentous actin, and actin recruited into VSFs.

Changes in α

We investigate the effect of changes to the empirical parameter α by considering the range $0 \leq \alpha \leq 10$ whilst fixing all other parameters to their baseline values (those outlined in Sec. 2.4). As above, we quantify changes in the cell with increasing α by considering the partition of integrins (Fig. 2.3a) and the partition of actin (Fig. 2.3b) 10000 s after the cell has been introduced to the substrate. For $\alpha \lesssim 5$, an increase in α is observed to lead to only a modest increase in FA density (Fig. 2.3a) and has negligible effect on VSF (and actin filament) concentration (Fig. 2.3b). Beyond this threshold (i.e. for $\alpha \gtrsim 5$), the response is dramatically different: there is essentially no adhesion maturation, with SF formation significantly diminished. In all other results presented in this Chapter we use $\alpha = 2$, which is sufficient to capture the positive feedback loop evident in experiments (Parsons et al., 2010). Note that the sharp transition at $\alpha \approx 5$ suggests a bifurcation analysis may be beneficial to characterise changes in the stability of steady states of the system.

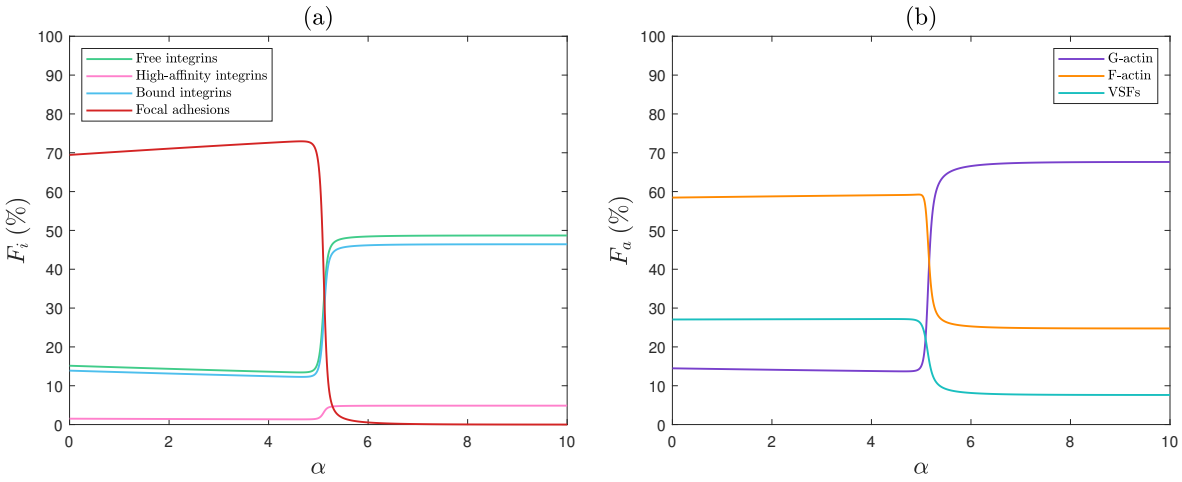

Figure 2.3: Effect of changing α on FA and VSF formation. As a function of α, at $t = 10000$ s: (a) fraction, F_i, of integrins that are free, high-affinity, bound or recruited into FAs; (b) fraction, F_a, of monomeric and filamentous actin, and actin recruited into VSFs.

Changes in β

In a similar manner, we investigate the effect of changes to the empirical parameter β by considering the range $0 < \beta \leq 1$ (note that $\beta = 1$ corresponds to all actin recruited into SFs), whilst fixing all other parameters to their baseline values (those outlined in Sec. 2.4). We quantify changes in the cell with increasing β by again considering the partition of integrins (Fig. 2.4a) and the partition of actin (Fig. 2.4b) 10000 s after the cell has been introduced to the substrate. As would be expected from Eq. (2.7), an increase in β precipitates a decrease in FA density (Fig. 2.4a) and an increase in bound, high-affinity and free integrins, as the rate of adhesion maturation is reduced. In particular, increasing β corresponds to a larger fraction of actin that must be recruited into VSFs to facilitate a half-maximal rate of adhesion maturation. Consequently, through reduced signaling (in line with Eq. 2.5), there is also a reduction in VSF and actin filament concentration (Fig. 2.4b). However, this effect only becomes significant for $\beta \gtrsim 0.3$ (i.e. when more than 30% of actin needs to be recruited into VSFs to facilitate a half-maximal adhesion maturation rate), particularly for SF formation. In all other results presented in this Chapter we use $\beta = 0.25$, which is sufficient to capture the positive feedback loop.

2.6.3 Varying dynamics of stress fibre formation

In this Section we investigate changes to the reaction kinetics through the governing biochemistry equations described in Sec. 2.1, and their effect on the formation of FAs and VSFs. In particular, we consider the effect of changes to the actin polymerisation rate, myosin II activation rate and the rate of myosin II cross-linking. This work informs

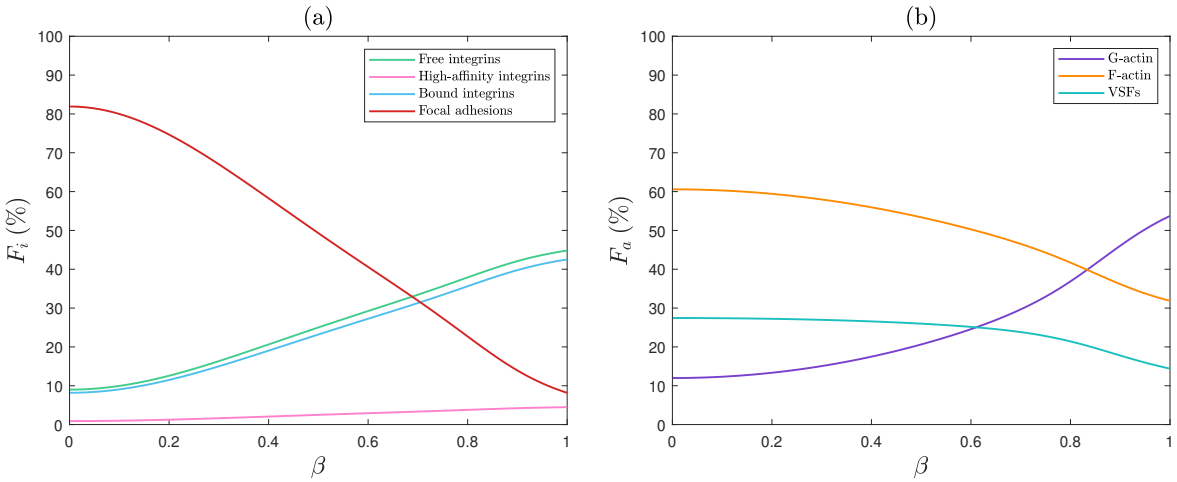

Figure 2.4: Effect of changing β on FA and VSF formation. As a function of β, at $t = 10000$ s: (a) fraction, F_i, of integrins that are free, high-affinity, bound or recruited into FAs; (b) fraction, F_a, of monomeric and filamentous actin, and actin recruited into VSFs.

estimation of rate constants that are poorly estimated in existing literature, which we subsequently use in Chs. 3-5 (below).

Changes in actin polymerisation

In Fig. 2.5 we investigate the effect of altering the actin polymerisation rate, whilst fixing all other parameters to their baseline values outlined in Sec. 2.4. In particular, as a function K_p^+, we plot the partition of integrins (Fig. 2.5a) and actin (Fig. 2.5b) 10000 s after the cell has been introduced to the substrate. As K_p^+ increases, we observe an almost switch-like onset in the formation of FAs and VSFs, where we see an abrupt increase in FA and VSF formation at a threshold polymerisation rate of $K_p^+ \approx 5 \times 10^{-4}\,\text{adhesion}^{-1}\,\text{s}^{-1}$. The concentration of actin filaments also increases significantly with increasing K_p^+, particularly near the threshold value, though this dependence is less steep.

When $K_p^+ \lesssim 5 \times 10^{-4}\,\text{adhesion}^{-1}\,\text{s}^{-1}$, a small amount of actin filaments form. In particular, the formation of bound integrins (Fig. 2.5a) leads to weak activation of ROCK (commensurate with Eq. 2.5) which, in turn, precipitates phosphorylation of MLCP, MLCK and cofilin. However, the polymerisation of actin when $K_p^+ \lesssim 5 \times 10^{-4}\,\text{adhesion}^{-1}\,\text{s}^{-1}$ is slow and severing of actin filaments dominates dynamics. Hence, few actin filaments are formed (Fig. 2.5b). Consequently, no VSFs can form (Fig. 2.5b) and, per Eq. (2.7), cell-substrate adhesions do not mature. Hence, in line with Eq. (2.5), ROCK activation remains weak and the positive feedback loop described in Sec. 2.3 is never activated, further suppressing actin filament formation.

It emerges that $K_p^+ \approx 5 \times 10^{-4}\,\text{adhesion}^{-1}\,\text{s}^{-1}$ represents a thresholding value (when all other parameters are given by their baseline values from Sec. 2.4). In particular, as K_p^+

increases through this value, several features of the feedback loop become evident. The increasing actin polymerisation rate facilitates the formation of actin filaments that can be cross-linked by myosin II to form VSFs (Fig. 2.5b). In turn, through Eq. (2.7), there is an increase in adhesion maturation (Fig. 2.5a). Adhesion maturation leads to a significant increase in ROCK activation (in line with Eq. 2.5) and, consequently, phosphorylation of its downstream effectors MLCK, MLCP and cofilin. This results simultaneously in enhanced (reduced) actin polymerisation (depolymerisation) and myosin II activation (inactivation), leading to significantly enhanced VSF formation (Fig. 2.5b). Through the positive feedback loop, there is also a commensurate further increase in adhesion maturation.

Further increasing K_p^+ much beyond this threshold value leads to a modest increase in actin filament formation but has little effect on VSF and FA formation as the pool of myosin II available for actin cross-linking becomes a limiting factor. We therefore choose a baseline value in simulations of $K_p^+ = 2 \times 10^{-3}\,\text{adhesion}^{-1}\,\text{s}^{-1}$, which is sufficient to allow the positive feedback loop to be initiated in well-adhered cells.

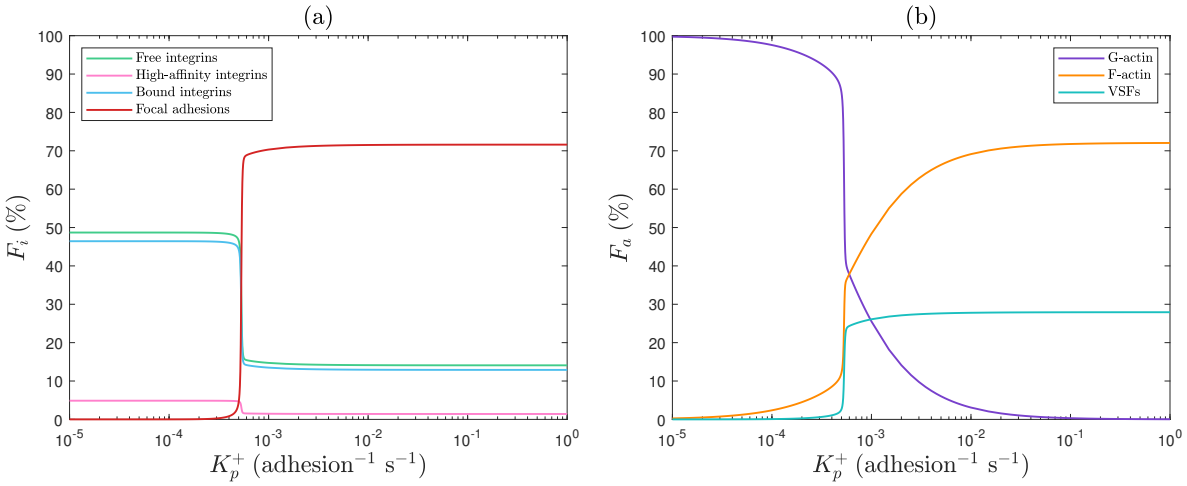

Figure 2.5: Effect of changing actin polymerisation rate on FA and VSF formation. As a function of K_p^+, at $t = 10000$ s: (a) fraction, F_i, of integrins that are free, high-affinity, bound or recruited into FAs; (b) fraction, F_a, of monomeric and filamentous actin, and actin recruited into VSFs.

Changes in myosin II activation

We investigate, in a similar manner, the effect of changes to the rate of myosin II activation on the dynamics of cell-substrate adhesion. We fix all other parameters to their values described in Sec. 2.4 and plot in Fig. 2.6 the partition of integrins (Fig. 2.6a) and of actin (Fig. 2.6b) 10000 s after the cell has been introduced to the substrate as a function of the myosin activation rate, K_a^+. We observe, similar to Fig. 2.5, an approximately switch-like onset in the formation of FAs and VSFs with increasing K_a^+, with a threshold

of $K_a^+ \approx 1 \times 10^{-3}\,\mathrm{s}^{-1}$.

When $K_a^+ \lesssim 1 \times 10^{-3}\,\mathrm{s}^{-1}$, the formation of bound integrins (Fig. 2.6a) leads to weak ROCK signaling (through Eq. 2.5). Consequently, a sizable pool of actin filaments form (Fig. 2.6b). However, the low myosin II activation rate ensures no VSFs form (Fig. 2.6b). Consequently, in line with Eq. (2.7), adhesions do not mature. Hence, the positive feedback loop connecting adhesion maturation and VSF formation is never initiated.

Crossing the threshold value of $K_a^+ \approx 1 \times 10^{-3}\,\mathrm{s}^{-1}$ activates several features of the feedback loop. In particular, the increased activation of myosin II facilitates its ability to cross-link actin filaments to form VSFs (Fig. 2.6b). In response, through Eq. (2.7), there is a significant increase in the formation of FAs. Adhesion maturation precipitates enhanced ROCK signaling, through Eq. (2.5). This, in turn, leads to a significant increase in MLCP, MLCK and cofilin phosphorylation. Consequently, there is a significant increase (decrease) in actin polymerisation (depolymerisation) and myosin II activation (inactivation), leading to further VSF and FA formation.

Further increases in K_a^+ cause a decrease in the concentration of actin filaments, as these are cross-linked by activated myosin II to form VSFs (Fig. 2.6b). We set $K_a^+ = 1 \times 10^{-2}\,\mathrm{s}^{-1}$ in baseline simulations, ensuring the positive feedback loop is activated in well-adhered cells.

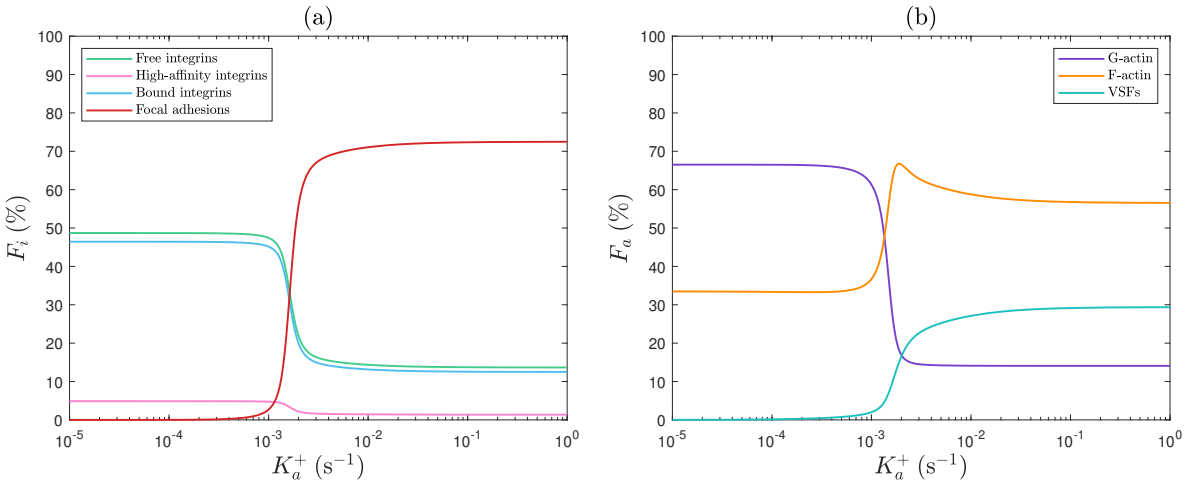

Figure 2.6: Effect of changing myosin II activation rate on FA and VSF formation. As a function of K_a^+, at $t = 10000$ s: (a) fraction, F_i, of integrins that are free, high-affinity, bound or recruited into FAs; (b) fraction, F_a, of monomeric and filamentous actin, and actin recruited into VSFs.

Changes in myosin II cross-linking

We observe a similar dependence of the dynamics of cell-substrate adhesion on the rate of myosin II cross-linking of actin filaments. In particular, fixing all other parameters to their values described in Sec. 2.4, in Fig. 2.7 we explore the influence that increasing k_m^+

has on the partition of integrins (Fig. 2.6a) and of actin (Fig. 2.6b) 10000 s after the cell has been introduced to the substrate. We find that $k_m^+ \approx 1 \times 10^1\ \mu\text{M}^{-2}\,\text{s}^{-1}$ acts as a threshold value, below which there is little maturation of adhesions (Fig. 2.6a) and little cross-linking of actin filaments to form VSFs (Fig. 2.6b). However, a sizable proportion of actin will be polymerised into filaments due to the weak ROCK signaling associated with bound integrins (see Eq. 2.5). Crossing the threshold of $k_m^+ \approx 1 \times 10^1\ \mu\text{M}^{-2}\,\text{s}^{-1}$ leads to a significant increase in FA, actin filament and VSF formation as the positive feedback loop can become activated, in a similar manner described for the effect of increasing myosin II activation rate. Moreover, we similarly observe that further increases in k_m^+ much beyond the threshold value causes a reduction in actin filament concentration as filaments are cross-linked by activated myosin II to form VSFs (Fig. 2.6b). In all baseline simulations we set $k_m^+ = 1 \times 10^2\ \mu\text{M}^{-2}\,\text{s}^{-1}$, which ensures the positive feedback loop is activated in well-adhered cells.

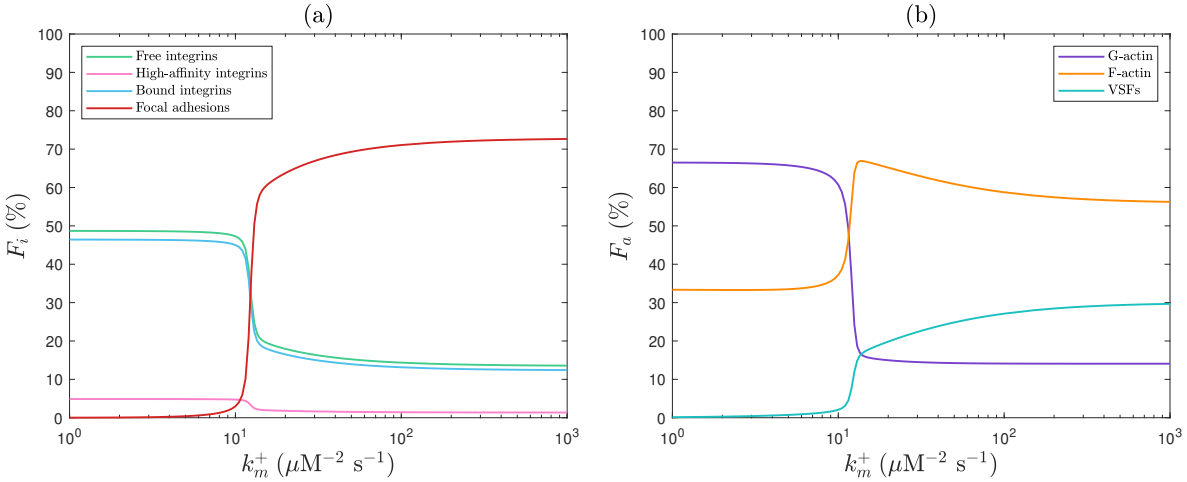

Figure 2.7: Effect of changing myosin II cross-linking rate on FA and VSF formation. As a function of k_m^+, at $t = 10000$ s: (a) fraction, F_i, of integrins that are free, high-affinity, bound or recruited into FAs; (b) fraction, F_a, of monomeric and filamentous actin, and actin recruited into VSFs.

2.6.4 Varying ligand density

In order to elucidate the effect of ECM ligand density (governed by the parameter N_S) on FA and VSF development, in Fig. 2.8 we vary $\tilde{N}_S = N_S/N_I$, the relative density of ECM ligands to the average integrin density (assumed to be $N_I = N_0^I = 100\ \mu\text{m}^{-2}$ in the base case), whilst holding all other parameter values equal to their baseline values. We illustrate the effect of varying $\tilde{N}_S$ by again plotting the partition of integrins (Fig. 2.8a) and the partition of actin (Fig. 2.8b) 10000 s after the cell has been introduced to the substrate. In this model, we observe approximately switch-like behaviour in the formation of FAs

and VSFs. In particular, when ECM ligand density is lower or comparable to cell integrin density then no FAs or SFs form. In this regime, only a modest amount of integrins will become bound to the ECM and consequently only a small amount of actin is polymerised and a correspondingly small amount of myosin II is activated. The cell eventually develops the ability to form mature FAs and contractile VSFs as the ligand density increases to approximately five times greater than integrin density, with a reduction in the density of nascent adhesions as these structures mature. There is saturation of FA, actin filament and VSF formation when ligand density becomes sufficiently high, approximately when ten times greater than the integrin density (i.e. for ligand densities of roughly greater than 1000 μm^{-2}). Thereafter, further increases in ECM ligand density yield little or no further increase in VSF and FA formation. This switch-like behaviour has been observed experimentally (e.g. by Arnold et al., 2004, Cavalcanti-Adam et al., 2007), with insufficient clustering of integrins at low densities to facilitate adhesion maturation (and subsequent signaling for VSF formation).

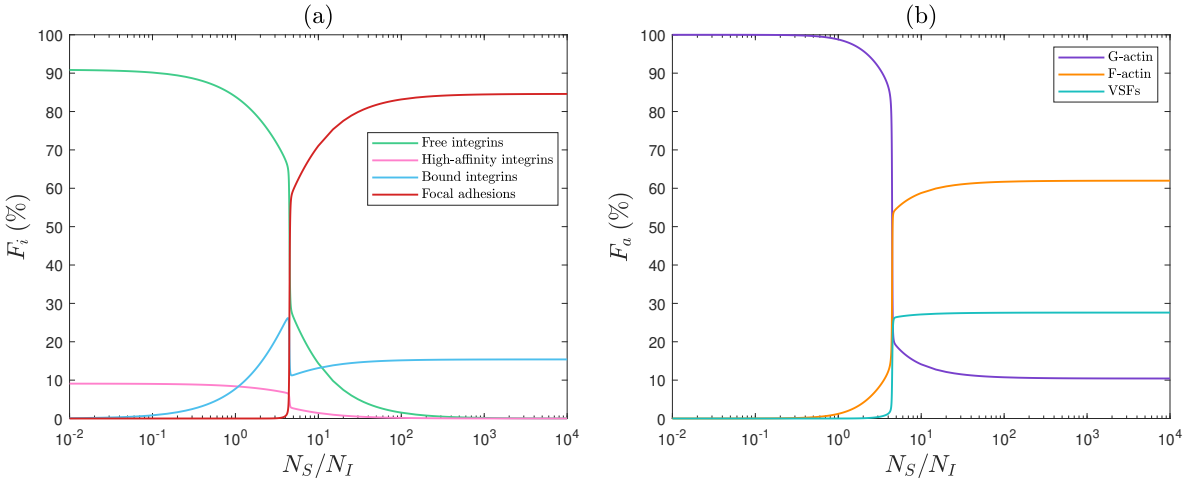

Figure 2.8: Effect of ligand density on FA and VSF formation. As a function of N_S/N_I (the ratio of ligand density to integrin density), at $t = 10000$ s: (a) fraction, F_i, of integrins that are free, high-affinity, bound or recruited into FAs; (b) fraction, F_a, of monomeric and filamentous actin, and actin recruited into VSFs.

2.6.5 Introduction of ROCK inhibitor

A crucial component of the positive feedback loop connecting the development of cell cytoskeleton and maturate cell-substrate adhesions is Rho signaling. Such signaling is strengthened by adhesion maturation and precipitates activation of ROCK, this is captured in our spatially-averaged model by Eq. (2.5). In turn, activated ROCK leads to the phosphorylation of downstream effectors, precipitating increased (decreased) actin polymerisation (depolymerisation) and myosin II activation (inactivation). Consequently,

ROCK activation is necessary for the formation of contractile VSFs and is critical to the positive feedback loop. In real cells, as discussed in Ch. 1, these exert contractile forces on their attached adhesions, causing adhesions to mature, further enhancing ROCK signaling. In our spatially-averaged model, the effect of increased SF concentration on FA formation is captured through the empirical relation Eq. (2.7). In this Section, we focus on inhibition of ROCK only and explore the influence that a ROCK inhibitor has on the sustainability of cell-substrate adhesions and cell cytoskeleton. However, a similar analysis could be employed for inhibition of any of the chemical species in our model. Indeed, in Sec. 4.6.2 (below) we explore the influence of an inhibitor of myosin II activation on predictions from our one-dimensional model developed in Ch. 3 (below).

We discuss inhibitors and their various functions in more detail in Ch. 4 (below), but we briefly introduce a few necessary concepts here. We focus on competitive and allosteric inhibitors. Competitive inhibitors compete with a substrate for a binding site on a catalyst, occupying this site to block the ability of the catalyst to bind to the substrate. On the other hand, allosteric inhibitors bind to a catalyst at a different location to the substrate binding site. Instead, allosteric inhibitors induce a conformational change in the catalyst, reducing its ability to bind to the substrate (Monod et al., 1965). Throughout our analysis we will assume allosteric inhibitors are potent, ensuring that they fully prevent the catalyst from binding to the substrate when in a complex with the catalyst. Under this assumption, allosteric inhibitors do not need a distinct mathematical treatment from competitive inhibitors.

ROCK inhibitors have a variety of clinical applications, including in statins, and have been identified as a potential treatment for erectile dysfunction, high blood pressure and glaucoma (Bivalacqua et al., 2004, Honjo et al., 2001, Liao et al., 2007). To investigate the effect of ROCK inhibition on cytoskeleton and adhesion dynamics, we take a general approach rather than focusing on specific inhibitors (e.g. the allosteric inhibitor Y-27623 or competitive inhibitor fasudil). In particular, we employ lumped parameters for the inhibitor dynamics in our model, to illustrate the potential applicability of our spatially-averaged modelling approach more widely (Amano et al., 2010).

This analysis requires modification of our governing equations from Sec. 2.1.3. Recall that ROCK, average concentration $\bar{c}_R$, becomes activated at rate k_R^+ to form activated ROCK, average concentration $\bar{c}_R^+$. We suppose that an inhibitor (either competitive or a potent allosteric) has average concentration $\bar{c}_I$ and prevents activation of ROCK. Binding of inactivated ROCK to the inhibitor occurs at a rate proportional to k_{IR}^+, leading to the formation of ROCK-inhibitor complexes which have average concentration $\bar{c}_{IR}$. ROCK bound to an inhibitor cannot be activated, but ROCK-inhibitor complexes can dissociate at rate k_{IR}^-. We also include a source term, p, capturing the introduction of the ROCK inhibitor to the cell. Hence, the dynamics of ROCK, the inhibitor and ROCK-inhibitor

complexes can be described by

$$\frac{d\bar{c}_R}{dt} = -k_R^+\bar{c}_R + k_R^-\bar{c}_R^+ - k_{IR}^+\bar{c}_I\bar{c}_R + k_{IR}^-\bar{c}_{IR}, \tag{2.8a}$$

$$\frac{d\bar{c}_I}{dt} = p(t) - k_{IR}^+\bar{c}_I\bar{c}_R + k_{IR}^-\bar{c}_{IR}, \tag{2.8b}$$

$$\frac{d\bar{c}_{IR}}{dt} = k_{IR}^+\bar{c}_I\bar{c}_R - k_{IR}^-\bar{c}_{IR}. \tag{2.8c}$$

In all simulations k_R^+ and k_R^- are defined by their baseline values given in Sec. 2.4. Additionally, we set $k_I^- = 1 \times 10^{-3}\,\mathrm{s}^{-1}$ and set the source term to be

$$p(t) = \begin{cases} 0, & t < t_p,\ t_p < t < t_s \\ p_I, & t = t_p \end{cases}, \tag{2.9}$$

where $p_I = M_I/V$, with M_I the total mass of inhibitor introduced and V the volume of the cell. In particular, we assume the inhibitor is instantaneously introduced (at $t = t_p$). In all simulations we set $t_p = 5000$ s and $M_I = 100$ nM, with V given by its baseline value from Sec. 2.4. We end simulations at $t = t_s = 10000$ s. We vary the value of k_{IR}^+ as this essentially dictates the potency of the inhibitor.

We demonstrate the effect that the introduction of a ROCK inhibitor has on the dynamics of cell-substrate adhesion in Fig. 2.9. In particular, setting $k_{IR}^+ = 200\,\mu\mathrm{M}^{-1}\,\mathrm{s}^{-1}$, we illustrate time-traces of the partition of integrins into their various forms (Fig. 2.9a), and the partition of actin (Fig. 2.9b). We highlight the key times $t = t_p$ ($t = t_s$) using blue (orange) open circles. The introduction of a ROCK inhibitor (inset in Fig. 2.9a) leads to rapid dissociation of SFs (Fig. 2.9b) due to the reduction (increase) in actin polymerisation (depolymerisation) and myosin II activation (inactivation). After some time, there is a transient increase in actin filament concentration (Fig. 2.9b) as some actin continues to be polymerised but cannot be cross-linked by myosin II to form VSFs, before the actin filament concentration continues to fall. In line with Eq. (2.7), SF dissociation leads to the disassembly of FAs (Fig. 2.9a) and further reduced ROCK signaling (inset in Fig. 2.9b). Consequently, VSF and actin filament concentration continue to fall. For this potent inhibitor, the cell eventually returns to its early (poorly-adhered) state, with many immature adhesions to the substrate (Fig. 2.9a), but little cytoskeleton development (Fig. 2.9b) and negligible adhesion maturation (Fig. 2.9a).

To investigate how the potency of the ROCK inhibitor influences cytoskeleton and adhesion dynamics, we vary k_{IR}^+, the rate per concentration at which the inhibitor binds to inactive ROCK and prevents its activation. Particularly, we consider the range $1 \times 10^{-2}\ \mu\mathrm{M}^{-1}\,\mathrm{s}^{-1} < k_{IR}^+ < 1 \times 10^3\ \mu\mathrm{M}^{-1}\,\mathrm{s}^{-1}$, whilst fixing all other parameters to their baseline values (as outlined in Sec. 2.4 or above). We introduce the ROCK inhibitor at

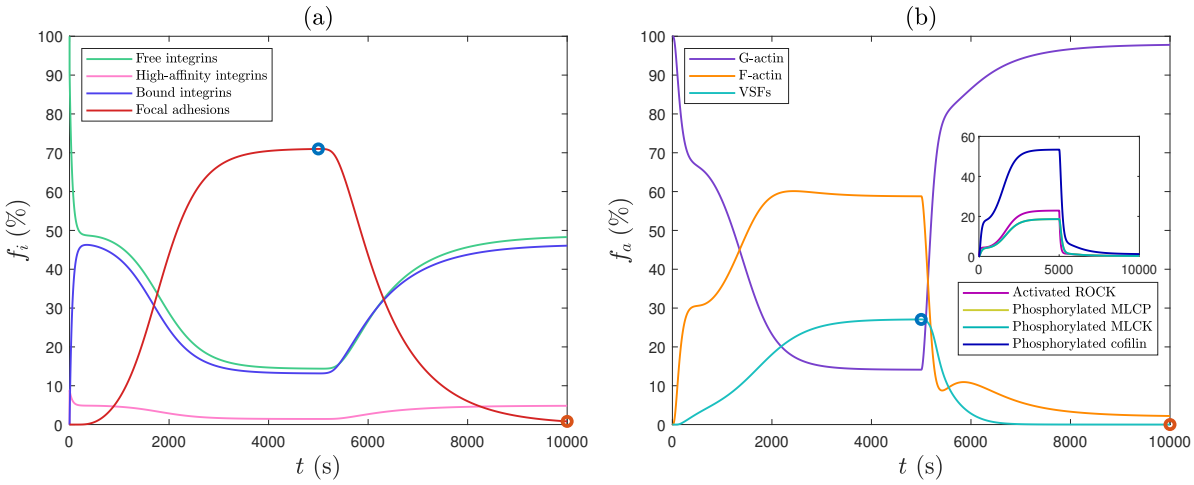

Figure 2.9: Investigating the effect of a ROCK inhibitor introduced to the cell. Time-dependent evolution of percentage of total: (a) integrins in their various forms (free low-affinity integrins, high-affinity integrins, bound integrins and recruited into FAs), (b) actin in its different forms (monomeric, polymerised into filaments or recruited into SFs). Inset in (b) shows fraction of ROCK activated and of its downstream effectors phosphorylated as a function of time.

$t = t_p = 5000$ s after the cell has been introduced to the substrate and is therefore well-adhered (Fig. 2.1). We plot global measures of cell-substrate adhesion and cytoskeleton development, particularly the partition of integrins (Fig. 2.10a) and the partition of actin (Fig. 2.10b) 10000 s after the cell has been introduced to the substrate (5000 s after the introduction of the inhibitor). We indicate with dashed lines in Fig. 2.10 the partition of integrins and actin in the absence of any inhibitor introduction. We observe that for low inhibitor-ROCK binding rates, the dynamics of inactivated ROCK is dominated by its activation, leading to negligible effect on adhesion (Fig. 2.10a) and cytoskeleton (Fig. 2.10b) dynamics. When the inhibition rate of ROCK becomes sufficiently high, approximately when $k_{IR}^{+} \approx 20\ \mu\text{M}^{-1}\,\text{s}^{-1}$, there is a significant decrease in VSF concentration (Fig. 2.10b). In line with Eq. (2.7), the reduction in VSF concentration leads to reduced FA density (Fig. 2.10a). In turn, through Eq. (2.5), FA disassembly leads to further reduced activated ROCK concentration and so further decreases in VSF formation (Fig. 2.10b). A reduction in actin filament concentration occurs in tandem with reduced VSF concentration (Fig. 2.10b) with increasing k_{IR}^{+}. However, at moderately high rates of ROCK inhibition, with $k_{IR}^{+} \approx 100\ \mu\text{M}^{-1}\,\text{s}^{-1}$, there is still limited actin filament formation as ROCK activation is not completely suppressed and weak signaling from bound integrins (see Eq. 2.5) facilitates actin polymerisation (Fig. 2.10b). Thereafter, further increases in k_{IR}^{+} leads to nearly all actin returning to its monomeric form as actin polymerisation (depolymerisation) decreases (increases).

It is worth emphasising the similarity in qualitative predictions of this model in re-

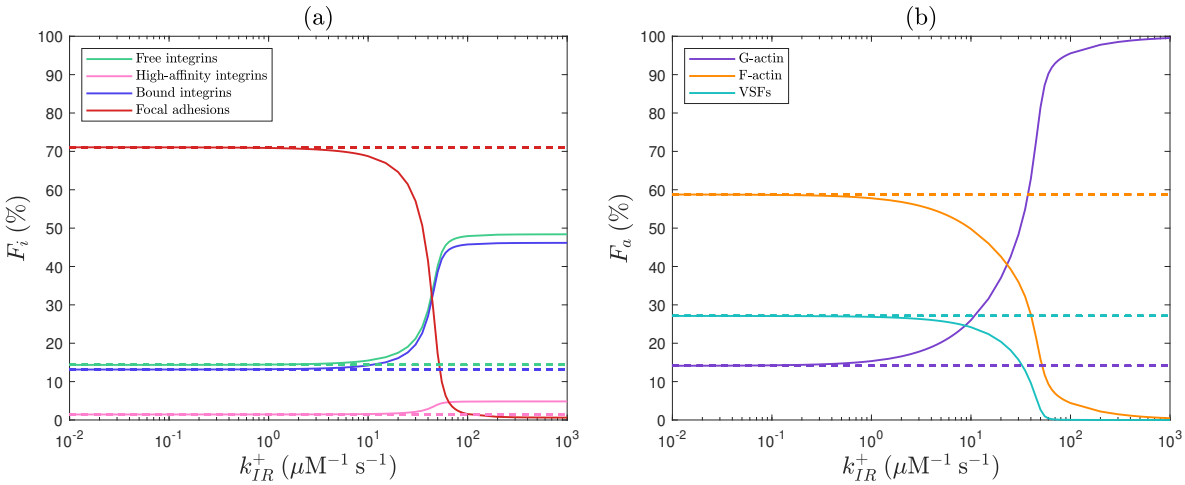

Figure 2.10: Effect of ROCK inhibitor strength. As a function of the binding rate of the ROCK inhibitor to ROCK, at $t = 10000$ s (5000 s after the inhibitor has been applied): (a) fraction, F_i, of integrins that are free, high-affinity, bound or recruited into FAs; (b) fraction, F_a, of monomeric and filamentous actin, and actin recruited into VSFs.

sponse to the introduction of ROCK inhibitor (Figs. 2.9- 2.10), to the predictions made by the one-dimensional model presented in Sec. 4.6.1 in Ch. 4 (below). This suggests again that, despite some quantitative differences, likely owing to the empirical relation connecting adhesion maturation to VSF formation (Eq. 2.7), this simple spatially-averaged approach is successful at capturing the global dynamics of cell-substrate adhesion.

2.7 Summary

In this Chapter we have formulated a spatially spatially-averaged model for the development of cell-substrate adhesions and cell cytoskeleton. In particular, we have formulated a large system of ODEs to describe the reaction kinetics of important cytoskeletal, adhesion and signaling proteins as a cell interacts with a substrate. By imposing various constitutive assumptions, we have been able to link the formation of FAs and VSFs, capturing in a simple way the positive feedback loop that connects their development. Furthermore, we have demonstrated the efficacy of this model to quickly predict the global dynamics of cell-substrate adhesion, to identify how changes to reaction kinetics can influence this process and to investigate how environmental and biochemical cues can be applied to control this process. However, this model is insufficient to capture the full cytoskeletal and adhesion dynamics as it fails to incorporate the mechanics of the cell, ECM and adhesions, consideration of which is necessary to predict localisation of proteins in the cell. Extending this model to consider these effects is the aim of the remainder of this thesis, particularly the formation (Ch. 3) and analysis (Ch. 4) of a one-dimensional bio-chemo-mechanical model, followed by analysis of a two-dimensional bio-chemo-mechanical model (Ch. 5).

Chapter 3

One-dimensional modelling

In Ch. 2 we presented a simple spatially-averaged bio-chemical model to describe the formation and maturation of SFs and FAs in non-motile cells. Having identified the strengths and weaknesses of this approach, we proceed in this Chapter to formulate a one-dimensional bio-chemo-mechanical continuum model to describe the coupled formation and maturation of FAs and VSFs as a cell adheres to a substrate. The model takes the form of a system of reaction-diffusion-advection equations that describe the evolution of a large family of scaffolding, structural and signaling proteins integral to this process (those identified in Figs. 1.4-1.5), coupled to the mechanical deformation of the cell induced by adhesion to an ECM substrate and subsequent contraction under the action of myosin motors.

As discussed in Sec. 1.3.2, we treat the cell as a Kelvin-Voigt viscoelastic material, with additional active stresses in the cell reflecting myosin II motor contractility. We link the mechanical properties of the cell and cell-substrate adhesions to the evolution of the key scaffolding proteins (as in Figs. 1.4-1.5). By connecting the cytoskeletal mesh scale to the microscale using discrete-to-continuum upscaling, our approach advances on the homogenised account of the cell provided by many existing models by rationally connecting the nanoscale and microscale features of cell-substrate adhesion and the cell cytoskeleton. Moreover, by treating the ECM as a Kelvin-Voigt viscoelastic continuum material, coupled to the cell through viscoelastic adhesions, our model predicts the deformation of the ECM, facilitating prediction of FA and SF localisation. Additionally, in this Chapter, as in Ch. 2, we link the formation and maturation of cell-substrate adhesions to increased activated ROCK concentration. However, in this Chapter, SFs can exert contractile forces that facilitate cell deformation, stretching cell-substrate adhesions, enhancing their maturation (through exposure of VBSs). We incorporate this into our model by assuming the rate of adhesion maturation depends on the relative deformation of the cell to the ECM, making this modelling approach significantly more biologically realistic (compared with the Hill type function employed in Ch. 2 to link adhesion maturation rate to SF concentration).

This Chapter is structured as follows. In Sec. 3.1 we present our mechanical model to describe the deformation of the cell, ECM and adhesions. Particularly, in Secs. 3.1.1-3.1.4 we treat the cell and ECM as a string of discrete (contractile) Kelvin-Voigt elements, connected by Kelvin-Voigt viscoelastic adhesions. We employ discrete-to-continuum upscaling (Sec. 3.1.5) to rationally formulate a system of continuum momentum balance equations to describe the coupled deformation of the cell and ECM (Sec. 3.1.6). We consider the mechanical behaviour of the ECM away from the cell in Sec. 3.1.7. In Sec. 3.2 we formulate a large system of PDEs to describe the formation and maturation of SFs (Sec. 3.2.1) and FAs (Sec. 3.2.2), linked by intracellular signaling proteins (Sec. 3.2.3), before presenting the imposed boundary and initial conditions on the bio-chemo-mechanical system in Sec. 3.3. To simplify our analysis, we non-dimensionalise our governing mechanical and biochemical equations in Sec. 3.4. Thereafter, in Sec. 3.5 we introduce our constitutive assumptions. Particularly we specify how ROCK activation and phosphorylation of downstream effectors is enhanced by adhesion maturation (Sec. 3.5.1), the mechanism by which SF formation (and the associated cell deformation) leads to enhanced adhesion maturation (Sec. 3.5.2) and couple the mechanical properties of the cytoskeleton and adhesions to the cell biochemistry (Sec. 3.5.3). In Sec. 3.6 we provide estimates, together with justification, of our assumed (baseline) parameter values and briefly detail our computational method in Sec. 3.7. We then apply the developed model in Sec. 3.8, illustrating for a baseline case (with parameters as outlined in Sec. 3.6) both the global and local, mechanical and biochemical behaviour of the cell, ECM and adhesions as a cell interacts with a stiff collagen substrate and develops cytoskeleton. We validate our computational method in Sec. 3.8.1 before investigating the effect that changes in feedback strength have on our predictions (Sec. 3.8.2). Finally, we summarise the work of this Chapter in Sec. 3.9.

3.1 Mechanical model

We idealise the cell as a cuboid with initial length L, width W, and height H, so that the total cell volume is $V = WLH$. We suppose that the cell is thin in the direction normal to the substrate, so that $H \ll W, L$. We reduce the problem to one spatial dimension by cross-sectionally averaging the protein concentration and mechanical properties over the cell width and height and consider variations across the cell length only.

We parameterise the cell using the coordinate x such that the initial configuration of the cell is described by a set of material points with coordinates spanning $-L/2 \leq x \leq L/2$. The left and right boundaries of the cell are displaced to $x = l(t)$ and $x = r(t)$, respectively, whilst the internal points are displaced to x' so that for all $t \geq 0$ we have

$$l(t) = x'(-L/2, t) \leq x'(x, t) \leq x'(L/2, t) = r(t); \tag{3.1}$$

a similar set up was considered by Gracheva and Othmer (2004).

In our approach we suppose that the ECM consists of three regions, one below the cell, of length L, and regions to the left and right, both of length L_1, as indicated in Fig. 3.1. The initial configuration of the ECM is described by a set of material points with coordinates spanning $-L_1 - L/2 \leq x \leq L_1 + L/2$. We assume that the outer boundaries of the ECM are fixed for all time (Fig. 3.1), whilst internal points are displaced to $\bar{x}'$.

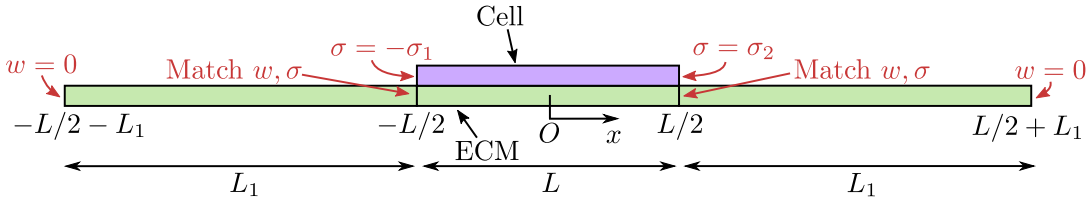

Figure 3.1: Overview of cell-ECM set-up. Boundary conditions imposed on the cell and ECM, we consider the ECM as consisting of three connected compartments and match stress and displacement across the boundaries connecting these.

The corresponding displacement of points in the cell cytoplasm, $u(x,t)$, and in the ECM, $w(x,t)$, are described by

$$u(x,t) = x'(x,t) - x, \quad w(x,t) = \bar{x}'(x,t) - x; \tag{3.2}$$

for simplicity, u and w are assumed small, allowing us to use linearised constitutive laws for the cell rheology (see Secs. 3.1.1-3.1.2 below).

We assume that the motion of the cell boundaries results from a combination of externally applied forces on the cell, active and passive stresses within the cell itself and restoring forces due to cell-substrate interaction, resisted by friction due to repeated detachment and attachment of the cell to the substrate and restoring forces due to cell-substrate interaction. We neglect inertial effects and other body forces.

3.1.1 Constitutive law for the cytoplasm

The cell cytoplasm consists of a viscous fluid phase (cytosol) and a scaffold structure (cytoskeleton) formed from cross-linked protein filaments (actin filaments, microtubules, intermediate filaments and SFs). In this model we describe the cytoplasm as a linearly viscoelastic material which exhibits both a passive stress and a contractile active stress. To inform the constitutive law for the rheological response of the cell, the cytoskeletal network is modelled as a line of N contractile Kelvin-Voigt elements connected in series (N is assumed even for simplicity). Similar constitutive assumptions for the cell have been employed by others (e.g. Besser and Schwarz, 2007, Gracheva and Othmer, 2004, Larripa and Mogilner, 2006) since VSFs dominate cytoskeletal dynamics in non-motile cells and carry load at constant deformation for long periods of times (i.e. behave as an

elastic material). These elements are assumed to be of uniform initial length a_c (where $a_c = L/N$), mimicking the mesh spacing between cytoskeletal cross-links. This approach then discretises the cell domain onto a uniform grid with $x_n = a_c n$, $n = -N/2, -N/2+1, \ldots, N/2$, where the two end points are the cell boundaries, as shown in Fig. 3.2.

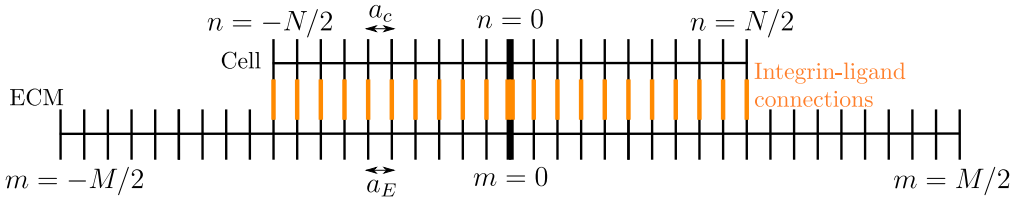

Figure 3.2: Discretisation of the cell and ECM. Nodes are equally spaced (corresponding to $a_c = a_E$) with connections between cell and ECM representing integrin-ligand connections.

In this model each element represents a bundle of actin filaments, SFs and other cytoskeletal proteins together with viscous cytoplasmic fluid. The cross-link at junction n is connected to two elements on either side which are indexed as $n - 1/2$ (element to the left) and $n + 1/2$ (element to the right), as indicated in Fig. 3.3.

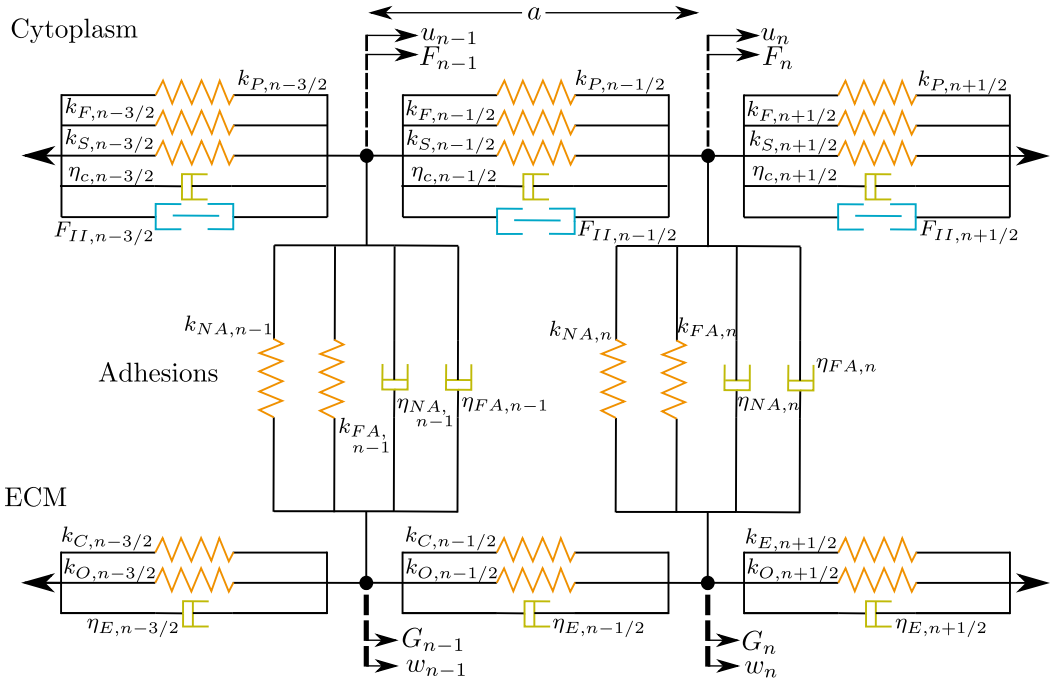

Figure 3.3: Full rheological diagram. A string of contractile Kelvin-Voigt elements represent the cytoplasm, each of these is connected, through a Kelvin-Voigt element representing nascent and focal adhesions, to another Kelvin-Voigt element capturing the stiffness and viscosity of the ECM.

To mimic the multiple elastic components of the cytoskeleton, each element is formed of three elastic springs connected in parallel (see rheological diagram in Fig. 3.3) representing actin filaments (with stiffness $k_{F,n+1/2}$ for element $n+1/2$), SFs (with stiffness $k_{S,n+1/2}$ for

element $n+1/2$) and a passive stiffness due to microtubules, intermediate tubules and the nucleus (with stiffness $k_{P,n+1/2}$ for element $n+1/2$). The form of the passive stiffness is discussed in Sec. 3.5 (below); briefly, these elements are assumed to be stiffer near the cell centre (mimicking the stiff nucleus) and softer towards the cell boundary (accounting for microtubules and intermediate filaments).

Within each rheological element (see Fig. 3.3), we further include a dashpot (with viscosity $\eta_{c,n+1/2}$ for element $n+1/2$), in parallel with the springs, to mimic the viscous fluid, and an active element which generates a contractile force due to myosin II motor action ($F_{II,n+1/2}$ for element $n+1/2$). In particular, we assume that the contractile force can be described using the linearised relationship

$$F_{II,n+\frac{1}{2}}(v_{n+1/2}) = F_{stall,n+\frac{1}{2}}\left(1-\frac{v_{n+\frac{1}{2}}}{v_0}\right), \quad v_{n+\frac{1}{2}} = \frac{\partial}{\partial t}\left(u_{n+1}-u_n\right), \tag{3.3}$$

where v_0 is the zero-load velocity (assumed identical for all elements) and $F_{stall,n+1/2}$ is the stall force of the motor (i.e. the maximal force allowing for motor movement) for element $n+1/2$ (Besser and Schwarz, 2007).

Analysis of a single sarcomeric unit in the cell

In Fig. 3.4 we describe a single sarcomeric unit for the cell, this forms the repeating unit in the string of contractile Kelvin-Voigt viscoelastic elements that describe the cell cytoplasm, as indicated in Fig. 3.3. Each element consists of three springs connected in parallel to capture the stiffness of actin filaments, k_F, SFs, k_S, and passive stiffness due to microtubules, intermediate tubules and the nucleus, k_P. These are connected in parallel with a dashpot, viscosity η_c, and a contractile element, which generates a force F_{II}. In a similar manner to Besser and Schwarz (2007), we assume that the force-velocity relation for myosin II motor action can be described using the linearised relationship

$$F_{II}(v) = F_{stall}\left(1-\frac{v}{v_0}\right), \quad v = -\frac{du}{dt}, \tag{3.4}$$

where F_{II} is the force exerted by a myosin II motor moving with velocity v, v_0 is the zero-load velocity and F_{stall} is the stall force of the motor (the maximal force allowing for motor movement); this is the single unit equivalent of Eq. (3.3). We note the connection between the contraction velocity, v, and displacement of the unit, u, with displacement becoming negative in response to contractile myosin II motor activity. The sum of all forces, F, exerted on each element is then

$$F = -\eta_c\frac{du}{dt} - \left(k_F+k_S+k_P\right)u - F_m. \tag{3.5}$$

Neglecting inertial effects and external forces then we deduce from Eq. (3.5), with $F = 0$, that

$$\left(\eta_c + \frac{F_{stall}}{v_0}\right)\frac{du}{dt} + (k_F + k_S + k_P)\,u = -F_{stall}. \tag{3.6}$$

Eq. (3.6) indicates two effects of myosin II motors (as discussed by Besser and Schwarz, 2007). In particular, myosin motor action alters the effective viscosity of the cytoplasm (by increasing the viscosity of the damping term) and generates a forcing term, resulting in an inhomogeneous ODE. Assuming $u(0) = 0$ and that all parameters remain fixed (which is not the case in the full model), then solving Eq. (3.6) yields

$$u(t) = \frac{-F_{stall}}{k_F + k_S + k_P}\left(1 - e^{-\frac{t}{T}}\right), \tag{3.7}$$

where $T = \eta_e/(k_F + k_S + k_P)$ is the relaxation time of the Kelvin-Voigt model with effective viscosity $\eta_e = \eta_c + F_{stall}/v_0$.

We illustrate some representative solutions to Eq. (3.6) in Fig. 3.4. We observe that, characteristic of a long-time solid, viscous stresses eventually dissipate, leaving a finite elastic stress (dashed lines in Fig. 3.4). In particular, the long-time behaviour of the material is determined entirely by the ratio of the stall force to spring stiffness. We hence conclude that the assumption of Kelvin-Voigt viscoelasticity is appropriate for the cell cytoplasm, given that SFs carry load at constant deformation over long periods of time (Besser and Schwarz, 2007).

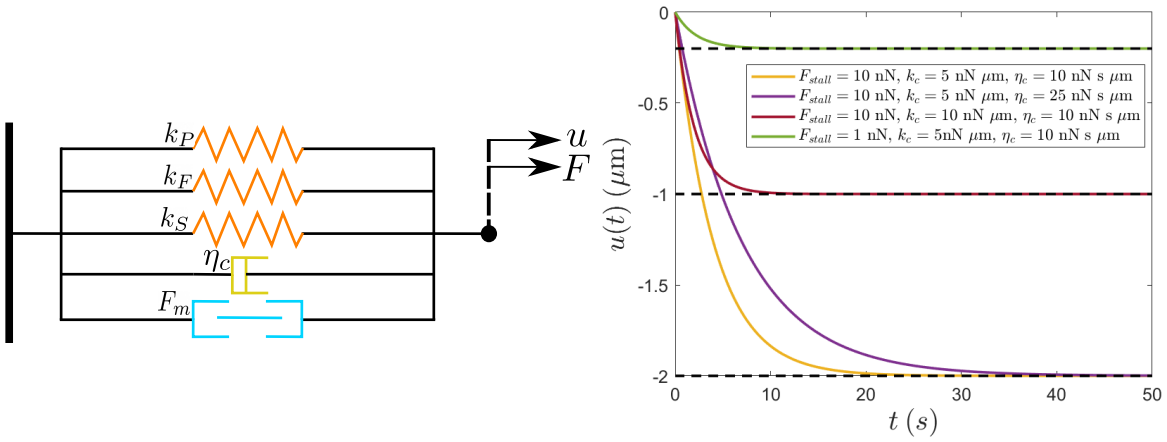

Figure 3.4: Left panel: single contractile Kelvin-Voigt element, consisting of three resistors, a dashpot and a battery connected in parallel. Right panel: representative deformations (solutions to Eq. 3.6) for varied mechanical properties, with $k_c = k_P + k_F + k_S$ and $u(0) = 0$; dashed lines indicate steady state deformation.

3.1.2 Constitutive law for the ECM

We discretise the ECM in a similar manner to the cell so that it is described by M cross-link junctions (we assume M is even) with indexing $m = -M/2, -M/2+1, \ldots, M/2$, with the centre of the ECM (at $x = 0$) denoted by $m = 0$ as indicated in Fig. 3.2.

Similar to the cell, we assume that the ECM also consists of a mesh of cross-linked protein filaments, modelled as a line of Kelvin-Voigt elements connected in series, each of length $a_E = (L + 2L_1)/M$ (see Fig. 3.2). Similar simple rheological assumptions (i.e. that the ECM behaves as a long-time solid) have been employed for the ECM by others (e.g. Byrne and Chaplain, 1996, Murray et al., 1988), though some other studies have considered more complicated descriptions. Also similar to the cell, each ECM element is indexed by the average of the two cross-link indices on either side (see Fig. 3.3). Each ECM element is assumed to consist of two springs connected in parallel representing collagen fibres (with stiffness $k_{C,m+1/2}$ for element $m+1/2$) and other ECM fibres (e.g. fibronectin, with stiffness $k_{O,m+1/2}$ for element $m+1/2$). To mimic the viscous extracellular fluid within the ECM these filaments are connected in parallel with a dashpot (viscosity $\eta_{E,m+1/2}$ for element $m + 1/2$).

The regions of ECM below the cell exhibit spatially and temporally dependent properties (which can be due to remodelling by the cell itself). Conversely, for simplicity the regions of ECM away from the cell are assumed to have spatially uniform and constant stiffness and viscosity, allowing for an analytical description of ECM displacement and stress in each of these regions (though in real cells signals will diffuse away from the cell); see details in Sec. 3.1.7.

Analysis of single sarcomeric unit in the ECM

In Fig. 3.5 we analyse a single sarcomeric unit for the cell, this forms the repeating unit in the string of Kelvin-Voigt viscoelastic elements that describe the ECM, as indicated in Fig. 3.3. Each element consists of two springs connected in parallel to capture the stiffness of collagen, k_C, and other fibres (e.g. fibronectin), k_O. These are connected in parallel with a dashpot, viscosity η_E. In contrast with the cytoplasm, contractile motors are absent.

We let w denote the displacement of points in the ECM so that the sum of all forces acting on an individual element is

$$G = -\eta_E \frac{dw}{dt} - (k_C + k_O)\, w. \tag{3.8}$$

Hence, in the absence of external forces, $G = 0$ and, assuming $w(0) = 0$, then $w(t) = 0$.

In Fig. 3.5 we illustrate some representative solutions of Eq. (3.8) with $w(0) \neq 0$, particularly showing the influence of the stiffness and viscosity of the ECM components on stress relaxation. In the absence of external forcing, the material stress dissipates, with

a characteristic time scale determined by the ratio of the ECM viscosity to ECM stiffness.

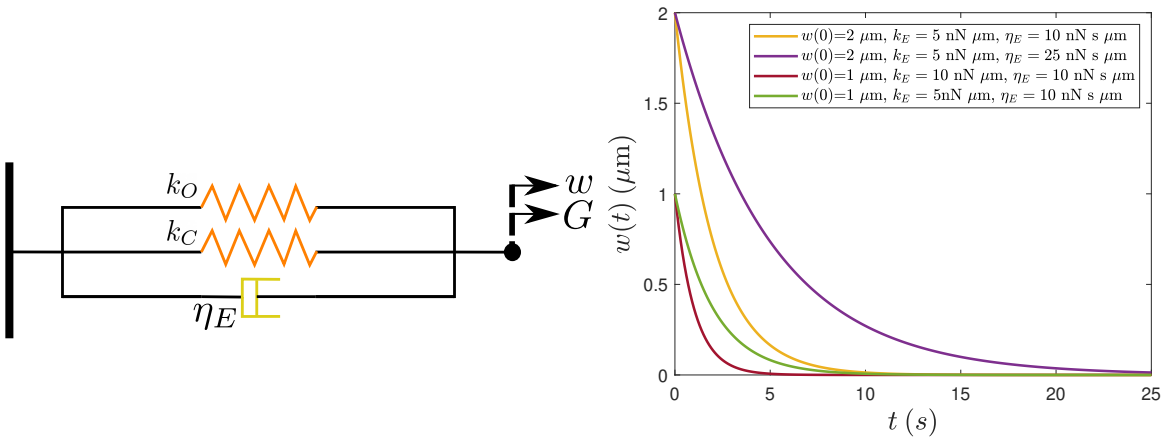

Figure 3.5: Left panel: single Kelvin-Voigt element for the ECM, consisting of two resistors and a dashpot connected in parallel. Right panel: representative deformations (solutions to Eq. 3.8 with $G = 0$) for varied mechanical properties, with $k_E = k_C + k_O$.

3.1.3 Coupling the ECM and cell networks

For simplicity, we assume that the cytoskeletal mesh spacing in the cell, a_c, and the collagen network mesh spacing, a_E, are identical ($a_c = a_E = a$) and the cross-links are co-located at the same $x-$location. This simplified set up is illustrated in Fig. 3.2.

3.1.4 Force balance at cross-links

The overall rheology of the cell-ECM system is summarised in Fig. 3.3. The resultant force on the n^{th} cross-link in the cell is given by (see Besser and Schwarz, 2007)

$$\begin{aligned} F_n =& \eta_{c,n+\frac{1}{2}} \frac{\partial}{\partial t}\left(u_{n+1} - u_n\right) - \eta_{c,n-\frac{1}{2}} \frac{\partial}{\partial t}\left(u_n - u_{n-1}\right) \\ &+ k_{c,n+\frac{1}{2}}\left(u_{n+1} - u_n\right) - k_{c,n-\frac{1}{2}}\left(u_n - u_{n-1}\right) + F_{II,n+\frac{1}{2}} - F_{II,n-\frac{1}{2}}, \end{aligned} \tag{3.9a}$$

where $k_{c,n\pm1/2} = k_{F,n\pm1/2} + k_{S,n\pm1/2} + k_{P,n\pm1/2}$. Similarly, the resultant force on the m^{th} cross-link in the ECM is given by

$$\begin{aligned} G_m =& \eta_{E,m+\frac{1}{2}} \frac{\partial}{\partial t}\left(w_{m+1} - w_m\right) - \eta_{E,m-\frac{1}{2}} \frac{\partial}{\partial t}\left(w_m - w_{m-1}\right) \\ &+ k_{E,m+\frac{1}{2}}\left(w_{m+1} - w_m\right) - k_{E,m-\frac{1}{2}}\left(w_m - w_{m-1}\right), \end{aligned} \tag{3.9b}$$

where $k_{E,m\pm1/2} = k_{C,m\pm1/2} + k_{O,m\pm1/2}$.

In the region of ECM below the cell ($-L/2 < x < L/2$) these internal forces are balanced by a restoring force due to integrins connected to the ECM and due to viscous

cell-substrate interaction, as shown in Fig. 3.3. We suppose that these integrin connections are also linear Kelvin-Voigt viscoelastic materials; similar rheological assumptions have been employed for cell-cell adhesions by Jamali et al. (2010), whilst Di Stefano et al. (2022) treat cell-substrate adhesions as purely elastic. Hence, we have

$$F_n = k_{I,n}\left(u_n - w_n\right) + \eta_{I,n}\frac{\partial}{\partial t}\left(u_n - w_n\right) = -G_n, \tag{3.10}$$

where $k_{I,n} = k_{NA,n} + k_{FA,n}$ and $\eta_{I,n} = \eta_{NA,n} + \eta_{FA,n}$, where $k_{NA,n}$ and $\eta_{FA,n}$ are used to represent the stiffness and viscosity of nascent adhesions and $k_{NA,n}$ and $\eta_{FA,n}$ are used to represent the stiffness and viscosity of mature focal adhesions.

In ECM regions away from the cell ($-L_1 - L/2 < x < -L/2,\ L/2 < x < L/2 + L_1$) there are no adhesion-based restoring or drag forces to balance internal forces so we have $G_m = 0$.

3.1.5 Upscaling to a continuum description

Upscaling this discrete force balance to obtain a continuum description (e.g. Barry et al., 2022, Besser and Schwarz, 2007) we assume displacements in the cell and ECM respectively are described by continuum functions $u(x,t)$ and $w(x,t)$ such that $u(x = x_n, t) = u_n(t)$ and $w(x = x_n, t) = w_n(t)$. Moreover, we assume that the stiffness and viscosity of integrin-ligand connections (at the cross-link locations) can be described by continuous functions $k_I(x,t)$ and $\eta_I(x,t)$ such that $k_I(x = x_n, t) = k_{I,n}(t)$ and $\eta_I(x = x_n, t) = \eta_{I,n}(t)$, where $k_{I,n}(t) = k_{NA,n}(t) + k_{FA,n}(t)$ and $\eta_{I,n}(t) = \eta_{NA,n}(t) + \eta_{FA,n}(t)$.

We similarly assume that mesh-dependent functions such as cytoplasm stiffness, ECM stiffness, cytoplasm viscosity, ECM viscosity and contractile forces can all be described by continuum functions. In particular, we set $k_i(x = x_{n+1/2}, t) = k_{i,n+1/2}(t)$ where $i = F, S, P, C, O$. Moreover, the viscosity of the cell and ECM are described by continuum functions $n_p(x,t)$ where $\eta_p(x = x_{n+1/2}, t) = \eta_{p,n+1/2}(t)$ where $p = c, E$. The myosin II motor generated contraction force is described by the continuum function $F_{II}(x = x_{n+1/2}, t) = F_{II,n+1/2}(t)$. Finally, for simplicity we combine some of the elastic parameters by writing $k_c(x,t) = k_F(x,t) + k_S(x,t) + k_P(x,t)$ and $k_E(x,t) = k_C(x,t) + k_O(x,t)$.

For $a \ll L, L_1$ we employ Taylor series expansions of each of these functions around a given meshpoint (assuming smoothness within small distances a). Retaining only leading-order terms (i.e. neglecting terms $O(a^2/L^2)$) gives the continuum force in the cell, $F(x,t)$, and in the ECM, $G(x,t)$, as

$$F(x,t) = a^2\frac{\partial}{\partial x}\left(\eta_c(x,t)\frac{\partial^2}{\partial x \partial t} + k_c(x,t)\frac{\partial}{\partial x}\right)u(x,t) + a\frac{\partial F_{II}(x,t)}{\partial x}, \tag{3.11a}$$

$$G(x,t) = a^2\frac{\partial}{\partial x}\left(\eta_E(x,t)\frac{\partial^2}{\partial x \partial t} + k_E(x,t)\frac{\partial}{\partial x}\right)w(x,t). \tag{3.11b}$$

Similarly, Taylor expansion of our expression for the contractile velocity of each cell element from Eq. (3.3) leads to the continuum description for contraction velocity

$$v = -a\frac{\partial}{\partial t}\left(\frac{\partial u}{\partial x}\right), \tag{3.12}$$

where $v(x = x_{n+1/2}, t) = v_{n+1/2}(t)$. Hence, by upscaling Eq. (3.3) we have

$$F_{II}(x,t) = F_{stall}\left(1 + \frac{a}{v_0}\frac{\partial}{\partial t}\left(\frac{\partial u}{\partial x}\right)\right). \tag{3.13}$$

It follows that the continuum force in the cell can instead be expressed as

$$F(x,t) = a^2\frac{\partial}{\partial x}\left(\eta_e\frac{\partial^2}{\partial x \partial t} + k_c\frac{\partial}{\partial x}\right)u + a\frac{\partial F_{stall}}{\partial x}, \tag{3.14}$$

where the effective viscosity is $\eta_e = \eta_c + F_{stall}/v_0$ (described previously for SFs by Besser and Schwarz, 2007). We relabel η_c as η_0 and relabel η_e as η_c and so, henceforth, $\eta_c = \eta_0 + F_{stall}/v_0$ refers to the effective viscosity of the cell cytoplasm.

The internal continuum forces in the cell and ECM, $F(x,t)$ and $G(x,t)$, given by Eqs. (3.11b) and (3.14) respectively, are balanced by a restoring force due to integrins connected to the ECM and due to viscous cell-substrate interaction, as shown in Fig. 3.3. We then derive the continuum version of Eq. (3.10) in the form

$$F(x,t) = k_I\,(u - w) + \eta_I\frac{\partial}{\partial t}\,(u - w) = -G(x,t). \tag{3.15}$$

3.1.6 Conversion of our force balance to a stress balance

We convert the one-dimensional force balance description of Eq. (3.15) to a description involving a stress balance by dividing by an appropriate scale factor. In particular, we let V_C (V_E) be the volume of a segment of the cell (ECM) and set $V_c = aA_c$, $V_E = aA_E$ where A_c, A_E are the cross-sectional areas of the cell and ECM respectively. We rewrite the mechanical properties of the cell and ECM by writing

$$k_c = \frac{E_c A_c}{L_c^0}, \quad \eta_c = \frac{\mu_c A_c}{L_c^0}, \quad F_{stall} = \tau A_c, \quad k_E = \frac{E_E A_E}{L_E^0}, \quad \eta_E = \frac{\mu_E A_E}{L_E^0}, \tag{3.16}$$

where E_c, E_E are the Young's modulus of the cell cytoplasm and ECM respectively, μ_c, μ_E are the (effective) viscosity of the cytoplasm and ECM respectively and τ is the stress exerted inside the cell by contractile SFs. Moreover, L_c^0 and L_E^0 are the natural lengths of the cell and ECM segments. We suppose that $L_c^0 = L_E^0 = a$ so that this length scale does not feature in the point-wise momentum balance equations. We hence obtain the stress

counterparts of Eq. (3.11) as

$$\hat{F}(x,t) = \frac{\partial}{\partial x}\left(\mu_c(x,t)\frac{\partial^2}{\partial x \partial t} + E_c(x,t)\frac{\partial}{\partial x}\right)u(x,t) + \frac{\partial \tau(x,t)}{\partial x}, \tag{3.17a}$$

$$\hat{G}(x,t) = \frac{\partial}{\partial x}\left(\mu_E(x,t)\frac{\partial^2}{\partial x \partial t} + E_E(x,t)\frac{\partial}{\partial x}\right)w(x,t). \tag{3.17b}$$

In Eq. (3.15) we assume that $A_c = A_E$ and write $k_I = \kappa_I a A_c$, $\eta_I = \beta_I a A_c$, where κ_I is the stiffness of adhesions per cell (or ECM) volume and η_I is the drag due to adhesions. We hence conclude that

$$\hat{F}(x,t) = \kappa_I\,(u-w) + \beta_I \frac{\partial}{\partial t}\,(u-w) = -\hat{G}(x,t). \tag{3.18}$$

Finally, comparison of Eqs. (3.17) and (3.18) produces the governing (momentum balance) equations in terms of the Cauchy stress in the cytoplasm and ECM of the form

$$\frac{\partial \sigma_c}{\partial x} = \kappa_I\,(u-w) + \beta_I \frac{\partial}{\partial t}\,(u-w)\,, \quad \frac{\partial \sigma_E}{\partial x} = \kappa_I\,(w-u) + \beta_I \frac{\partial}{\partial t}\,(w-u)\,, \tag{3.19a}$$

where κ_I is the stiffness (per unit cell volume) of adhesions (both nascent and focal) and β_I is the drag per unit volume; this is similar to that of Gracheva and Othmer (2004), Larripa and Mogilner (2006), but both considered the cell only. The drag term is decomposed into three components in the form

$$\beta_I = \beta_e + \beta_{NA} + \beta_{FA}, \tag{3.19b}$$

where β_e is a (small) uniform background drag (introduced mainly for computational ease), whilst β_{NA} and β_{FA} are the drag associated with nascent and focal adhesions (which are specified in terms of the adhesion densities in Sec. 3.5.3 below). The additional uniform drag term is necessary in simulations owing to our imposed initial conditions (see Table 3.2 below). In particular, we assume the cell is initially well spread but has formed no adhesions to resist deformation; this additional drag ensures the cell is initially in contact with the ECM long enough to begin forming adhesions. An alternative approach would be to assume some adhesions have already formed at the initialisation of simulations. We infer the corresponding continuum Cauchy stress tensors of the cell and ECM as

$$\sigma_c = \left(\mu_c \frac{\partial^2}{\partial x \partial t} + E_c \frac{\partial}{\partial x}\right)u + \tau, \quad \sigma_E = \left(\mu_E \frac{\partial^2}{\partial x \partial t} + E_E \frac{\partial}{\partial x}\right)w, \tag{3.19c}$$

where $\mu_c = \mu_0 + \tau/v_0$ is the effective viscosity of the cell cytoplasm (with μ_0 the unmodified cytoplasm viscosity), μ_E is the viscosity of the ECM, $E_c = E_F + E_S + E_P$ is the effective Young's modulus of the cytoplasm (a sum of the Young's modulus of actin filaments, E_F,

VSFs, E_S, and a passive contribution due to the cell nucleus, microtubules and intermediate filaments, E_P), $E_E = E_C + E_O$ is the effective Young's modulus of the ECM (a sum of the Young's modulus of collagen fibres, E_C, and other proteins, E_O) and τ is the active stress generated by myosin II motor action. Note that for the remainder of this Chapter we consider an ECM consisting of collagen alone and hence neglect E_O.

3.1.7 Extension of ECM beyond the footprint of the cell

We assume that the domain of the ECM extends beyond the edges of the cell and is described by a set of material points $-L_1 - L/2 \leq x \leq L_1 + L/2$. In particular, we suppose that the ECM is composed of three compartments as indicated in Fig. 3.1, with region 1 described by points $-L_1 - L/2 \leq x \leq -L/2$, region 2 described by points $L/2 \leq x \leq L/2 + L_1$ and region 3 (lying underneath the cell) described by points $-L/2 \leq x \leq L/2$.

For simplicity, we assume that the ECM has constant Young's modulus and viscosity in regions 1 and 2 so that $E_E(x,t) = \bar{E}$, $\mu_E(x,t) = \bar{\mu}$, in these regions. We denote the continuum displacement of the ECM in each of these regions by $\bar{w}_i$ $(i = 1, 2)$ and note that the Cauchy stress, $\bar{\sigma}_{E,1}$ $(\bar{\sigma}_{E,2})$, in region 1 (2) is given by

$$\bar{\sigma}_{E,1} = \bar{E}\frac{\partial \bar{w}_1}{\partial x} + \bar{\mu}\frac{\partial^2 \bar{w}_1}{\partial x \partial t}, \quad \bar{\sigma}_{E,2} = \bar{E}\frac{\partial \bar{w}_2}{\partial x} + \bar{\mu}\frac{\partial^2 \bar{w}_2}{\partial x \partial t}. \tag{3.20}$$

Given these regions are not connected to the cell (and so there are no adhesion mediated drag or restoring forces), we thus solve Eq. (3.19a) with $\kappa_I = 0$, $\beta_I = 0$. Given that $\bar{E}$ and $\bar{\mu}$ are independent of x, we have

$$\bar{E}\frac{\partial^2 \bar{w}_i(x,t)}{\partial x^2} + \bar{\mu}\frac{\partial^3 \bar{w}_i(x,t)}{\partial x^2 \partial t} = 0. \tag{3.21}$$

Integrating with respect to x twice we obtain

$$\bar{E}\bar{w}_i + \bar{\mu}\frac{\partial \bar{w}_i}{\partial t} = A_i(t)x + B_i(t), \tag{3.22}$$

where A_i, B_i are functions of time. Treating x as a parameter, Eq. (3.22) is a first-order linear inhomogeneous PDE which can be solved for $\bar{w}_i$ using an appropriate integrating factor. We focus our attention on region 1, with the calculation for region 2 analogous.

In region 1 we impose no displacement initial conditions, $\bar{w}_1(x,0) = 0$. For the boundaries of region 1 we impose the following boundary/matching conditions

$$\bar{w}_1(-L/2 - L_1, t) = 0, \quad \bar{w}_1(-L/2, t) = w(-L/2, t), \quad \bar{\sigma}_{E,1}(-L/2, t) = \sigma(-L/2, t), \tag{3.23}$$

where $w(x,t)$ denotes the (numerically calculated) continuum displacement in region 3 (underneath the cell). The first condition imposes no displacement on the far field boundary

(the ECM is fixed at some distance L_1 from the cell), the second and third equations represent matching of displacement and stress (these must be continuous) across the boundary connecting region 1 and region 3. Imposing no displacement in the far field gives

$$\bar{E}\bar{w}_1 + \bar{\mu}\frac{\partial \bar{w}_1}{\partial t} = A_1(t)\left(x + L_1 + \frac{L}{2}\right), \tag{3.24}$$

which yields

$$\bar{w}_1 = \frac{1}{\bar{\mu}L_1}\left(x + L_1 + \frac{L}{2}\right)e^{-t\bar{E}/\bar{\mu}}\int_0^t A_1(T)e^{T\bar{E}/\bar{\mu}}dT. \tag{3.25}$$

In order to apply our matching conditions we require the numerically calculated (discussed in Sec. 3.7 below) displacement and stress at the left boundary of region 3. The displacement at this point is given by $w(-L/2, t) = w_0(t)$. Applying the displacement matching conditions at the boundary of regions 1 and 3 hence gives

$$\bar{w}_1(x,t) = \frac{1}{L_1}\left(x + L_1 + \frac{L}{2}\right)w_0(t), \tag{3.26a}$$

a linearly decreasing function of displacement away from the cell, governed by the time-dependent displacement of the boundary with region 3.

In a similar calculation we deduce the displacement of points in region 2 are given by

$$\bar{w}_2(x,t) = \frac{1}{L_1}\left(L_1 + \frac{L}{2} - x\right)w_N(t), \tag{3.26b}$$

where $w_N(t)$ is the numerically calculated value of displacement at the right boundary of region 3.

With our analytical description from Eq. (3.26) for displacement in regions 1 and 2, we match stress across each boundary between different regions (as discussed in detail below in Sec. 3.3). In particular, we incorporate this into our numerical method to describe the displacement of the ECM underneath the cell (region 3), as discussed in Sec. 3.7 (below). In Ch. 4 we explore the effect that changes to this far field boundary condition have on the cell, mimicking, for example, the influence of ECM remodelling by other cells.

3.2 Biochemical Model

The mechanical properties of the cell depend on the concentrations of intra- and extracellular proteins. In particular, the scaffolding protein actin in its various forms contributes to cell stiffness, whilst SFs generate contractile forces (due to the action of myosin motors) within the cell that are transmitted to the ECM through adhesions (Besser and Schwarz, 2007, Gracheva and Othmer, 2004). Moreover, nascent and focal adhesions provide drag

forces due to viscous resistance to motion through the membrane. Furthermore, certain signaling proteins are activated in response to the formation and maturation of adhesions which promote SF assembly and contraction causing maturation of the cytoskeleton. Therefore, to fully describe the deformation of the cell, we must also characterise the internal signaling pathways and the dynamics of scaffolding proteins and couple to the mechanical components discussed above.

Diagrams summarising the reactions considered in this model are shown in Figs. 1.4-1.5 and are similar to those explored in Ch. 2. In particular, free integrins (with a low-affinity for binding to ECM ligands) become activated to form high-affinity integrins, which bind to the ECM ligands to form nascent adhesions. Nascent adhesions can mature to form FAs in a force-dependent manner (i.e. forces applied to adhesions promotes maturation). The formation and maturation of adhesions leads to an increase in intracellular signaling for increased (decreased) myosin II activation (inactivation) and increased (decreased) actin polymerisation (depolymerisation). Consequently, actin monomers polymerise into filaments and myosin II becomes activated, facilitating cross-linking of actin filaments to form VSFs. In turn, VSFs exert forces that stretch adhesions, exposing VBSs on talin, leading to adhesion maturation and closing a positive feedback loop.

A key feature of our one-dimensional model in this Chapter is the assumption that the ECM ligands can be divided into two distinct families, as summarised in Fig. 3.6. For simplicity, we distinguish these families by the direction in which the anchored actin filaments grow; see sketch in Fig. 3.6(a). Such an approach is designed to ensure the two families of filaments grow toward one another, in order to mimic the growth of filaments (and hence VSFs) between FAs. As these two families of ECM ligands bind to the cell, this naturally results in two corresponding families of adhesions and actin filaments; we denote these as family 1 and family 2, indicated with a superscript (1) or (2), respectively. Ligands associated with family 1 (2) have density $n_s^{(1)}$ ($n_s^{(2)}$) and connect to high-affinity integrins to form family 1 (2) nascent adhesions, density $n_b^{(1)}$ ($n_b^{(2)}$). Nascent adhesions can mature into FAs, density $n_A^{(1)}$ ($n_A^{(2)}$), from which family 1 (2) actin filaments are polymerised and grow, with concentration $c_F^{(1)}$ ($c_F^{(2)}$). Each family is endowed with a corresponding actin polymerisation velocity. Note that this categorisation only works in one dimension.

In this model we prescribe the spatial profile of ligand patterning so that the total ECM ligand density is constant along the length of the cell. Each family of ligands can be described at $t = 0$ by

$$n_s^{(i)}(x, 0) = N_0^S S_{(i)}(x), \tag{3.27}$$

where $i = 1, 2$, N_0^S is a constant (the maximum ligand density) and $0 \leq S_{(i)}(x) \leq 1$ is a prescribed function which decays to zero at the right (left) boundary of the cell for family 1 (family 2) ligands. We choose $S_{(1)}$, $S_{(2)}$ so that $S_{(1)} + S_{(2)} = N_0^S$ at any point x. A typical spatial profile of ligand patterning is shown in Fig. 3.6(b).

Moreover, for simplicity, we assume that treadmilling of actin filaments occurs at (approximately) constant velocity U_0, maintaining initial direction, with family 1 filaments treadmilled to the right (increasing x) and family 2 filaments treadmilled to the left (decreasing x). The assumed spatial profile of the treadmilling velocity is shown in Fig. 3.6(c). In particular, we assume that treadmilling within each family of filaments is reduced at the boundaries to ensure mass conservation within the cell, which we capture by multiplying by a dimensionless function, $\tilde{U}^{(1)}$, $\tilde{U}^{(2)}$, which are both broadly constant but decay significantly near the boundaries (as indicated in Fig. 3.6c). Hence, actin treadmilling velocity terms can be written in the form

$$U^{(1)} = U_0\tilde{U}^{(1)}, \quad U^{(2)} = U_0\tilde{U}^{(2)}. \tag{3.28}$$

Note that this velocity profile neglects the effect that rapid changes in actin concentration at adhesions could have on the treadmilling velocity, but this simple expression is used for tractability.

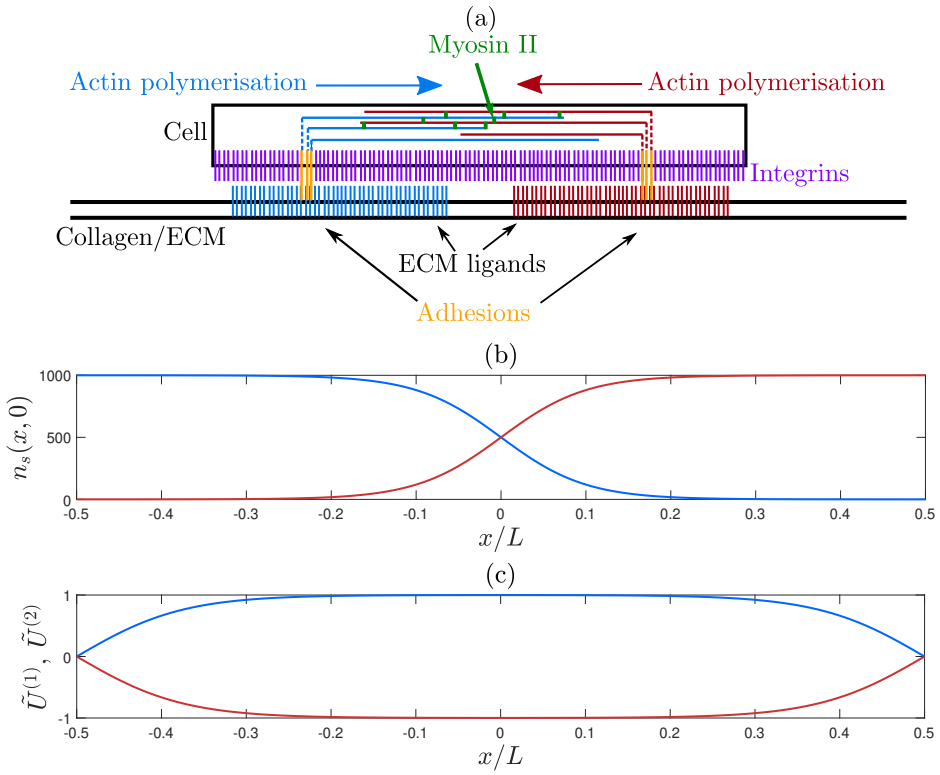

Figure 3.6: Overview of biochemical set-up. (a) Two families of adhesions: family 1 (2) ligands in blue (red) connect to integrins on the cell membrane to form family 1 (2) adhesions, from which actin filaments grow. Imposed ligand patterning shown in panel (b) and actin treadmilling velocity for both families shown in panel (c).

We now outline the dynamical equations for each of the respective protein families in the model. Note that, as we assume deformations of the cell and ECM are small, for simplicity we solve these biochemical equations in the reference configuration. Moreover,

note that several of the reaction rates describing the dynamics of scaffolding proteins are coupled to the concentration of signaling proteins or cell deformation; constitutive assumptions describing these dynamics are presented in Secs. 3.5.1-3.5.2 (below). In particular, these rates will be non-constant and spatially non-uniform functions of other variables, preventing simple decoupled solutions of the system.

3.2.1 Cytoskeleton proteins

Our model for maturation of the cytoskeleton incorporates the polymerisation of actin protein monomers into actin filaments. These filaments become cross-linked by activated myosin II to form contractile SFs. In this one-dimensional framework we propose a system of reaction-diffusion-advection PDEs to describe the dynamics of actin and myosin and conversion between different states (*cf.* simple reaction ODEs presented in Sec. 2.1.1).

The concentration of G-actin monomers, c_G, satisfies

$$\frac{\partial c_G}{\partial t} = -k_p^+ c_G \left(n_b^{(1)} + n_b^{(2)} + n_A^{(1)} + n_A^{(2)}\right) + k_p^- \left(c_F^{(1)} + c_F^{(2)}\right) + k_m^- c_S^+ + D_G \frac{\partial^2 c_G}{\partial x^2}, \quad (3.29a)$$

where k_p^+ represents the rate per adhesion of polymerisation of actin monomers (at adhesions), k_p^- represents the dissociation rate of actin filaments and k_m^- is the dissociation rate of VSFs, concentration c_S^+. Note the similarities with Eq. (2.1a), describing actin monomer concentration in our simple spatially-averaged model; in this model the rates of actin polymerisation and depolymerisation similarly depend on the concentration of signaling proteins, as detailed in Sec. 3.5.1 (below). However, we now account for spatial variations in protein concentration and assume that G-actin is diffusive, with (constant) diffusion coefficient D_G, allowing monomer concentration to be replenished in regions with high polymerisation rates.

The resulting actin filament families can be cross-linked by activated myosin II, concentration $c_m^+(x,t)$, to form SFs, with the concentration of each family of filaments given by

$$\begin{aligned}\frac{\partial c_F^{(i)}}{\partial t} + \frac{\partial}{\partial x}\left(c_F^{(i)} U^{(i)}\right) = k_p^+ c_G \left(n_b^{(i)} + n_A^{(i)}\right) - k_p^- c_F^{(i)} \\ - k_m^+ \left(c_F^{(i)} c_F^{(i)} + c_F^{(1)} c_F^{(2)} + c_F^{(i)} c_S^+\right) c_m^+ + D_F \frac{\partial^2 c_F^{(i)}}{\partial x^2},\end{aligned} \quad (3.29b)$$

where $i = 1, 2$. Actin filaments form due to polymerisation of G-actin and are recruited into SFs at rate proportional to k_m^+ through cross-linking by active myosin II to other filaments or existing SFs. As discussed above, we include the directed treadmilling of filaments at speed $U^{(i)}$ due to polymerisation at the attached adhesion; this motion is directed away from the nearest cell edge using an advection-like term (see prescribed form in Fig. 3.6c). To ensure these PDEs are parabolic, we include a small diffusion term, with constant diffusivity D_F, allowing application of boundary conditions at both ends of the

domain (this is similar to Larripa and Mogilner, 2006). This formulation is similar to our description of actin filament dynamics in Ch. 2 (see Eq. 2.1b), but actin filaments in this one-dimensional model have variable concentration spatially, can diffuse and can be treadmilled (advected).

Actin bundles from the two families can interact with others from the same family or from the other family and with active myosin II to form SFs; their concentration satisfies the PDE

$$\frac{\partial c_S^+}{\partial t} = k_m^+ \left(2c_F^{(1)}c_F^{(2)} + c_F^{(1)}c_F^{(1)} + c_F^{(2)}c_F^{(2)} + c_F^{(1)}c_S^+ + c_F^{(2)}c_S^+\right) c_m^+ - k_m^- c_S^+, \tag{3.29c}$$

where k_m^- is the rate of SF disassembly. Upon disassembly SFs are assumed to decompose directly into the constituent active myosin II and actin monomers (not filaments). This formulation is similar to our description of SF formation in our spatially-averaged modelling approach in Ch. 2 (see Eq. 2.1c).

Unbound myosin II motors exist in two states: inactive and active (where they can cross-link actin bundles and facilitate contraction). Transition between these states occurs in response to Rho-signaling, which is strengthened in response to FA formation. The concentration of free inactive myosin II motors, denoted c_m, is given by

$$\frac{\partial c_m}{\partial t} = -k_a^+ c_m + k_a^- c_m^+ + D_m \frac{\partial^2 c_m}{\partial x^2}, \tag{3.29d}$$

where D_m is the (constant) diffusion coefficient for inactive myosin II motors and where myosin II is activated and deactivated at rate k_a^+ and k_a^- respectively; in a similar manner to Ch. 2 these rates are non-constant and depend on the concentration of signaling proteins, as detailed in Sec. 3.5.1 (below). The concentration of free activated myosin II in the cell is then described by

$$\begin{aligned}\frac{\partial c_m^+}{\partial t} = {} & k_a^+ c_m - k_a^- c_m^+ - k_m^+ \left(2c_F^{(1)}c_F^{(2)} + c_F^{(1)}c_F^{(1)} + c_F^{(2)}c_F^{(2)} + c_F^{(1)}c_S^+ + c_F^{(2)}c_S^+\right) c_m^+ \\ & + k_m^- c_S^+ + D_m^+ \frac{\partial^2 c_m^+}{\partial x^2},\end{aligned} \tag{3.29e}$$

where D_m^+ is the (constant) diffusivity of active myosin II. These equations, describing the activation of myosin II, and its subsequent cross-linking of actin, are similar to their counterparts Eqs. (2.1e)-(2.1f) in the spatially-averaged model developed in Ch. 2. However, we additionally incorporate diffusivity of myosin II in this one-dimensional model.

3.2.2 Adhesion proteins

Adhesions connect the cell to the underlying ECM through integrin-ligand mediated connections. This process begins inside the cell, where talin binds integrins to the cytoskeleton. In response, integrins change conformation and develop a high-affinity for ECM

binding. This conversion from low-affinity to high-affinity occurs at rate k_h^+ and is reversible with rate k_h^-. These low-affinity integrins can also diffuse along the membrane (Pathak et al., 2008), with (constant) diffusivity D_f, replenishing regions where integrins have become high-affinity (and have subsequently bound to the ECM). Hence, the density, n_f, of free, low-affinity integrins, satisfies

$$\frac{\partial n_f}{\partial t} = -k_h^+ n_f + k_h^- n_h + D_f \frac{\partial^2 n_f}{\partial x^2}, \tag{3.29f}$$

where n_h represents the number density of high-affinity unbound integrins.

In their high-affinity state, integrins can now bind to ligands of density $n_s^{(1)}$ and $n_s^{(2)}$, representing, respectively, the two families in the underlying ECM, allowing for the formation of nascent adhesions (bound integrins). This binding occurs at a rate k_b^+ per ligand, whilst bonds between the integrins and the substrate break at rate k_b^-. We describe the dynamics of high-affinity integrins and substrate ligands respectively by the PDEs

$$\frac{\partial n_h}{\partial t} = k_h^+ n_f - k_h^- n_h - k_b^+ n_h \left(n_s^{(1)} + n_s^{(2)}\right) + k_b^- \left(n_b^{(1)} + n_b^{(2)}\right), \tag{3.29g}$$

$$\frac{\partial n_s^{(i)}}{\partial t} = -k_b^+ n_h n_s^{(i)} + k_b^- n_b^{(i)}, \tag{3.29h}$$

with $i = 1, 2$, where $n_b^{(1)}$ and $n_b^{(2)}$ are used to describe the density of bound integrins related to each family of ligands, with densities $n_s^{(1)}$ and $n_s^{(2)}$, respectively.

The concentration of bound integrins, $n_b^{(i)}$, is given by

$$\frac{\partial n_b^{(i)}}{\partial t} = k_b^+ n_h n_s^{(i)} - k_b^- n_b^{(i)} - k_F^+ n_b^{(i)} + k_F^- n_A^{(i)}, \tag{3.29i}$$

$i = 1, 2$, describing the formation of nascent adhesions and their subsequent maturation into FAs. The conversion from nascent to focal adhesions occurs, through recruitment of vinculin, at rate k_F^+, whilst FAs can dissociate at rate k_F^-.

Finally, the concentration of FAs associated with each cluster can be described by

$$\frac{\partial n_A^{(i)}}{\partial t} = k_F^+ n_b^{(i)} - k_F^- n_A^{(i)}. \tag{3.29j}$$

In a similar manner to Ch. 2, the rate of adhesion maturation is non-constant. However, in this one-dimensional framework we link this rate to the stretch of adhesions as detailed in Sec. 3.5.2 (below); *cf.* the highly empirical relation employed in Ch. 2, which couples this rate to SF concentration.

Note that, as purely reaction equations, Eqs. (3.29g)-(3.29j) are very similar to their counterparts (Eqs. 2.1h-2.1k) in the spatially-averaged model developed in Ch. 2. However, this one-dimensional model allows for spatial variation in the density of each species and

requires distinction between two families of ligands and adhesions. The description of free integrin dynamics (see Eq. 3.29f) is similar to the spatially-averaged description presented in Ch. 2 (Eq. 2.1g). However, in this one-dimensional framework free integrins can diffuse along the cell membrane.

3.2.3 Signaling proteins

Recall that, in response to cell-substrate adhesion formation, the Rho signaling protein is activated, regulating actin polymerisation rates and myosin II activation (Deguchi and Sato, 2009) through a variety of mechanisms including upregulation of mDia1 and Rho-kinase (ROCK), as shown in Fig. 1.5 (Feng et al., 1999, Maekawa et al., 1999). Recall also that for our modelling purposes we assume that increases in mDia1 activity occurs in tandem with ROCK activation and so we use activated ROCK as a proxy measure for mDia1 activity and hence the actin polymerisation rate. Our modelling approach here is similar to that presented in Sec. 2.1.3 in the formulation of our spatially-averaged biochemical model developed in Ch. 2. However, this one-dimensional framework allows for spatial variation in the concentration of ROCK and its downstream effectors. Additionally, we now incorporate diffusivity of downstream effectors of ROCK. It is worth emphasising that, although the subsequent proposed dynamics for signaling proteins appears simple, several of the reaction rates are non-constant; the constitutive relations required to fully describe these rates are presented in Secs. 3.5.1-3.5.2 (below).

We let c_R denote the concentration of inactive ROCK and c_R^+ denote the concentration of activated ROCK. We assume that both forms of ROCK are non-diffusive and so their dynamics are described by a set of kinetic equations, with activation at rate k_R^+ and inactivation occurring at rate k_R^-, in the form

$$\frac{\partial c_R}{\partial t} = -k_R^+ c_R + k_R^- c_R^+, \tag{3.30a}$$

$$\frac{\partial c_R^+}{\partial t} = k_R^+ c_R - k_R^- c_R^+. \tag{3.30b}$$

In response to ROCK activation, myosin light chain phosphatase (MLCP), which inactivates active myosin II, is phosphorylated to form phosphorylated myosin light chain phosphatase (MLCP-P); this phosphorylation suppresses the inhibitory ability of MLCP on myosin II activation. Phosphorylation of MLCP, concentration c_P, occurs at rate k_1^+, whilst dephosphorylation of MLCP-P, concentration c_{P-P}, occurs at rate k_1^-. Their dynamics are described by the reaction-diffusion equations

$$\frac{\partial c_P}{\partial t} = -k_1^+ c_P + k_1^- c_{P-P} + D_P \frac{\partial^2 c_P}{\partial x^2}, \tag{3.30c}$$

$$\frac{\partial c_{P-P}}{\partial t} = k_1^+ c_P - k_1^- c_{P-P} + D_{P-P} \frac{\partial^2 c_{P-P}}{\partial x^2}, \tag{3.30d}$$

where MLCP and MLCP-P are assumed to be diffusive with constant diffusivities D_P and D_{P-P} respectively.

Furthermore, ROCK activation triggers phosphorylation of myosin light chain kinase (MLCK), concentration c_K, to form phosphorylated myosin light chain kinase (MLCK-P), concentration c_{K-P} (Dalby et al., 2018). In its phosphorylated form, MLCK-P facilitates activation of myosin II. We describe the dynamics of MLCK phosphorylation by

$$\frac{\partial c_K}{\partial t} = -k_2^+ c_K + k_2^- c_{K-P} + D_K \frac{\partial^2 c_K}{\partial x^2}, \tag{3.30e}$$

$$\frac{\partial c_{K-P}}{\partial t} = k_2^+ c_K - k_2^- c_{K-P} + D_{K-P} \frac{\partial^2 c_{K-P}}{\partial x^2}, \tag{3.30f}$$

where k_2^+ is the phosphorylation rate of MLCK, k_2^- is the rate at which MLCK-P is dephosphorylated and where D_K and D_{K-P} are the constant diffusivities of MLCK and MLCK-P, respectively.

Finally, ROCK also phosphorylates cofilin, concentration c_C, at rate k_3^+ to form phosphorylated cofilin, concentration c_{C-P}, whilst this process is also reversible with rate k_3^-. These dynamics are described by reaction-diffusion equations in the form

$$\frac{\partial c_C}{\partial t} = -k_3^+ c_C + k_3^- c_{C-P} + D_C \frac{\partial^2 c_C}{\partial x^2}, \tag{3.30g}$$

$$\frac{\partial c_{C-P}}{\partial t} = k_3^+ c_C - k_3^- c_{C-P} + D_{C-P} \frac{\partial^2 c_{C-P}}{\partial x^2}, \tag{3.30h}$$

where D_C and D_{C-P} represent the (constant) diffusivities of cofilin and phosphorylated cofilin respectively. Note that phosphorylation of cofilin inhibits its ability to sever actin filaments and so the actin depolymerisation rate, k_p^-, decreases, as discussed in Sec. 3.5 below.

It should be noted that, despite their simple appearance, the dynamics of signaling proteins described are still coupled to the dynamics of the wider system. Indeed several of the reaction rates are non-constant and spatially non-uniform functions of other variables, preventing a simple decoupled solution for the dynamics of signaling proteins.

3.3 Initial and boundary conditions

In this Section we outline the initial and boundary conditions we impose on the governing equations describing the deformation of the cell, ECM and adhesions (see Sec. 3.1) and the cell biochemistry (see Sec. 3.2).

3.3.1 Mechanical conditions

Initially, we assume zero displacement everywhere in the cell and ECM in the form

$$u(x,0) = 0, \quad w(x,0) = 0. \tag{3.31a}$$

We prescribe boundary stresses on the cell in the form

$$\sigma_c\left(-L/2,t\right) = -\sigma_1, \quad \sigma_c\left(L/2,t\right) = \sigma_2, \tag{3.31b}$$

where σ_1, σ_2 can be used to represent stresses due to actin polymerisation at the boundaries pushing against the membrane (in a similar manner to Gracheva and Othmer, 2004) or external stresses. In the absence of contractility, these stresses would lead to expansion of the cell. However, in a non-motile cell these forces are negligible. Hence, we set $\sigma_1 = 0$ Pa, $\sigma_2 = 0$ Pa.

The boundary conditions imposed on the ECM require a different treatment, as indicated in Fig. 3.1. In particular, we impose zero displacement in the ECM far field

$$w\left(-L/2 - L_1,t\right) = 0, \quad w\left(L/2 + L_1,t\right) = 0, \tag{3.31c}$$

whilst at the junctions between ECM regions either side of the cell boundary we match stress and displacement. It then emerges (see Sec. 3.1.7) that we can semi-analytically solve the ECM mechanical equations away from the cell to obtain a description of the displacement of the ECM in these regions, given by Eq. (3.26). As discussed in Sec. 3.1.7, we use these displacements to match displacement between region 1 and region 3 and region 2 and region 3, providing boundary conditions for the region of ECM below the cell in the form

$$\sigma_E(-L/2,t) = \bar{\sigma}_{E,1}(-L/2,t), \quad \sigma_E(L/2,t) = \bar{\sigma}_{E,2}(L/2,t), \tag{3.31d}$$

where $\bar{\sigma}_{E,i}$ is the analytically calculated stress in the ECM regions to the left and right of the cell.

3.3.2 Biochemistry conditions

We assume that the cell is newly introduced to the substrate so that no adhesions have formed and all integrins are in their low-affinity state for ECM ligand binding. Moreover we assume that no SFs or actin filaments have formed so that all actin is monomeric. We additionally assume that ROCK is initially wholly inactive and consequently, MLCP, MLCK and cofilin are all initially unphosphorylated and myosin II is found entirely in its inactive state. We detail the full initial conditions for each protein in Sec. 3.6.

To conserve the mass of each family of proteins in the cell, we assume no flux boundary

conditions for each species. In general, the flux, j_α, of an advective (with velocity U_α) and diffusive (with diffusivity D_α) protein, with concentration c_α, satisfies

$$j_\alpha = U_\alpha c_\alpha - D_\alpha \frac{\partial c_\alpha}{\partial x} = 0, \tag{3.32}$$

at the boundaries $x = -L/2$ and $x = L/2$, i.e. advective and diffusive effects must balance. For non-diffusive and non-advective proteins we immediately satisfy no-flux boundary conditions and solve the reaction equations at the boundary as we do at the interior. For diffusive proteins that do not experience advection then Eq. (3.32) becomes

$$\frac{\partial c_\alpha}{\partial x} = 0, \tag{3.33}$$

at $x = -L/2$, $x = L/2$. The only protein species in our model that is assumed to be advected (treadmilled) are actin filaments. We deduce that at the boundaries we must satisfy

$$D_F \frac{\partial c_F^{(i)}}{\partial x} = U_0 \tilde{U}^{(i)} c_F^{(i)}, \tag{3.34}$$

for $i = 1, 2$.

Assuming that the boundary condition Eq. (3.32) is satisfied for all species then, together with Eqs. (3.29a)-(3.30h), we derive the following conservation laws

$$\begin{gathered}
\frac{\partial}{\partial t}\int_{-\frac{L}{2}}^{\frac{L}{2}} \left(c_G(x,t) + c_F^{(1)}(x,t) + c_F^{(2)}(x,t) + c_S^{+}(x,t)\right) dx = 0, \\
\frac{\partial}{\partial t}\int_{-\frac{L}{2}}^{\frac{L}{2}} \left(n_f(x,t) + n_h(x,t) + n_b^{(1)}(x,t) + n_b^{(2)}(x,t) + n_A^{(1)}(x,t) + n_A^{(2)}(x,t)\right) dx = 0, \\
\frac{\partial}{\partial t}\int_{-\frac{L}{2}}^{\frac{L}{2}} \left(c_R(x,t) + c_R^{+}(x,t)\right) dx = 0, \quad \frac{\partial}{\partial t}\int_{-\frac{L}{2}}^{\frac{L}{2}} \left(c_P(x,t) + c_{P-P}(x,t)\right) dx = 0, \\
\frac{\partial}{\partial t}\int_{-\frac{L}{2}}^{\frac{L}{2}} \left(c_K(x,t) + c_{K-P}(x,t)\right) dx = 0, \quad \frac{\partial}{\partial t}\int_{-\frac{L}{2}}^{\frac{L}{2}} \left(c_C(x,t) + c_{C-P}(x,t)\right) dx = 0,
\end{gathered} \tag{3.35}$$

representing, respectively, conservation of actin (in all its forms), of integrins (in their various forms), of ROCK (in its inactivated and activated forms) and of MLCP, MLCK and cofilin (in their phosphorylated and unphosphorylated forms) in the cell.

3.4 Non-dimensionalisation

In a similar way to Ch. 2, to simplify our analysis we non-dimensionalise our biochemical and mechanical equations. Given that our primary interest is in the microscale patterning of adhesion to the substrate we scale all lengths on the cell length, L, and time on $\langle t \rangle =$

$1/\left(k_b^+ N_S\right)$, the characteristic timescale of the formation of nascent adhesions (due to the binding of high-affinity integrins with ECM ligands), where N_S is the initial average free ligand density. Note that this process is rapid compared to adhesion maturation into focal structures, and so we consider the dynamics of the model over a large number of dimensionless time units. However, we are interested in all timescales. We scale stresses on E_0^F, the Young's modulus of actin filaments when they are at a typical concentration (defined below). Furthermore, as discussed in detail in Sec. 3.4.2 (below), we scale actin concentrations on C_A, the initial average concentration of actin (in all its forms), scale myosin concentrations on C_M, the initial average concentration of myosin (in its inactive and active forms). We scale integrin and adhesion density on the average initial integrin density (in all its forms), N_I, and scale ligand density on N_S. A similar treatment is given to signaling proteins with ROCK concentration scaled on C_R, the average initial ROCK concentration (in its active and inactive forms), MLCP concentration scaled on C_P, the average concentration of MLCP (in its phosphorylated and unphosphorylated forms), MLCK concentration scaled on C_K, the average total concentration of MLCK (in its phosphorylated and unphosphorylated forms) and cofilin concentration scaled on C_C, the average total concentration of cofilin (in its phosphorylated and unphosphorylated forms).

3.4.1 Mechanical equations

In order to non-dimensionalise the mechanical equations Eq. (3.19a) we write

$$\begin{gathered} E_F = E_0^F \tilde{f}_F, \quad E_S = E_0^S \tilde{f}_S, \quad E_P = E_0^P \tilde{f}_P, \quad E_C = E_0^C \tilde{f}_C, \\ E_O = E_0^O \tilde{f}_O, \quad \tau = \tau_0 \tilde{f}_\tau, \quad \mu_c = \mu_0^c \tilde{g}_c, \quad \mu_E = \mu_0^E \tilde{g}_E, \\ \kappa_{NA} = \kappa_0^{NA} \tilde{f}_{NA}, \quad \kappa_{FA} = \kappa_0^{FA} \tilde{f}_{FA}, \quad \beta_{NA} = \beta_0^{NA} \tilde{f}_{NA}, \quad \beta_{FA} = \beta_0^{FA} \tilde{f}_{FA}, \end{gathered} \tag{3.36}$$

where E_0^F, E_0^S, E_0^P, E_0^C, E_0^O, κ_0^{NA}, κ_0^{FA}, β_0^{NA}, β_0^{FA}, τ_0, μ_0^c and μ_0^E are dimensional constants, and all variables with tildes are dimensionless functions. By scaling position, time and velocity by writing $x' = x/L$, $t' = t/\langle t \rangle$, $v' = v\langle t \rangle / L$ then the dimensionless form of the governing equations Eq. (3.19a) are

$$\begin{aligned} &\left(\frac{\partial}{\partial x'} \left(\tilde{\mu}_0^c \tilde{g}_c \right) \frac{\partial^2}{\partial x' \partial t'} + \frac{\partial}{\partial x'} \left(\tilde{f}_F + \tilde{E}_0^S \tilde{f}_S + \tilde{E}_0^P \tilde{f}_P \right) \frac{\partial}{\partial x'} \right) u' + \tilde{\tau}_0 \frac{\partial}{\partial x'} \left(\tilde{f}_\tau \right) \\ &= \left(\tilde{\kappa}_0^{NA} \tilde{f}_{NA} + \tilde{\kappa}_0^{FA} \tilde{f}_{FA} \right) (u' - w') + \left(\tilde{\beta}_0^{NA} \tilde{f}_{NA} + \tilde{\beta}_0^{FA} \tilde{f}_{FA} + \tilde{\beta}_e \right) \frac{\partial}{\partial t'} (u' - w'), \end{aligned} \tag{3.37a}$$

$$\begin{aligned} &\left(\frac{\partial}{\partial x'} \left(\tilde{\mu}_0^E \tilde{g}_E \right) \frac{\partial^2}{\partial x' \partial t'} + \frac{\partial}{\partial x'} \left(\tilde{E}_0^C \tilde{f}_C + \tilde{E}_0^O \tilde{f}_O \right) \frac{\partial}{\partial x'} \right) w' \\ &= \left(\tilde{\kappa}_0^{NA} \tilde{f}_{NA} + \tilde{\kappa}_0^{FA} \tilde{f}_{FA} \right) (w' - u') + \left(\tilde{\beta}_0^{NA} \tilde{f}_{NA} + \tilde{\beta}_0^{FA} \tilde{f}_{FA} + \tilde{\beta}_e \right) \frac{\partial}{\partial t'} (w' - u'), \end{aligned} \tag{3.37b}$$

where we have the following dimensionless groups

$$\begin{gathered}\tilde{\mu}_0^c = \mu_0^c/E_0^F\langle t\rangle, \quad \tilde{\tau}_0 = \tau_0/E_0^F, \quad \tilde{E}_0^S = E_0^S/E_0^F, \\ \tilde{E}_0^P = E_0^P/E_0^F, \quad \tilde{\kappa}_0^{NA} = \kappa_0^{NA}L^2/E_0^F, \quad \tilde{\kappa}_0^{FA} = \kappa_0^{FA}L^2/E_0^F, \\ \tilde{\beta}_0^{NA} = \beta_0^{NA}L^2/E_0^F\langle t\rangle, \quad \tilde{\beta}_0^{FA} = \beta_0^{FA}L^2/E_0^F\langle t\rangle, \quad \tilde{\beta}_e = \beta_e L^2/E_0^F\langle t\rangle, \\ \tilde{\mu}_0^E = \mu_0^E/E_0^F\langle t\rangle, \quad \tilde{E}_0^C = E_0^C/E_0^F, \quad \tilde{E}_0^O = E_0^O/E_0^F.\end{gathered} \tag{3.38}$$

The initial and boundary conditions from Eq. (3.31a)-(3.31b) transform to

$$u'(x',0) = 0, \quad w'(x',0) = 0, \quad \tilde{\sigma}_c(-1/2,t') = -\tilde{\sigma}_1(=0), \quad \tilde{\sigma}_c(1/2,t') = \tilde{\sigma}_2(=0), \tag{3.39}$$

where the dimensionless Cauchy stress, scaled on E_0^F, is given by

$$\tilde{\sigma}_c = \tilde{\mu}_0^c\tilde{g}_c\frac{\partial^2 u'}{\partial x'\partial t'} + \left(\tilde{f}_F + \tilde{E}_0^S\tilde{f}_S + \tilde{E}_0^P\tilde{f}_P\right)\frac{\partial u'}{\partial x'} + \tilde{\tau}_0\tilde{f}_\tau, \tag{3.40a}$$

$$\tilde{\sigma}_E = \tilde{\mu}_0^E\tilde{g}_E\frac{\partial^2 w'}{\partial x'\partial t'} + \left(\tilde{E}_0^C\tilde{f}_C + \tilde{E}_0^O\tilde{f}_O\right)\frac{\partial w'}{\partial x'}, \tag{3.40b}$$

for the cell and ECM respectively.

In order to non-dimensionalise conditions for the ECM underneath the cell cytoplasm, we recall our semi-analytical expressions for the displacement in the ECM far field given by Eq. (3.26). We non-dimensionalise by setting $L_1 = \alpha L$, so that α is the dimensionless length of far field regions, to obtain expressions for the dimensionless displacement of the ECM in regions 1 and 2. In particular, we have

$$\bar{w}_1'(x',t') = \frac{1}{\alpha}\left(x' + \alpha + \frac{1}{2}\right)w_0'(t'), \tag{3.41a}$$

$$\bar{w}_2'(x',t') = \frac{1}{\alpha}\left(\alpha + \frac{1}{2} - x'\right)w_N'(t'), \tag{3.41b}$$

where $\bar{w}_1'$, $\bar{w}_2'$ are the dimensionless displacements in region 1 ($-1/2-\alpha \le x' \le -1/2$), and region 2 ($1/2 \le x' \le 1/2+\alpha$), respectively and where $w_0'(t')$ and $w_N'(t')$ are the numerically calculated dimensionless displacements of the ECM below the cell at the boundaries with region 1 and region 2 respectively. From Eq. (3.31d), the dimensionless stress matching boundary conditions for the region of ECM below the cell are then given by

$$\tilde{\sigma}_E(-1/2,t') = \tilde{\bar{\sigma}}_{E,1}(-1/2,t'), \quad \tilde{\sigma}_E(1/2,t') = \tilde{\bar{\sigma}}_{E,2}(1/2,t'), \tag{3.42}$$

where $\tilde{\bar{\sigma}}_{E,i}$ is the analytically calculated dimensionless stress in the ECM regions to the left and right of the cell.

3.4.2 Scaffolding and signaling proteins

In addition to the aforementioned length- and time-scales introduced, we compute the initial average concentration of actin, integrins, myosin, ECM ligands, ROCK, MLCP, MLCK and cofilin (in their various forms), which we use as scales in order to non-dimensionalise the equations describing cell biochemistry (Eqs. 3.29a-3.30h). In particular, we set

$$
\begin{aligned}
C_A &= \frac{1}{L}\int_{-L/2}^{L/2}\left(c_G(x,0)+c_F^{(1)}(x,0)+c_F^{(2)}(x,0)+c_S^{+}(x,0)\right)\,dx,\\
N_I &= \frac{1}{L}\int_{-L/2}^{L/2}\left(n_f(x,0)+n_h(x,0)+n_b^{(1)}(x,0)+n_b^{(2)}(x,0)+n_A^{(1)}(x,0)+n_A^{(2)}(x,0)\right)\,dx,\\
C_M &= \frac{1}{L}\int_{-L/2}^{L/2}\left(c_M(x,0)+c_M^{+}(x,0)\right)\,dx, \quad N_S = \frac{1}{L}\int_{-L/2}^{L/2}\left(n_s^{(1)}(x,0)+n_s^{(2)}(x,0)\right)\,dx,\\
C_R &= \frac{1}{L}\int_{-L/2}^{L/2}\left(c_R(x,0)+c_R^{+}(x,0)\right)\,dx, \quad C_P = \frac{1}{L}\int_{-L/2}^{L/2}\left(c_P(x,0)+c_{P-P}(x,0)\right)\,dx,\\
C_K &= \frac{1}{L}\int_{-L/2}^{L/2}\left(c_K(x,0)+c_{K-P}(x,0)\right)\,dx, \quad C_C = \frac{1}{L}\int_{-L/2}^{L/2}\left(c_C(x,0)+c_{C-P}(x,0)\right)\,dx,
\end{aligned}
\tag{3.43}
$$

representing, respectively, a concentration scale for actin species (monomers, filaments and stress fibres), for integrin species (low and high-affinity integrins, nascent and focal adhesions), for myosin II (inactive and active), ligands, ROCK (inactive and active), MLCP (phosphorylated and unphosphorylated), MLCK (phosphorylated and unphosphorylated) and cofilin (phosphorylated and unphosphorylated).

We introduce the following dimensionless groups:

$$
\begin{gathered}
\tilde{k}_p^{+}=k_p^{+}\langle t\rangle N_I, \quad \tilde{k}_p^{-}=k_p^{-}\langle t\rangle, \quad \tilde{k}_m^{+}=k_m^{+}\langle t\rangle C_M C_A, \quad \bar{k}_m^{+}=k_m^{+}\langle t\rangle C_A^2,\\
\tilde{k}_m^{-}=k_m^{-}\langle t\rangle, \quad \bar{k}_m^{-}=k_m^{-}\langle t\rangle C_A/C_M, \quad \tilde{k}_a^{+}=k_a^{+}\langle t\rangle, \quad \tilde{k}_a^{-}=k_a^{-}\langle t\rangle,\\
\tilde{k}_h^{+}=k_h^{+}\langle t\rangle, \quad \tilde{k}_h^{-}=k_h^{-}\langle t\rangle, \quad \tilde{k}_b^{+}=k_b^{+}\langle t\rangle N_S(=1), \quad \bar{k}_b^{+}=k_b^{+}\langle t\rangle N_I,\\
\tilde{k}_b^{-}=k_b^{-}\langle t\rangle, \quad \bar{k}_b^{-}=k_b^{-}\langle t\rangle N_I/N_S, \quad \tilde{k}_F^{+}=k_F^{+}\langle t\rangle, \quad \tilde{k}_F^{-}=k_F^{-}\langle t\rangle,\\
\tilde{D}_G=D_G\langle t\rangle/L^2, \quad \tilde{D}_F=D_F\langle t\rangle/L^2, \quad \tilde{D}_m=D_m\langle t\rangle/L^2, \quad \tilde{D}_m^{+}=D_m^{+}\langle t\rangle/L^2,\\
\tilde{D}_f=D_f\langle t\rangle/L^2, \quad \tilde{k}_R^{+}=k_R^{+}\langle t\rangle, \quad \tilde{k}_R^{-}=k_R^{-}\langle t\rangle, \quad \tilde{k}_1^{+}=k_1^{+}\langle t\rangle, \quad \tilde{k}_1^{-}=k_1^{-}\langle t\rangle,\\
\tilde{k}_2^{+}=k_2^{+}\langle t\rangle, \quad \tilde{k}_2^{-}=k_2^{-}\langle t\rangle, \quad \tilde{k}_3^{+}=k_3^{+}\langle t\rangle, \quad \tilde{k}_3^{-}=k_3^{-}\langle t\rangle,\\
\tilde{D}_P=D_P\langle t\rangle/L^2, \quad \tilde{D}_{P-P}=D_{P-P}\langle t\rangle/L^2, \quad \tilde{D}_K=D_K\langle t\rangle/L^2,\\
\tilde{D}_{K-P}=D_{K-P}\langle t\rangle/L^2, \quad \tilde{D}_C=D_C\langle t\rangle/L^2, \quad \tilde{D}_{C-P}=D_{C-P}\langle t\rangle/L^2.
\end{gathered}
\tag{3.44}
$$

With these dimensionless groups we can construct the following dimensionless biochemical equations (where primes are used to denote dimensionless quantities)

$$
\frac{\partial c_G'}{\partial t'} = -\tilde{k}_p^{+}c_G'\left(n_b^{(1)\prime}+n_b^{(2)\prime}+n_A^{(1)\prime}+n_A^{(2)\prime}\right)+\tilde{k}_p^{-}\left(c_F^{(1)\prime}+c_F^{(2)\prime}\right)+\tilde{k}_m^{-}c_S^{+\prime}+\tilde{D}_G\frac{\partial^2 c_G'}{\partial x'^2}, \tag{3.45a}
$$

$$\frac{\partial c_F^{(i)\prime}}{\partial t'} + \frac{\partial}{\partial x'}\left(c_F^{(i)\prime} U^{(i)\prime}\right) = \tilde{k}_p^+ c'_G \left(n_b^{(i)\prime} + n_A^{(i)\prime}\right) - \tilde{k}_p^- c_F^{(i)\prime} - \tilde{k}_m^+ \left(c_F^{(1)\prime} c_F^{(2)\prime} + c_F^{(i)\prime} c_S^{+\prime}\right) c_m^{+\prime} + \tilde{D}_F \frac{\partial^2 c_F^{(i)\prime}}{\partial x'^2}, \tag{3.45b}$$

$$\frac{\partial c_S^{+\prime}}{\partial t'} = \tilde{k}_m^+ \left(2c_F^{(1)\prime} c_F^{(2)\prime} + c_F^{(1)\prime} c_S^{+\prime} + c_F^{(2)\prime} c_S^{+\prime}\right) c_m^{+\prime} - \tilde{k}_m^- c_S^{+\prime}, \tag{3.45c}$$

$$\frac{\partial c_m{}'}{\partial t'} = -\tilde{k}_a^+ c'_m + \tilde{k}_a^- c_m^{+\prime} + \tilde{D}_m \frac{\partial^2 c'_m}{\partial x'^2}, \tag{3.45d}$$

$$\frac{\partial c_m^{+\prime}}{\partial t'} = \tilde{k}_a^+ c'_m - \tilde{k}_a^- c_m^{+\prime} - \bar{k}_m^+ \left(c_F^{(1)\prime} c_F^{(2)\prime} + c_F^{(1)\prime} c_S^{+\prime} + c_F^{(2)\prime} c_S^{+\prime}\right) c_m^{+\prime} + \bar{k}_m^- c_S^{+\prime} + \tilde{D}_m^+ \frac{\partial^2 c_m^{+\prime}}{\partial x'^2}, \tag{3.45e}$$

$$\frac{\partial n'_f}{\partial t'} = -\tilde{k}_h^+ n'_f + \tilde{k}_h^- n'_h + \tilde{D}_f \frac{\partial^2 n'_f}{\partial x'^2}, \tag{3.45f}$$

$$\frac{\partial n'_h}{\partial t'} = \tilde{k}_h^+ n'_f - \tilde{k}_h^- n'_h - \tilde{k}_b^+ n'_h \left(n_s^{(1)\prime} + n_s^{(2)\prime}\right) + \tilde{k}_b^- \left(n_b^{(1)\prime} + n_b^{(2)\prime}\right), \tag{3.45g}$$

$$\frac{\partial n_b^{(i)\prime}}{\partial t'} = \tilde{k}_b^+ n'_h n_s^{(i)\prime} - \tilde{k}_b^- n_b^{(i)\prime} - \tilde{k}_F^+ n_b^{(i)\prime} + \tilde{k}_F^- n_A^{(i)\prime}, \tag{3.45h}$$

$$\frac{\partial n_s^{(i)\prime}}{\partial t'} = -\bar{k}_b^+ n'_h n_s^{(i)\prime} + \bar{k}_b^- n_b^{(i)\prime}, \tag{3.45i}$$

$$\frac{\partial n_A^{(i)\prime}}{\partial t'} = \tilde{k}_F^+ n_b^{(i)\prime} - \tilde{k}_F^- n_A^{(i)\prime}, \tag{3.45j}$$

$$\frac{\partial c'_R}{\partial t'} = -\tilde{k}_R^+ c'_R + \tilde{k}_R^- c_R^{+\prime}, \tag{3.45k}$$

$$\frac{\partial c_R^{+\prime}}{\partial t'} = \tilde{k}_R^+ c'_R - \tilde{k}_R^- c_R^{+\prime}, \tag{3.45l}$$

$$\frac{\partial c'_P}{\partial t'} = -\tilde{k}_1^+ c'_P + \tilde{k}_1^- c'_{P-P} + \tilde{D}_P \frac{\partial^2 c'_P}{\partial x'^2}, \tag{3.45m}$$

$$\frac{\partial c'_{P-P}}{\partial t'} = \tilde{k}_1^+ c'_P - \tilde{k}_1^- c'_{P-P} + \tilde{D}_{P-P} \frac{\partial^2 c'_{P-P}}{\partial x'^2}, \tag{3.45n}$$

$$\frac{\partial c'_K}{\partial t'} = -\tilde{k}_2^+ c'_K + \tilde{k}_2^- c'_{K-P} + \tilde{D}_K \frac{\partial^2 c'_K}{\partial x'^2}, \tag{3.45o}$$

$$\frac{\partial c'_{K-P}}{\partial t'} = \tilde{k}_2^+ c'_K - \tilde{k}_2^- c'_{K-P} + \tilde{D}_{K-P} \frac{\partial^2 c'_{K-P}}{\partial x'^2}, \tag{3.45p}$$

$$\frac{\partial c'_C}{\partial t'} = -\tilde{k}_3^+ c'_C + \tilde{k}_3^- c'_{C-P} + \tilde{D}_C \frac{\partial^2 c'_C}{\partial x'^2}, \tag{3.45q}$$

$$\frac{\partial c'_{C-P}}{\partial t'} = \tilde{k}_3^+ c'_C - \tilde{k}_3^- c'_{C-P} + \tilde{D}_{C-P} \frac{\partial^2 c'_{C-P}}{\partial x'^2}. \tag{3.45r}$$

The dimensionless initial conditions imposed on the system are easily deduced using values from Table 3.2 in Sec. 3.6 (below), together with the concentration scales from Eq. (3.43).

Recall that for the cell biochemistry, to conserve protein mass in the cell, we assume no flux boundary conditions for each protein species. In general, from Eq. (3.46), the dimensionless flux, j'_α, of an advective (with dimensionless velocity $\tilde{U}_\alpha$) and diffusive (with dimensionless diffusivity $\tilde{D}_\alpha$) protein, with dimensionless concentration c'_α, satisfies

$$j'_\alpha = \tilde{U}_\alpha c'_\alpha - \tilde{D}_\alpha \frac{\partial c'_\alpha}{\partial x'} = 0, \tag{3.46}$$

at the boundaries $x = -1/2$ and $x = 1/2$. For non-diffusive and non-advective proteins we immediately satisfy no-flux boundary conditions and solve the reaction equations at the boundary as we do at the interior. For diffusive proteins that do not experience advection then Eq. (3.32) becomes

$$\frac{\partial c'_\alpha}{\partial x'} = 0, \tag{3.47}$$

at $x = -1/2$, $x = 1/2$. For actin filaments (that are treadmilled), we deduce that at the boundaries we must satisfy

$$\tilde{D}_F \frac{\partial c_F^{(i)\prime}}{\partial x'} = \tilde{U}_0 \tilde{U}^{(i)'} c_F^{(i)\prime}, \tag{3.48}$$

for $i = 1, 2$, where $\tilde{U}_0 = U_0 \langle t \rangle / L$.

3.5 Constitutive assumptions

In order to close the positive feedback loop connecting FA and SF formation and to connect the cell biochemistry to the underlying mechanical properties we link various reaction rates to the concentration of signaling proteins (Sec. 3.5.1), link the rate of adhesion maturation to adhesion stretch (Sec. 3.5.2) and couple mechanical properties of the cytoskeleton and adhesions to the cell biochemistry (Sec. 3.5.3).

3.5.1 Signaling proteins effect on reaction rates

In a similar manner to Ch. 2, we suppose that the activation rate of ROCK is dependent on the local density of nascent and focal adhesions by setting

$$k_R^+ = K_R^+ \left(n_b + \delta n_A \right) / N_I, \quad n_b = n_b^{(1)} + n_b^{(2)}, \quad n_A = n_A^{(1)} + n_A^{(2)}, \tag{3.49}$$

so that the relative strength of signaling due to FAs compared to nascent adhesions is increased by a factor of $\delta = O(1)$.

To incorporate the effects of ROCK activation on MLCP, MLCK and cofilin phosphorylation, we set $k_j^+ = K_j^+ g_j \left(c_R^+ / C_R \right)$, $j = 1, 2, 3$, where K_j^+ are dimensional rate constants and g_j are dimensionless functions of activated ROCK concentration.

To capture the effect that MLCK phosphorylation has on myosin II activation and that MLCP phosphorylation has on myosin II inactivation we set

$$k_a^+ = K_a^+ g_a^+ \left(c_{K-P}/C_K\right), \quad g_a^+ \left(c_{K-P}/C_K\right) = c_{K-P}/C_K, \tag{3.50a}$$

$$k_a^- = K_a^- g_a^- \left(c_P/C_P\right), \quad g_a^- \left(c_P/C_P\right) = c_P/C_P, \tag{3.50b}$$

where K_a^+, K_a^- are dimensional constants and g_a^+, g_a^- are dimensionless functions of MLCK-P and MLCP concentration, respectively.

Finally, to capture the effects increased Rho and ROCK activation has on actin polymerisation (Hirata et al., 2008, 2014b) and that cofilin phosphorylation has on actin depolymerisation, we set

$$k_p^+ = K_p^+ g_p^+ \left(c_R^+/C_R\right), \quad g_p^+ \left(c_R^+/C_R\right) = c_R^+/C_R, \tag{3.50c}$$

$$k_p^- = K_p^- g_p^- \left(c_C/C_C\right), \quad g_p^- \left(c_C/C_C\right) = c_C/C_C, \tag{3.50d}$$

where K_p^+, K_p^- are dimensional constants and g_p^+, g_p^- are dimensionless functions of the concentration of ROCK and unphosphorylated cofilin.

3.5.2 The effect of contractile forces

In response to contractile forces generated by SFs, nascent adhesions mature into FAs. These contractile forces stretch bound integrins, exposing VBSs on talin leading to vinculin recruitment (Hirata et al., 2014c) and maturation into FAs (which in turn leads to Rho and ROCK activation). Hence, the rate of formation of FAs is assumed to depend on the length (or stretch) of integrin-ligand connections. Approximating this length by $\lambda_I(x,t) = u(x,t) - w(x,t)$ (the relative deformation of the cell to the ECM), we write

$$k_F^+ = K_F^+ g_s^+ \left(\lambda_I/L\right), \quad g_s^+ \left(\lambda_I/L\right) = \left(\lambda_I/L\right)^2, \tag{3.51}$$

where K_F^+ is a dimensionless constant and g_s^+ is a dimensionless function of adhesion length. We assume a quadratic dependence in a similar manner to the stored elastic energy. This is in contrast with with our purely empirical formula linking the adhesion maturation rate to SF concentration in Ch. 2 (see Eq. 2.7); this was necessary as mechanical deformation was neglected in Ch. 2.

3.5.3 Coupling mechanics and biochemistry

In order to allow the protein concentrations to influence the mechanical properties of the cytoplasm and adhesions we select a key set of dimensional parameters and multiply each by a dimensionless function of a particular protein concentration, as discussed in Sec. 3.4.

We link each of these mechanical properties to the biochemical properties of the cell and adhesions (in a similar manner to Gracheva and Othmer, 2004, Larripa and Mogilner, 2006).

In particular, we describe the Young's modulus of actin filaments by

$$E_F = E_0^F \tilde{f}_F, \quad \tilde{f}_F\left(c_F^{(1)} + c_F^{(2)}\right) = \left(c_F^{(1)} + c_F^{(2)}\right)/C_A, \tag{3.52}$$

where E_0^F is a dimensional constant and $\tilde{f}_F$ is a dimensionless function of actin filament concentration. Similarly, the Young's modulus of SFs is described by

$$E_S = E_0^S \tilde{f}_S, \quad \tilde{f}_S\left(c_S^+\right) = c_S^+/C_A, \tag{3.53}$$

where E_0^S is a dimensional constant and $\tilde{f}_S\left(c_S^+\right)$ is a dimensionless function of SF concentration. We also link the (active) contractile stress due to myosin II motor action to the SF concentration by setting

$$\tau = \tau_0 \tilde{f}_\tau, \quad \tilde{f}_\tau\left(c_S^+\right) = c_S^+/C_A, \tag{3.54}$$

where τ_0 is a dimensional constant and $\tilde{f}_\tau\left(c_S^+\right)$ is a dimensionless function of SF concentration. The Young's modulus of the cytosol due to the nucleus, microtubules and intermediate filaments is assumed to satisfy

$$E_P = E_0^P \tilde{f}_P, \quad \tilde{f}_P = \gamma + (1-\gamma)\cos^6(\pi x/L), \tag{3.55}$$

where $\tilde{f}_P$ is chosen so that it attains a maximum at the cell centre (representing the stiff nucleus) and decays towards the cell edges. We set $\gamma = 0.1$ in all simulations so that the nuclear region of the cell is approximately ten times stiffer than (the passive contributions) near the cell edge, where the only contributing components are assumed to be microtubules and intermediate filaments.

Additionally, we describe the restoring forces and drag induced by nascent adhesions by

$$\kappa_{NA} = \kappa_0^{NA}\tilde{f}_{NA}, \quad \beta_{NA} = \beta_0^{NA}\tilde{f}_{NA}, \quad \tilde{f}_{NA} = \left(n_b^{(1)} + n_b^{(2)}\right)/N_I, \tag{3.56}$$

where κ_0^{NA} is a dimensional constant and $\tilde{f}_{NA}$ is a dimensionless function of nascent adhesion concentration. Similarly, the restoring forces and drag induced by FAs are assumed to be given by

$$\kappa_{FA} = \kappa_0^{FA}\tilde{f}_{FA}, \quad \beta_{FA} = \beta_0^{FA}\tilde{f}_{FA}, \quad \tilde{f}_{FA} = \left(n_A^{(1)} + n_A^{(2)}\right)/N_I, \tag{3.57}$$

where κ_0^{FA} is a dimensional constant and $\tilde{f}_{FA}$ is a dimensionless function of FA concen-

tration.

3.6 Parameter estimation

Our model includes a large family of parameters, we outline their assumed values for the baseline case below and provide (where possible) justification for the chosen parameter value. In particular, we specify the assumed mechanical properties of the cell, ECM and cell-substrate adhesions in Table 3.1. We give further detail on the imposed initial conditions on the concentration and density of protein species in Table 3.2. In Table 3.3 we present the reaction rates, diffusivities and treadmilling velocity assumed for scaffolding proteins and provide similar details on these biochemical properties for signaling proteins in Table 3.4.

Mechanical Property	**Value**	**Justification/Interpretation**
a	50 nm	Repeating unit length. Order of magnitude estimate based on integrin-ligand connection (and cytoskeletal mesh) spacing (Cavalcanti-Adam et al., 2007, Dalby et al., 2014, Hu et al., 2019).
L	25 μm	Typical MSC length. Based on Krueger et al. (2018) who quote MSC lengths of 15-30 μm.
S	50 μm^2	Cell cross-sectional area based on Gracheva and Othmer (2004) who quote values of 30-50 μm^2. Note that we assume the cell is nearly flat with $W = 25\,\mu$m, $H = 2\,\mu$m.
E_0^F	1 $\times 10^3$ Pa	Typical stiffness generated by actin filaments. Order of magnitude estimate based on Mathieu and Loboa (2012) who quote the Young's modulus of hMSCs to be roughly 3.2 kPa, in line with Darling et al. (2008), Titushkin and Cho (2009).
E_0^S	5 $\times 10^3$ Pa	Typical stiffness generated by actin SFs. Order of magnitude estimate based on Mathieu and Loboa (2012) who quote the Young's modulus of hMSCs to be roughly 3.2 kPa, in line with Darling et al. (2008), Titushkin and Cho (2009).

Continued on the next page

Table 3.1 – continued from previous page

Mechanical Property	Value	Justification/Interpretation
E_0^P	5×10^3 Pa	Typical stiffness generated by nucleus, microtubules and intermediate filaments. Order of magnitude estimate based on Lammerding (2011) who suggest the Young's modulus of the nucleus varies between 1-10 kPa for different cell types.
τ_0	1×10^3 Pa	Contractile stress generated by stress fibres at a typical concentration. Consistent with Larripa and Mogilner (2006) who use values of $10^2 - 10^3$ pN μm^{-2} and Gracheva and Othmer (2004) who quote the force in the cell as 500-1000 nN.
κ_0^{NA}	10 Pa μm^{-2}	Typical stiffness per unit volume of nascent adhesions. Chosen to be five times weaker than FAs and to be of comparable stiffness to actin filaments.
κ_0^{FA}	50 Pa μm^{-2}	Typical stiffness per unit volume of focal adhesions. Chosen to be five times stiffer than nascent adhesions and to be of comparable stiffness to SFs.
β_0^{NA}	1 Pa s μm^{-2}	Typical drag generated by nascent adhesions. Chosen to be five times less viscous than FAs and so that elastic effects dominate adhesive stresses (see dimensionless groups in Sec. 3.4).
β_0^{FA}	5 Pa s μm^{-2}	Typical drag generated by FAs. Chosen to be five times more viscous than nascent adhesions and so that elastic effects dominate adhesive stresses (see dimensionless groups in Sec. 3.4).
E_0^C	1×10^6 Pa	Typical Young's modulus of ECM collagen, assumed much stiffer than cell cytoplasm. Estimated based on approximate collagenous bone Young's modulus of >100 kPa (Engler et al., 2006).
μ_0	1×10^2 Pa s	Typical cell viscosity. Estimate in line with Gracheva and Othmer (2004) who quote a typical cell viscosity of 2×10^3 dyn s cm^{-2}.

Continued on the next page

Table 3.1 – continued from previous page

Mechanical Property	Value	Justification/Interpretation
μ_0^E	1 Pa s	Typical ECM viscosity. Assumed less viscous than cytosol.
σ_1	0 Pa	Stress at left boundary of cell. Neglected.
σ_2	0 Pa	Stress at right boundary of cell. Neglected.
β_e	1.6×10^{-8} Pa s μm^{-2}	Extra (small) drag for computational simplicity. Assumed small (compared to β_0^{NA} and β_0^{FA}).
v_0	1 μm s^{-1}	Maximum motor velocity, identical value is used by Besser and Schwarz (2007).

Table 3.1: Baseline parameters for mechanical properties of the cytosol and ECM.

Protein	Value	Justification/interpretation
$c_G(x,0)$	$(100/V)$ μM μm^{-3}	All actin is initially sequestered. In line with Kiuchi et al. (2011) who suggest that most living cells contain roughly 100 μM of G-actin.
$c_F^{(1)}(x,0)$, $c_F^{(2)}(x,0)$	0 μM μm^{-3}	All actin is initially sequestered.
$c_S^+(x,0)$	0 μM μm^{-3}	All actin is initially sequestered.
$c_m(x,0)$	$(30/V)$ μM μm^{-3}	All myosin II initially inactive. Estimated based on Besser and Schwarz (2007), who use a total amount of myosin II of 30 μM (based on Butler et al., 1994); and on Gracheva and Othmer (2004) who assume a total amount of myosin II of 20 μM.
$c_m^+(x,0)$	0 μM μm^{-3}	All myosin II initially inactive.
$n_f(x,0)$	100 μm^{-2}	Initially no adhesions have formed. The same value has been used by Bidone et al. (2019) (based on Oakes et al., 2018) and by Paszek et al. (2009).
$n_h(x,0)$	0 μm^{-2}	Initially no adhesions have formed.
$n_b^{(1)}(x,0), n_b^{(2)}(x,0)$	0 μm^{-2}	Initially no adhesions have formed.
$n_A^{(1)}(x,0), n_A^{(2)}(x,0)$	0 μm^{-2}	Initially no adhesions have formed.

Continued on the next page

Table 3.2 – continued from previous page

Protein	Value	Justification/Interpretation
$N_s^{(1)}(x,0), N_s^{(2)}(x,0)$	1000 μm^{-2}	Maximum free ligand population for each family (their sum is uniform across the cell length as indicated in Fig. 3.6b in Sec. 3.2). The same value has been used by Bidone et al. (2019) and is consistent with Paszek et al. (2009).
$c_R(x,0)$	$(1/V)$ nM μm^{-3}	Assume all ROCK is initially inactive. Besser and Schwarz (2007) use values for the total amount of ROCK of 0-5 nM (based on Feng et al., 1999).
$c_R^+(x,0)$	0 nM μm^{-3}	Assume all ROCK is initially inactive.
$c_K(x,0)$	$(0.1/V)$ μM μm^{-3}	All MLCK is initially unphosphorylated. Besser and Schwarz (2007) use a value for the total amount of MLCK of 0.1 μM (based on Nagamoto and Yagi, 1984).
$c_{K-P}(x,0)$	0 μM μm^{-3}	Assume MLCK is initially unphosphorylated.
$c_P(x,0)$	$(1/V)$ μM μm^{-3}	All MLCP is initially unphosphorylated. Besser and Schwarz (2007) use values for the total amount of MLCP of 0-1.2 μM (based on Hartshorne et al., 1998).
$c_{P-P}(x,0)$	0 μM μm^{-3}	Assume MLCP is initially unphosphorylated.
$c_C(x,0)$	$(1/V)$ μM μm^{-3}	Assume cofilin is initially unphosphorylated.
$c_{C-P}(x,0)$	0 μM μm^{-3}	Assume cofilin is initially unphosphorylated.

Table 3.2: Baseline initial conditions imposed on protein concentrations.

Parameter	Value	Justification/Interpretation
K_p^+	2×10^{-3} adhesion^{-1} s^{-1}	Typical actin polymerisation rate. Order of magnitude estimate based on Larripa and Mogilner (2006), Svitkina et al. (1997) (and the noted difference in filament density between the cell centre and edge).
k_p^-	1×10^{-2} s^{-2}	Actin filament sequestering rate. Estimate inferred from Larripa and Mogilner (2006) (based on Svitkina et al., 1997).

Continued on the next page

Table 3.3 – continued from previous page

Parameter	Value	Justification/Interpretation
K_a^+	$1 \times 10^{-2}\ \mathrm{s}^{-1}$	Typical myosin II activation rate. Estimated (chosen so that activation occurs on the order of minutes).
K_a^-	$1 \times 10^{-2}\ \mathrm{s}^{-1}$	Typical rate of myosin II inactivation. (chosen so that inactivation occurs on the order of minutes).
k_m^+	$1 \times 10^{2}\ \mu\mathrm{M}^{-2}\ \mathrm{s}^{-1}$	Rate of cross-linking of actin bundles by myosin II. Order of magnitude inferred from Larripa and Mogilner (2006).
k_m^-	$1 \times 10^{-2}\ \mathrm{s}^{-1}$	Rate of stress fibre disassembly into constituent actin monomers and myosin II. Estimate inferred from Larripa and Mogilner (2006).
k_h^+	$0.5\ \mathrm{s}^{-1}$	Rate of conversion of free integrins to high-affinity. The same value is used by Paszek et al. (2009) (based on Iber and Campbell, 2006, Tadokoro et al., 2003).
k_h^-	$5\ \mathrm{s}^{-1}$	Rate of conversion of integrins from high-affinity to low-affinity. The same value is used by Paszek et al. (2009) (based on Iber and Campbell, 2006, Tadokoro et al., 2003).
k_b^+	$1 \times 10^{-4}\ \mathrm{ligand}^{-1}\ \mathrm{s}^{-1}$	Rate of integrin-ligand binding (nascent adhesion formation). Estimated based on rapid formation of bound integrins (on the order of tens of seconds).
k_b^-	$1 \times 10^{-2}\ \mathrm{s}^{-1}$	Rate of nascent adhesion disassembly. Estimated based on expected short lifetime (compared to FAs) on the order of tens of seconds to minutes.
K_F^+	$25\ \mathrm{s}^{-1}$	Rate of FA formation. Order of magnitude estimate chosen so that reverse reaction dominates when adhesions are unstretched but forward reaction dominates when (approximate) adhesion length $\gtrsim 100$ nm (a maximum length of 130 nm is assumed by Keshavanarayana et al., 2018).
k_F^-	$1 \times 10^{-3}\ \mathrm{s}^{-1}$	Rate of FA disassembly. Estimated based on expected long lifetime (compared to nascent adhesions) on the order of tens of minutes.

Continued on the next page

Table 3.3 – continued from previous page

Parameter	Value	Justification/Interpretation
D_G	$10\ \mu\text{m}^2\ \text{s}^{-1}$	Diffusivity of actin monomers. Based on Kiuchi et al. (2011) who quote a value of 13.7 $\mu\text{m}^2\ \text{s}^{-1}$.
D_F	$0.3\ \mu\text{m}^2\ \text{s}^{-1}$	Diffusivity of actin filaments. Similar to Larripa and Mogilner (2006) who use a value of $0.1\ \mu\text{m}^2\ \text{s}^{-1}$.
D_m	$1\ \mu\text{m}^2\ \text{s}^{-1}$	Diffusivity of inactive myosin II. Estimate based on Uehara et al. (2010) who quote a value for myosin II diffusivity of $0.8\ \mu\text{m}^2\ \text{s}^{-1}$.
D_m^+	$1\ \mu\text{m}^2\ \text{s}^{-1}$	Diffusivity of active myosin II. Estimate based on Uehara et al. (2010) who quote a value for myosin II diffusivity of $0.8\ \mu\text{m}^2\ \text{s}^{-1}$.
D_f	$0.1\ \mu\text{m}^2\ \text{s}^{-1}$	Diffusivity of free integrins. The same value is used by Bidone et al. (2019) (based on Rossier et al., 2012).
U_0	$0.1\ \mu\text{m}\ \text{s}^{-1}$	Advection (treadmilling) velocity. The same value is used by Larripa and Mogilner (2006).

Table 3.3: Baseline parameters for scaffolding protein dynamics.

Parameter	Value	Justification/Interpretation
K_R^+	$1 \times 10^{-2}\ \text{s}^{-1}$	Typical activation rate of phosphorylation of ROCK. Estimated (chosen to ensure little ROCK activation when adhesions have not matured).
k_R^-	$1 \times 10^{-1}\ \text{s}^{-1}$	Typical inactivation rate of activated ROCK. Estimated (chosen to ensure little ROCK activation without adhesion maturation).
δ	4	Increase in ROCK activation rate due to adhesion maturation. Based on parameter sweep outlined in Sec. 3.8.2 (below).
K_1^+	$1 \times 10^{-2}\ \text{s}^{-1}$	Typical rate of phosphorylation of MLCP. Estimated (chosen to ensure little phosphorylation without adhesion maturation).

Continued on the next page

Table 3.4 – continued from previous page

Parameter	Value	Justification/Interpretation
k_1^-	$1 \times 10^{-2}\ \mathrm{s}^{-1}$	Rate of dephosphorylation of MLCP-P. Estimated (chosen to ensure little phosphorylation without adhesion maturation).
K_2^+	$1 \times 10^{-2}\ \mathrm{s}^{-1}$	Rate of phosphorylation of MLCK. Estimated (chosen to ensure little phosphorylation without adhesion maturation).
k_2^-	$1 \times 10^{-2}\ \mathrm{s}^{-1}$	Rate of dephosphorylation of MLCK-P. Estimated (chosen to ensure little phosphorylation without adhesion maturation).
K_3^+	$5 \times 10^{-2}\ \mathrm{s}^{-1}$	Rate of phosphorylation of cofilin. Estimated based on 10-30% phosphorylation of cofilin for myeloid cells (Prudent et al., 2018); our steady state value is roughly 40% phosphorylation.
k_3^-	$1 \times 10^{-2}\ \mathrm{s}^{-1}$	Rate of dephosphorylation of phosphorylated cofilin. Estimated based on 10-30% phosphorylation of cofilin for myeloid cells (Prudent et al., 2018); our steady state value is roughly 40% phosphorylation.
D_P	$15\ \mu\mathrm{m}^2\ \mathrm{s}^{-1}$	Diffusivity of MLCP. Besser and Schwarz (2007) use a value of $14\ \mu\mathrm{m}^2\ \mathrm{s}^{-1}$ (based on Lippincott-Schwartz et al., 2001).
D_{P-P}	$15\ \mu\mathrm{m}^2\ \mathrm{s}^{-1}$	Diffusivity of MLCP-P. Besser and Schwarz (2007) use a value of $14\ \mu\mathrm{m}^2\ \mathrm{s}^{-1}$ (based on Lippincott-Schwartz et al., 2001).
D_K	$1\ \mu\mathrm{m}^2\ \mathrm{s}^{-1}$	Diffusivity of MLCK. Order of magnitude estimate based on large molecular weight (Gallagher et al., 1991) and relationship between diffusivity and molecular radius (Lippincott-Schwartz et al., 2001).
D_{K-P}	$1\ \mu\mathrm{m}^2\ \mathrm{s}^{-1}$	Diffusivity of MLCK-P. Order of magnitude estimate based on large molecular weight (Gallagher et al., 1991) and relationship between diffusivity and molecular radius (Lippincott-Schwartz et al., 2001).

Continued on the next page

Table 3.4 – continued from previous page

Parameter	Value	Justification/Interpretation
D_C	$10\ \mu m^2\ s^{-1}$	Diffusivity of cofilin. Order of magnitude estimate based on small molecular weight (Muneyuki et al., 1985) and relationship between diffusivity and molecular radius (Lippincott-Schwartz et al., 2001).
D_{C-P}	$10\ \mu m^2\ s^{-1}$	Diffusivity of phosphorylated cofilin. Order of magnitude estimate based on small molecular weight (Muneyuki et al., 1985) and relationship between diffusivity and molecular radius (Lippincott-Schwartz et al., 2001).

Table 3.4: Baseline parameters for signaling protein dynamics.

3.7 Computational method

The resulting large system of governing mechanical and biochemical PDEs is parabolic and so we solve the system numerically using a finite difference method based on the method of lines. In particular, we discretise the spatial domain $-1/2 \leq x \leq 1/2$ using a uniform grid size Δx (the other ECM spatial domains away from the cell are solved semi-analytically, as in Sec. 3.1.7). We discretise all spatial derivatives using a second-order finite difference stencil and solve the resulting large family of ODEs numerically using the Matlab solver ode15s. We employ the fictitious nodes procedure to apply the boundary conditions but note that for the ECM we need to incorporate our far field treatment (Sec. 3.1.7). In most cases we discretise the (dimensionless) domain with $\Delta x = 0.01$ (i.e. $N = 100$) and use Matlab's default error bounds for the time-stepping. In this case, mass is conserved in the system within 1% error over long simulations. We have also validated that using finer mesh resolutions and more stringent error tolerances makes no qualitative (and negligible quantitative) differences to the predictions, as discussed in Sec. 3.8.1 (below).

3.8 Results

In order to investigate the temporal and spatial dynamics of a cell binding to a stiff (i.e. significantly greater Young's modulus than the cell cytoplasm) collagen ECM, Figs. 3.7-3.11 illustrate a baseline output from our model using the parameters listed in Sec. 3.6. We solve the dimensionless governing equations, with dimensionless parameters (based

on our parameter estimation in Sec. 3.6) detailed in Table 3.5, and present dimensionless output from our model for all independent and dependent variables with the exception of time, which we convert back to dimensional units for ease of interpretation. We firstly summarise the global response (Fig. 3.7), followed by the local behaviour of individual components of the system, including the mechanical deformation of the cell cytoplasm and the ECM (Fig. 3.8), the integrins and adhesions (Fig. 3.9), the signaling proteins (Fig. 3.10) and actin and myosin (Fig. 3.11). We have already been able to access the global biochemical response of the cell through our spatially-averaged model developed in Ch. 2 (see Fig. 2.1). However, the ability to predict changes in the mechanical properties of the cell, ECM and adhesions, and to predict localisation of proteins within the cell is novel in this Chapter. Note that in Figs. 3.9-3.11 we consider the temporal dynamics of proteins at five spatial locations in the left half of the cell (noting the assumed symmetry in the cell in this base case), in particular at the cell boundary (black line), cell centre (green line) and three equidistant locations between these points (the red, yellow and purple lines respectively as we move from the boundary towards the cell centre); these are marked as open squares on spatial plots in Figs. 3.7-3.11. Similarly, we plot the spatial dynamics of proteins (and mechanical properties) at certain snapshots in time, in particular at $t = 250$ s (grey), $t = 500$ s (dark blue), $t = 1000$ s (orange), $t = 1500$ s (yellow), $t = 2000$ s (purple), $t = 2500$ s (green), $t = 5000$ s (maroon) and $t = 10000$ s (black) after the cell has been introduced to the substrate; these times are marked as open circles on temporal plots in Figs. 3.7-3.11.

Dimensionless parameter	**Value**	**Dimensionless parameter**	**Value**
$\tilde{K}_p^+$	2	$\tilde{K}_p^-$	0.1
$\tilde{K}_a^+$	0.1	$\tilde{K}_a^-$	0.1
$\tilde{k}_m^+$	1.92	$\tilde{k}_m^-$	0.1
$\check{k}_m^+$	6.4	$\check{k}_m^-$	$0.\bar{3}$
$\tilde{k}_h^+$	5	$\tilde{k}_h^-$	50
$\tilde{k}_b^+$	1	$\tilde{k}_b^-$	0.1
$\check{k}_b^+$	0.1	$\check{k}_b^-$	0.01
$\tilde{K}_F^+$	250	$\tilde{k}_F^-$	0.01
$\tilde{K}_R^+$	0.1	$\tilde{K}_R^+$	1
$\tilde{K}_1^+$	0.1	$\tilde{K}_1^-$	0.1
$\tilde{K}_2^+$	0.1	$\tilde{K}_2^-$	0.1
$\tilde{K}_3^+$	0.5	$\tilde{K}_3^-$	0.1
$\tilde{D}_G$	0.16	$\tilde{D}_F$	0.0048
$\tilde{D}_m$	0.016	$\tilde{D}_m^+$	0.016

Continued on the next page

Table 3.5 – continued from previous page

Dimensionless parameter	**Value**	**Dimensionless parameter**	**Value**
$\tilde{D}_f$	0.0016	$\tilde{U}_0$	0.04
$\tilde{D}_P$	0.24	$\tilde{D}_{P-P}$	0.24
$\tilde{D}_K$	0.016	$\tilde{D}_{K-P}$	0.016
$\tilde{D}_C$	0.16	$\tilde{D}_{C-P}$	0.16
$\tilde{\mu}_0$	0.01	$\tilde{\tau}_0$	1
$\tilde{E}_0^S$	5	$\tilde{E}_0^P$	5
$\tilde{\kappa}_0^{NA}$	6.25	$\tilde{\kappa}_0^{FA}$	31.25
$\tilde{\beta}_0^{NA}$	0.0625	$\tilde{\beta}_0^{FA}$	0.3125
$\tilde{\beta}_e$	1×10^{-8}	$\tilde{\mu}_0^E$	1×10^{-4}
$\tilde{E}_0^C$	1000	$\tilde{E}_0^O$	0
$\tilde{v}_0$	0.4		

Table 3.5: Dimensionless parameters employed in baseline simulations of the one-dimensional model.

In order to elucidate the overall temporal dynamics of cell-substrate binding, Fig. 3.7 illustrates a number of global (i.e. spatially-independent) measures of the system which summarise the adhesion strength over time, including the total cell length (Fig. 3.7a), the partition of integrins across their different forms (Fig. 3.7b), the relative concentrations of activated/phosphorylated proteins compared to the total (Fig. 3.7c) and the partition of the total concentration of actin into its different forms (Fig. 3.7d). In the early stages after the cell is introduced to the substrate, the cell length remains almost fixed (Fig. 3.7a), while there is a rapid (almost instantaneous) conversion of free integrins into high-affinity integrins (Fig. 3.7b). These high-affinity integrins are then able to bind to ECM ligands to form bound integrins (nascent adhesions) in line with Eq. (3.29i), as shown in Fig. 3.7(b); this is also captured by our spatially-averaged model (see Fig. 2.1a). As nascent adhesions form, ROCK becomes weakly activated which leads to phosphorylation of MLCP, MLCK and cofilin (Fig. 3.7c), as is also observed in Fig. 2.1(c). Consequently, actin is polymerised and a small amount of myosin II is activated, leading to an increase in actin filament concentration and a small increase in VSF concentration (Fig. 3.7d, see also Fig. 2.1c). In response to the formation of VSFs, the cell begins to contract (Fig. 3.7a), in turn pulling on bound integrins, stretching them and exposing VBSs. As bound integrins become stretched, they mature into FAs, which leads to a significant increase in ROCK activation and consequently MLCP, MLCK and cofilin phosphorylation. This instigates our positive feedback loop, with the activation of signaling proteins leading to an increase (decrease) in actin polymerisation (depolymerisation) and in myosin II activation (inactivation), leading

to significant increases in actin filament and VSF formation and so the cell continues to contract (Fig. 3.7a). After approximately 2500 s, the cell settles to an apparent steady state (Fig. 3.7). However, within the cell the redistribution of myosin II bound actin filaments and localisation of FAs continues on a longer time scale (several hours) before the cell finally reaches a full steady state as seen in Figs. 3.8-3.11 (below). It should be noted that this final steady state is a consequence of our modelling approach, whereas the cell would continue to grow, interact with neighbouring cells and remodel its environment. In summary, Fig. 3.7 illustrates the global changes in the cell when adhering to a substrate, particularly capturing the changes in length (contraction) commensurate with the coupled formation and maturation of FAs and VSFs. Moreover, note the similarities of Figs. 3.7(b)-(d) with Figs. 2.1(a)-(c) in Ch. 2, illustrating the success of the spatially-averaged model in describing global measures of the system during the development and maturation of cell-substrate adhesions and cell cytoskeleton.

We now proceed to examine in detail how this global process manifests locally within the cell. In order to elucidate the mechanical changes during cell-substrate binding, Fig. 3.8 illustrates spatial profiles of the cell cytoplasm and ECM (at the eight time-points highlighted above), including the coupled displacement (and strain) of material points (Fig. 3.8a-b) and the corresponding Cauchy stress (Fig. 3.8c-d). Initially there is no deformation or stress inside the cell but, over time, in response to the formation and maturation of cell-substrate adhesions and associated formation of VSFs, the cell contracts (i.e. exhibits inward displacement, Figs. 3.7a, 3.8a). In particular, after around 250-500 s, the feedback loop connecting FA and VSF formation becomes evident, where there is a significant increase in displacement within the cell due to the contractile action of myosin II motors. This displacement is particularly pronounced near the cell boundary, where there is concentrated myosin II cross-linking of actin filaments (as in Fig. 3.11 below). We observe a non-uniform striation pattern (see spatial variations in cell contraction in the inset in Fig. 3.8a) where the cell is particularly contracted near the edges but with little deformation near the centre. This spatial inhomogeneity blunts overall cell contraction and maintains almost isometric tension (Fig. 3.7a). Moreover, there is a significant increase in stress in response to FA and VSF formation (Fig. 3.8c), which is nearly uniform across the cell interior but rapidly decays to zero at the boundary (in line with the boundary conditions imposed in Eq. 3.31b). The adhesive coupling between the cell and the ECM consequently leads to ECM displacement and strain (Fig. 3.8b), coupled to an ECM stress (Fig. 3.8d). However, the ECM is significantly stiffer than the cell and so exhibits much smaller relative displacements and strain compared to the cell (whilst exhibiting similar levels of stress), with a qualitatively similar distribution of each. Given that we measure adhesion length using the relative deformation of the cell to the ECM, in this case (where the much stiffer ECM resists deformation) the adhesions between the

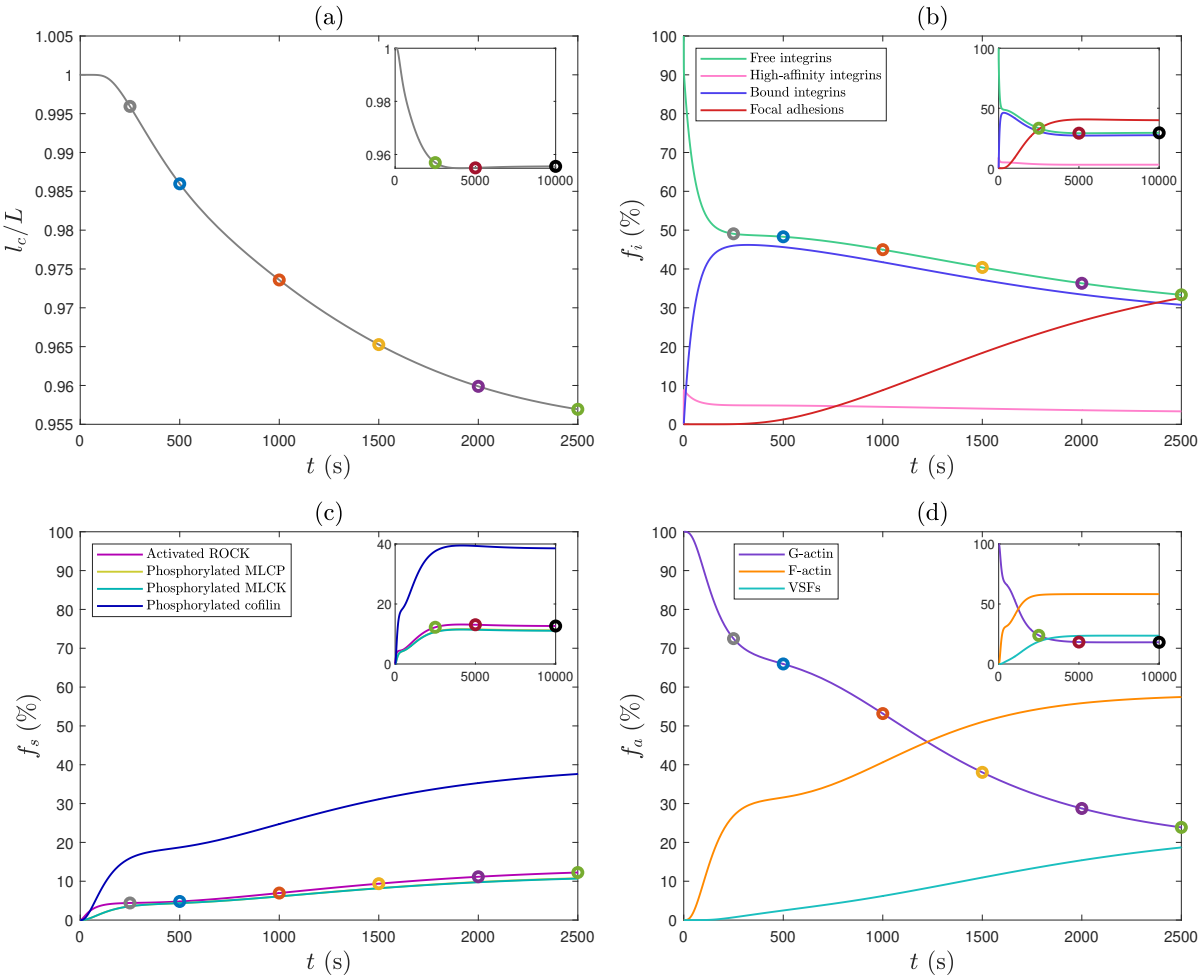

Figure 3.7: Global measures of cytoskeleton and adhesion development. (a) Evolution of dimensionless cell length with time. Time-dependent evolution of percentage of total: (b) integrins in their various forms (free low-affinity integrins, high-affinity integrins, bound integrins and recruited into FAs), (c) ROCK activated and MLCP, MLCK and cofilin phosphorylated, (d) actin in its different forms (monomeric, polymerised into filaments or recruited into SFs). Insets show large time dynamics for each property, open circles indicate times of interest, corresponding to identically coloured lines in spatial distributions in Figs. 3.8-3.11. Parameter values are given in Table 3.5.

cell and ECM become highly stretched, following a similar pattern of deformation to the cell. Consequently, FAs form predominantly near the cell boundaries (as shown in Fig. 3.9 below), leading to an increase in ROCK signaling in this region (as shown in Fig. 3.10 below). In summary, Fig. 3.8 illustrates the mechanical changes (displacement, stress and strain) that occur in both the cell and ECM when a cell adheres to a substrate. The diverse range in behaviour observed over the cell length is indicative of the need to consider local behaviour (in addition to global), which we now explore.

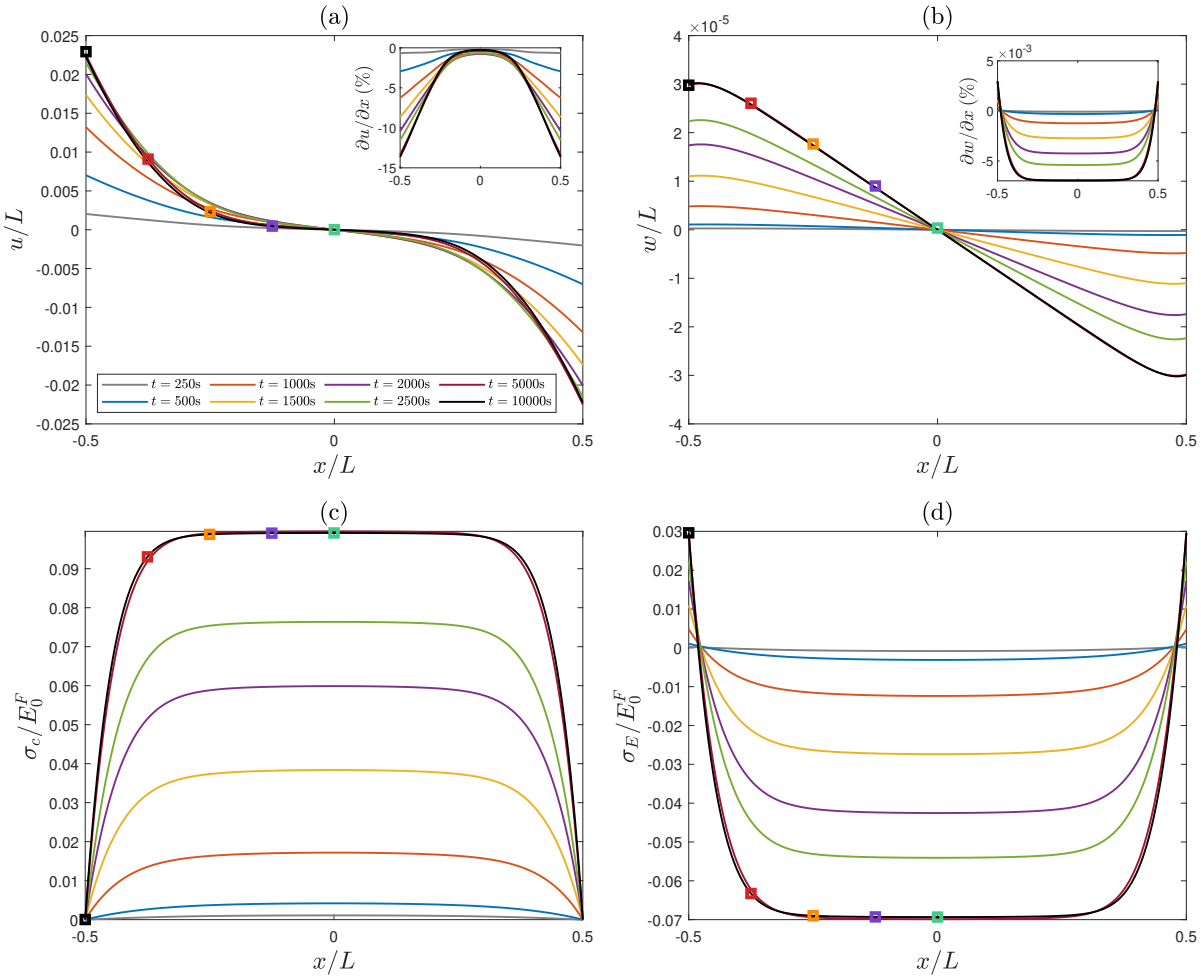

Figure 3.8: Mechanical properties of the cell and ECM. At snapshots in time, as a function of initial dimensionless position, dimensionless (a) displacement of points in cell from their initial position, (b) displacement of points in ECM from their initial position, (c) stress in cytosol, (d) stress in ECM. Insets in (a), (b) show strain, percentage stretch (positive)/compression (negative), of the cell and ECM respectively. Coloured squares correspond to positions of identically coloured lines in temporal plots in Figs. 3.9-3.11. Away from the cell, ECM stress and displacement decay linearly to zero towards the far field. Parameter values are given in Table 3.5.

In Figs. 3.9-3.11 we summarise the dynamics of the key cytoskeletal, adhesion and signaling proteins in the baseline case shown in Figs. 3.7-3.8. We account for the spatial and temporal changes in integrin and adhesion distribution in Fig. 3.9. Initially there are

no adhesions between the cell and substrate, with all integrins uniformly dispersed and in a free state with low-affinity to the ECM (Fig. 3.9a-b). These integrins rapidly bind to talin to form high-affinity integrins (Fig. 3.9c-d), which are able to bind to ligands in the underlying ECM to form bound integrins (Fig. 3.9e-f). The early formation of high-affinity and bound integrins occurs almost uniformly, owing to the high diffusivity of free integrins and the assumed uniformity in initial free integrin and ligand density. The bound integrins will eventually (in response to signaling) go on to mature into FAs (Fig. 3.9g-h).

The formation of nascent adhesions initiates weak signaling inside the cell, the dynamics of this process are summarised in Fig. 3.10. In particular, ROCK becomes weakly activated (Fig. 3.10a-b). This occurs nearly uniformly, reflecting the early uniform distribution of nascent adhesions (and lack of FAs). In response to ROCK activation, phosphorylation of MLCP (Fig. 3.10c-d), MLCK (Fig. 3.10e-f) and cofilin (Fig. 3.10g-h) occurs. These are also uniform at early times, resultant from a combination of uniform ROCK activation and because they are all assumed to be diffusive. The weak activation of ROCK leads to an increase in actin polymerisation across the cell at nascent adhesions. Moreover, the phosphorylation of MLCP (MLCK) leads to a decrease (increase) in myosin II inactivation (activation) and cofilin phosphorylation leads to a reduction in actin depolymerisation.

In response to signaling, actin is polymerised and myosin II is activated, leading to the formation of actin filaments and VSFs. The dynamics of these are summarised in Fig. 3.11. In particular we consider the temporal (spatial) dynamics of actin monomers in Fig. 3.11(a) (Fig. 3.11b), of actin filaments in Fig. 3.11(c) (Fig. 3.11d), of VSFs in Fig. 3.11(e) (Fig. 3.11f) and of myosin II in Fig. 3.11(g) (Fig. 3.11h). At early times there is, consistent with the near uniform weak signaling, a nearly uniform decrease in actin monomer concentration (Fig. 3.11a-b) as actin is polymerised, leading to an increase in actin filament concentration (Fig. 3.11c-d). The small amount of activated myosin II (Fig. 3.11g-h) then begins to cross-link actin filaments and form contractile VSFs (Fig. 3.11e-f). As a consequence of contraction of resultant VSFs, bound integrins are pulled (stretched), enhancing FA formation and, in turn, signaling and VSF formation. Consequently, Figs. 3.9-3.11 are intimately linked and feed back to one another.

In response to VSF formation, particularly the contractile action of myosin motors, the cell begins to contract approximately 250-500 s after being introduced to the substrate (Figs. 3.7a, 3.8a) and the positive feedback loop becomes activated. This contraction is most keenly felt near the cell edge, leading to maturation of bound integrins into FAs here (Fig. 3.9g-h) as VBSs become exposed as bound integrins become stretched (Fig. 3.8a-b). Consequently, there is also a transient increase in the cell in the number of bound integrins (Fig. 3.9e-f). Reflecting the inhomogeneity in FA formation (Fig. 3.9g-h), spatial variations emerge in free integrin (Fig. 3.9a-b) and high-affinity integrin density (Fig. 3.9c-d), though these differences remain relatively small owing to the high-diffusivity of free

integrins. As ROCK activation is significantly enhanced in response to FA formation (compared to nascent adhesions) and because ROCK (in both inactive and active forms) is assumed to be non-diffusive, significant spatial disparities arise in activated ROCK concentration (Fig. 3.10a-b), mirroring the spatial distribution in FA density. Consequently, phosphorylation of MLCP (Fig. 3.10c-d), MLCK (Fig. 3.10e-f) and cofilin (Fig. 3.10g-h) is significantly enhanced, though these proteins are diffusive and so are comparatively spatially homogeneous (as would be expected based on dimensionless parameters presented in Table 3.5). These phosphorylated signaling proteins consequently lead to a significant increase in actin polymerisation (Fig. 3.11c-d) in the locality of FAs and, in turn, a significant decrease in actin monomer concentration (Fig. 3.11a-b). Owing to the high diffusivity of actin monomers, the reduction in monomer concentration occurs approximately uniformly. The resultant filaments are treadmilled towards the cell centre and are cross-linked, in the vicinity of FAs, by activated myosin II (Fig. 3.11g-h), leading to a significant increase in VSF concentration near FAs (Fig. 3.11e-f). These VSFs exert further contractile forces on bound integrins, leading to more FA formation (Fig. 3.9g-h), strengthened signaling (Fig. 3.10) and, consequently, more VSF formation (Fig. 3.11e-f). This process of rapid increases in FA and VSF formation occurs over the course of around 500-2000 s after the cell is introduced to the substrate. Thereafter, redistribution of adhesions (Fig. 3.9e-h), signaling hubs (Fig. 3.10) and VSFs (Fig. 3.11e-f) dominates dynamics until a steady state is reached (after around 10000 s).

In summary Figs. 3.9-3.11, when taken together, demonstrate the effect of the positive feedback loop in the cell. They show how adhesion formation precipitates signaling inside the cell which, in turn, leads to the formation of actin filaments and VSFs, and are able to capture how increased SF formation leads (through cell contraction, as shown in Figs. 3.7-3.8) to increased and localised FA formation. This one-dimensional modelling approach is significantly more sophisticated than the spatially-averaged approach taken in Ch. 2, with an ability now to predict changes in the mechanical properties of the cell, ECM and cell-substrate adhesions and to predict localisation of adhesions, actin filaments, VSFs and stress inside the cell. Nonetheless, the similarity in the prediction of global biochemical dynamics (see Figs. 2.1, 3.7) demonstrates the ability of the spatially-averaged model to capture key aspects of cell-substrate adhesion and cytoskeleton development in a simple manner.

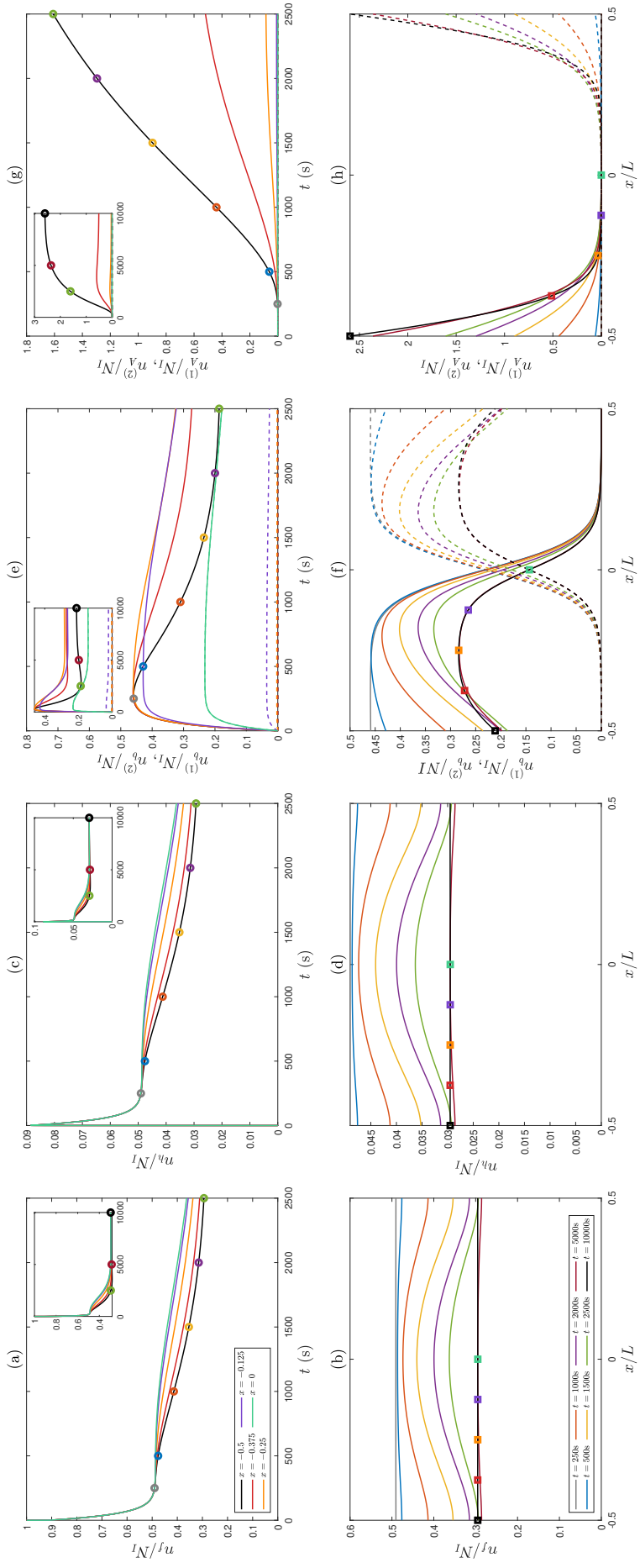

Figure 3.9: Integrin and adhesion dynamics. Temporal and spatial dynamics of integrins and adhesions where solid (dashed) lines are used to denote family 1 (family 2) adhesions. Temporal dynamics of (a) free integrins, (c) high-affinity, (e) nascent adhesions and (g) FAs where density is dimensionless and time is dimensional (measured in seconds), insets show long time dynamics (up to $t = 10000$ s). Spatial distribution at snapshots in time of (b) free integrins, (d) high-affinity integrins, (f) nascent adhesions and (h) FAs where density and position are dimensionless. Parameter values are given in Table 3.5.

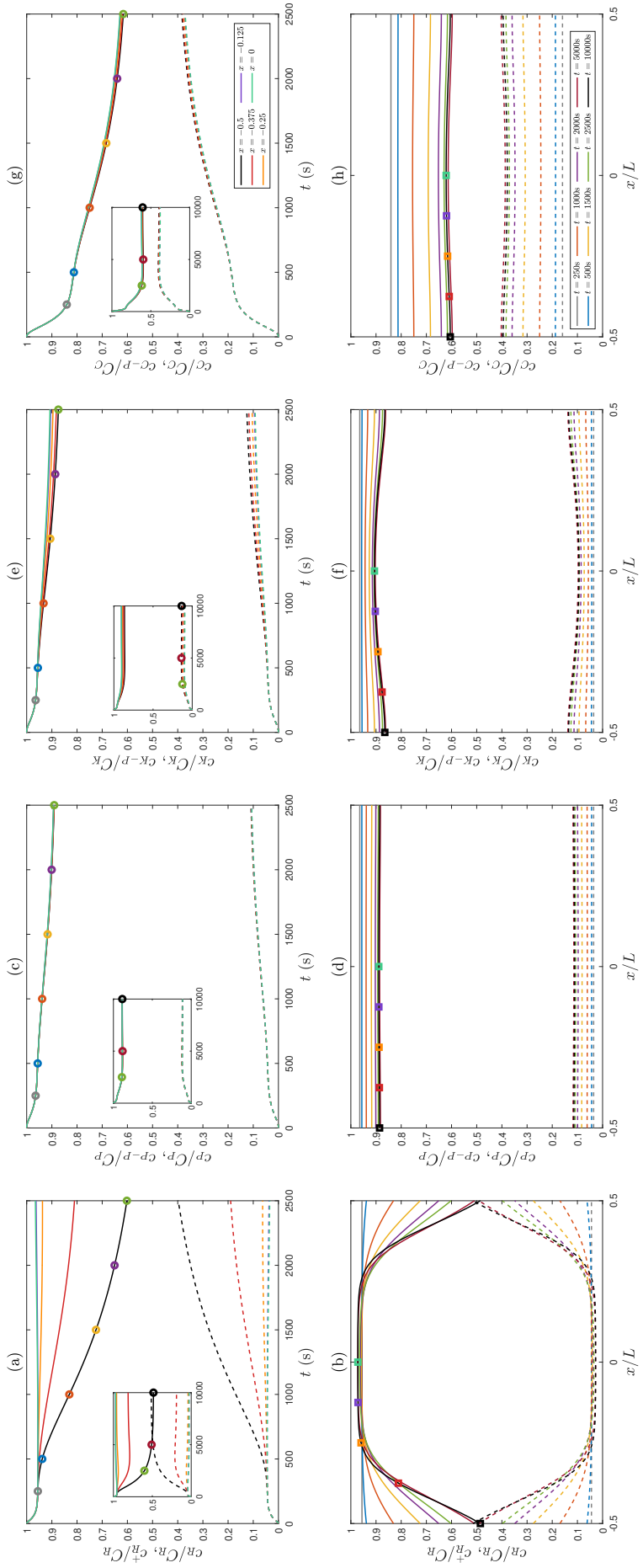

Figure 3.10: Signaling protein dynamics. Temporal and spatial dynamics of signaling proteins and downstream effectors where solid (dashed) lines are used to denote inactivated (activated) ROCK or unphosphorylated (phosphorylated) MLCP, MLCK and cofilin. Temporal dynamics of (a) ROCK, (c) MLCP, (e) MLCK and (g) cofilin where concentration is dimensionless and time is dimensional (measured in seconds), insets show long time dynamics (up to $t = 10000$ s). Spatial distribution at snapshots in time of (b) ROCK, (d) MLCP, (f) MLCK and (h) cofilin where concentration and position are dimensionless. Parameter values are given in Table 3.5.

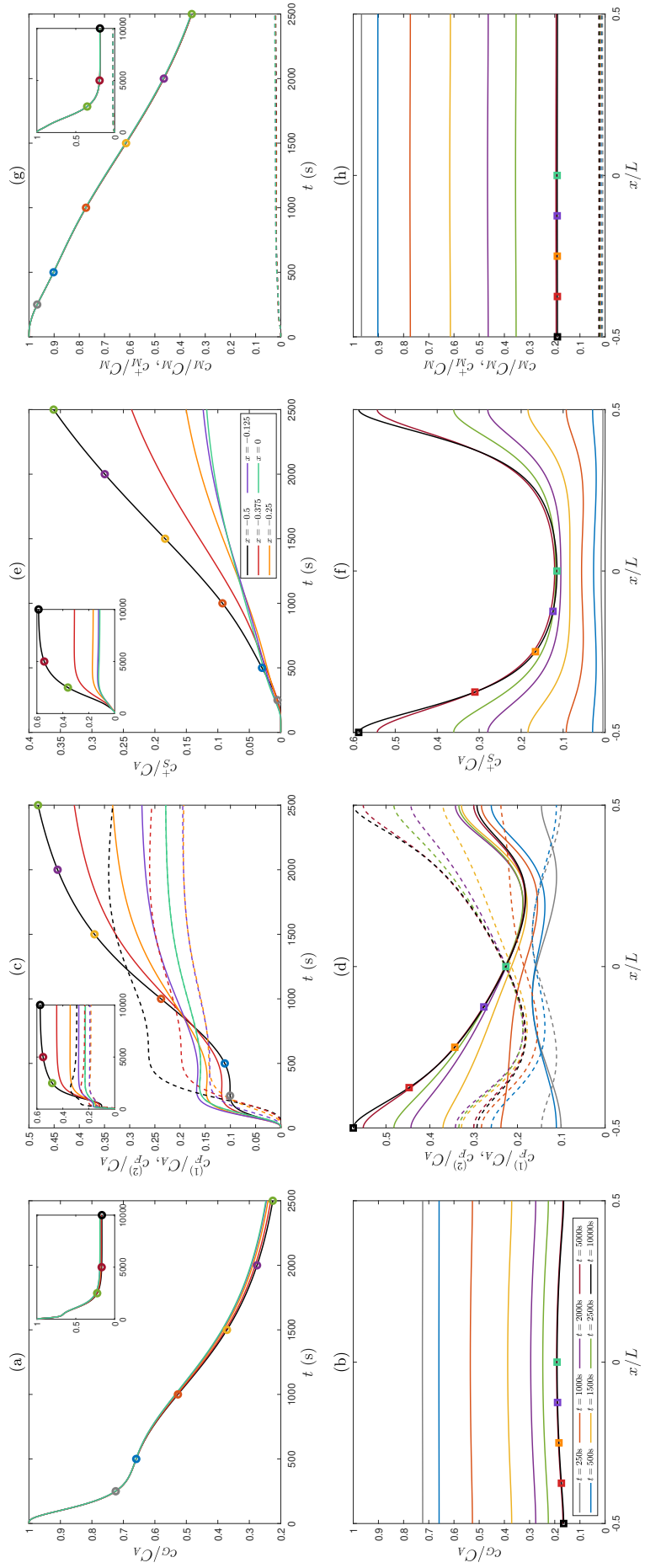

Figure 3.11: Actin and myosin dynamics. Temporal and spatial dynamics of actin families and myosin II where solid (dashed) lines are used to denote family 1 (family 2) actin filaments or to denote inactivated (activated) myosin II. Temporal dynamics of (a) actin monomers, (c) actin filaments, (e) actomyosin VSFs and (g) myosin II where concentration is dimensionless and time is dimensional (measured in seconds), insets show long time dynamics (up to $t = 10000$ s). Spatial distribution at snapshots in time of (b) actin monomers, (d) actin filaments, (f) actomyosin VSFs and (h) myosin II where concentration and position are dimensionless. Parameter values are given in Table 3.5.

3.8.1 Model validation

In this Section we demonstrate the mesh independent convergence of our computational model discussed in Sec. 3.7. In particular, to ensure that it sufficiently accurately identifies solutions to our large system of governing mechanical and biochemical PDEs, in Figs. 3.12-3.14 we quantify the effect of increasing grid resolution and introducing more stringent error tolerances.

Throughout this Section we evaluate the model in terms of three quantities. Firstly, we test the conservation of mass in the cell, particularly ensuring that actin in its various forms (monomeric, filamentous or recruited into SFs) and integrins in their various forms (free, high-affinity, bound or recruited into FAs) are appropriately conserved. In particular, Eq. (3.35) should be satisfied to ensure no mass leaves the system, which we test by integrating the concentration of actin and density of integrins over the cell length. We consider mass to be suitably conserved if less than 1% is lost over the (long) simulation time; of-course this choice is arbitrary, and is chosen because a mass loss (or gain) of 1% leads to little change in the qualitative behaviour of the system, but more stringent error tolerances could be employed if required. We also test the discrepancy in the momentum balance equation for the cell, calculating the difference between the left-hand side and right-hand side of Eq. (3.37a) according to our numerical model. Moreover, we test the predicted stress at the left boundary of the cell, which should be zero in our baseline case (according to Eq. 3.39).

Increasing grid resolution

In Fig. 3.12 we investigate the effect of increasing grid resolution, with $20 \leq N \leq 200$, on predictions from the computational model by considering mass loss of actin and integrins from the cell due to advection and diffusion at the cell boundaries (Fig. 3.12a) and by checking the consistency of our mechanical governing equations (Fig. 3.12b). In particular, to quantify the accuracy of the model, in Fig. 3.12(a) we plot the percentage of actin (left y-axis) and percentage of integrins (left y-axis) lost or gained from the cell 10000 s after the cell has been introduced to the substrate. In Fig. 3.12(b) we plot the discrepancy in the momentum balance equation for the cell (left y-axis) and the predicted stress at the left boundary of the cell (right y-axis) 10000 s after the cell has been introduced to the substrate. We additionally illustrate the computational time taken to run a single simulation, using the baseline parameter values outlined in Sec. 3.6, for each N, as indicated on the right y-axis of Fig. 3.12(a). Broadly we observe that an increase in grid resolution leads to a reduction in mass loss from the system (Fig. 3.12a) and better describes the mechanical equations (Fig. 3.12b). However, computational time also increases rapidly with N (Fig. 3.12a) meaning a balance must be struck, choosing N so that the computational model sufficiently emulates the developed mathematical model but can be solved

in reasonable time scales. Hence, we typically set $N = 100$ in simulations, but increase this grid resolution if this leads to unacceptably high mass loss (i.e. >1% loss over the simulation time).

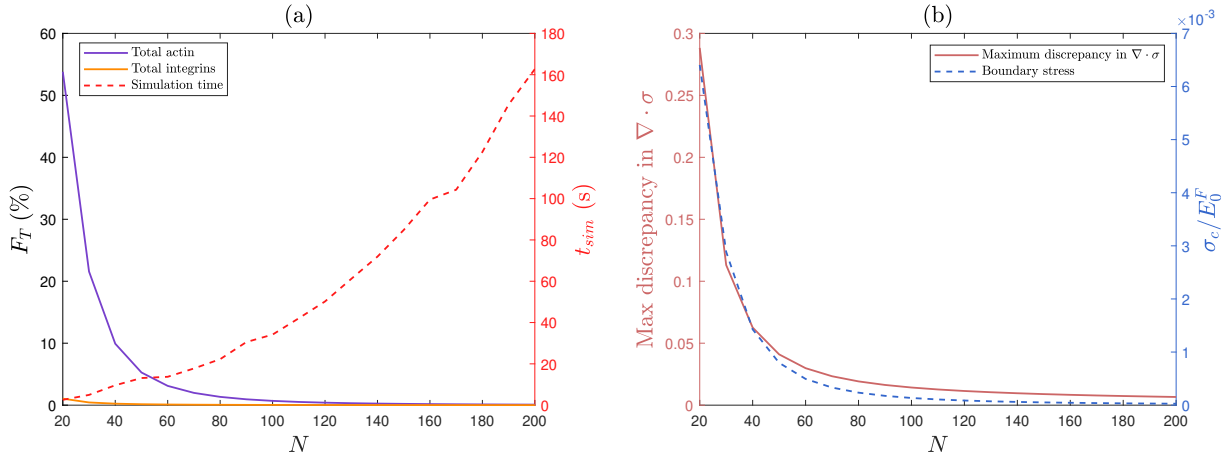

Figure 3.12: Effect of increasing grid resolution on numerical results. As a function of N, at $t = 10000$ s: (a, left $y-$axis) fraction (percentage), F_T, of total integrins (orange) and actin (purple) lost or gained from the system; (a, right $y-$axis) computational time (red) taken to run a single simulation at that grid resolution in Matlab; (b, left $y-$axis) maximum discrepancy in calculation of $\nabla \cdot \sigma$; (b, right $y-$axis) boundary stresses (note this should be zero from our boundary conditions).

Changes in error tolerance

In Fig. 3.13 (Fig. 3.14) we investigate the effect on model predictions of changing Matlab's relative (absolute) error tolerance by again considering mass loss from the cell due to advection and diffusion at the cell boundaries in Fig. 3.13(a) (Fig. 3.14a), and checking the consistency of our mechanical governing equations in Fig. 3.13(b) (Fig. 3.14b). To quantify the accuracy of the model, we plot in Fig. 3.13(a) (Fig. 3.14a) the percentage of actin (left y-axis) and percentage of integrins (left y-axis) lost or gained by the cell 10000 s after the cell has been introduced to the substrate. In Fig. 3.13(b) (Fig. 3.14b) we plot the error in the momentum balance equation for the cell (left y-axis) and the predicted stress at the left boundary of the cell (right y-axis). We additionally illustrate the computational time taken to run a single simulation, using the baseline parameter values outlined in Sec. 3.6, for each tolerance; this is indicated on the right y-axis of Fig. 3.13(a) (Fig. 3.14a). We broadly observe that more stringent relative (Fig. 3.13) or absolute (Fig. 3.14) error tolerances have little effect on model predictions, and also have little effect on computational time (see Fig. 3.13a and Fig. 3.14a). Consequently, we choose to adopt Matlab's standard error tolerances, i.e. we set the relative tolerance to RelTol=1×10^{-3} and absolute tolerance to AbsTol=1×10^{-6}.

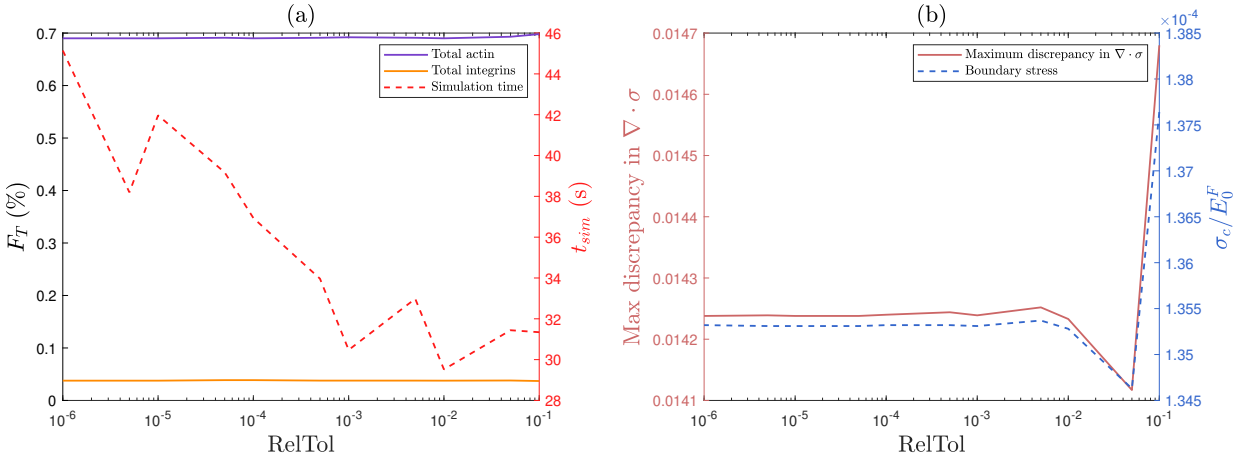

Figure 3.13: Effect of changing relative error tolerance, RelTol, in ODE solver in Matlab. As a function of RelTol at $t = 10000$ s: (a, left $y-$axis) fraction (percentage), F_T, of total integrins (orange) and actin (purple) lost or gained from the system; (a, right $y-$axis) computational time (red) taken to run a single simulation at that grid resolution in Matlab; (b, left $y-$axis) maximum discrepancy in calculation of $\nabla \cdot \sigma$; (b, right $y-$axis) boundary stresses (note this should be zero from our boundary conditions).

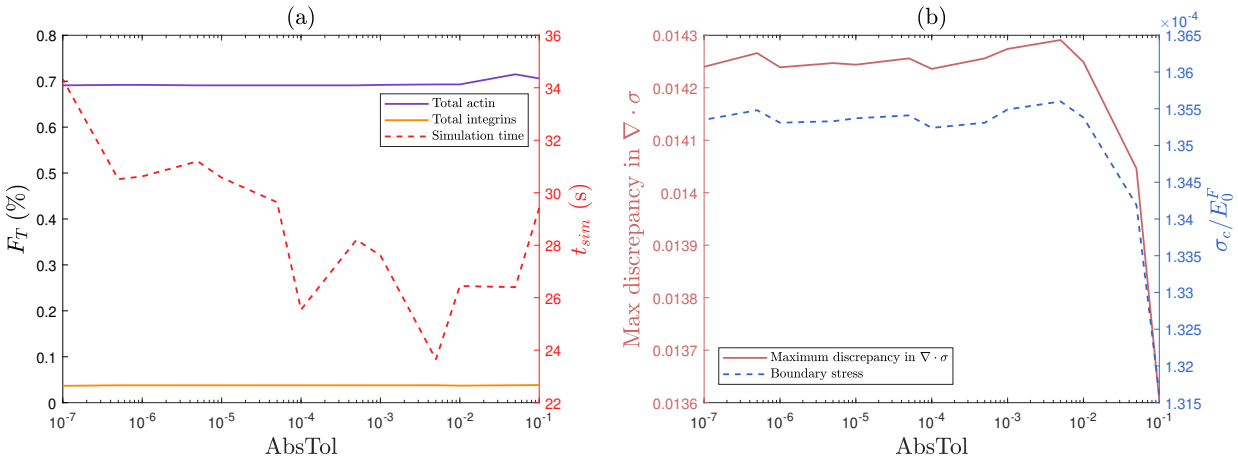

Figure 3.14: Effect of changing absolute error tolerance, AbsTol, in ODE solver in Matlab. As a function of RelTol at $t = 10000$ s: (a, left $y-$axis) fraction (percentage), F_T, of total integrins (orange) and actin (purple) lost or gained from the system; (a, right $y-$axis) computational time (red) taken to run a single simulation at that grid resolution in Matlab; (b, left $y-$axis) maximum discrepancy in calculation of $\nabla \cdot \sigma$; (b, right $y-$axis) boundary stresses (note this should be zero from our boundary conditions).

3.8.2 Changes in feedback strength

In forming the model, in Eq. (3.49) we introduced the empirical parameter δ, which measures the relative increase in the rate of ROCK activation when adhesions mature into FAs compared to when they are immature (i.e. bound integrins). This parameter effectively governs the strength of the positive feedback loop, ensuring that maturation of adhesions into FAs (in response to contraction of VSFs) leads to increased phosphorylation of MLCP, MLCK and cofilin and, consequently, increased VSF formation.

Since the parameter is empirical, we investigate its effect by considering the range $0 \leq \delta \leq 10$ whilst fixing all other parameters to their baseline values (as outlined in Sec. 3.6). To quantify changes in the cell with increasing δ, we consider the global measure of the partition of integrins (Fig. 3.15a) and the partition of actin (Fig. 3.15b) 10000 s after the cell has been introduced to the substrate. As would be expected, an increase in δ leads to an increase in both FA density (Fig. 3.15a) and VSF (and actin filament) concentration (Fig. 3.15b). However, this effect becomes significantly less pronounced when $\delta \gtrsim 2$, particularly for FA formation. By considering the maximum and average activated ROCK concentration (inset in Fig. 3.15a), we demonstrate that there is increased FA localisation within the cell with increasing δ (note that local activated ROCK concentration is directly linked to local FA density). This is reflective of an increase in the maximum and average relative deformation of the cell compared to the ECM (as seen in the inset in Fig. 3.15b), leading to adhesion stretch and maturation (per Eq. 3.51).

In all other results presented in this Chapter we use $\delta = 4$, which is sufficient to capture the positive feedback loop. Note also that the influence of δ saturates beyond this value (Fig. 3.15).

3.9 Summary

In this Chapter we have presented a one-dimensional bio-chemo-mechanical continuum model to describe the coupled development of cell-substrate adhesions and cell cytoskeleton. In particular, treating the cell and ECM as Kelvin-Voigt viscoelastic materials, coupled to each other through viscoelastic adhesions, we have formulated a discrete mechanical model to describe the deformation of each of these structures during cell-substrate interaction. By employing discrete-to-continuum upscaling we have been able to rationally connect nanoscale features of adhesions and the cytoskeleton to the microscale and have formulated a continuum system of momentum balance equations to describe the coupled deformation of the cell and ECM. We have formulated a large system of reaction-diffusion-advection equations to describe the evolution of important cytoskeletal, adhesion and signaling proteins and have linked the concentration and density of these proteins to the mechanical properties of the cell, ECM and adhesions. By imposing various constitutive

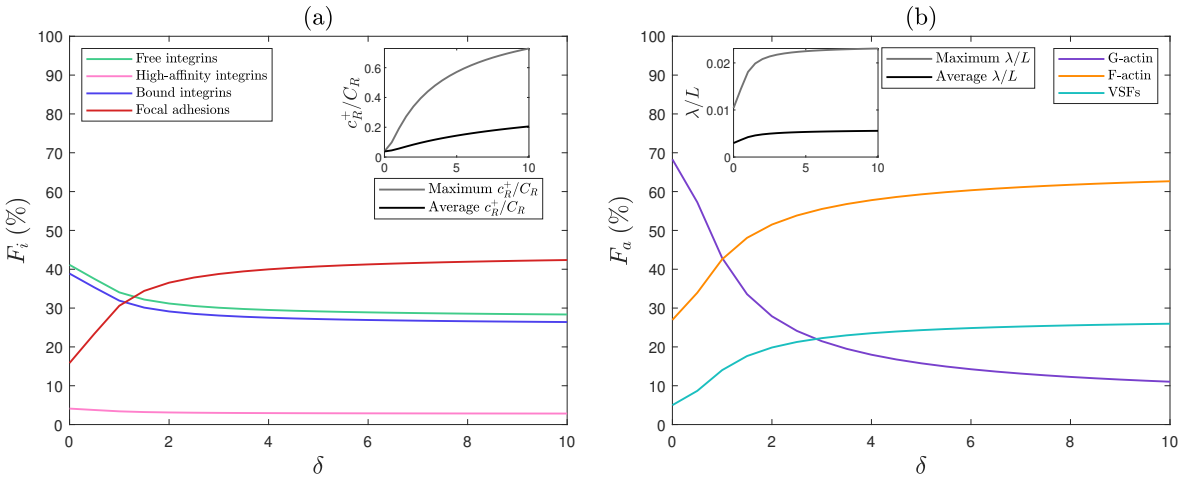

Figure 3.15: Effect of changing feedback strength on FA and VSF formation. As a function of δ, at $t = 10000$ s: (a) fraction, F_i, of integrins that are free, high-affinity, bound or recruited into FAs; (b) fraction, F_a, of monomeric and filamentous actin and actin recruited into VSFs. Insets show (a) maximum (light grey) and average (black) dimensionless concentration of c_R^+ in the cell and (b) maximum (light grey) and average (black) relative dimensionless displacement of the cell to ECM.

assumptions, we have been able to link the formation of FAs and VSFs, capturing in a simple way the positive feedback loop that connects the development of both of these structures. Application of this model has demonstrated its ability to predict the global dynamics of cell-substrate interaction and we have demonstrated striking similarity with predictions from the significantly simpler spatially-averaged model developed in Ch. 2. However, this one-dimensional framework reduces the need for empiricism, incorporates the mechanics of the cell, ECM and adhesions and is able to predict localisation of proteins, deformation and stress. We conclude that this model successfully incorporates the key components needed to describe cell-substrate adhesion and cytoskeleton development. We now proceed in Ch. 4 to consider sweeps of the parameter space, elucidating the mechanism of several experimentally observed phenomena.

Chapter 4

Influence of microenvironment cues

In Ch. 1 we discussed how cells respond to cues from their microenvironment through changes in cell-substrate adhesion, cytoskeleton development and activation (or inhibition) of intracellular signaling cascades. Building on this, in Ch. 3 we developed a one-dimensional bio-chemo-mechanical continuum model to describe the coupled formation and maturation of cell-substrate adhesions and SFs, together with the deformation of the cell and ECM. Particularly, using baseline model parameters discussed in Sec. 3.6, we applied the model to illustrate the local and global dynamics of a cell binding to a stiff ECM (see Sec. 3.8).

In this Chapter we use the model developed in Ch. 3 to investigate the influence of various environmental and biochemical cues, elucidating the mechanism by which they cause changes in cell-substrate adhesion. Particularly, in Sec. 4.1 we investigate the effect of ECM ligand density on the formation of FAs and SFs. In Sec. 4.2 we explore how ligand micropatterning influences localisation of FAs, SFs and intracellular stress. In Sec. 4.3 we elucidate the mechanism by which increased substrate stiffness precipitates increased adhesion and SF formation. We continue in Sec. 4.4 by quantifying the sensitivity of the cell to its microenvironment by examining the mechanosensing distance of the cell (i.e. the maximal distance from the cell at which mechanical perturbations applied to the ECM can induce a biochemical response in a well-adhered cell). In Sec. 4.5, mimicking, for example, magnetic tweezer or atomic force microscopy experiments, we investigate the effect of externally probing the cell, predicting how the magnitude and the position of the applied force can influence adhesion and cytoskeleton dynamics. Finally, in Sec. 4.6 we explore the effect of various inhibitors on reaction kinetics, particularly how inhibition of ROCK (Sec. 4.6.1) and myosin II (Sec. 4.6.2) can lead to FA and SF disassembly in a well-adhered cell. Having identified that the model developed in Ch. 3 is capable of predicting the impact of various mechanotransductive and chemotransductive cues on the development of cell-substrate adhesion and cell cytoskeleton, in Sec. 4.7 we outline a range of future research questions that this model can now be employed to address.

4.1 The influence of ECM ligand density

In order to elucidate the effect of ECM ligand density (governed by the parameter N_0^S) on FA and VSF development in Fig. 4.1 we vary $\tilde{N}_0^S$, the relative density of ligands (assumed to be constant over the ECM) to the average integrin density (assumed to be $N_I = N_0^I = 100\,\mu\text{m}^{-2}$ in the base case), whilst holding all other parameter values equal to their baseline values (as outlined in Sec. 3.6). We illustrate the effect of varying $\tilde{N}_0^S$ by plotting the partition of integrins (Fig. 4.1a) and the partition of actin (Fig. 4.1b) 10000 s after the cell has been introduced to the substrate (the model may allow for FAs to form at even later times, but other effects likely become dominant at these long times, reducing model applicability).

We broadly observe that increases in ligand density lead to increases in FA and VSF formation. This effect is particularly pronounced when ligand density is comparable to integrin density (i.e. when ligand density is between one and ten times greater than integrin density). We predict saturation of the integrin density as the ligand density becomes sufficiently high (with a density of approximately 1000-10000 μm^{-2}) and little further increase in VSF and FA formation. Increasing ligand density further (with density around 10000-100000 μm^{-2}, likely outwith the scope of most experiments) leads to a small decrease in FA formation. We hypothesise that this is because the cell struggles to contract when ligand density becomes sufficiently high due to the increasing uniformity (and strength) of cell-substrate adhesions. This leads to a reduction in bound integrin stretch (see inset in Fig. 4.1b) and, in turn, a reduction in the maximum concentration of activated ROCK (see inset in Fig. 4.1a) due to reduced FA formation.

These observations are compatible with experimental results. For example, it has been shown by Cavalcanti-Adam et al. (2007) (studying rat fibroblasts) that increasing ligand density leads to more pronounced FA formation, but has little effect on nascent adhesion formation. Moreover, Arnold et al. (2004) demonstrated that FAs struggle to form when ligand spacing is above approximately 73 nm, which corresponds to a minimum ligand density of approximately 200 μm^{-2}; comparable with our model predictions showing sudden onset of FA formation when ligand densities reach around 350 μm^{-2} (below this level there is insufficient clustering of integrins to form mature adhesions). Note that this sudden onset behaviour was predicted by the spatially-averaged model developed in Ch. 2 (see Fig. 2.8); however, this simplified modelling approach was unable to access reductions in adhesion maturation at very high ligand densities.

4.2 The influence of ECM ligand patterning

In order to assess how micropatterning of ECM ligands can be employed to influence localisation of cell-substrate adhesion, cytoskeleton development and intracellular stress,

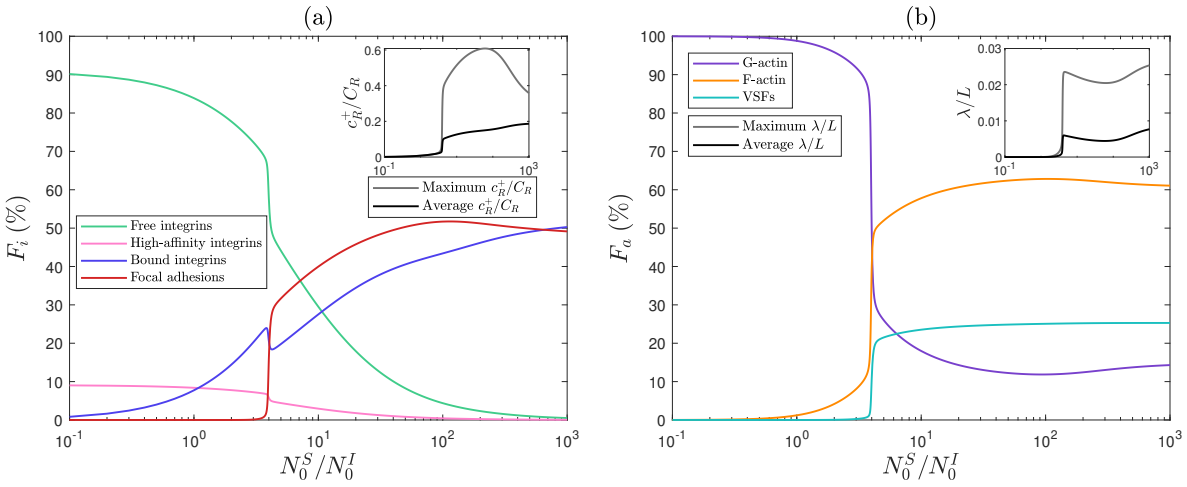

Figure 4.1: Effect of ligand patterning on FA and VSF formation. As a function of N_S^0/N_I^0 (the ratio of ligand density to integrin density), at $t = 10000$ s: (a) fraction, F_i, of integrins that are free, high-affinity, bound or recruited into FAs; (b) fraction, F_a, of monomeric and filamentous actin and actin recruited into VSFs. Insets show (a) maximum (light grey) and average (black) dimensionless concentration of c_R^+ in the cell and (b) maximum (light grey) and average (black) relative dimensionless displacement of the cell to ECM.

we illustrate examples of the model using a prescribed ligand pattern (Fig. 4.2a) and a random ligand pattern (Fig. 4.2b). Note that we obtain an approximation of a random ligand pattern by repeatedly smoothing a random distribution of ECM ligands at each grid point, to ensure the initial conditions are continuous, multiplied by a weighting factor (of the form seen in Fig. 3.6) across the domain to ensure family 1 (2) ligands are found predominantly below the left (right) half of the cell. We subsequently multiply by an appropriate scale factor to ensure the same average density of ligands over the domain as in baseline simulations. Assuming all other parameters are given by their baseline values outlined in Sec. 3.6, we demonstrate this effect by plotting the spatial dynamics of proteins, alongside the mechanical properties of the cell, at certain snapshots in time. In particular, we present snapshots at $t = 250$ s (grey), $t = 500$ s (dark blue), $t = 1000$ s (orange), $t = 1500$ s (yellow), $t = 2000$ s (purple), $t = 2500$ s (green), $t = 5000$ s (maroon) and $t = 10000$ s (black) after the cell has been introduced to the substrate. We indicate in Fig. 4.3(a) (Fig. 4.4a) the density of bound integrins at these snapshots in time for the prescribed (random) ligand pattern. These nascent adhesions can mature into FAs, the profiles of which are indicated in Fig. 4.3(b) (Fig. 4.4b). As in Sec. 3.8 of Ch. 3, the formation and maturation of adhesions precipitates increased Rho signaling inside the cell, leading to increased actin filament and VSF formation, which is documented in Fig. 4.3(c) (Fig. 4.4c). The formation of FAs and, in turn, contractile SFs leads to deformation of the cell as indicated in Fig. 4.3(d) (Fig. 4.4d), with the intracellular stress indicated in an inset in Fig. 4.3(d) (Fig. 4.4d). We present the ECM ligand patterning (as an initial ECM

ligand density) in Fig. 4.3(c) (Fig. 4.4c).

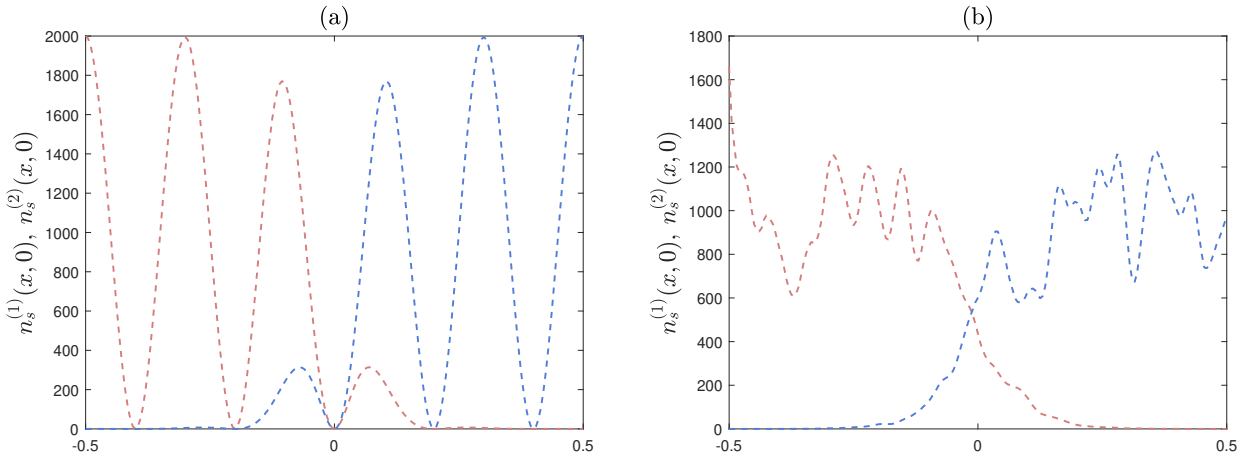

Figure 4.2: Panel (a) shows imposed initial ligand patterning and corresponds to cell-substrate dynamics in Fig. 4.3; panel (b) shows random initial ligand patterning and corresponds to cell-substrate dynamics in Fig. 4.4. ECM density profile for family 1 (2) ligands are indicated in pink (blue).

In a similar manner to our baseline case outlined in Sec. 3.8 in Ch. 3, there are initially no adhesions between the cell and substrate. At this time, integrins are dispersed uniformly over the cell membrane and are in their free, low-affinity state, whilst all ECM ligands are unbound and distributed as indicated in Fig. 4.3(c) (Fig. 4.4c). The integrins rapidly bind to talin and form high-affinity integrins (not shown) which in turn bind to ECM ligands to form bound integrins. The pattern of bound integrin formation reflects the pattern of ECM ligands and can be highly variable across the cell length, as observed in Fig. 4.3(a) (Fig. 4.4a); note the contrast with the approximately uniform formation of bound integrins at early times when the cell is cultured on a substrate with uniform ligand density (as presented in Sec. 3.8). The formation of bound integrins leads to weak signaling inside the cell, facilitating polymerisation of actin and activation of myosin II. Consequently, in Fig. 4.3(c) (Fig. 4.4c) we observe a small increase in VSF concentration. In turn, the cell contracts, as observed in Fig. 4.3(d) (Fig. 4.4d). This initial development of SFs (and hence contraction of the cell) is (weakly) spatially non-uniform, owing to the variable bound integrin density (Figs. 4.3a, 4.4a). Contraction of the cell stretches bound integrins, exposing VBSs, and causing maturation of adhesions into FAs (Figs. 4.3b, 4.4b). As in the baseline case illustrated in Sec. 3.8 of Ch. 3, generally FAs preferentially form in the vicinity of the cell boundary, where contraction of the cell is greatest (Figs. 4.3d, 4.4d). However, owing to variations in ligand and bound integrin density, and in SF formation, pockets of FAs can also form away from the cell edge (Figs. 4.3b, 4.4b), in regions where the ligand patterning is particularly dense. Over time, there is a competitive aspect to continued FA maturation, with smaller adhesions (regions with lower FA density) dissociating, with

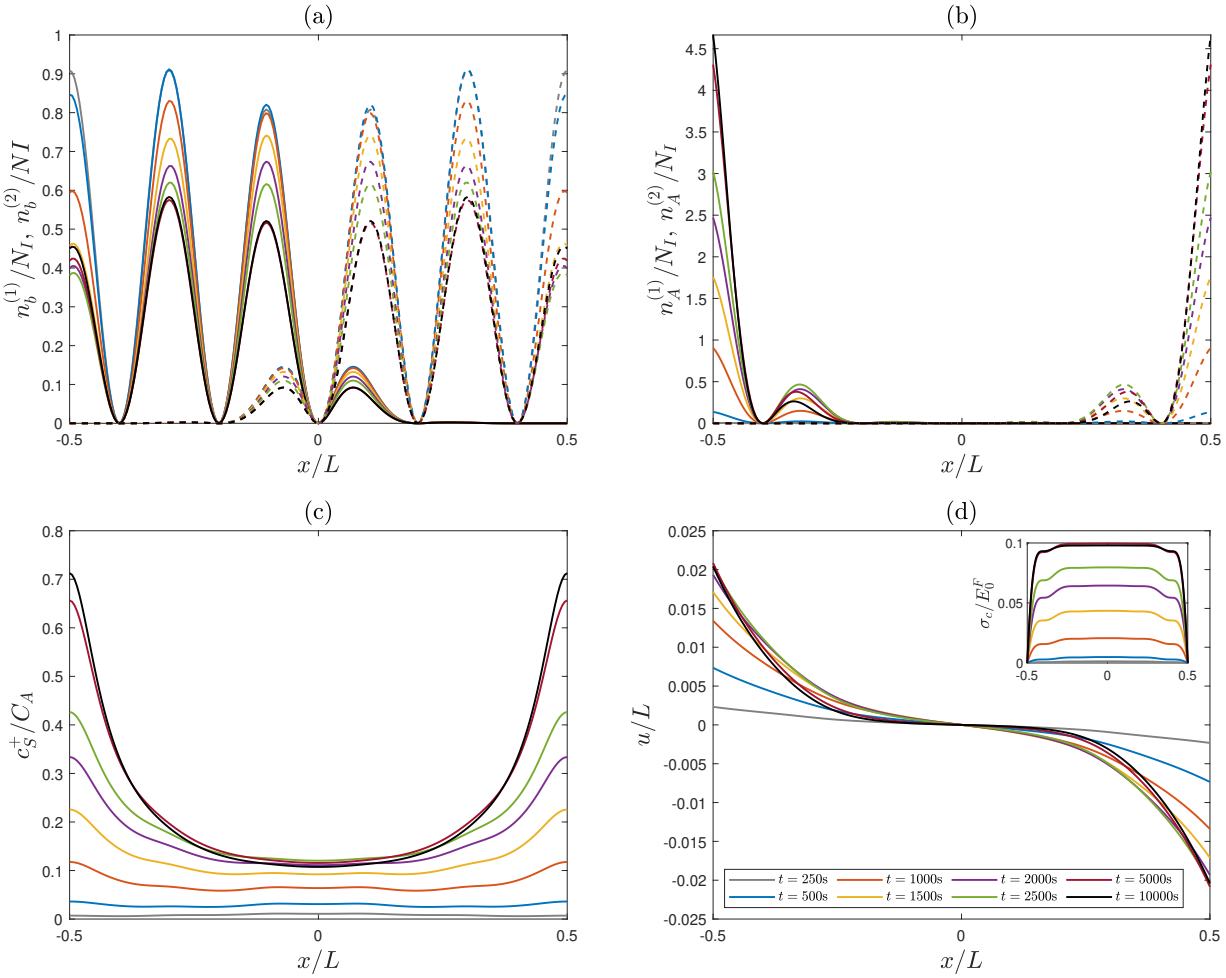

Figure 4.3: Effect of imposed ligand micropatterning (pattern shown in Fig. 4.2a). At snapshots in time, as a function of initial dimensionless position, dimensionless (a) density of bound integrins, (b) density of FAs, (c) concentration of SFs (left axis), (d) displacement of points in cell from their initial position. Solid lines in (a), (b) correspond to family 1 adhesions whilst dashed lines correspond to family 2 adhesions. Insets in (d) shows dimensionless stress as a function of dimensionless initial position.

integrins subsequently absorbed into larger adhesions (Figs. 4.3b, 4.4b). In the case of random ligand patterning (or patterning with an imposed bias), this can lead to further localisation of FAs and SFs in the cell, though cell displacement and stress remains largely symmetric (Figs. 4.3d, 4.4d). However, asymmetries in the mechanical properties of the cell may arise if sufficient asymmetries exist in the initial ligand patterning (e.g. many more ligands in the ECM below the left half of the cell compared to the right).

4.3 The influence of substrate stiffness

In order to assess how the mechanical properties of the ECM influence cell-substrate adhesion and cytoskeleton formation, we consider the effect of changing ECM (collagen)

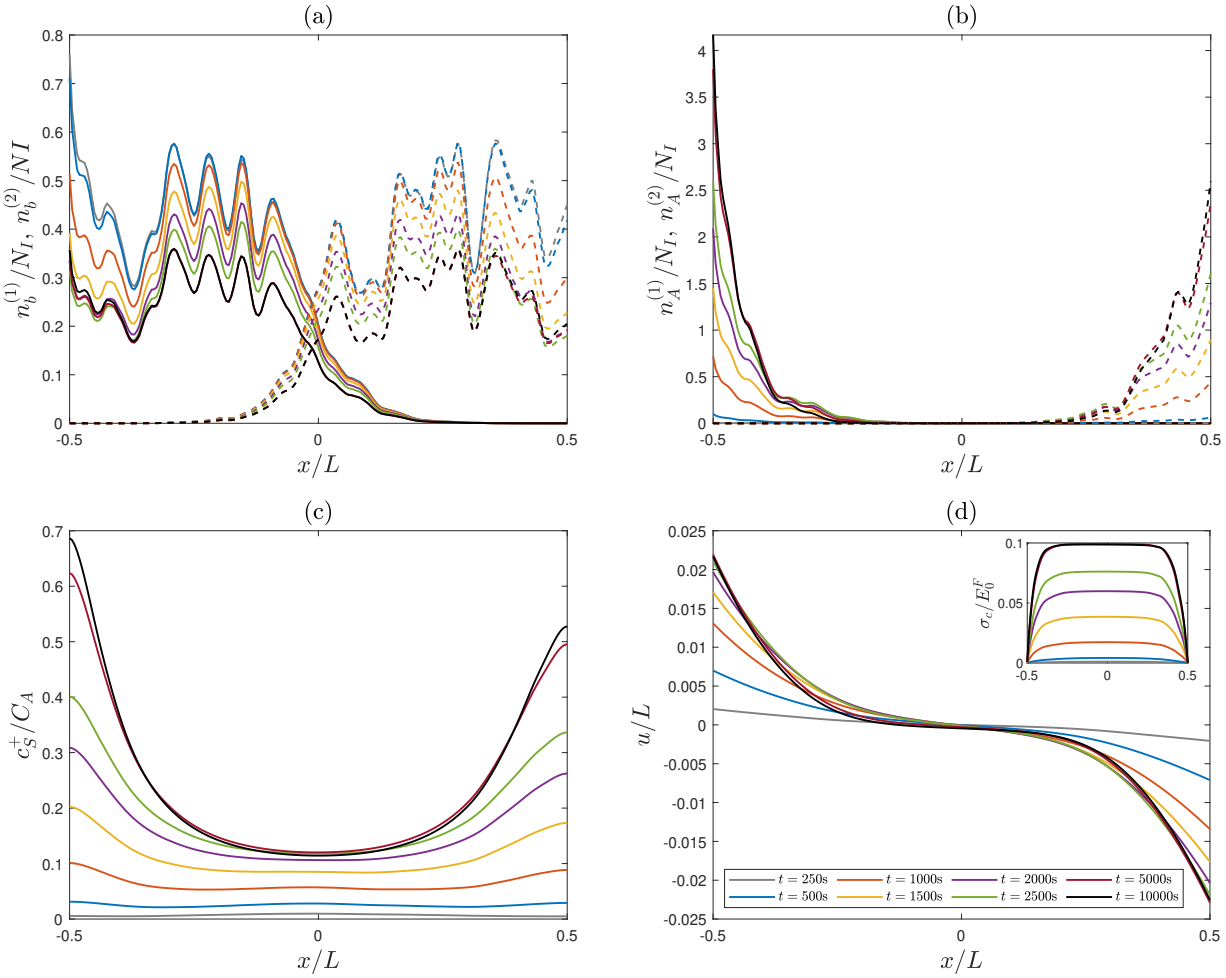

Figure 4.4: Effect of random ligand micropatterning (pattern shown in Fig. 4.2b). At snapshots in time, as a function of initial dimensionless position, dimensionless (a) density of bound integrins, (b) density of FAs, (c) concentration of SFs (left axis), (d) displacement of points in cell from their initial position. Solid lines in (a), (b) correspond to family 1 adhesions whilst dashed lines correspond to family 2 adhesions. Insets in (d) shows dimensionless stress as a function of dimensionless initial position.

stiffness. In theory the model can also be applied to demonstrate how increased substrate viscosity can enhance adhesion and cytoskeleton development, as observed by Cantini et al. (2020). However, we neglect such an analysis here, as predicting this behaviour in a noteworthy way requires model parameter values that are difficult to realise experimentally.

We examine the effect of increasing the stiffness of the ECM on the maturation of adhesion and development of VSFs in Fig. 4.5. Particularly, we vary the relative Young's modulus of the ECM compared to a typical Young's modulus of actin filaments (assumed to be $E_0^F = 1$ kPa) whilst holding all other parameter values constant, using the baseline parameters outlined in the Sec. 3.6. We illustrate the effect of E_0^C by plotting the partition of integrins (Fig. 4.5a) and the partition of actin (Fig. 4.5b) 10000 s after the cell has been introduced to the substrate.

We observe in Fig. 4.5(a) that the model replicates the well-established experimental result that cells cultured on stiffer substrates form more FAs (Engler et al., 2006). Consequently, more actin becomes recruited into SFs due to the positive feedback loop (consistent with Ronan et al., 2014). This effect is particularly pronounced as the Young's modulus becomes comparable to a typical value in the cell cytoplasm. As the Young's modulus increases (and becomes comparable to a typical value in the cell cytoplasm, i.e. when $E_0^C/E_0^F \approx 1$) the density of integrins recruited into FAs is increased (Fig. 4.5a). Furthermore, more actin is recruited into SFs (Fig. 4.5b), consistent with an increase in ROCK activation and intracellular signaling (inset in Fig. 4.5a). The model elucidates the underlying mechanism: on more compliant substrates the ECM deforms in tandem with the cell and so these integrins remain largely unstretched (inset in Fig. 4.5b). However, as the substrate becomes stiffer, bound integrins become more stretched (inset in Fig. 4.5b), exposing VBSs, allowing maturation of bound integrins into FAs (Hirata et al., 2014a). Increased adhesion maturation precipitates increased ROCK activation (inset in Fig. 4.5a), leading to increased VSF formation, adhesion stretching and maturation and, in turn, increased signaling. Note that as ECM stiffness increases we also observe a significant increase in localisation of FAs in the cell (inset in Fig. 4.5a).

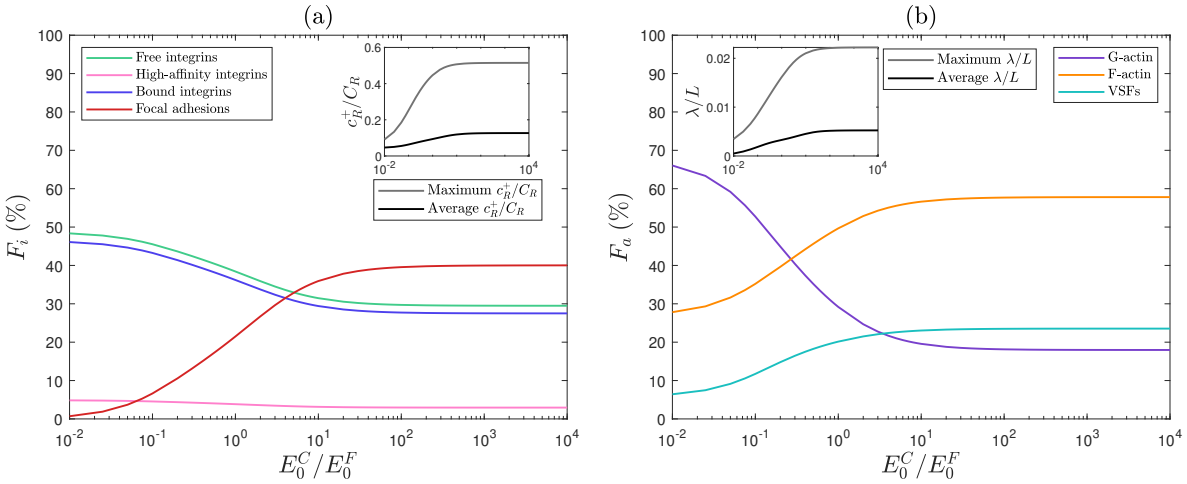

Figure 4.5: Effect of ECM stiffness on FA and VSF formation. As a function of E_0^C/E_0^F (relative ECM stiffness to that of actin filaments) at $t = 10000$ s: (a) fraction, F_i, of integrins that are free, high-affinity, bound or recruited into FAs; (b) fraction, F_a, of monomeric and filamentous actin and actin recruited into VSFs. Insets show (a) maximum (light grey) and average (black) dimensionless concentration of c_R^+ in the cell and (b) maximum (light grey) and average (black) relative dimensionless displacement of the cell to ECM.

4.4 Mechanosensing distance

Recall from Ch. 3 that we assume the displacement (and hence stress) in the ECM decays to zero in the far field, at some distance L_1 from the cell edge (see Fig. 3.1). Setting $L_1 = \alpha L$ then α defines the relative distance from the cell edge at which the zero displacement boundary condition in the ECM is applied (see Eq. 3.31c). Cells, however, rarely exist in isolation and there are continual external perturbations to the ECM to which they are adhered, applied by a range of stimuli (e.g. remodelling by other cells). To investigate how far away cells can sense these stimuli in their microenvironment, we introduce a prescribed displacement (i.e. displacement changes resulting from a prescribed forcing) at the far field edge of the ECM. In particular, using the notation developed in Ch. 3, the dimensionless displacement of the ECM in the far field to the left and right of the cell (i.e. in regions 1 and 2 respectively) is given by

$$\bar{w}_1(x,t) = \left(1 - \frac{1}{\alpha}\left(x + \alpha + \frac{1}{2}\right)\right) w_{a,1}(t) + \frac{1}{\alpha}\left(x + \alpha + \frac{1}{2}\right) w_0(t), \tag{4.1a}$$

$$\bar{w}_2(x,t) = \left(1 + \frac{1}{\alpha}\left(x - \frac{1}{2} - \alpha\right)\right) w_{a,2}(t) + \frac{1}{\alpha}\left(\alpha + \frac{1}{2} - x\right) w_N(t), \tag{4.1b}$$

where $w_{a,1}$, $w_{a,2}$ are the time-dependent applied dimensionless displacements of the ECM at $x = -1/2 - \alpha$ and $x = 1/2 + \alpha$ respectively. Recall also from Eq. (3.41) that $w_0(t)$ and $w_N(t)$ are the numerically calculated dimensionless displacements in the ECM at the boundary between region 1 and region 3 and region 2 and region 3 respectively. Note that Eq. (4.1) is consistent with Eq. (3.41) in Ch. 3, in which there is no applied displacement in the ECM far field and so $w_{a,1}(t) = w_{a,2}(t) = 0$.

In order to investigate the sensitivity of the cell to its microenvironment we introduce simple perturbations to the ECM far field. In a similar manner to our baseline case outlined in Sec. 3.8, we introduce the cell to a stiff collagen substrate. We allow sufficient time to pass to allow the cell to become well adhered to the ECM. Then, t_p seconds after the cell has been introduced to the substrate, we introduce the following (dimensionless) perturbations to the ECM far field, namely

$$\begin{aligned} w_{a,1}(t) &= \begin{cases} 0, & t < t_p \\ -\gamma\left(t - t_p\right)/t_d, & t_p \le t \le t_p + t_d \\ -\gamma, & t_p + t_d < t \le t_s \end{cases}, \\ w_{a,2}(t) &= \begin{cases} 0, & t < t_p \\ \gamma\left(t - t_p\right)/t_d, & t_p \le t \le t_p + t_d \\ \gamma, & t_p + t_d < t \le t_s \end{cases} \end{aligned} \tag{4.2}$$

i.e. we introduce linearly increasing deformation in the ECM far field at time t_p for t_d seconds until deformation reaches a maximum dimensionless deformation of γ. After t_d seconds from the initial perturbation, we maintain the deformation, holding the ECM far field in this new configuration until simulations are ended at time t_s. This displacement could mimic, for example, sustained deformation of the ECM due to contraction of a nearby cell. In our subsequent analysis, we set $\gamma = 0.01$ (which corresponds to a dimensionless displacement of $0.25\,\mu$m, 1% of the initial length of the cell and on the order of the length of contraction of the cell) and set $t_p = 5000$ s, $t_d = 100$ s and $t_s = 10000$ s.

To demonstrate the effect of the applied perturbation we present a baseline case in Fig. 4.6. Setting $\alpha = 0.5$ (i.e. perturbing the ECM at a distance of one half the cell length from the cell edge), we illustrate the global dynamics of the cell. Particularly, as a function of time, we plot in Fig. 4.6(a) the partition of integrins into their various forms (free, high-affinity, bound and recruited into FAs) and in Fig. 4.6(b) the partition of actin (into monomers, filamentous or recruited into SFs). We highlight the key times $t = t_p$ ($t = t_s$) using blue (orange) open circles.

We observe that, in response to the applied perturbation described in Eq. (4.2), there is an increase in FA formation (Fig. 4.6a) owing to increased stretching (and subsequent maturation) of cell-substrate adhesions. In response, there is a modest increase in ROCK signaling and phosphorylation of its downstream effectors, leading to enhanced actin filament formation Fig. 4.6(b). There is, however, little further increase in VSF formation as a large proportion of myosin II has already been recruited into VSFs. This analysis suggests that mechanosensing at a distance occurs primarily through cell-substrate adhesions (in well-adhered cells). However, mechanosensing through the cytoskeleton may be an important feature of less well-adhered cells (e.g. those cultured on more compliant substrates), where maturation of adhesions could facilitate increased VSF formation.

We investigate the mechanosensing distance of the cell by varying the dimensionless parameter α (the ratio of the length L_1 of regions 1 and 3 of the ECM to the length of the cell L). In particular, we consider the range $0 < \alpha \leq 5$ whilst fixing all other parameters to their baseline values (as outlined in Sec. 3.6). Introducing the perturbation described by Eq. (4.2), we consider the global measure of the partition of integrins (Fig. 4.7a) and the partition of actin (Fig. 4.7b) 10000 s after the cell has been introduced to the substrate (5000 s after the initial applied displacement). Indicated with dashed lines in Fig. 4.7 are the partition of integrins and actin in the absence of far field ECM deformation (from the baseline output discussed in Sec. 3.8). Compared with the scenario where no displacement is applied in the ECM far field, for all α there is an increase in FA, actin filament and VSF formation at the expense of the density of free, high-affinity and bound integrins and actin monomer concentration. This is due to increased stretch of cell-substrate adhesions (inset in Fig. 4.7b), leading to increased ROCK activation (inset in Fig. 4.7a). However,

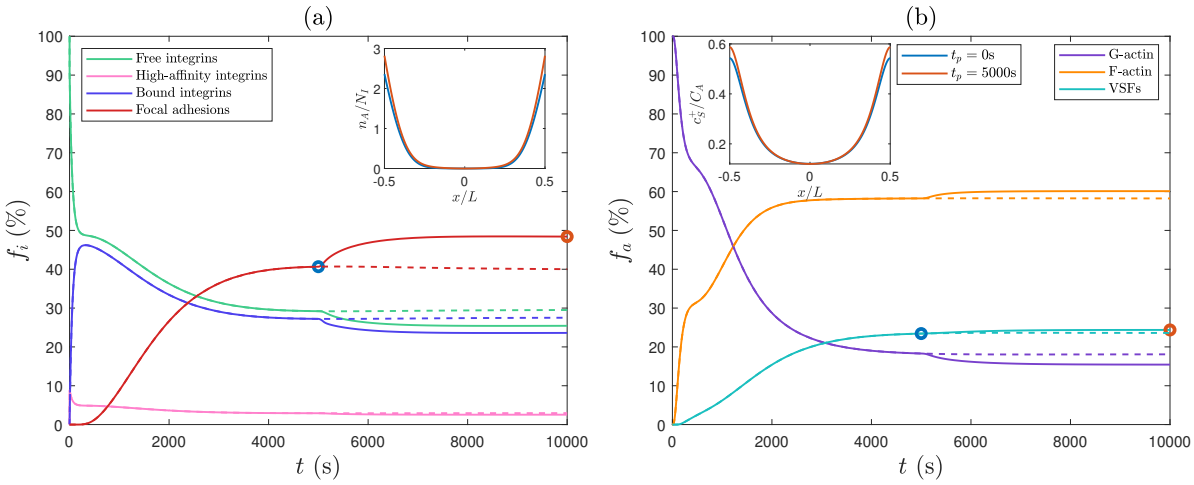

Figure 4.6: Investigating the mechanosensing distance of the cell. Effect of applied displacement in the ECM at a dimensionless distance of $\alpha = 0.5$ from the cell. Time-dependent evolution of percentage of total: (a) integrins in their various forms (free low-affinity integrins, high-affinity integrins, bound integrins and recruited into FAs), (b) actin in its different forms (monomeric, polymerised into filaments or recruited into SFs). Dashed lines indicate adhesion and cytoskeleton dynamics in the absence of a perturbation. Insets show (a) enhanced FA localisation, (b) enhanced SF localisation in response to perturbations.

this effect becomes more muted with increasing α and is negligible beyond $\alpha \gtrsim 4$. This suggests that well-adhered cells can sense mechanical changes in their environment several cell lengths away. Our observations are consistent with existing experimental data (Merkel et al., 2007) and modelling studies, particularly the demonstration by He et al. (2014) that both displacement and stress in the substrate decay exponentially with distance, with a characteristic decay length on the order of the cell radius (Chen et al., 2015). Additionally, it has been reported by Ruimerman et al. (2005) that bone cells have a mechanosensing distance of approximately 100 μm, in agreement with our predictions for hMSCs (which can subsequently differentiate into bone cells).

We also demonstrate (not shown) using this modelling approach that the mechanosensing length is generally independent of substrate stiffnesses (for typical ECM stiffnesses), and that larger perturbations to the ECM lead to a stronger cell response. Of-course, the model could also be adapted, through modification of Eq. (4.2), to consider the influence of transient perturbations to the ECM (where the far field displacement in the ECM is relaxed at some time $t_p + t_d < t_r < t_s$).

It is important to note that, because of the linear decay in the ECM far field in this one-dimensional model, this approach is unable to fully capture stress decay in the ECM. In reality, and as described in Ch. 5, displacements in the ECM decay exponentially away from the cell. Nonetheless, this work demonstrates proof of concept, and is readily adaptable to test perturbations in higher dimensions. Moreover, this analysis justifies our

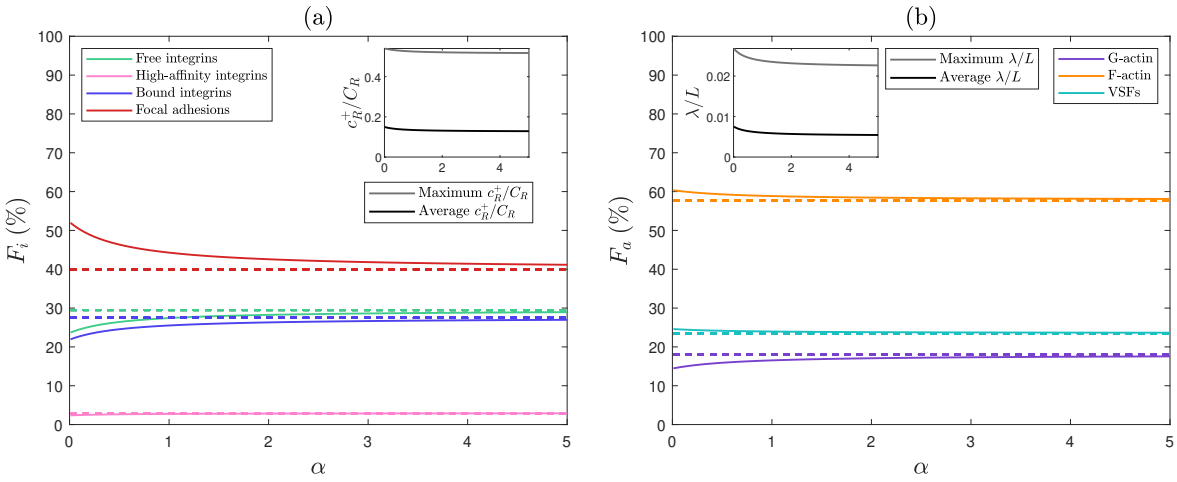

Figure 4.7: Effect of distance from cell at which perturbations are applied to the ECM. As a function of dimensionless distance α, at $t = 10000$ s (5000 s after the ECM perturbation has been applied): (a) fraction, F_i, of integrins that are free, high-affinity, bound or recruited into FAs; (b) fraction, F_a, of monomeric and filamentous actin and actin recruited into VSFs. Insets show (a) maximum (light grey) and average (black) dimensionless concentration of c_R^+ in the cell and (b) maximum (light grey) and average (black) relative dimensionless displacement of the cell to ECM. Dashed lines indicate observed partition of integrins and actin when no perturbations are applied.

boundary condition of zero displacement in the ECM far field, provided α is sufficiently large.

4.5 Introduction of external forces

To demonstrate potential application of the model to optimise experimental protocols, in this Section we examine the influence of applied body forces (e.g. mimicking atomic force microscopy, applied shear stress or magnetic tweezers in this one-dimensional framework) on the development of cell cytoskeleton and cell-substrate adhesions. For example, this has applications in atomic force microscopy, used to probe the mechanical properties of cells, where it is desirable to suppress the influence of the force on adhesion dynamics to ensure more accurate measurement of cell properties. In a similar manner to Sec. 4.5, we introduce the cell to a stiff collagen ECM and allow the cell to become well adhered to the substrate. After t_p seconds we apply an external body force to the cell. Particularly, the stress inside the cell (which is given by Eq. 3.19c in the absence of an applied stress) satisfies

$$\sigma_c = \left(\mu_c \frac{\partial^2}{\partial x \partial t} + E_c \frac{\partial}{\partial x}\right) u + \tau + \sigma_a, \tag{4.3}$$

where σ_a is the applied stress (a body force). In all simulations we describe the applied stress by

$$\sigma_a(x,t) = \begin{cases} 0, & t < t_p \\ F_a(x)/S, & t_p \leq t \leq t_s \end{cases}, \tag{4.4}$$

where $S = HW$ is the cross-sectional area of the cell and F_a is the applied force. In particular, we introduce an instantaneous increase in the cell stress at time t_p which is then maintained until the end of simulations at time t_s. In our subsequent study, we consider $t_p = 5000$ s and $t_s = 10000$ s. In experiments, the active force will be a near point-force (due to the small spatial extent of the probe), which should modelled using a Dirac delta function. However, to ensure stress is continuous in the cell, in dimensional variables we assume that the applied force takes the following form

$$F_a(x) = \frac{F_{max}}{\sqrt{2\pi\epsilon^2}} e^{-(x-x_a)^2/2\epsilon^2 L}, \tag{4.5}$$

an approximation of the Dirac delta function, where the force is applied at the position x_a, ϵ is a (small) smoothing parameter and F_{max} is the applied force. In subsequent simulations we set $F_{max} = 10$ nN and $\epsilon = 0.02$.

To demonstrate the effect of an applied force, we present an example case in Fig. 4.8. Setting $x_a/L = 0.25$ (i.e. applying a force to the cell at the midpoint between the cell centre and boundary), we illustrate the global dynamics of the cell. Particularly, as a function of time, we plot in Fig. 4.8(a) the partition of integrins into their various forms (free, high-affinity, bound and recruited into FAs) and in Fig. 4.8(b) the partition of actin (into monomers, filamentous or recruited into SFs). We highlight the key time $t = t_p$ ($t = t_s$) using blue (orange) open circles. In Fig. 4.8(c) we illustrate the effect the applied force has on FA and SF localisation and present in Fig. 4.8(d) how it influences the displacement and stress in the cytoplasm. We observe that, in response to the application of force (which is indicated in Fig. 4.8d), there is a modest increase in the density of FAs (Fig. 4.8a), owing to the forced stretching of bound integrins (Fig. 4.8d) and their subsequent maturation. Consequently, there is a small increase in actin filament formation (Fig. 4.8b), but only negligible increase in VSF formation, as myosin II has largely already been recruited into VSFs (i.e. myosin II availability is a limiting factor). However, application of force to a cell that is not already well-adhered to its substrate will likely lead a significant increase in VSF formation. We observe that the application of force does not dramatically influence the profile of FAs and SFs within the cell (Fig. 4.8c). However, local to the region where force is applied, FA profiles resemble cell displacement profiles (Fig. 4.8d), reflecting the dependence of adhesion maturation on adhesion stretch (see Eq. 3.51).

Using this modelling approach, we also demonstrate that the location at which external forces are applied can influence the impact forcing has on cytoskeleton and adhesion

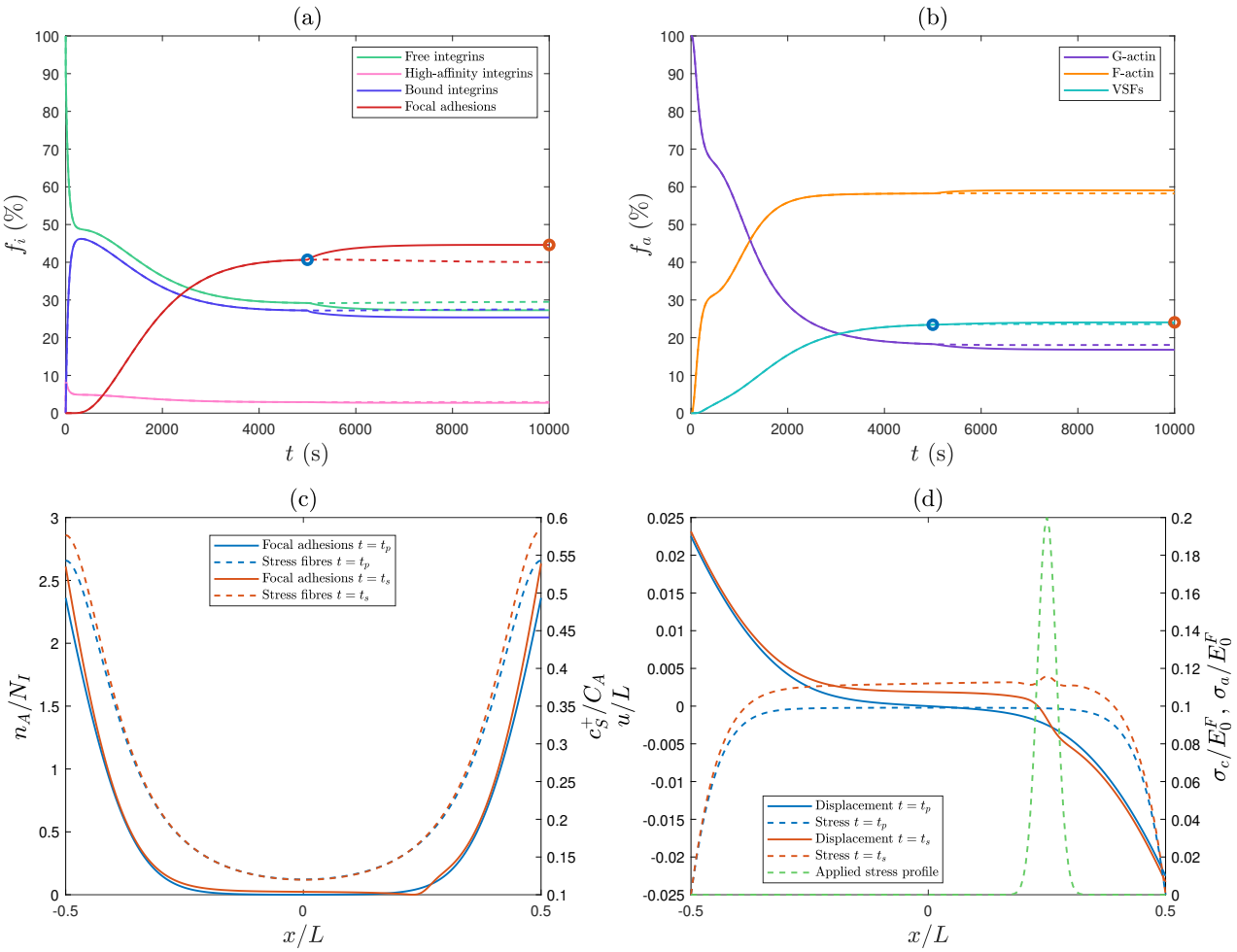

Figure 4.8: The effect of an imposed force on the cell. Time-dependent evolution of percentage of total: (a) integrins in their various forms (free low-affinity integrins, high-affinity integrins, bound integrins and recruited into FAs), (b) actin in its different forms (monomeric, polymerised into filaments or recruited into SFs). Dashed lines in (a), (b) indicate adhesion and cytoskeleton dynamics in the absence of a perturbation. Panel (c) shows the changes to FA (solid lines) and SF (dashed lines) localisation. Panel (d) indicates the displacement of the cell in response to forcing (solid lines) and associated change in stress (dashed lines), the green dashed line indicates the applied stress to the cell.

dynamics. Particularly, fixing all other parameters to their baseline values outlined in Sec. 3.6 or above, we apply the stress described in Eq. (4.4) and consider the partition of integrins (Fig. 4.9a) and the partition of actin (Fig. 4.9b) 10000 s after the cell has been introduced to the substrate (5000 s after the initial applied displacement), varying the dimensionless position at which the force is applied with $0 \leq x_a/L \leq 0.5$. We indicate with dashed lines in Fig. 4.9 the partition of integrins and actin in the absence of an applied force (using the baseline output presented in Sec. 3.8). We observe that the application of external stresses near the cell boundary has a negligible effect on adhesion and cytoskeleton dynamics. However, moving away from the cell centre, the application of

force can precipitate an increase in FA density (Fig. 4.9a) and actin filament concentration (Fig. 4.9b). This is because cell-substrate adhesions in these regions (in the absence of force) are generally immature and so comparatively weak. Hence, bound integrins away from the cell boundary can become stretched (inset in Fig. 4.9b), leading to a modest increase in adhesion maturation (Fig. 4.9a). This effect again becomes more muted towards the cell centre, where the stiff nucleus dominates mechanics and resists deformation.

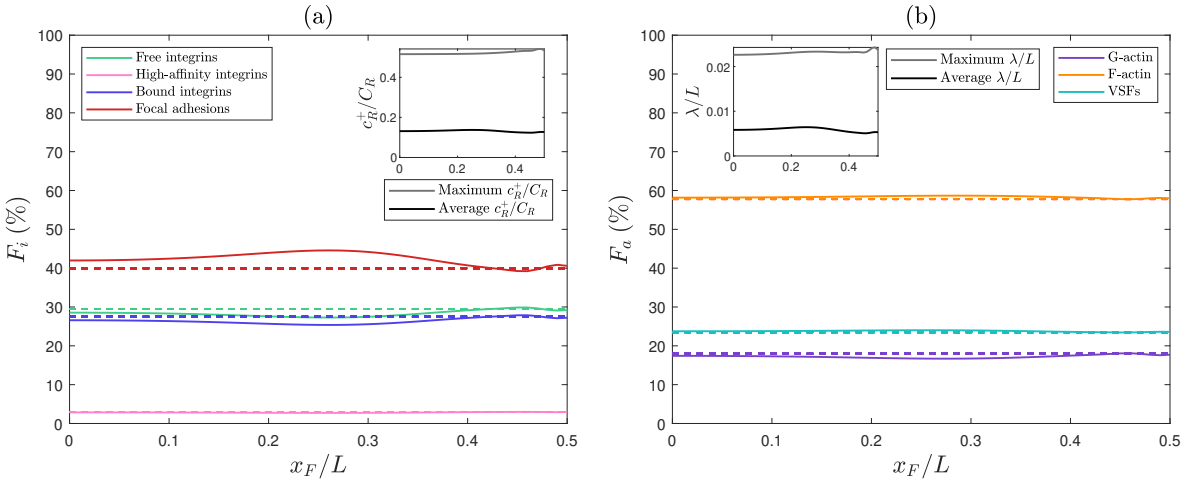

Figure 4.9: Effect of changing the position at which an external force is applied. As a function of dimensionless initial position, at $t = 10000$ s (5000 s after the ECM perturbation has been applied): (a) fraction, F_i, of integrins that are free, high-affinity, bound or recruited into FAs; (b) fraction, F_a, of monomeric and filamentous actin and actin recruited into VSFs. Insets show (a) maximum (light grey) and average (black) dimensionless concentration of c_R^+ in the cell and (b) maximum (light grey) and average (black) relative dimensionless displacement of the cell to ECM. Dashed lines indicate observed partition of integrins and actin when no perturbations are applied. Dashed lines indicate observed partition of integrins and actin when no partitions are applied.

It follows that this model serves as a platform to investigate the effect of applied forces on the development and sustainability of cell-substrate adhesions and VSFs. Particularly, the model can be employed to explore how the magnitude and direction of the force, the position at which it is applied and the stage of cell-substrate adhesion at which it is introduced can be optimised to induce (or prevent) increased adhesion and cytoskeleton development.

4.6 Inhibition of ROCK and its effectors

The development of cell cytoskeleton and mature cell-substrate adhesions is highly interdependent. In particular, signaling through ROCK, which is enhanced by adhesion maturation, is required to lead to significant actin polymerisation, myosin II activation and, consequently, the formation of VSFs. Ventral SFs, in turn, exert contractile forces

inside the cell, causing stretching of bound integrins (when the cell is cultured on a stiff ECM), leading to adhesion maturation through recruitment of vinculin. Therefore, disruption of any one component of this feedback loop can lead to several downstream effects. We focus in this Section on the effect of inhibiting ROCK activation and of inhibiting myosin II cross-linking of actin filaments. A similar analysis was performed using our spatially-averaged model in Sec. 2.6.5 to investigate the influence of a ROCK inhibitor only. Of-course, our analysis could be extended to consider inhibition of any scaffolding or signaling protein species (e.g. inhibition of the ability of talin to activate integrins), but our aim here is to illustrate the ability of the model to investigate these dynamics.

Inhibitors can influence reaction kinetics in a variety of ways, we focus on competitive and allosteric inhibitors. Competitive inhibitors act by competing with a substrate for a binding site on a catalyst; when occupying this site, the inhibitor blocks the catalyst from binding to the substrate. Allosteric inhibitors instead act by binding to the catalyst at a different location to the substrate binding site, where they induce a conformational change in the catalyst, reducing the ability of the substrate to bind to the catalyst (Monod et al., 1965). Allosteric inhibitors do still allow for the possibility of the substrate binding to the catalyst (-inhibitor complex), though this will occur at a significantly reduced rate. However, for simplicity, we assume that allosteric inhibitors are potent and, when bound to a catalyst, fully prevent the catalyst from binding to a substrate. Under this assumption, allosteric inhibitors do not need a distinct mathematical treatment from competitive inhibitors.

To illustrate the general approach taken throughout this Section we consider a competitive inhibitor I, with concentration c_i, which can bind to E, an enzyme with concentration c_e, forming a complex C, with concentration c_c. When the enzyme is not bound to an inhibitor it can facilitate the conversion of a substrate S, with concentration c_s, to form a product P, with concentration c_p. It follows that the concentration of each of these species can be described by

$$\frac{\partial c_s}{\partial t} = f_s + D_s \frac{\partial^2 c_s}{\partial x^2}, \tag{4.6a}$$

$$\frac{\partial c_p}{\partial t} = f_p + D_p \frac{\partial^2 c_p}{\partial x^2}, \tag{4.6b}$$

$$\frac{\partial c_i}{\partial t} = p(x,t) - k_i^+ c_i c_e + k_i^- c_c + D_i \frac{\partial^2 c_i}{\partial x^2}, \tag{4.6c}$$

$$\frac{\partial c_e}{\partial t} = f_e - k_i^+ c_e c_s + k_i^- c_c + D_e \frac{\partial^2 c_e}{\partial x^2}, \tag{4.6d}$$

$$\frac{\partial c_c}{\partial t} = k_i^+ c_i c_e - k_i^- c_c + D_c \frac{\partial^2 c_c}{\partial x^2}, \tag{4.6e}$$

where f_s, f_p and f_e capture reaction terms involving the conversion of substrate to product, $p(x,t)$ is a source term capturing the introduction of inhibitor (e.g. by injection into the

cell), k_i^+ is proportional to the binding rate of the inhibitor to the enzyme, k_i^- is the rate at which (enzyme-inhibitor) complexes dissociate and where D_s, D_p, D_i, D_e and D_c are the diffusivities of the substrate, product, inhibitor, enzyme and complexes respectively.

We now illustrate the ability of the model developed in Ch. 3 to explore the effect of ROCK inhibition (Sec. 4.6.1) and of myosin II inhibition (Sec. 4.6.2) on the stability of cell-substrate adhesions and cell cytoskeleton.

4.6.1 ROCK inhibition

ROCK is critical to the cell feedback loop, it is activated in response to adhesion formation and this activation is significantly enhanced by adhesion maturation (see Eq. 3.49 in Ch. 3). Inhibitors of ROCK have a demonstrated clinical application in statins (to lower cholesterol and improve cardiovascular health) and have been identified as a potential treatment for erectile dysfunction, high blood pressure and glaucoma (Bivalacqua et al., 2004, Honjo et al., 2001, Liao et al., 2007). Understanding the mechanism by which these inhibitors influence cell cytoskeleton and adhesion viability and, consequently, intracellular signaling is therefore highly relevant. To investigate the effect of ROCK inhibition we take a general approach, rather than focusing on specific inhibitors (e.g. the allosteric inhibitor Y-27623 or competitive inhibitor fasudil), using lumped parameters to illustrate the potential applicability of our modelling approach more widely (Amano et al., 2010).

We suppose that inactivated ROCK, concentration c_R, becomes activated at rate k_R^+ to form activated ROCK, concentration c_R^+. As discussed in Ch. 3 (see Eqs. 3.30a-3.30b), we assume ROCK in both its inactivated and activated forms is non-diffusive. Inactivated ROCK can be prevented from being activated if bound to an inhibitor (either competitive or a potent allosteric), which has concentration c_I. Binding of inactivated ROCK to the inhibitor occurs at a rate proportional to k_{IR}^+, leading to the formation of ROCK-inhibitor complexes which have concentration c_{IR}. ROCK bound to an inhibitor cannot be activated, but ROCK-inhibitor complexes can dissociate at rate k_{IR}^-. We assume that the inhibitor can diffuse with diffusivity D_I. Moreover, inhibitor-ROCK complexes can theoretically diffuse, with diffusivity D_{IR}. However, given that we assume ROCK is non-diffusive, we set $D_{IR} = 0$ μm^2 s^{-1}. We also include a source term, p, capturing the introduction of the ROCK inhibitor to the cell. Hence, since we neglect diffusion of ROCK-inhibitor complexes, the dynamics of ROCK, the inhibitor and ROCK-inhibitor complexes can be described by

$$\frac{\partial c_R}{\partial t} = -k_R^+ c_R + k_R^- c_R^+ - k_{IR}^+ c_I c_R + k_{IR}^- c_{IR}, \tag{4.7a}$$

$$\frac{\partial c_I}{\partial t} = p(x,t) - k_{IR}^+ c_I c_R + k_{IR}^- c_{IR} + D_I \frac{\partial^2 c_I}{\partial x^2}, \tag{4.7b}$$

$$\frac{\partial c_{IR}}{\partial t} = k_{IR}^{+} c_I c_R - k_{IR}^{-} c_{IR}. \tag{4.7c}$$

In all simulations k_R^+ and k_R^- are defined by their baseline parameters in Sec. 3.6 in Ch. 3. Additionally, we set $D_I = 10\ \mu\text{m}^2\,\text{s}^{-1}$, $k_I^- = 1 \times 10^{-3}\,\text{s}^{-1}$ and set the source term to be

$$p(x,t) = \begin{cases} 0, & t < t_p,\ t_p < t < t_s \\ p_I, & t = t_p \end{cases}, \tag{4.8}$$

where $p_I = M_I/V$, with M_I the total mass of inhibitor introduced and V the volume of the cell. In particular, we assume the inhibitor is instantaneously introduced (at $t = t_p$) spatially uniformly to the cell. In all simulations we set $t_p = 5000$ s and $M_I = 100$ nM, with V given by its baseline value from Sec. 3.6. We end simulations at $t = t_s = 10000$ s. We vary the value of k_{IR}^+ as this essentially dictates the potency of the inhibitor.

To demonstrate the effect that the introduction of a ROCK inhibitor has on the dynamics of cell-substrate adhesions, we consider various global measures of the cell in Fig. 4.10. Particularly, setting $k_{IR}^+ = 200\,\mu\text{M}^{-1}\,\text{s}^{-1}$, in Fig. 4.10(a) we illustrate as a function of time the partition of integrins into their various forms (free, high-affinity, bound and recruited into FAs), and in Fig. 4.10(b) the partition of actin (into monomers, filamentous or recruited into SFs). We highlight $t = t_p$ ($t = t_s$) using blue (orange) open circles. As would be expected, the introduction of a ROCK inhibitor (inset in Fig. 4.10a) leads to rapid dissociation of SFs (Fig. 4.10b) owing to the reduction in actin polymerisation and myosin II activation. After some time, there is a transient increase in actin filament concentration (Fig. 4.10b) as some actin continues to be polymerised but cannot be cross-linked by myosin II to form VSFs, before the actin filament concentration continues to fall. As SFs dissociate and the contractile forces exerted on the cell reduce, there is an increase in cell length (inset in Fig. 4.10b). In turn, bound integrins and integrins recruited into FAs experience a reduction in their stretch. Over time, this manifests itself as a reduction in FA density (Fig. 4.10a), leading to reduced ROCK signaling (inset in Fig. 4.10a) and hence further reduced VSF and actin filament concentration. For a sufficiently potent inhibitor, such as this, the cell eventually returns to its early state, with many immature adhesions to the substrate (Fig. 4.10a) but little cytoskeleton development (Fig. 4.10b), negligible deformation (inset in Fig. 4.10b) and negligible adhesion maturation (Fig. 4.10a).

To investigate how the potency of the ROCK inhibitor influences cytoskeleton and adhesion dynamics we vary k_{IR}^+, the rate per concentration at which the inhibitor binds to inactive ROCK and prevents its activation. Particularly, we consider the range $1 \times 10^{-2}\ \mu\text{M}^{-1}\,\text{s}^{-1} < k_{IR}^+ < 1 \times 10^3\ \mu\text{M}^{-1}\,\text{s}^{-1}$ whilst fixing all other parameters to their baseline values (as outlined in Sec. 3.6 or above). We introduce the ROCK inhibitor at $t = t_p = 5000$ s after the cell has been introduced to the stiff substrate (and therefore

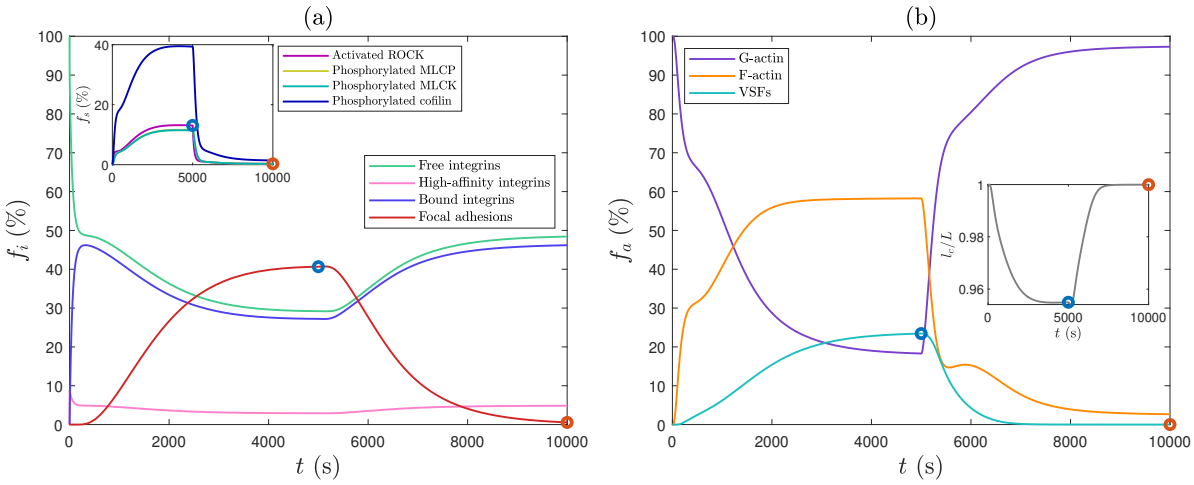

Figure 4.10: Investigating the effect of a ROCK inhibitor introduced to the cell. Time-dependent evolution of percentage of total: (a) integrins in their various forms (free low-affinity integrins, high-affinity integrins, bound integrins and recruited into FAs), (b) actin in its different forms (monomeric, polymerised into filaments or recruited into SFs). Insets show (a) fraction of ROCK activated and of its downstream effectors phosphorylated as a function of time, (b) cell length as a function of time.

is well-adhered). We plot global measures of cell-substrate adhesion and cytoskeleton development, particularly the partition of integrins (Fig. 4.11a) and the partition of actin (Fig. 4.11b) 10000 s after the cell has been introduced to the substrate (5000 s after the introduction of the inhibitor). We indicate with dashed lines in Fig. 4.11 the partition of integrins and actin in the absence of any inhibitor introduction.

We observe that for low inhibitor-ROCK binding rates, the dynamics of inactivated ROCK is dominated by its activation, leading to negligible effect on adhesion (Fig. 4.11a) and cytoskeleton (Fig. 4.11b) dynamics. When the inhibition rate of ROCK becomes sufficiently high, roughly when $k_{IR}^{+} \approx 10\,\mu\mathrm{M}^{-1}\,\mathrm{s}^{-1}$, there is a significant decrease in VSF concentration (Fig. 4.11b), leading to a decrease in cell contraction and adhesion stretch (inset in Fig. 4.11b). The reduction in adhesion stretch leads to reduced FA density (Fig. 4.11a), in turn leading to further reduced activated ROCK concentration (inset in Fig. 4.11a) and so further decreases in VSF formation (Fig. 4.11b). A reduction in actin filament concentration occurs in tandem with reduced VSF concentration with increasing k_{IR}^{+} (Fig. 4.11b). However, at moderately high rates of ROCK inhibition with $k_{IR}^{+} \approx 100\,\mu\mathrm{M}^{-1}\,\mathrm{s}^{-1}$, there is still limited actin filament formation as ROCK activation is not completely suppressed and weak signaling from bound integrins can facilitate actin polymerisation (Fig. 4.11b). Thereafter, further increases in k_{IR}^{+} leads to nearly all actin returning to its monomeric form as actin polymerisation (depolymerisation) decreases (increases).

It is worth emphasising the striking similarity to the qualitative predictions (see Figs. 2.9-2.10) made by the spatially-averaged model developed in Ch. 2. This again gives us con-

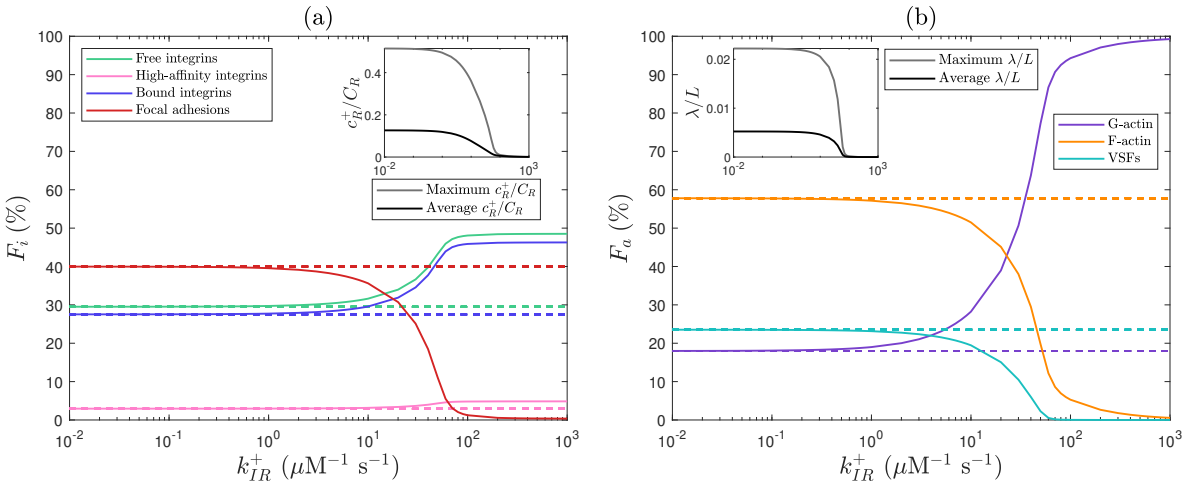

Figure 4.11: Effect of ROCK inhibitor strength. As a function of the binding rate of the ROCK inhibitor to ROCK, at $t = 10000$ s (5000 s after the ECM perturbation has been applied): (a) fraction, F_i, of integrins that are free, high-affinity, bound or recruited into FAs; (b) fraction, F_a, of monomeric and filamentous actin and actin recruited into VSFs. Insets show (a) maximum (light grey) and average (black) dimensionless concentration of c_R^+ in the cell and (b) maximum (light grey) and average (black) relative dimensionless displacement of the cell to ECM. Dashed lines indicate observed partition of integrins and actin when no perturbations are applied.

fidence that a simple ODE model can capture several important aspects of cell-substrate adhesion and cytoskeleton development.

4.6.2 Myosin inhibition

Myosin II cross-linking of actin filaments is required to form contractile VSFs, which in turn stretch cell-substrate adhesions leading to their maturation and enhanced ROCK signaling. The most commonly used myosin II inhibitor is blebbistatin, which has been previously employed to improve cell survival times *in vitro* (Kabaeva et al., 2008). This allosteric inhibitor prevents binding of activated myosin II to actin filaments, hindering its cross-linking ability to form contractile VSFs.

To model the effect of myosin II inhibition on cytoskeleton and adhesion dynamics, we consider activated myosin II, concentration c_m^+, which forms from the activation of inactive myosin II at rate k_a^+ and which can diffuse with diffusivity D_m^+ (see Eq. 3.29e). Activated myosin II can cross-link actin filaments to form VSFs at a rate proportional to k_m^+ and these VSFs dissociate at rate k_m^-. Activated myosin II can be prevented from cross-linking actin filaments if bound to an inhibitor (e.g. blebbistatin), which has concentration c_I. Binding of activated myosin II to the inhibitor occurs at rate k_{Im}^+, leading to the formation of myosin-inhibitor complexes which have concentration c_{Im}. These myosin-inhibitor complexes can dissociate at rate k_{Im}^-. We assume that the inhibitor can diffuse

with diffusivity D_I. Moreover, inhibitor-myosin complexes can diffuse, with diffusivity D_{Im}. We also include a distributed source term, p, capturing the introduction of the myosin inhibitor to the cell. Hence, the dynamics of activated myosin II, the inhibitor and myosin-inhibitor complexes can be described by

$$\frac{\partial c_m^+}{\partial t} = k_a^+ c_m - k_a^- c_m^+ - k_m^+ \left(2c_F^{(1)}c_F^{(2)} + c_F^{(1)}c_F^{(1)} + c_F^{(2)}c_F^{(2)} + c_F^{(1)}c_S^+ + c_F^{(2)}c_S^+\right) c_m^+ + k_m^- c_S^+ + k_{Im}^+ c_I c_m^+ + k_{Im}^- c_{Im} + D_m^+ \frac{\partial^2 c_m^+}{\partial x^2}, \tag{4.9a}$$

$$\frac{\partial c_I}{\partial t} = p(x,t) - k_{Im}^+ c_I c_m + k_{Im}^- c_{Im} + D_I \frac{\partial^2 c_I}{\partial x^2}, \tag{4.9b}$$

$$\frac{\partial c_{Im}}{\partial t} = k_{Im}^+ c_I c_m^+ - k_{Im}^- c_{Im} + D_{Im} \frac{\partial^2 c_{Im}}{\partial x^2}. \tag{4.9c}$$

In all simulations k_a^+, k_a^-, k_m^+, k_m^- and D_m^+ are defined by their baseline parameters in Sec. 3.6 in Ch. 3. Additionally, we set $D_I = 10\ \mu\text{m}^2\ \text{s}^{-1}$, $D_{Im} = D_m^+$, $k_I^- = 1 \times 10^{-3}\ \text{s}^{-1}$ and use an identical form of source term as for the ROCK inhibitor (i.e. identical to Eq. 4.8), except we set $M_I = 10\ \mu\text{M}$. In all simulations we set $t_p = 5000$ s, with the cell volume, V, given by its baseline value from Sec. 3.6. We end simulations at $t = t_s = 10000$ s and vary the value of k_{Im}^+, which governs the strength of the myosin inhibitor.

To examine the influence that the strength of myosin II inhibitor has on cytoskeleton and adhesion dynamics, we vary k_{Im}^+, the rate per concentration at which the inhibitor binds to activated ROCK, preventing actin cross-linking. Particularly, we set $1 \times 10^{-2}\ \mu\text{M}^{-1}\ \text{s}^{-1} < k_{Im}^+ < 1 \times 10^3\ \mu\text{M}^{-1}\ \text{s}^{-1}$ whilst fixing all other parameters to their baseline values (as outlined in Sec. 3.6) or as outlined above. At $t = t_p = 5000$ s after the cell has been introduced to the stiff substrate, at which point the cell is well-adhered, we introduce the myosin inhibitor. To illustrate the effect of this inhibitor, we again plot global measures of cell-substrate adhesion and cytoskeleton development, particularly the partition of integrins (Fig. 4.12a) and the partition of actin (Fig. 4.12b) 10000 s after the cell has been introduced to the substrate (5000 s after the introduction of the myosin inhibitor). As before, we indicate with dashed lines in Fig. 4.12 the partition of integrins and actin in the absence of any inhibitor introduction.

When the rate of binding of the inhibitor to myosin II is low, myosin II continues to cross-link actin filaments, leading to the formation of contractile VSFs (Fig. 4.12b), which, in turn, stretch cell-substrate adhesions (inset Fig. 4.12b), leading to adhesion maturation (Fig. 4.12a) and a high degree of ROCK activation (inset in Fig. 4.12a). Activated ROCK, in turn, facilitates VSF formation through increased actin filament formation and myosin II activation. As the strength of myosin II inhibitor increases (i.e. as k_{Im}^+ increases), there is a decrease in myosin II cross-linking of actin filaments, leading to a decrease in VSF formation (Fig. 4.12b), reduced adhesion stretch (inset Fig. 4.12b) and, consequently, a reduction in adhesion maturation (Fig. 4.12a). However, increasing k_{Im}^+ through interme-

diate values (approximately $1 \times 10^{-1}\ \mu\mathrm{M}^{-1}\,\mathrm{s}^{-1} < k_{Im}^{+} < 1 \times 10^{0}\ \mu\mathrm{M}^{-1}\,\mathrm{s}^{-1}$) leads to a small increase in actin filament formation (Fig. 4.12b) as actin polymerisation continues but filaments are not cross-linked by myosin II. Further increases in myosin II inhibitor strength leads to significant reductions in VSF concentration (Fig. 4.12a) and, through reduced adhesion stretch (inset in Fig. 4.12b), reduced FA maturation (Fig. 4.12b). At high values of k_{Im}^{+}, no VSFs or FAs remain some time after the application of inhibitor. However, bound integrins can still form and a substantial amount of actin remains in filamentous form (Fig. 4.12b), polymerised at bound integrins but not cross-linked by myosin II to form VSFs. Contrast this with the response of the cell to a ROCK inhibitor (Fig. 4.11), which causes a collapse in both actin filament and VSF concentration. Consequently, if the aim of an inhibitor is to prevent contraction alone and not disrupt the entire cytoskeleton, it is beneficial to employ a myosin II inhibitor.

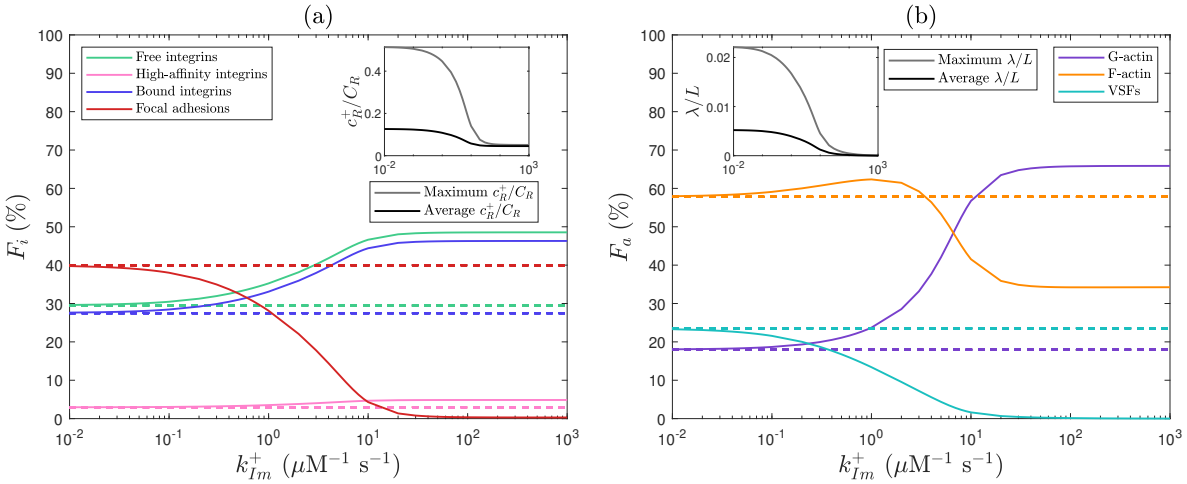

Figure 4.12: Effect of myosin inhibitor strength. As a function of the binding rate of the myosin II inhibitor to activated myosin II, at $t = 10000$ s (5000 s after the ECM perturbation has been applied): (a) fraction, F_i, of integrins that are free, high-affinity, bound or recruited into FAs; (b) fraction, F_a, of monomeric and filamentous actin and actin recruited into VSFs. Insets show (a) maximum (light grey) and average (black) dimensionless concentration of c_R^+ in the cell and (b) maximum (light grey) and average (black) relative dimensionless displacement of the cell to ECM. Dashed lines indicate observed partition of integrins and actin when no perturbations are applied.

4.7 Summary

In this Chapter we have employed our one-dimensional bio-chemo-mechanical model developed in Ch. 3 to investigate the influence of various biochemical and mechanical cues on the development and sustainability of cell-substrate adhesions and cell cytoskeleton. In particular, we have been able to predict the influence that ligand density and micropatterning has on the formation and localisation of FAs, SFs and mechanical stress inside the cell.

Moreover, the model has elucidated the mechanism by which more mature cell-substrate adhesions and contractile VSFs develop on more stiff and viscous substrates (Cantini et al., 2020, Engler et al., 2006), through increased adhesion stretch and, consequently, enhanced signaling. Allowing the cell to become well-adhered to the underlying ECM, we have also demonstrated the ability of the model to predict the sensitivity of the cell to distant mechanical perturbations in its microenvironment, identifying a mechanosensing distance on the order of several cell lengths; this agrees with existing experimental and modelling studies (Chen et al., 2015, He et al., 2014, Merkel et al., 2007, Ruimerman et al., 2005). We have also been able to demonstrate that the model can predict the influence that applied stresses (e.g. from atomic force microscopy) have on cell-substrate adhesion and cytoskeleton development, and have shown that this response can depend on the location in the cell at which forces are applied. Finally, we have illustrated how the model can be used to investigate the effect of various chemotransductive cues on cell-substrate interaction, particularly the effect of ROCK and myosin II inhibitors on adhesion and cytoskeleton viability in well-adhered cells.

Having demonstrated the ability of the model to make predictions about how the cell reacts to a variety of environmental and biochemical cues, the model now serves as a platform for several future investigations. For example, the model can be employed to investigate how simultaneous control over ECM ligand density and the mechanical properties of the ECM can be used to influence cell-substrate adhesion development. The model can also be applied to describe mechanical communication between different cells through the ECM. Moreover, further investigation would allow for application of the model to optimise experimental protocols in, for example, atomic force microscopy or magnetic and optical tweezer experiments. In particular, to address how to apply forces in such a way to instigate or suppress changes in the cytoskeletal and adhesion properties of the cell. Finally, the model provides a framework for exploring how to optimally apply inhibitors (or activators) to the cell (e.g. inhibitor strength, its target and the position within the cell and stage of cell-substrate adhesion at which the inhibitor is applied) to influence cytoskeleton and adhesion dynamics. Potential applications of this work include in providing mechanistic insight into the influence of ROCK inhibition in treatments for erectile dysfunction, high blood pressure and glaucoma (Bivalacqua et al., 2004, Honjo et al., 2001, Liao et al., 2007).

Chapter 5

Two-dimensional modelling

In this Chapter we develop a two-dimensional analogue of our one-dimensional model for the formation and maturation of cell-substrate adhesions and the cell cytoskeleton, presented and analysed in Ch. 3 (and based on the work of Besser and Schwarz, 2007, Gracheva and Othmer, 2004, Larripa and Mogilner, 2006). This two-dimensional framework allows for more complicated and realistic modelling of the cell-substrate interaction. In particular, we now incorporate a cell nucleus, which we treat as a rigid body but which could instead be treated as a stiff viscoelastic material. The formulation also explicitly includes the cell membrane, although this additional influence is not considered in our present work; similar two-dimensional axisymmetric modelling by Vernerey and Farsad (2014) of an elastic cell coupled to an elastic substrate explicitly includes a cortical membrane, which facilitates cell spreading. Our goal for this Chapter is to understand how cells adhere to a substrate and to predict whether they remain axisymmetric or develop surface patterns during this process. Our strategy is as follows: we consider the cell to be initially cylindrical and introduce it to a collagen ECM; we assume an initially axisymmetric deformation of the cell; after some time we introduce small biochemical and mechanical perturbations to this axisymmetric deformation, evolving the system in time in order to determine the stability of the cell to various normal modes of deformation. Two-dimensional axisymmetric deformation of the cell, coupled to an elastic ECM via cell-substrate adhesions, has also been considered by Banerjee and Marchetti (2013), Edwards and Schwarz (2011), He et al. (2014), Schwarz and Safran (2013). These models have taken a purely mechanical approach, in contrast with the bio-chemo-mechanical approach employed in our work. More generally, simple geometry (ellipsoidal) deformations are considered by Dunlop (2019), Friedrich and Safran (2012), to investigate the links between cellular anisotropy and contractility. By introducing perturbations to the axisymmetric state with a simple sinusoidal dependency on polar angle, a suitable ansatz reduces our governing equations to quasi-one-dimensional, parameterised by the azimuthal mode number, circumventing computational difficulty associated with two-dimensional modelling. This allows us, in a similar manner

to Ch. 3, to employ finite difference methods to solve the governing PDEs. This strategy is summarised in Fig. 5.1 and is similar to the method employed by Greenspan (1976) to investigate tumour growth. Such an analysis facilitates investigation of the ability of cells to undergo self-driven surface patterning *in vitro*; Solowiej-Wedderburn and Dunlop (2022, 2023) similarly consider two-dimensional deformations, but force changes in cell shape through adhesion patterning (in a similar manner to our work Sec. 4.2).

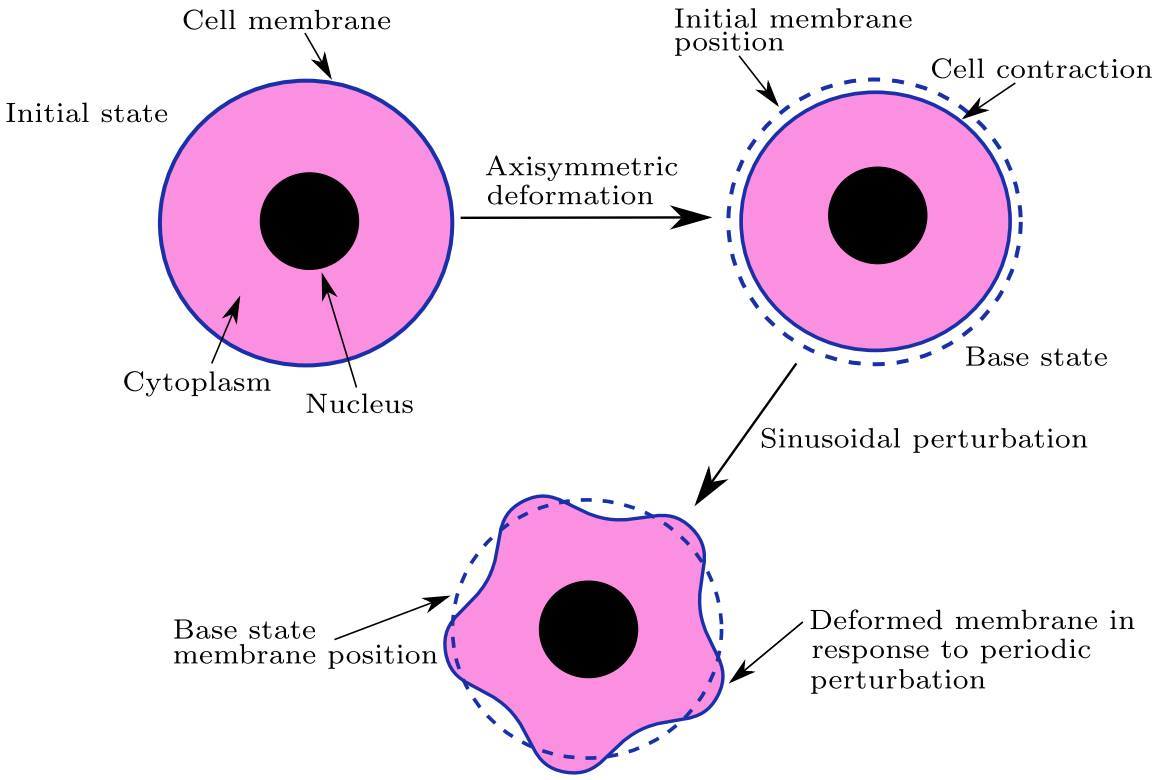

Figure 5.1: Overview of approach in two-dimensions: an initially cylindrical cell undergoes an axisymmetric deformation, settling to a steady state around which we conduct a linear stability analysis to various modes of deformation.

This Chapter is structured as follows. In Secs. 5.1-5.5 we outline the full two-dimensional problem, which has strong similarity to our work in Ch. 3, but with several important modifications. In Sec. 5.6 we solve the two-dimensional axisymmetric problem, identifying a base state around which we linearise in Sec. 5.7. In Sec. 5.8 we assume perturbations to this axisymmetric base state are sinusoidal in nature, seeking spatially periodic solutions, with a given mode number, in all quantities in order to deduce the stability of the cell to various normal modes of deformation, with results presented in Sec. 5.10. Finally, in Sec. 5.11 we interpret the predictions from this two-dimensional approach and outline potential directions for further research.

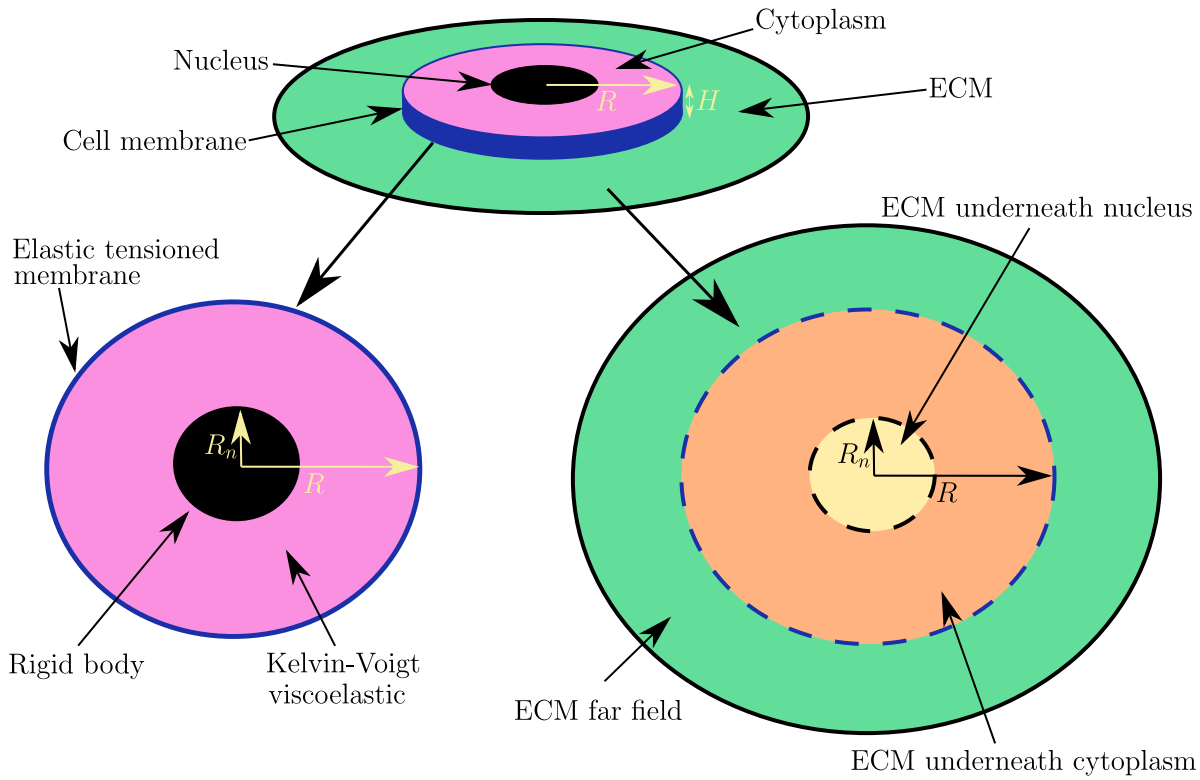

Figure 5.2: Cell and nucleus set-up in two-dimensional problem. We consider the cell to be composed of three distinct components and the ECM to have three distinct regions.

5.1 Mechanical model

As indicated in Fig. 5.2, we idealise the cell in its reference configuration as a cylinder. We treat the cell to be composed of three distinct regions: a rigid nucleus (of radius R_n) and a viscoelastic cytoplasm, encased by an elastic membrane. We assume that the initial radius of the cell is R and that its height is H (so that the total cell volume is $V = \pi R^2 H$) and suppose that the cell is thin in the direction orthogonal to the substrate, so that $H \ll R$.

We parameterise the cell using the coordinates (r, θ, z) such that the initial configuration of the cell is described by a set of material points $\boldsymbol{x}(r, \theta, z)$, with coordinates spanning $0 \leq r \leq R$, $0 \leq \theta \leq 2\pi$, $0 \leq z \leq H$. Throughout this Chapter we depth-average over the $z-$direction, neglecting variations in the biochemical and mechanical properties of the cell and ECM in the direction orthogonal to the substrate. Additionally, we assume that the cell centre remains at a fixed position and that the outer boundary of the cell is displaced to $r = \zeta(\theta, t)$, whilst the internal points are displaced to r' so that for all $t \geq 0$ we have

$$0 \leq r'(r, \theta, t) \leq r'(R, \theta, t) = \zeta(\theta, t); \tag{5.1}$$

this is analogous to our set-up in Ch. 3.

We suppose that the ECM consists of three regions, one below the cell nucleus, of radius R_n, another below the cell cytoplasm, occupying the region $R_n \leq r \leq R$ and

another region beyond the cell with $R \leq r < \infty$. This is also indicated in Fig. 5.2. We assume that the ECM is fixed in the far field and at $r = 0$, whilst internal points are displaced to $\bar{\boldsymbol{x}}'$.

The corresponding displacement of points in the cell cytoplasm, $\boldsymbol{u}(r, \theta, t)$, and in the ECM, $\boldsymbol{w}(r, \theta, t)$, are described by

$$\boldsymbol{u}(r, \theta, t) = \boldsymbol{x}'(r, \theta, t) - \boldsymbol{x}, \quad \boldsymbol{w}(r, \theta, t) = \bar{\boldsymbol{x}}'(r, \theta, t) - \boldsymbol{x}; \tag{5.2}$$

for simplicity, we assume displacements $|\boldsymbol{u}|$ and $|\boldsymbol{w}|$ are small, allowing us to use linearised constitutive laws for the cytoplasm and ECM rheology. We denote radial (azimuthal) displacements of the cell cytoplasm by u_r (u_θ) and of the ECM by w_r (w_θ) so that the displacement of points in the cell cytoplasm and ECM can be decomposed into

$$\boldsymbol{u} = u_r \boldsymbol{e}_r + u_\theta \boldsymbol{e}_\theta, \quad \boldsymbol{w} = w_r \boldsymbol{e}_r + w_\theta \boldsymbol{e}_\theta. \tag{5.3}$$

We generalise the one-dimensional discrete-to-continuum model developed in Ch. 3 and, in a similar manner, we assume that the deformation of the cell results from a combination of externally applied forces on the cell and active and passive stresses within the cell itself, with this motion resisted by friction due to repeated detachment and attachment of the cell to the substrate and restoring forces due to cell-substrate interaction. However, we can now additionally include a tensioned cell membrane, though we neglect the properties of this membrane in our subsequent analysis. Moreover, we assume that no adhesions between the cell and substrate can form underneath the cell nucleus (this is primarily for modelling simplicity, however we observe in Ch. 3 that FAs localise near the cell boundary), which is now explicitly accounted for. We neglect inertial effects and other body forces. Letting $\boldsymbol{\sigma}_c$ denote the Cauchy stress in the cell cytoplasm and $\boldsymbol{\sigma}_E$ denote the Cauchy stress in the ECM then we assume an analogous form of mechanical governing equations to Eq. (3.19a). In particular, we have

$$\nabla \cdot \boldsymbol{\sigma}_c = \kappa_I \left(\boldsymbol{u} - \boldsymbol{w}\right) + \beta_I \frac{\partial}{\partial t}\left(\boldsymbol{u} - \boldsymbol{w}\right), \quad \nabla \cdot \boldsymbol{\sigma}_E = \kappa_I \left(\boldsymbol{w} - \boldsymbol{u}\right) + \beta_I \frac{\partial}{\partial t}\left(\boldsymbol{w} - \boldsymbol{u}\right), \tag{5.4a}$$

where κ_I is the stiffness per unit volume of nascent and focal adhesions and β_I is the drag induced by such adhesions and where we neglect derivatives in the $z-$direction (through depth-averaging). We write

$$\boldsymbol{\sigma}_c = E_c(r, \theta)\boldsymbol{\epsilon}_c + \mu_c(r, \theta)\frac{\partial \boldsymbol{\epsilon}_c}{\partial t} + \boldsymbol{\tau}(r, \theta), \quad \boldsymbol{\sigma}_E = E_E(r, \theta)\boldsymbol{\epsilon}_E + \mu_E(r, \theta)\frac{\partial \boldsymbol{\epsilon}_E}{\partial t}, \tag{5.4b}$$

where E_c is the Young's modulus of the cell cytoplasm, μ_c is the effective viscosity of the cell cytoplasm (as defined in Sec. 3.1 for the one-dimensional model), $\boldsymbol{\tau}$ is a tensor

capturing the (radial) contraction of the cytoplasm due to myosin II motor action, E_E is the Young's modulus of the ECM and μ_E is the viscosity of the ECM. The infinitesimal strain tensors satisfy

$$\boldsymbol{\epsilon}_c = \frac{\partial u_r}{\partial r}\boldsymbol{e}_r \otimes \boldsymbol{e}_r + \frac{1}{r}\left(\frac{\partial u_\theta}{\partial \theta} + u_r\right)\boldsymbol{e}_\theta \otimes \boldsymbol{e}_\theta + \frac{1}{2}\left(\frac{1}{r}\frac{\partial u_r}{\partial \theta} + \frac{\partial u_\theta}{\partial r} - \frac{u_\theta}{r}\right)(\boldsymbol{e}_r \otimes \boldsymbol{e}_\theta + \boldsymbol{e}_\theta \otimes \boldsymbol{e}_r), \tag{5.4c}$$

$$\boldsymbol{\epsilon}_E = \frac{\partial w_r}{\partial r}\boldsymbol{e}_r \otimes \boldsymbol{e}_r + \frac{1}{r}\left(\frac{\partial w_\theta}{\partial \theta} + w_r\right)\boldsymbol{e}_\theta \otimes \boldsymbol{e}_\theta + \frac{1}{2}\left(\frac{1}{r}\frac{\partial w_r}{\partial \theta} + \frac{\partial w_\theta}{\partial r} - \frac{w_\theta}{r}\right)(\boldsymbol{e}_r \otimes \boldsymbol{e}_\theta + \boldsymbol{e}_\theta \otimes \boldsymbol{e}_r). \tag{5.4d}$$

We assume the contractile action of VSFs is purely radial so that it can described by

$$\boldsymbol{\tau} = \tau \boldsymbol{e}_r \otimes \boldsymbol{e}_r, \tag{5.4e}$$

where τ is a scalar function that depends on the concentration of VSFs.

In a similar manner to Ch. 3, we suppose that the Young's modulus and viscosity of the cell cytoplasm and the Young's modulus of the ECM can be decomposed as follows

$$E_c = E_F + E_S + E_P, \quad \mu_c = \mu_0 + \tau/v_0, \quad E_E = E_C + E_O, \tag{5.5}$$

where E_F is the contribution to the Young's modulus of the cytoplasm due to actin filaments, E_S is the contribution to the Young's modulus of the cytoplasm due to VSFs and E_P is the contribution to the Young's modulus of the cytoplasm due to microtubules and intermediate filaments. Moreover, μ_0 is the viscosity of the cell cytoplasm, v_0 is the stall speed of myosin II motor action, as defined in Sec. 3.1.1, and so μ_c is the effective viscosity of the cell cytoplasm. Furthermore, E_C is the contribution to the Young's modulus of the ECM due to collagen fibres and E_O is the contribution to the Young's modulus of the ECM due to other fibres (e.g. fibronectin). We also decompose the restoring forces exerted by connections between the cell and substrate, κ_I, and the drag due to cell-substrate adhesions and interaction, β_I, into their constituent contributions with

$$\kappa_I = \kappa_{NA} + \kappa_{FA}, \quad \beta_I = \beta_e + \beta_{NA} + \beta_{FA}, \tag{5.6}$$

where β_e is a (small) uniform background drag whilst β_{NA} (κ_{NA}) and β_{FA} (κ_{FA}) are the drag (restoring forces) associated with nascent and focal adhesions, which are specified in terms of the adhesion densities below.

5.2 Biochemical model

In two-dimensions our governing biochemical equations are similar to their one-dimensional analogue outlined in Sec. 3.2. All quantities are defined analogously to those in Sec. 3.2, with the exception of the actin treadmilling velocity, which is now denoted by $\boldsymbol{v}(r,\theta,t)$. However, the presence of the cell nucleus, and the assumption that actin filaments cannot grow into this structure, leads to a natural simplification in our biochemistry in that we do not need to consider two separate families of ligands, adhesions and actin filaments. Hence, there is some modification to our governing PDEs.

We describe actin and myosin dynamics, by analogue with Eqs. (3.29a)-(3.29e) in Ch. 3, in the form

$$\frac{\partial c_G}{\partial t} = -k_p^+ c_G\left(n_b + n_A\right) + k_p^- c_F + k_m^- c_S^+ + D_G\nabla^2 c_G, \tag{5.7a}$$

$$\frac{\partial c_F}{\partial t} + \nabla\cdot(\boldsymbol{v}c) = k_p^+\left(n_b + n_A\right) - k_p^- c_F - k_m^+ c_F c_m^+\left(c_F + c_S^+\right) + D_F\nabla^2 c_F, \tag{5.7b}$$

$$\frac{\partial c_S^+}{\partial t} = k_m^+ c_F c_m^+\left(c_F + c_S^+\right) - k_m^+ c_S^+, \tag{5.7c}$$

$$\frac{\partial c_m}{\partial t} = -k_a^+ c_m + k_a^- c_m^+ + D_m\nabla^2 c_m, \tag{5.7d}$$

$$\frac{\partial c_m^+}{\partial t} = k_a^+ c_m - k_a^- c_m^+ - k_m^+ c_F c_m^+\left(c_F + c_S^+\right) + k_m^- c_S^+ + D_m^+\nabla^2 c_m^+. \tag{5.7e}$$

This system of reaction-diffusion-advection equations captures the polymerisation of actin monomers into actin filaments and the subsequent treadmilling and cross-linking of actin filaments by activated myosin II to form activated VSFs. We assume radial treadmilling of actin filaments (i.e. $\boldsymbol{v}$ is parallel to $\boldsymbol{e}_r$), towards the nucleus, which is arrested in the vicinity of the nucleus and cell membrane, in a similar manner to Ch. 3.

We describe the recruitment of integrins and ECM ligands into adhesions by

$$\frac{\partial n_f}{\partial t} = -k_h^+ n_f + k_h^- n_h + D_f\nabla^2 n_f, \tag{5.7f}$$

$$\frac{\partial n_h}{\partial t} = k_h^+ n_f - k_h^- n_h - k_b^+ n_h n_s + k_b^- n_b, \tag{5.7g}$$

$$\frac{\partial n_b}{\partial t} = k_b^+ n_h n_s - k_b^- n_b - k_F^+ n_b + k_F^- n_A, \tag{5.7h}$$

$$\frac{\partial n_A}{\partial t} = k_F^+ n_b - k_F^- n_A, \tag{5.7i}$$

$$\frac{\partial n_s}{\partial t} = -k_b^+ n_h n_s + k_b^- n_b, \tag{5.7j}$$

in analogue with their counterparts Eqs. (3.29f)-(3.29j) in Ch. 3. This captures the conversion of low-affinity free integrins to high-affinity free integrins, the subsequent binding of these integrins to ECM ligands to form bound integrins (nascent adhesions), and the

maturation of these adhesions into mature FAs.

We describe the activation of ROCK and phosphorylation of its downstream effectors by

$$\frac{\partial c_R}{\partial t} = -k_R^+ c_R + k_R^- c_R^+, \tag{5.7k}$$

$$\frac{\partial c_R^+}{\partial t} = k_R^+ c_R - k_R^- c_R^+, \tag{5.7l}$$

$$\frac{\partial c_P}{\partial t} = -k_1^+ c_P + k_1^- c_{P-P} + D_P \nabla^2 c_P, \tag{5.7m}$$

$$\frac{\partial c_{P-P}}{\partial t} = k_1^+ c_P - k_1^- c_{P-P} + D_{P-P} \nabla^2 c_{P-P}, \tag{5.7n}$$

$$\frac{\partial c_K}{\partial t} = -k_2^+ c_K + k_2^- c_{K-P} + D_K \nabla^2 c_K, \tag{5.7o}$$

$$\frac{\partial c_{K-P}}{\partial t} = k_2^+ c_K - k_2^- c_{K-P} + D_{K-P} \nabla^2 c_{K-P}, \tag{5.7p}$$

$$\frac{\partial c_C}{\partial t} = -k_3^+ c_C + k_3^- c_{C-P} + D_C \nabla^2 c_C, \tag{5.7q}$$

$$\frac{\partial c_{C-P}}{\partial t} = k_3^+ c_C - k_3^- c_{C-P} + D_{C-P} \nabla^2 c_{C-P}. \tag{5.7r}$$

This system of reaction-diffusion equations captures, in direct analogue with Eq. (3.30) in Ch. 3, the activation of ROCK and the subsequent phosphorylation of MLCP, MLCK and cofilin.

5.3 Initial and boundary conditions

5.3.1 Mechanical conditions

Initially, we assume zero displacement everywhere in the cell and ECM in the form

$$\boldsymbol{u}(r, \theta, 0) = \mathbf{0}, \quad \boldsymbol{w}(r, \theta, 0) = \mathbf{0}. \tag{5.8a}$$

We prescribe the following boundary conditions on the cell cytoplasm. Firstly, we enforce zero displacement of the cell cytoplasm on the boundary with the cell nucleus (which we treat as a rigid body and are neglecting translation), i.e. we have

$$\boldsymbol{u}(R_n, \theta, t) = \mathbf{0}. \tag{5.8b}$$

Such an assumption (i.e. that solutions are pinned on the inner boundary of the cell cytoplasm) is highly idealised, and may suppress non-axisymmetric modes of deformation in our later analysis (see Secs. 5.7-5.10 below). Hence, future developments of this model should incorporate a stiff, deformable nucleus. On the cell membrane we impose the

normal stress balance

$$(\boldsymbol{\sigma}_c(R,\theta,t)\,\boldsymbol{n}_m)\cdot\boldsymbol{n}_m = (\boldsymbol{\sigma}_b\boldsymbol{n}_m)\cdot\boldsymbol{n}_m + f_m, \tag{5.8c}$$

where $\boldsymbol{n}_m$ is the unit normal to the membrane, $\boldsymbol{\sigma}_b$ can capture stresses due to actin polymerisation at the boundaries pushing against the membrane or externally applied stresses (in a similar manner to Ch. 3 we set $\boldsymbol{\sigma}_b = \mathbf{0}$). We could also incorporate the mechanical effect of the elastic cell membrane (e.g. bending rigidity or membrane tension) through f_m but for the remainder of this Chapter we set $f_m = 0$ (in a similar manner to Solowiej-Wedderburn and Dunlop, 2022). We also assume no tangential stress on the cell membrane, i.e.

$$(\boldsymbol{\sigma}_c(R,\theta,t)\,\boldsymbol{n}_m)\cdot\boldsymbol{t}_m = 0, \tag{5.8d}$$

where $\boldsymbol{t}_m$ is the unit tangent to the cell membrane. Note that, as we are in the regime of linear viscoelasticity, $\boldsymbol{n}_m = \boldsymbol{e}_r$, $\boldsymbol{t}_m = \boldsymbol{e}_\theta$ throughout this Chapter (following the work of Biot, 1963, Martin and Payton, 1964).

In the ECM we impose zero-displacement at $r = 0$ and in the far field so that

$$\boldsymbol{w}(0,\theta,t) = \mathbf{0}, \quad \lim_{r\to\infty}\boldsymbol{w}(r,\theta,t) = \mathbf{0}, \tag{5.8e}$$

whilst at the junctions between ECM regions either side of the cytoplasmic boundary we match normal and tangential stress and displacement. Throughout this Chapter, we refer to the ECM below the cell nucleus as region 1 and in the far field (i.e. beyond the edge of the cell) as region 2. For simplicity, following Ch. 3, we will assume that the ECM has constant Young's modulus and viscosity in these regions so that $E_E(r,\theta,t) = \bar{E}$, $\mu_E(r,\theta,t) = \bar{\mu}$. It then emerges (in a similar manner to Sec. 3.1.7) that we can semi-analytically solve the ECM mechanical equations in these regions. For $i = 1, 2$ we denote the continuum displacement of the ECM in each of these regions by $\check{\boldsymbol{w}}_i$ and denote the Cauchy stress by $\check{\boldsymbol{\sigma}}_{E,i}$. Matching of the normal and tangential stresses at each of these boundaries yields

$$(\boldsymbol{\sigma}_E(R_n,\theta,t)\,\boldsymbol{n}_1)\cdot\boldsymbol{n}_1 = (\check{\boldsymbol{\sigma}}_{E,1}(R_n,\theta,t)\,\boldsymbol{n}_1)\cdot\boldsymbol{n}_1, \tag{5.8f}$$

$$(\boldsymbol{\sigma}_E(R_n,\theta,t)\,\boldsymbol{n}_1)\cdot\boldsymbol{t}_1 = (\check{\boldsymbol{\sigma}}_{E,1}(R_n,\theta,t)\,\boldsymbol{n}_1)\cdot\boldsymbol{t}_1, \tag{5.8g}$$

$$(\boldsymbol{\sigma}_E(R,\theta,t)\,\boldsymbol{n}_2)\cdot\boldsymbol{n}_2 = (\check{\boldsymbol{\sigma}}_{E,2}(R,\theta,t)\,\boldsymbol{n}_2)\cdot\boldsymbol{n}_2, \tag{5.8h}$$

$$(\boldsymbol{\sigma}_E(R,\theta,t)\,\boldsymbol{n}_2)\cdot\boldsymbol{t}_2 = (\check{\boldsymbol{\sigma}}_{E,2}(R,\theta,t)\,\boldsymbol{n}_2)\cdot\boldsymbol{t}_2, \tag{5.8i}$$

where, for $i = 1, 2$, the unit normal (tangent) of the ECM to the interface with region i is denoted by $\boldsymbol{n}_i$ ($\boldsymbol{t}_i$). Note that, as we are in the regime of linear viscoelasticity, $\boldsymbol{n}_i = \pm\boldsymbol{e}_r$, $\boldsymbol{t}_i = \pm\boldsymbol{e}_\theta$ throughout this Chapter (following Biot, 1963, Martin and Payton, 1964).

5.3.2 Biochemistry conditions

We assume that the cell is newly introduced to the substrate so that no adhesions have formed and all integrins are in their low-affinity state for ECM ligand binding. Moreover, we assume that no SFs or actin filaments have formed so that all actin is monomeric. We additionally assume that ROCK is initially wholly inactive and consequently, MLCP, MLCK and cofilin are all initially unphosphorylated and myosin II is found entirely in its inactive state.

To preserve the mass of the various proteins in the cell, we assume no flux boundary conditions for each protein species at the cytoplasm edge. Hence, at the edge of the cytoplasm, the flux, $\boldsymbol{j}_\alpha$, of each protein satisfies

$$\boldsymbol{j}_\alpha \cdot \boldsymbol{n}_n = 0, \quad \boldsymbol{j}_\alpha \cdot \boldsymbol{n}_m = 0, \quad \boldsymbol{j}_\alpha = D_\alpha \nabla c_\alpha - \boldsymbol{v}_\alpha c_\alpha, \tag{5.8j}$$

where $\boldsymbol{n}_n = -\boldsymbol{e}_r$ is the unit normal to the cytoplasm at the boundary with the cell nucleus. Here α is used to represent any of the concentrations (or densities), with the first term representing diffusive effects and the second representing advective effects (with velocity $\boldsymbol{v}_\alpha$). For non-diffusive and non-advective proteins we immediately satisfy no-flux boundary conditions and solve the reaction equations at the boundary as we do at the interior.

5.4 Non-dimensionalisation

To simplify our analysis, in a similar manner to Sec. 3.4, we non-dimensionalise our governing biochemical and mechanical governing Eqs. (5.4)-(5.7), together with with their associated boundary and initial conditions from Eq. (5.8). Once again, given that our primary interest is in the microscale patterning of adhesion to the substrate, we scale all lengths on the cell radius, R, and time on $\langle t \rangle = 1/\left(k_b^+ N_S\right)$, the characteristic timescale of the formation of nascent adhesions (due to the binding of high-affinity integrins with ECM ligands), where N_S is the initial average free ligand density. Note that this process is rapid compared to adhesion maturation into focal structures, and so we consider the dynamics of the model over a large number of dimensionless time units. We scale stresses on E_0^F, the Young's modulus of actin filaments when they are at a typical concentration (defined below). Furthermore, we scale actin concentrations on C_A, the initial average concentration of actin (in all its forms), scale myosin concentrations on C_M, the initial average concentration of myosin (in its inactive and active forms). We scale integrin and adhesion density on the average initial integrin (in all its forms) density, N_I, and scale ligand density on N_S. A similar treatment is given to signaling proteins with ROCK concentration scaled on C_R, the average initial ROCK concentration (in its active and inactive forms), MLCP concentration scaled on C_P, the average concentration of MLCP (in

its phosphorylated and unphosphorylated forms), MLCK concentration is scaled on C_K, the average total concentration of MLCK (in its phosphorylated and unphosphorylated forms) and cofilin concentration is scaled on C_C, the average total concentration of cofilin (in its phosphorylated and unphosphorylated forms).

5.4.1 Mechanical equations

In order to non-dimensionalise the mechanical equations Eq. (5.4) we write

$$\begin{gathered} E_F = E_0^F \tilde{f}_F, \quad E_S = E_0^S \tilde{f}_S, \quad E_P = E_0^P \tilde{f}_P, \quad E_C = E_0^C \tilde{f}_C, \\ E_O = E_0^O \tilde{f}_O, \quad \tau = \tau_0 \tilde{f}_\tau, \quad \mu_c = \mu_0^c \tilde{g}_c, \quad \mu_E = \mu_0^E \tilde{g}_E, \\ \kappa_{NA} = \kappa_0^{NA} \tilde{f}_{NA}, \quad \kappa_{FA} = \kappa_0^{FA} \tilde{f}_{FA}, \quad \beta_{NA} = \beta_0^{NA} \tilde{f}_{NA}, \quad \beta_{FA} = \beta_0^{FA} \tilde{f}_{FA}, \end{gathered} \tag{5.9}$$

where E_0^F, E_0^S, E_0^P, E_0^C, E_0^O, κ_0^{NA}, κ_0^{FA}, β_0^{NA}, β_0^{FA}, τ_0, μ_0^c and μ_0^E are dimensional constants, and all variables with tildes are dimensionless functions. We scale position, time and velocity by writing $r' = r/L$, $t' = t/\langle t \rangle$, $v' = v\langle t \rangle / L$. Hence, the dimensionless form of the governing equations Eq. (5.4) are

$$\frac{E_0^F}{R} \tilde{\nabla} \cdot \boldsymbol{\sigma}'_c = \kappa_I R \left(\boldsymbol{u}' - \boldsymbol{w}' \right) + \beta_I \frac{R}{\langle T \rangle} \frac{\partial}{\partial t} \left(\boldsymbol{u}' - \boldsymbol{w}' \right), \tag{5.10a}$$

$$\frac{E_0^F}{R} \tilde{\nabla} \cdot \boldsymbol{\sigma}'_E = \kappa_I R \left(\boldsymbol{w}' - \boldsymbol{u}' \right) + \beta_I \frac{R}{\langle t \rangle} \frac{\partial}{\partial t} \left(\boldsymbol{w}' - \boldsymbol{u}' \right). \tag{5.10b}$$

Hence

$$\tilde{\nabla} \cdot \boldsymbol{\sigma}'_c = \tilde{\kappa}_I \left(\boldsymbol{u}' - \boldsymbol{w}' \right) + \tilde{\beta}_I \frac{\partial}{\partial t} \left(\boldsymbol{u}' - \boldsymbol{w}' \right), \tag{5.11a}$$

$$\tilde{\nabla} \cdot \boldsymbol{\sigma}'_E = \tilde{\kappa}_I \left(\boldsymbol{w}' - \boldsymbol{u}' \right) + \tilde{\beta}_I \frac{\partial}{\partial t} \left(\boldsymbol{w}' - \boldsymbol{u}' \right), \tag{5.11b}$$

where

$$\boldsymbol{\sigma}'_c = \tilde{E}_c(r', \theta) \boldsymbol{\epsilon}'_c + \tilde{\mu}_c(r', \theta) \frac{\partial \boldsymbol{\epsilon}'_c}{\partial t} + \boldsymbol{\tau}', \tag{5.11c}$$

$$\boldsymbol{\sigma}'_E = \tilde{E}_E(r', \theta) \boldsymbol{\epsilon}'_E + \tilde{\mu}_E(r', \theta) \frac{\partial \boldsymbol{\epsilon}'_E}{\partial t}. \tag{5.11d}$$

Note that we have the following dimensionless groups

$$\begin{gathered} \tilde{\mu}_0^c = \mu_0^c / E_0^F \langle t \rangle, \quad \tilde{\tau}_0 = \tau_0 / E_0^F, \quad \tilde{E}_0^S = E_0^S / E_0^F, \\ \tilde{E}_0^P = E_0^P / E_0^F, \quad \tilde{\kappa}_0^{NA} = \kappa_0^{NA} R^2 / E_0^F, \quad \tilde{\kappa}_0^{FA} = \kappa_0^{FA} R^2 / E_0^F, \\ \tilde{\beta}_0^{NA} = \beta_0^{NA} R^2 / E_0^F \langle t \rangle, \quad \tilde{\beta}_0^{FA} = \beta_0^{FA} R^2 / E_0^F \langle t \rangle, \quad \tilde{\beta}_e = \beta_e R^2 / E_0^F \langle t \rangle, \\ \tilde{\mu}_0^E = \mu_0^E / E_0^F \langle t \rangle, \quad \tilde{E}_0^C = E_0^C / E_0^F, \quad \tilde{E}_0^O = E_0^O / E_0^F. \end{gathered} \tag{5.11e}$$

The infinitesimal strain tensors from Eq. (5.4d) are already dimensionless, but we can rewrite them as

$$\boldsymbol{\epsilon}'_c = \frac{\partial u'_r}{\partial r'}\boldsymbol{e}_r \otimes \boldsymbol{e}_r + \frac{1}{r'}\left(\frac{\partial u'_\theta}{\partial \theta} + u'_r\right)\boldsymbol{e}_\theta \otimes \boldsymbol{e}_\theta + \frac{1}{2}\left(\frac{1}{r'}\frac{\partial u'_r}{\partial \theta} + \frac{\partial u'_\theta}{\partial r'} - \frac{u'_\theta}{r'}\right)(\boldsymbol{e}_r \otimes \boldsymbol{e}_\theta + \boldsymbol{e}_\theta \otimes \boldsymbol{e}_r), \tag{5.11f}$$

$$\boldsymbol{\epsilon}'_E = \frac{\partial w'_r}{\partial r'}\boldsymbol{e}_r \otimes \boldsymbol{e}_r + \frac{1}{r'}\left(\frac{\partial w'_\theta}{\partial \theta} + w'_r\right)\boldsymbol{e}_\theta \otimes \boldsymbol{e}_\theta + \frac{1}{2}\left(\frac{1}{r'}\frac{\partial w'_r}{\partial \theta} + \frac{\partial w'_\theta}{\partial r'} - \frac{w'_\theta}{r'}\right)(\boldsymbol{e}_r \otimes \boldsymbol{e}_\theta + \boldsymbol{e}_\theta \otimes \boldsymbol{e}_r). \tag{5.11g}$$

The initial conditions Eq. (5.8a) transform to

$$\boldsymbol{u}'(r', \theta, 0) = \boldsymbol{0}, \quad \boldsymbol{w}'(r', \theta, 0) = \boldsymbol{0}. \tag{5.12a}$$

The boundary conditions on the cell from Eqs. (5.8b)-(5.8d) become

$$\boldsymbol{u}'(R'_n, \theta, t') = \boldsymbol{0}, \tag{5.12b}$$

$$(\boldsymbol{\sigma}'_c(R', \theta, t')\,\boldsymbol{e}_r) \cdot \boldsymbol{e}_r = 0, \tag{5.12c}$$

$$(\boldsymbol{\sigma}'_c(R', \theta, t')\,\boldsymbol{e}_r) \cdot \boldsymbol{e}_\theta = 0. \tag{5.12d}$$

From Eq. (5.8e) the boundary conditions imposed on the ECM become

$$\boldsymbol{w}'(0, \theta, t') = 0, \quad \lim_{r' \to \infty} \boldsymbol{w}'(r', \theta, t') = 0, \tag{5.12e}$$

and we match the dimensionless displacement and stress at the boundaries between the ECM underneath the cell cytoplasm and regions 1 and 2. In particular, from Eqs. (5.8f)-(5.8i) we have

$$(\boldsymbol{\sigma}'_E(R'_n, \theta, t')\,\boldsymbol{e}_r) \cdot \boldsymbol{e}_r = \left(\check{\boldsymbol{\sigma}}'_{E,1}(R'_n, \theta, t')\,\boldsymbol{e}_r\right) \cdot \boldsymbol{e}_r, \tag{5.12f}$$

$$(\boldsymbol{\sigma}'_E(R'_n, \theta, t')\,\boldsymbol{e}_r) \cdot \boldsymbol{e}_\theta = \left(\check{\boldsymbol{\sigma}}'_{E,1}(R'_n, \theta, t')\,\boldsymbol{e}_r\right) \cdot \boldsymbol{e}_\theta, \tag{5.12g}$$

$$(\boldsymbol{\sigma}'_E(R', \theta, t')\,\boldsymbol{e}_r) \cdot \boldsymbol{e}_r = \left(\check{\boldsymbol{\sigma}}'_{E,2}(R', \theta, t')\,\boldsymbol{e}_r\right) \cdot \boldsymbol{e}_r, \tag{5.12h}$$

$$(\boldsymbol{\sigma}'_E(R', \theta, t')\,\boldsymbol{e}_r) \cdot \boldsymbol{e}_\theta = \left(\check{\boldsymbol{\sigma}}'_{E,2}(R', \theta, t')\,\boldsymbol{e}_r\right) \cdot \boldsymbol{e}_\theta, \tag{5.12i}$$

where $\check{\boldsymbol{\sigma}}'_{E,i} = \check{\boldsymbol{\sigma}}_{E,i}/E_0^F$ for $i = 1, 2$.

5.4.2 Biochemistry

We let $A_c = \pi(R^2 - R_n^2)$ denote the surface area of the cell cytoplasm in contact with the ECM and $V_c = \pi H(R^2 - R_n^2)$ denote the volume of the cell cytoplasm. In order to

non-dimensionalise the cell biochemistry we introduce the following scales

$$C_A = \frac{1}{V_c}\int_0^H \int_0^{2\pi} \int_{R_n}^R \left(c_G(r,\theta,0) + c_F(r,\theta,0) + c_S^+(r,\theta,0)\right)\, r dr d\theta dz, \tag{5.13a}$$

$$N_I = \frac{1}{A_c}\int_0^{2\pi} \int_{R_n}^R (n_f(r,\theta,0) + n_h(r,\theta,0) + n_b(r,\theta,0) + n_A(r,\theta,0))\, r dr d\theta, \tag{5.13b}$$

$$C_M = \frac{1}{V_c}\int_0^H \int_0^{2\pi} \int_{R_n}^R \left(c_m(r,\theta,0) + c_m^+(r,\theta,0)\right)\, r dr d\theta dz, \tag{5.13c}$$

$$N_S = \frac{1}{A_c}\int_0^{2\pi} \int_{R_n}^R n_s(r,\theta,0)\, r dr d\theta, \tag{5.13d}$$

$$C_R = \frac{1}{V_c}\int_0^H \int_0^{2\pi} \int_{R_n}^R \left(c_R(r,\theta,0) + c_R^+(r,\theta,0)\right)\, r dr d\theta dz, \tag{5.13e}$$

$$C_P = \frac{1}{V_c}\int_0^H \int_0^{2\pi} \int_{R_n}^R (c_P(r,\theta,0) + c_{P-P}(r,\theta,0))\, r dr d\theta dz, \tag{5.13f}$$

$$C_K = \frac{1}{V_c}\int_0^H \int_0^{2\pi} \int_{R_n}^R (c_K(r,\theta,0) + c_{K-P}(r,\theta,0))\, r dr d\theta dz, \tag{5.13g}$$

$$C_C = \frac{1}{V_c}\int_0^H \int_0^{2\pi} \int_{R_n}^R (c_C(r,\theta,0) + c_{C-P}(r,\theta,0))\, r dr d\theta dz, \tag{5.13h}$$

representing a concentration scale for actin species (monomers, filaments and stress fibres), for integrin species (low and high-affinity integrins, nascent and focal adhesions), for myosin II (inactive and active), ligands, ROCK (inactive and active), MLCP (phosphorylated and unphosphorylated), MLCK (phosphorylated and unphosphorylated) and cofilin (phosphorylated and unphosphorylated) respectively. Note the average concentration is computed as the total initial mass of each species averaged over the entire cell.

Given that we assume the cell is initially circular, with radius R, then using $c_i(r,\theta,t) = c_i(r,t)$ we can simplify our scales to

$$C_A = \frac{2}{(R^2 - R_n^2)}\int_{R_n}^R \left(c_G(r,0) + c_F(r,0) + c_S^+(r,0)\right)\, r dr, \tag{5.14a}$$

$$N_I = \frac{2}{(R^2 - R_n^2)}\int_{R_n}^R (n_f(r,0) + n_h(r,0) + n_b(r,0) + n_A(r,0))\, r dr, \tag{5.14b}$$

$$C_M = \frac{2}{(R^2 - R_n^2)}\int_{R_n}^R \left(c_m(r,0) + c_m^+(r,0)\right)\, r dr, \tag{5.14c}$$

$$N_S = \frac{2}{(R^2 - R_n^2)}\int_{R_n}^R n_s(r,0)\, r dr, \tag{5.14d}$$

$$C_R = \frac{2}{(R^2 - R_n^2)}\int_{R_n}^R \left(c_R(r,0) + c_R^+(r,0)\right)\, r dr, \tag{5.14e}$$

$$C_P = \frac{2}{(R^2 - R_n^2)}\int_{R_n}^R (c_P(r,0) + c_{P-P}(r,0))\, r dr, \tag{5.14f}$$

$$C_K = \frac{2}{(R^2 - R_n^2)} \int_{R_n}^{R} (c_K(r,0) + c_{K-P}(r,0))\ rdr, \tag{5.14g}$$

$$C_C = \frac{2}{(R^2 - R_n^2)} \int_{R_n}^{R} (c_C(r,0) + c_{C-P}(r,0))\ rdr. \tag{5.14h}$$

Our choice of scaling introduces the following additional dimensionless groups,

$$\begin{gathered}
\tilde{k}_p^+ = k_p^+\langle t\rangle N_I, \quad \tilde{k}_p^- = k_p^-\langle t\rangle, \quad \tilde{k}_m^+ = k_m^+\langle t\rangle C_M C_A, \quad \bar{k}_m^+ = k_m^+\langle t\rangle C_A^2, \\
\tilde{k}_m^- = k_m^-\langle t\rangle, \quad \bar{k}_m^- = k_m^-\langle t\rangle C_A/C_M, \quad \tilde{k}_a^+ = k_a^+\langle t\rangle, \quad \tilde{k}_a^- = k_a^-\langle t\rangle, \\
\tilde{k}_h^+ = k_h^+\langle t\rangle, \quad \tilde{k}_h^- = k_h^-\langle t\rangle, \quad \tilde{k}_b^+ = k_b^+\langle t\rangle N_S(=1), \quad \bar{k}_b^+ = k_b^+\langle t\rangle N_I, \\
\tilde{k}_b^- = k_b^-\langle t\rangle, \quad \bar{k}_b^- = k_b^-\langle t\rangle N_I/N_S, \quad \tilde{k}_F^+ = k_F^+\langle t\rangle, \quad \tilde{k}_F^- = k_F^-\langle t\rangle, \\
\tilde{D}_G = D_G\langle t\rangle/R^2, \quad \tilde{D}_F = D_F\langle t\rangle/R^2, \quad \tilde{D}_m = D_m\langle t\rangle/R^2, \quad \tilde{D}_m^+ = D_m^+\langle t\rangle/R^2, \\
\tilde{D}_f = D_f\langle t\rangle/R^2, \quad \tilde{k}_R^+ = k_R^+\langle t\rangle, \quad \tilde{k}_R^- = k_R^-\langle t\rangle, \quad \tilde{k}_1^+ = k_1^+\langle t\rangle, \quad \tilde{k}_1^- = k_1^-\langle t\rangle, \\
\tilde{k}_2^+ = k_2^+\langle t\rangle, \quad \tilde{k}_2^- = k_2^-\langle t\rangle, \quad \tilde{k}_3^+ = k_3^+\langle t\rangle, \quad \tilde{k}_3^- = k_3^-\langle t\rangle, \\
\tilde{D}_P = D_P\langle t\rangle/R^2, \quad \tilde{D}_{P-P} = D_{P-P}\langle t\rangle/R^2, \quad \tilde{D}_K = D_K\langle t\rangle/R^2, \\
\tilde{D}_{K-P} = D_{K-P}\langle t\rangle/R^2, \quad \tilde{D}_C = D_C\langle t\rangle/R^2, \quad \tilde{D}_{C-P} = D_{C-P}\langle t\rangle/R^2.
\end{gathered} \tag{5.15}$$

Hence, the dimensionless governing equations become

$$\frac{\partial c_G'}{\partial t'} = -\tilde{k}_p^+ c_G' \left(n_b' + n_A'\right) + \tilde{k}_p^- c_F' + \tilde{k}_m^- c_S^{+\prime} + \tilde{D}_G \tilde{\nabla}^2 c_G', \tag{5.16a}$$

$$\frac{\partial c_F'}{\partial t} + \tilde{\nabla}\cdot(\boldsymbol{v}' c') = \tilde{k}_p^+ \left(n_b' + n_A'\right) - \tilde{k}_p^- c_F' - \tilde{k}_m^+ c_F' c_m^{+\prime} \left(c_F' + c_S^{+\prime}\right) + \tilde{D}_F \tilde{\nabla}^2 c_F', \tag{5.16b}$$

$$\frac{\partial c_S^{+\prime}}{\partial t'} = \tilde{k}_m^+ c_F' \left(c_F' + c_S^{+\prime}\right) c_m^{+\prime} - \tilde{k}_m^- c_S^{+\prime}, \tag{5.16c}$$

$$\frac{\partial c_m'}{\partial t'} = -\tilde{k}_a^+ c_m' + \tilde{k}_a^- c_m^{+\prime} + \tilde{D}_m \tilde{\nabla}^2 c_m', \tag{5.16d}$$

$$\frac{\partial c_m^{+\prime}}{\partial t'} = \tilde{k}_a^+ c_m' - \tilde{k}_a^- c_m^{+\prime} - \bar{k}_m^+ c_F' \left(c_F' + c_S^{+\prime}\right) c_m^{+\prime} + \bar{k}_m^- c_S^{+\prime} + \tilde{D}_m^+ \tilde{\nabla}^2 c_m^{+\prime}, \tag{5.16e}$$

$$\frac{\partial n_f'}{\partial t'} = -\tilde{k}_h^+ n_f' + \tilde{k}_h^- n_h' + \tilde{D}_f \tilde{\nabla}^2 n_f', \tag{5.16f}$$

$$\frac{\partial n_h'}{\partial t'} = \tilde{k}_h^+ n_f' - \tilde{k}_h^- n_h' - \tilde{k}_b^+ n_h' n_s' + \tilde{k}_b^- n_b', \tag{5.16g}$$

$$\frac{\partial n_b'}{\partial t'} = \tilde{k}_b^+ n_h' n_s' - \tilde{k}_b^- n_b' - \tilde{k}_F^+ n_b' + \tilde{k}_F^- n_A', \tag{5.16h}$$

$$\frac{\partial n_A'}{\partial t'} = \tilde{k}_F^+ n_b' - \tilde{k}_F^- n_A', \tag{5.16i}$$

$$\frac{\partial n_s'}{\partial t'} = -\bar{k}_b^+ n_h' n_s' + \bar{k}_b^- n_b', \tag{5.16j}$$

$$\frac{\partial c_R'}{\partial t'} = -\tilde{k}_R^+ c_R' + \tilde{k}_R^- c_R^{+\prime}, \tag{5.16k}$$

$$\frac{\partial c_R^{+\prime}}{\partial t'} = \tilde{k}_R^+ c_R' - \tilde{k}_R^- c_R^{+\prime}, \tag{5.16l}$$

$$\frac{\partial c'_P}{\partial t'} = -\tilde{k}_1^+ c'_P + \tilde{k}_1^- c'_{P-P} + \tilde{D}_P \tilde{\nabla}^2 c'_P, \tag{5.16m}$$

$$\frac{\partial c'_{P-P}}{\partial t'} = \tilde{k}_1^+ c'_P - \tilde{k}_1^- c'_{P-P} + \tilde{D}_{P-P} \tilde{\nabla}^2 c'_{P-P}, \tag{5.16n}$$

$$\frac{\partial c'_K}{\partial t'} = -\tilde{k}_2^+ c'_K + \tilde{k}_2^- c'_{K-P} + \tilde{D}_K \tilde{\nabla}^2 c'_K, \tag{5.16o}$$

$$\frac{\partial c'_{K-P}}{\partial t'} = \tilde{k}_2^+ c'_K - \tilde{k}_2^- c'_{K-P} + \tilde{D}_{K-P} \tilde{\nabla}^2 c'_{K-P}, \tag{5.16p}$$

$$\frac{\partial c'_C}{\partial t'} = -\tilde{k}_3^+ c'_C + \tilde{k}_3^- c'_{C-P} + \tilde{D}_C \tilde{\nabla}^2 c'_C, \tag{5.16q}$$

$$\frac{\partial c'_{C-P}}{\partial t'} = \tilde{k}_3^+ c'_C - \tilde{k}_3^- c'_{C-P} + \tilde{D}_{C-P} \tilde{\nabla}^2 c'_{C-P}. \tag{5.16r}$$

Eqs. (5.16) are similar to their dimensionless counterparts from our one-dimensional formulation in Ch. 3 (see Eqs. 3.45), but with the a reduction in the number of equations due to the natural simplification of the system in this two-dimensional framework (see Sec. 5.2).

5.5 Constitutive assumptions

In a similar manner to Sec. 3.5, in order to close the positive feedback loop connecting FA and SF formation and to connect the cell biochemistry to the underlying mechanical properties, we link various reaction rates to the concentration of signaling proteins (Sec. 5.5.1), link the rate of adhesion maturation to adhesion stretch (Sec. 5.5.2) and couple mechanical properties of the cytoskeleton and adhesions to cell biochemistry (Sec. 5.5.3).

5.5.1 Signaling proteins effect on reaction rates

In analogue with Eq. (3.49) in Ch. 3 we suppose that the activation rate of ROCK is dependent on the local density of nascent and focal adhesions by setting

$$k_R^+ = K_R^+ \left(n_b + \delta n_A\right) / N_I, \tag{5.17}$$

so that the relative strength of signaling due to FAs compared to nascent adhesions is increased by a factor of $\delta = O(1)$.

To incorporate the effects of ROCK activation on MLCP, MLCK and cofilin phosphorylation, in an identical manner to Sec. 3.5.1 we set $k_j^+ = K_j^+ g_j\left(c_R^+/C_R\right)$, $j = 1, 2, 3$, where K_j^+ are dimensional rate constants and g_j are dimensionless functions of activated ROCK concentration.

To capture the effect that MLCK phosphorylation has on myosin II activation and

that MLCP phosphorylation has on myosin II inactivation we set

$$k_a^+ = K_a^+ g_a^+ \left(c_{K-P}/C_K\right), \quad g_a^+ \left(c_{K-P}/C_K\right) = c_{K-P}/C_K, \tag{5.18a}$$

$$k_a^- = K_a^- g_a^- \left(c_P/C_P\right), \quad g_a^- \left(c_P/C_P\right) = c_P/C_P, \tag{5.18b}$$

where K_a^+, K_a^- are dimensional constants and g_a^+, g_a^- are dimensionless functions of MLCK-P and MLCP concentration, respectively. These are identical to our assumptions in Sec. 3.5.1.

Finally, as in Sec. 3.5.1, to capture the effects increased Rho and ROCK activation has on actin polymerisation and that cofilin phosphorylation has on actin depolymerisation, we set

$$k_p^+ = K_p^+ g_p^+ \left(c_R^+/C_R\right), \quad g_p^+ \left(c_R^+/C_R\right) = c_R^+/C_R, \tag{5.18c}$$

$$k_p^- = K_p^- g_p^- \left(c_C/C_C\right), \quad g_p^- \left(c_C/C_C\right) = c_C/C_C, \tag{5.18d}$$

where K_p^+, K_p^- are dimensional constants and g_p^+, g_p^- are dimensionless functions of the concentration of ROCK and unphosphorylated cofilin.

5.5.2 The effect of contractile forces

In response to contractile forces generated by SFs, nascent adhesions mature into FAs through stretching of talin (which exposes VBSs). Hence, the rate of formation of FAs is assumed to depend on the length (or stretch) of integrin-ligand connections. In a similar manner to Sec. 3.5.2, we approximate this length by $\lambda_I(r,\theta,t) = |\boldsymbol{u}(r,\theta,t) - \boldsymbol{w}(r,\theta,t)|$ (the relative deformation of the cell to the ECM) and write

$$k_F^+ = K_F^+ g_s^+ \left(\lambda_I/R\right), \quad g_s^+ \left(\lambda_I/L\right) = \left(\lambda_I/R\right)^2, \tag{5.19}$$

where K_F^+ is a dimensionless constant and g_s^+ is a dimensionless function of adhesion length. We note that

$$\lambda_I = \sqrt{\left(u_r - w_r\right)^2 + \left(u_\theta - w_\theta\right)^2}, \tag{5.20}$$

where we consider only the positive branch of the square root.

5.5.3 Coupling mechanics and biochemistry

As in Sec. 3.5.3, in order to allow the protein concentrations to influence the mechanical properties of the cytoplasm and adhesions, we select a key set of dimensional parameters and multiply each by a dimensionless function of a particular protein concentration. We link each of these mechanical properties to the biochemical properties of the cell and

adhesions.

In particular, we describe the Young's modulus of actin filaments by

$$E_F = E_0^F \tilde{f}_F, \quad \tilde{f}_F\left(c_F\right) = c_F/C_A, \tag{5.21}$$

where E_0^F is a dimensional constant and $\tilde{f}_F$ is a dimensionless function of actin filament concentration. Similarly, the Young's modulus of SFs is described by

$$E_S = E_0^S \tilde{f}_S, \quad \tilde{f}_S\left(c_S^+\right) = c_S^+/C_A, \tag{5.22}$$

where E_0^S is a dimensional constant and $\tilde{f}_S\left(c_S^+\right)$ is a dimensionless functions of SF concentration. We also link the (active) contractile stress due to myosin II motor action to the SF concentration by setting

$$\tau = \tau_0 \tilde{f}_\tau, \quad \tilde{f}_\tau\left(c_S^+\right) = c_S^+/C_A, \tag{5.23}$$

where τ_0 is a dimensional constant and $\tilde{f}_\tau\left(c_S^+\right)$ is a dimensionless function of SF concentration. The Young's modulus of the cytoplasm due to the microtubules and intermediate filaments is assumed to be a constant, $E_P = E_0^P$. We note that this contrasts with Eq. (3.55) in Sec. 3.5.3, where we assume a non-constant term to additionally capture the stiff nucleus (we account for this in this two-dimensional model through the explicit inclusion of a rigid body at the cell centre).

Additionally, we describe the restoring forces and drag induced by nascent adhesions through

$$\kappa_{NA} = \kappa_0^{NA} \tilde{f}_{NA}, \quad \beta_{NA} = \beta_0^{NA} \tilde{f}_{NA}, \quad \tilde{f}_{NA} = n_b/N_I, \tag{5.24}$$

where κ_0^{NA} is a dimensional constant and $\tilde{f}_{NA}$ is a dimensionless function of nascent adhesion concentration. Similarly the restoring forces and drag induced by FAs are assumed to be given by

$$\kappa_{FA} = \kappa_0^{FA} \tilde{f}_{FA}, \quad \beta_{FA} = \beta_0^{FA} \tilde{f}_{FA}, \quad \tilde{f}_{FA} = n_A/N_I, \tag{5.25}$$

where κ_0^{FA} is a dimensional constant and $\tilde{f}_{FA}$ is a dimensionless function of FA concentration.

5.6 Axisymmetric problem

We shall henceforth work in dimensionless variables (unless otherwise stated), and drop all tildes and primes.

In this Section we solve the system outlined in Secs. 5.1-5.5 under the assumption of axisymmetry in all variables, in which there is no θ-dependence (and all derivatives with

respect to θ vanish). This allows us to identify an axisymmetric baseline state around which to linearise in Secs. 5.7-5.8.

5.6.1 Axisymmetric mechanics

In addition to assuming axisymmetry, we assume that the cell (and ECM) undergoes no rotation or twisting, so that $u_\theta(r,t) = 0$, $w_\theta(r,t) = 0$. Hence, the deformation of the cell cytoplasm and ECM can be written as $\boldsymbol{u} = u_r(r)\boldsymbol{e}_r$ and $\boldsymbol{w} = w_r(r)\boldsymbol{e}_r$, respectively. Consequently, the strain tensors given by Eq. (5.4c-5.4d) reduce to

$$\boldsymbol{\epsilon}_c = \frac{\partial u_r}{\partial r}\boldsymbol{e}_r \otimes \boldsymbol{e}_r + \frac{u_r}{r}\boldsymbol{e}_\theta \otimes \boldsymbol{e}_\theta, \quad \boldsymbol{\epsilon}_E = \frac{\partial w_r}{\partial r}\boldsymbol{e}_r \otimes \boldsymbol{e}_r + \frac{w_r}{r}\boldsymbol{e}_\theta \otimes \boldsymbol{e}_\theta. \tag{5.26}$$

It follows that the azimuthal component of Eq. (5.4a) is satisfied trivially and the radial components of the governing equations Eq. (5.4a) are given by

$$\begin{aligned}\frac{\partial \tau}{\partial r} + \frac{\tau}{r} + \left(E_c\frac{\partial^2 u_r}{\partial r^2} + \mu_c\frac{\partial^3 u_r}{\partial r^2 \partial t}\right) + \frac{1}{r}\left(E_c\frac{\partial u_r}{\partial r} + \mu_c\frac{\partial^2 u_r}{\partial r \partial t}\right) - \frac{1}{r^2}\left(E_c u_r + \mu_c\frac{\partial u_r}{\partial t}\right) \\ + \left(\frac{\partial E_c}{\partial r}\frac{\partial u_r}{\partial r} + \frac{\partial \mu_c}{\partial r}\frac{\partial^2 u_r}{\partial r \partial t}\right) = \beta_I\frac{\partial}{\partial t}\left(u_r - w_r\right) + \kappa_I\left(u_r - w_r\right), \end{aligned} \tag{5.27a}$$

$$\begin{aligned}\left(E_E\frac{\partial^2 w_r}{\partial r^2} + \mu_E\frac{\partial^3 w_r}{\partial r^2 \partial t}\right) + \frac{1}{r}\left(E_E\frac{\partial w_r}{\partial r} + \mu_E\frac{\partial^2 w_r}{\partial r \partial t}\right) - \frac{1}{r^2}\left(E_E w_r + \mu_E\frac{\partial w_r}{\partial t}\right) \\ + \left(\frac{\partial E_E}{\partial r}\frac{\partial w_r}{\partial r} + \frac{\partial \mu_E}{\partial r}\frac{\partial^2 w_r}{\partial r \partial t}\right) = \beta_I\frac{\partial}{\partial t}\left(w_r - u_r\right) + \kappa_I\left(w_r - u_r\right). \end{aligned} \tag{5.27b}$$

Initial and boundary conditions

In this axisymmetric framework Eq. (5.8a) becomes

$$\boldsymbol{u}(r,0) = \boldsymbol{0}, \quad \boldsymbol{w}(r,0) = \boldsymbol{0}. \tag{5.28a}$$

In order to apply the boundary conditions on the cell cytoplasm, recall that in this linear viscoelastic framework we have $\boldsymbol{n}_n = -\boldsymbol{e}_r$, $\boldsymbol{n}_m = \boldsymbol{e}_r$ and $\boldsymbol{t}_m = \boldsymbol{e}_\theta$. Hence, Eqs. (5.8b)-(5.8d) reduce to

$$\boldsymbol{u}(R_n,t) = \boldsymbol{0}, \tag{5.28b}$$

$$\left(\boldsymbol{\sigma}_c\left(R,t\right)\boldsymbol{e}_r\right)\cdot\boldsymbol{e}_r = 0, \tag{5.28c}$$

$$\left(\boldsymbol{\sigma}_c\left(R,t\right)\boldsymbol{e}_r\right)\cdot\boldsymbol{e}_\theta = 0. \tag{5.28d}$$

In axisymmetry, Eq. (5.28d) is trivially satisfied.

For the ECM we need to impose a boundary condition at the centre of the domain (i.e. at $r = 0$) and in the far field and match displacement and stress at the interface between

the ECM under the nucleus (region 1) and under the cytoplasm, and under the cytoplasm and in the far field (region 2). Given that we assume that the ECM has a uniform Young's modulus and viscosity in these regions (see Sec. 5.3.1) then the axisymmetric Cauchy stress can be written as

$$\check{\boldsymbol{\sigma}}_{E,1} = \left(\bar{E}\frac{\partial \check{w}_{r,1}}{\partial r} + \bar{\mu}\frac{\partial^2 \check{w}_{r,1}}{\partial r \partial t}\right)\boldsymbol{e}_r \otimes \boldsymbol{e}_r + \frac{1}{r}\left(\bar{E}\check{w}_{r,1} + \bar{\mu}\frac{\partial \check{w}_{r,1}}{\partial t}\right)\boldsymbol{e}_\theta \otimes \boldsymbol{e}_\theta, \tag{5.29a}$$

$$\check{\boldsymbol{\sigma}}_{E,2} = \left(\bar{E}\frac{\partial \check{w}_{r,2}}{\partial r} + \bar{\mu}\frac{\partial^2 \check{w}_{r,2}}{\partial r \partial t}\right)\boldsymbol{e}_r \otimes \boldsymbol{e}_r + \frac{1}{r}\left(\bar{E}\check{w}_{r,2} + \bar{\mu}\frac{\partial \check{w}_{r,2}}{\partial t}\right)\boldsymbol{e}_\theta \otimes \boldsymbol{e}_\theta, \tag{5.29b}$$

in regions 1 and 2 respectively. As these regions are not connected to the cell, they experience no adhesion mediated drag or restoring forces. Hence, from Eq. (5.27), we solve

$$\frac{\partial^2}{\partial r^2}\left(\bar{E}\check{w}_{r,i} + \bar{\mu}\frac{\partial \check{w}_{r,i}}{\partial t}\right) + \frac{1}{r}\frac{\partial}{\partial r}\left(\bar{E}\check{w}_{r,i} + \bar{\mu}\frac{\partial \check{w}_{r,i}}{\partial t}\right) - \frac{1}{r^2}\left(\bar{E}\check{w}_{r,i} + \bar{\mu}\frac{\partial \check{w}_{r,i}}{\partial t}\right) = 0, \tag{5.30}$$

with $i = 1, 2$. Writing $\check{W}_{r,i} = \left(\bar{E}_E\check{w}_{r,i} + \bar{\mu}_E\partial\check{w}_{r,i}/\partial t\right)$, then we identify Eq. (5.30) as an Euler-type ODE for $\check{W}_{r,i}$, which we solve by assuming solutions of the form $\check{W}_{r,i} = r^k$, $k \in \mathbb{R}$ (Hermann and Saravi, 2014). In particular, we deduce that the general solution to Eq. (5.30) is

$$\bar{E}\check{w}_{r,i} + \bar{\mu}\frac{\partial \check{w}_{r,i}}{\partial t} = A_i(t)r + \frac{B_i(t)}{r}, \tag{5.31}$$

where A_i, B_i are arbitrary functions of time.

ECM below the nucleus

At the origin we impose, from Eq. (5.8e), that $\check{w}_{r,1}(0,t) = 0$ and $\partial\check{w}_{r,1}(0,t)/\partial t = 0$ and deduce that $B_1(t) = 0$. It follows that, in the region of ECM below the nucleus, we can write

$$\bar{E}\check{w}_{r,1} + \bar{\mu}\frac{\partial \check{w}_{r,1}}{\partial t} = A_1(t)r. \tag{5.32}$$

Using an integrating factor we can write

$$\check{w}_{r,1}(r,t) = e^{-\frac{\bar{E}}{\bar{\mu}}t}\frac{r}{\bar{\mu}}\int_0^t e^{\frac{\bar{E}}{\bar{\mu}}T}A_1(T)\,dT. \tag{5.33}$$

Matching displacement at the boundary between region 1 and the region of the ECM underneath the cytoplasm, we set $\check{w}_{r,1}(R_n,t) = w_0(t)$, where $w_0(t)$ is the numerically calculated displacement of the cytoplasm at the boundary. Combining this with Eq. (5.33) then then deduce that

$$\check{w}_{r,1}(r,t) = \frac{r}{R_n}w_0(t), \tag{5.34}$$

for $0 \leq r \leq R_n$.

We provide a boundary condition by matching the normal stress at the interface between region 1 and region 3 (i.e. at the inner edge of the ECM underneath the cell cytoplasm). From Eq. (5.8f) we have

$$(\boldsymbol{\sigma}_E(R_n,t)\,\boldsymbol{e}_r)\cdot\boldsymbol{e}_r = (\check{\boldsymbol{\sigma}}_{E,1}(R_n,t)\,\boldsymbol{e}_r)\cdot\boldsymbol{e}_r. \tag{5.35}$$

Note that the tangential stress boundary condition from Eq. (5.8g) is identically satisfied in this axisymmetric framework. Note also that Eq. (5.35) can be written explicitly as

$$E_E\frac{\partial w(R_n,t)}{\partial r} + \mu_E\frac{\partial^2 w(R_n,t)}{\partial r\partial t} = \bar{E}\frac{1}{R_n}w_0(t) + \bar{\mu}\frac{1}{R_n}w_0'(t), \tag{5.36}$$

using $\check{w}_{r,1}$ from Eq. (5.34).

ECM in the far field

In the far field of the ECM, away from the cell, we impose, from Eq. (5.8e), that $\check{w}_{r,2}(r,t) = 0$ and $\partial\check{w}_{r,2}(r,t)/\partial t = 0$ as $r\to\infty$ and deduce that $B_2(t) = 0$. It follows that

$$\bar{E}\check{w}_{r,2} + \bar{\mu}\frac{\partial\check{w}_{r,2}}{\partial t} = \frac{B_2(t)}{r}. \tag{5.37}$$

Using an integrating factor we can write

$$\check{w}_{r,2}(r,t) = e^{-\frac{\bar{E}}{\bar{\mu}}t}\frac{1}{\bar{\mu}r}\int_0^t e^{\frac{\bar{E}}{\bar{\mu}}T}B_2(T)\,dT. \tag{5.38}$$

Matching displacement at the boundary between region 2 and the region of the ECM underneath the cytoplasm, we set $\check{w}_{r,2}(R,t) = w_N(t)$, where $w_N(t)$ is the numerically calculated displacement of the cytoplasm. Combining this with Eq. (5.38) then we deduce that

$$\check{w}_{r,2}(r,t) = \frac{R}{r}w_N(t), \tag{5.39}$$

for $R\le r<\infty$.

We provide a boundary condition by matching the normal stress at the interface between region 2 and region 3 (i.e. at the outer edge of the ECM underneath the cell cytoplasm). From Eq. (5.8h) we have

$$(\boldsymbol{\sigma}_E(R,t)\,\boldsymbol{e}_r)\cdot\boldsymbol{e}_r = (\check{\boldsymbol{\sigma}}_{E,2}(R,t)\,\boldsymbol{e}_r)\cdot\boldsymbol{e}_r, \tag{5.40}$$

Note that the tangential stress balance boundary condition from Eq. (5.8i) is identically satisfied in this axisymmetric framework. Note also that Eq. (5.40) can be written explic-

itly as

$$E_E \frac{\partial w(R,t)}{\partial r} + \mu_E \frac{\partial^2 w(R,t)}{\partial r \partial t} = \bar{E}\frac{1}{R} w_N(t) + \bar{\mu}\frac{1}{R} w'_N(t), \tag{5.41}$$

using $\check{w}_{r,2}$ from Eq. (5.39).

5.6.2 Biochemistry in axisymmetric problem

In the axisymmetric problem all quantities are independent of θ and we assume radial treadmilling of actin filaments so that $\boldsymbol{v} = v_r \boldsymbol{e}_r$. Hence Eqs. (5.7) become

$$\frac{\partial c_G}{\partial t} = -k_p^+ c_G \left(n_b + n_A\right) + k_p^- c_F + k_m^- c_S^+ + D_G \left(\frac{\partial^2 c_G}{\partial r^2} + \frac{1}{r}\frac{\partial c_G}{\partial r}\right), \tag{5.42a}$$

$$\frac{\partial c_F}{\partial t} + \frac{1}{r}\frac{\partial \left(r c_F v_r\right)}{\partial r} = k_p^+ \left(n_b + n_A\right) - k_p^- c_F - k_m^+ c_F c_m^+ \left(c_F + c_S^+\right) + D_F \left(\frac{\partial^2 c_F}{\partial r^2} + \frac{1}{r}\frac{\partial c_F}{\partial r}\right), \tag{5.42b}$$

$$\frac{\partial c_S^+}{\partial t} = k_m^+ c_F c_m^+ \left(c_F + c_S^+\right) - k_m^+ c_S^+, \tag{5.42c}$$

$$\frac{\partial c_m}{\partial t} = -k_a^+ c_m + k_a^- c_m^+ + D_m \left(\frac{\partial^2 c_m}{\partial r^2} + \frac{1}{r}\frac{\partial c_m}{\partial r}\right), \tag{5.42d}$$

$$\frac{\partial c_m^+}{\partial t} = k_a^+ c_m - k_a^- c_m^+ - k_m^+ c_F c_m^+ \left(c_F + c_S^+\right) + k_m^- c_S^+ + D_m^+ \left(\frac{\partial^2 c_m^+}{\partial r^2} + \frac{1}{r}\frac{\partial c_m^+}{\partial r}\right), \tag{5.42e}$$

$$\frac{\partial n_f}{\partial t} = -k_h^+ n_f + k_h^- n_h + D_f \left(\frac{\partial^2 n_f}{\partial r^2} + \frac{1}{r}\frac{\partial n_f}{\partial r}\right), \tag{5.42f}$$

$$\frac{\partial n_h}{\partial t} = k_h^+ n_f - k_h^- n_h - k_b^+ n_h n_s + k_b^- n_b, \tag{5.42g}$$

$$\frac{\partial n_b}{\partial t} = k_b^+ n_h n_s - k_b^- n_b - k_F^+ n_b + k_F^- n_A, \tag{5.42h}$$

$$\frac{\partial n_A}{\partial t} = k_F^+ n_b - k_F^- n_A, \tag{5.42i}$$

$$\frac{\partial n_s}{\partial t} = -k_b^+ n_h n_s + k_b^- n_b, \tag{5.42j}$$

$$\frac{\partial c_R}{\partial t} = -k_R^+ c_R + k_R^- c_R^+, \tag{5.42k}$$

$$\frac{\partial c_R^+}{\partial t} = k_R^+ c_R - k_R^- c_R^+, \tag{5.42l}$$

$$\frac{\partial c_P}{\partial t} = -k_1^+ c_P + k_1^- c_{P-P} + D_P \left(\frac{\partial^2 c_P}{\partial r^2} + \frac{1}{r}\frac{\partial c_P}{\partial r}\right), \tag{5.42m}$$

$$\frac{\partial c_{P-P}}{\partial t} = k_1^+ c_P - k_1^- c_{P-P} + D_{P-P} \left(\frac{\partial^2 c_{P-P}}{\partial r^2} + \frac{1}{r}\frac{\partial c_{P-P}}{\partial r}\right), \tag{5.42n}$$

$$\frac{\partial c_K}{\partial t} = -k_2^+ c_K + k_2^- c_{K-P} + D_K \left(\frac{\partial^2 c_K}{\partial r^2} + \frac{1}{r}\frac{\partial c_K}{\partial r}\right), \tag{5.42o}$$

$$\frac{\partial c_{K-P}}{\partial t} = k_2^+ c_K - k_2^- c_{K-P} + D_{K-P} \left(\frac{\partial^2 c_{K-P}}{\partial r^2} + \frac{1}{r}\frac{\partial c_{K-P}}{\partial r}\right), \tag{5.42p}$$

$$\frac{\partial c_C}{\partial t} = -k_3^+ c_C + k_3^- c_{C-P} + D_C \left(\frac{\partial^2 c_C}{\partial r^2} + \frac{1}{r} \frac{\partial c_C}{\partial r} \right), \tag{5.42q}$$

$$\frac{\partial c_{C-P}}{\partial t} = k_3^+ c_C - k_3^- c_{C-P} + D_{C-P} \left(\frac{\partial^2 c_{C-P}}{\partial r^2} + \frac{1}{r} \frac{\partial c_{C-P}}{\partial r} \right). \tag{5.42r}$$

Given that $\boldsymbol{n}_n = -\boldsymbol{e}_r$, $\boldsymbol{n}_m = \boldsymbol{e}_r$, it follows from Eq. (5.8j) that the flux, $\boldsymbol{j}_\alpha$, of each protein on each of the cytoplasmic boundaries is given by

$$D_\alpha \frac{\partial c_\alpha}{\partial r} - v_{\alpha,r} c_\alpha = 0, \tag{5.43}$$

where $v_{\alpha,r} = \boldsymbol{v}_\alpha \cdot \boldsymbol{e}_r$.

5.6.3 Computational method

The resulting large system of governing mechanical and biochemical PDEs is parabolic and so we solve the system numerically using a finite difference method based on the method of lines, in a similar manner to Sec. 3.7. In particular, we discretise the (dimensionless) spatial domain $R_n/R \leq x \leq 1$ using a uniform grid size Δr (the other ECM spatial domains away from the cell are solved semi-analytically, as in Sec. 5.6.1). We discretise all spatial derivatives using second-order finite difference stencils and solve the resulting large family of ODEs numerically using the Matlab solver ode15s. We employ the fictitious nodes procedure to apply the boundary conditions but note that for the ECM we need to incorporate our far field treatment (Sec. 5.6.1). In most cases we discretise the (dimensionless) domain with $\Delta r = 0.01(1 - R_n/R)$ and use Matlab's default error bounds for the time-stepping. In this case mass is conserved in the system within 1% error over long simulations.

5.6.4 Results

In Ch. 3 (see Sec. 3.8) we present a baseline output from our one-dimensional model, where in Figs. 3.7-3.11 we illustrate the temporal and spatial dynamics of a cell binding to a stiff ECM. We similarly illustrate these dynamics in this Section, using output from our two-dimensional model, under the assumption of axisymmetry. We generally use the parameters listed in Sec. 3.6 from Ch. 3, but with a few exceptions. Particularly, in order to replicate the observed localisation of myosin cross-linked actin filaments in the vicinity of the cell membrane, we assume that $k_m^+ = 1 \times 10^3\ \mu\text{M}^{-2}\ \text{s}^{-1}$ and $k_m^- = 1 \times 10^{-1}\ \text{s}^{-1}$ (*cf.* $k_m^+ = 1 \times 10^2\ \mu\text{M}^{-2}\ \text{s}^{-1}$ and $k_m^- = 1 \times 10^{-2}\ \text{s}^{-1}$ in Ch. 3). Moreover, owing to natural simplification in our two-dimensional model (in particular, the fact we only need to consider one family of ligands, adhesions and actin filaments), we assume our prescribed ECM ligand pattern, $n_s(r, 0)$, is uniform, with $n_s(r, 0)$=1000 μm^2. Additionally, we set

$E_0^P = 5 \times 10^2$ Pa, as this passive stiffness does not include contributions from the cell nucleus (in contrast with our work in Ch. 3, where we set $E_0^P = 5 \times 10^3$ Pa, but where there is spatial dependence to account for the cell nucleus). We assume that the cell radius is $R = 12.5$ μm, reflective of the assumed cell length of $L = 25$ μm in Ch. 3. Finally, we assume that the radius of the rigid nucleus is $R_n = 5$ μm (based on measurements by Lipowsky et al., 2018); note that this parameter is not present in the one-dimensional model. In a similar manner to Sec. 3.8, we solve the dimensionless governing equations, with dimensionless parameters detailed in Table 5.1; we present dimensionless output from our two-dimensional axisymmetric model for all independent and dependent variables with the exception of time, which we convert back to dimensional units for ease of interpretation. We summarise the global response (Fig. 5.3) followed by the local behaviour of individual components of the system, including the mechanical deformation of the cell cytoplasm and the ECM (Fig. 5.4), the integrins and adhesions (Fig. 5.5), the signaling proteins (Fig. 5.6) and actin and myosin (Fig. 5.7). Note that in Figs. 5.5-5.7 we consider the temporal dynamics of proteins at five radial locations in the cell (noting the assumed axisymmetry), in particular at the cell boundary (black line), the boundary of the cytoplasm with the cell nucleus (green line) and three equidistant locations between these points (the red, yellow and purple lines respectively as we move from the membrane towards the cell nucleus); these are marked as open squares on spatial plots in Figs. 5.4-5.7. Similarly, we plot the spatial dynamics of proteins (and mechanical properties) at certain snapshots in time, in particular $t = 250$ s (grey), $t = 500$ s (dark blue), $t = 1000$ s (orange), $t = 1500$ s (yellow), $t = 2000$ s (purple), $t = 2500$ s (green), $t = 5000$ s (maroon) and $t = 10000$ s (black) after the cell has been introduced to the substrate; these times are marked as open circles on temporal plots in Figs. 5.3-5.7.

Dimensionless parameter	**Value**	**Dimensionless parameter**	**Value**
$\tilde{K}_p^+$	2	$\tilde{K}_p^-$	0.1
$\tilde{K}_a^+$	0.1	$\tilde{K}_a^-$	0.1
$\tilde{k}_m^+$	$44.11\ldots$	$\tilde{k}_m^-$	1
$\check{k}_m^+$	$147.04\ldots$	$\check{k}_m^-$	$3.\overline{3}$
$\tilde{k}_h^+$	5	$\tilde{k}_h^-$	50
$\tilde{k}_b^+$	1	$\tilde{k}_b^-$	0.1
$\check{k}_b^+$	0.1	$\check{k}_b^-$	0.01
$\tilde{K}_F^+$	250	$\tilde{k}_F^-$	0.01
$\tilde{K}_R^+$	0.1	$\tilde{K}_R^+$	1
$\tilde{K}_1^+$	0.1	$\tilde{K}_1^-$	0.1
$\tilde{K}_2^+$	0.1	$\tilde{K}_2^-$	0.1

Continued on the next page

Table 5.1 – continued from previous page

Dimensionless parameter	**Value**	**Dimensionless parameter**	**Value**
$\tilde{K}_3^+$	0.5	$\tilde{K}_3^-$	0.1
$\tilde{D}_G$	0.64	$\tilde{D}_F$	0.0192
$\tilde{D}_m$	0.064	$\tilde{D}_m^+$	0.064
$\tilde{D}_f$	0.0064	$\tilde{U}_0$	0.08
$\tilde{D}_P$	0.96	$\tilde{D}_{P-P}$	0.96
$\tilde{D}_K$	0.064	$\tilde{D}_{K-P}$	0.064
$\tilde{D}_C$	0.64	$\tilde{D}_{C-P}$	0.64
$\tilde{\mu}_0$	0.01	$\tilde{\tau}_0$	1
$\tilde{E}_0^S$	5	$\tilde{E}_0^P$	0.5
$\tilde{\kappa}_0^{NA}$	6.25	$\tilde{\kappa}_0^{FA}$	31.25
$\tilde{\beta}_0^{NA}$	0.0625	$\tilde{\beta}_0^{FA}$	0.3125
$\tilde{\beta}_e$	2.5×10^{-9}	$\tilde{\mu}_0^E$	1×10^{-4}
$\tilde{E}_0^C$	1000	$\tilde{E}_0^O$	0
$\tilde{E}_0^N$	10	$\tilde{v}_0$	0.8

Table 5.1: Dimensionless parameters employed in baseline simulations of the two-dimensional model.

In direct correspondence with Fig. 3.7 in Ch. 3, in Fig. 5.3 we elucidate the overall temporal dynamics of cell-substrate binding by presenting a number of global (i.e. spatially-independent) measures of the system which summarise the adhesion strength over time. In particular, we show the radius of the cell (Fig. 5.3a), the partition of integrins across their different forms (Fig. 5.3b), the relative concentrations of activated/phosphorylated proteins compared to the total (Fig. 5.3c) and the partition of the total concentration of actin into its different forms (Fig. 5.3d). In the early stages after the cell is introduced to the substrate the cell diameter remains almost fixed (Fig. 5.3a, compare with Fig. 3.7a), whilst there is a rapid (almost instantaneous) conversion of free integrins into high-affinity integrins (Fig. 5.3b), this is also predicted by our one-dimensional model (see Fig. 3.7b). High-affinity integrins subsequently bind to ECM ligands to form nascent adhesions, as shown in Fig. 5.3(b). Just as we observe in our one-dimensional model in Fig. 3.7(c), in response to nascent adhesion formation, ROCK becomes weakly activated, leading to phosphorylation of MLCP, MLCK and cofilin (Fig. 5.3c). Consequently, actin is polymerised and a small amount of myosin II is activated, leading to an increase in actin filament concentration and a small increase in VSF concentration (Fig. 5.3d, compare with Fig. 3.7d). In response to the formation of VSFs, the cell begins to contract (Fig. 5.3a), in turn pulling on bound integrins, stretching them and exposing VBSs. Stretching of bound

integrins leads to maturation of adhesions and a significant increase in ROCK activation (in line with Eq. 5.17) and, consequently, MLCP, MLCK and cofilin phosphorylation (from Sec. 5.5.1). This, based on Eq. (5.18), initiates our positive feedback loop, with the activation of signaling proteins leading to an increase (decrease) in actin polymerisation (depolymerisation) and in myosin II activation (inactivation). Hence, there is a significant increase in actin filament and VSF formation and so the cell continues to contract (Fig. 5.3a). After approximately 2500 s, the cell settles to an apparent steady state (Fig. 5.3). However, within the cell the redistribution of myosin II bound actin filaments and localisation of FAs continues on a longer time scale before the cell finally reaches a full steady state as seen in Figs. 5.4-5.7 (below). As discussed in Sec. 3.8, this final steady state is a consequence of our modelling approach; in reality the cell would continue to grow, interact with neighbouring cells and remodel its environment. In summary, Fig. 5.3 illustrates the global changes in the cell when adhering to a substrate, particularly capturing the changes in diameter (contraction) commensurate with the coupled formation and maturation of FAs and VSFs. Again, we note the note the similarities of Figs. 5.3(b)-(d) with Figs. 2.1(a)-(c) in Ch. 2, reinforcing the idea that our simple spatially-averaged model is successful in describing the global dynamics of cell-substrate adhesion and cytoskeleton formation. We also note the overshoot in cell contraction in simulations of this model (see for example Fig. 5.3a), which is not particularly apparent in simulations of our one-dimensional model (see Fig. 3.7a). This results from the faster myosin dynamics assumed in this model (see Table 5.1), which leads to enhanced VSF formation and cell contraction before adhesions mature and further resist deformation.

Replicating our analysis in Sec. 3.8, we proceed to examine in detail how this global process manifests locally within the cell. We first elucidate the mechanical changes during cell-substrate binding. In particular, Fig. 5.4 illustrates (radial) spatial profiles of the cell cytoplasm and ECM (at the eight timepoints highlighted above), including the coupled radial displacement (and strain) of material points (Fig. 5.4a,b) and the corresponding radial component of the Cauchy stress (Fig. 5.4c,d). As we observe in Fig. 3.8, there is initially no deformation or stress inside the cell but, over time, in response to the formation and maturation of cell-substrate adhesions and associated formation of VSFs, the cell contracts (i.e. exhibits inward displacement, Figs. 5.3a, 5.4a). After approximately 250-500 s, the feedback loop connecting FA and VSF formation becomes evident and there is significant contraction of the cell due to the action of myosin II motors. This displacement is particularly pronounced near the cell boundary (Fig. 5.3a), where there is concentrated myosin II cross-linking of actin filaments (as in Fig. 5.7 below). We observe a non-uniform striation pattern (see spatial variations in cell contraction in the inset in Fig. 5.4a), where the cell is particularly contracted near the cell membrane but with little deformation near the nucleus. Particularly, there is no deformation on the boundary with the nucleus, in line

with our imposed boundary condition in Eq. (5.8b). This spatial inhomogeneity blunts overall cell contraction and maintains almost isometric tension (Fig. 5.3a). Moreover, there is a significant increase in stress in response to FA, actin filament and VSF formation (Fig. 5.4c). In our one-dimensional model, intracellular stress is approximately constant in the cell bulk throughout the development of cell-substrate adhesions and cell cytoskeleton (see Fig. 3.8c). In contrast, in this two-dimensional model, the rigid nucleus leads to a pronounced increase in intracellular stress towards the cell centre at early stages of adhesion, when the mechanical contribution of the rigid nucleus dominates. Over time, this disparity persists but reduces as the mechanical effects of mature adhesions and contractile VSFs near the cell edge begin to contribute significantly. Throughout this process of cell-substrate adhesion and cytoskeleton development, in a similar manner to the one-dimensional model, stress rapidly decays to zero at the boundary (this is enforced through the boundary condition Eq. 5.8c). The adhesive coupling between the cell and the ECM consequently leads to ECM displacement and strain (Fig. 5.4b), coupled to an ECM stress (Fig. 5.4d). However, as discussed in Sec. 3.8, the ECM is significantly stiffer than the cell and consequently exhibits much smaller relative displacements and strain compared to the cell (whilst showing comparable levels of stress), with a qualitatively similar distribution of each. Once again, given that we measure adhesion length using the relative deformation of the cell to the ECM (see Eq. 5.20), in this case (where the much stiffer ECM resists deformation) the adhesions between the cell and ECM become highly stretched, following a similar pattern of deformation to the cell. Consequently, FAs form predominantly near the cell boundaries (as shown in Fig. 5.5 below), leading to an increase in ROCK signaling in this region (as shown in Fig. 5.6 below). To summarise, Fig. 5.4 illustrates the mechanical changes (displacement, stress and strain) that occur in both the cell and ECM when a cell adheres to a substrate and can be compared directly with broadly similar predictions from our one-dimensional model presented in Fig. 3.8. We now, in a similar manner to Sec. 3.8, explore the local behaviour of adhesion, signaling protein and actin dynamics.

In Figs. 5.5-5.7 we summarise the dynamics of the key cytoskeletal, adhesion and signaling proteins in the baseline case shown in Figs. 5.3-5.4. In analogue with Fig. 3.9, we account for the spatial and temporal changes in integrin and adhesion distribution in Fig. 5.5. Initially there are no adhesions between the cell and substrate, with all integrins uniformly dispersed and in a free state with low-affinity to the ECM (Fig. 5.5a-b). These integrins rapidly bind to talin to form high-affinity integrins (Fig. 5.5c-d), which are able to bind to ligands in the underlying ECM to form bound integrins (Fig. 5.5e-f). As predicted by our one-dimensional model (see Fig. 3.9), early activation of integrins and binding to ECM ligands to form nascent adhesions occurs almost uniformly, owing to the high diffusivity of free integrins and the assumed uniformity in initial free integrin and ligand density. In response to signaling, the bound integrins will eventually go on to mature into

FAs (Fig. 5.5g-h).

The formation of nascent adhesions initiates weak signaling inside the cell, the dynamics of this process are summarised in Fig. 5.6 and can be compared with near identical dynamics in Fig. 3.10 predicted by our one-dimensional model. In particular, ROCK becomes weakly activated (Fig. 5.6a-b). This occurs nearly uniformly, reflecting the early uniform distribution of nascent adhesions (and lack of FAs). In response to ROCK activation, phosphorylation of MLCP (Fig. 5.6c-d), MLCK (Fig. 5.6e-f) and cofilin (Fig. 5.6g-h) occurs. These are also uniform at early times, resultant from a combination of uniform ROCK activation and because they are all assumed to be diffusive. The weak activation of ROCK leads to an increase in actin polymerisation across the cell at nascent adhesions. Moreover, the phosphorylation of MLCP (MLCK) leads to a decrease (increase) in myosin II inactivation (activation) and cofilin phosphorylation leads to a reduction in actin depolymerisation.

In response to signaling, actin is polymerised and myosin II is activated leading to the formation of actin filaments and VSFs. The dynamics of these are summarised in Fig. 5.7 and can be directly compared with predictions from our one-dimensional model presented in Fig. 3.9. In particular we consider the temporal (spatial) dynamics of actin monomers in Fig. 5.7(a) (Fig. 5.7b), of actin filaments in Fig. 5.7(c) (Fig. 5.7d), of VSFs in Fig. 5.7(e) (Fig. 5.7f) and of myosin II in Fig. 5.7(g) (Fig. 5.7h). At early times there is, consistent with the near uniform weak signaling, a nearly uniform decrease in actin monomer concentration (Fig. 5.7a-b) as actin is polymerised, leading to an increase in actin filament concentration (Fig. 5.7c-d). The small amount of activated myosin II (Fig. 5.7g-h) then begins to cross-link actin filaments and form contractile VSFs (Fig. 5.7e-f). As a consequence of contraction of resultant VSFs, bound integrins are pulled (stretched), enhancing FA formation and in turn signaling and VSF formation, consequently Figs. 5.5-5.7 are intimately linked and feedback to one another.

The formation of VSFs, particularly the contractile action of myosin motors, causes the cell to begin to contract approximately 250-500 s after being introduced to the substrate (Figs. 5.3a, 5.4a). At this time the positive feedback loop becomes activated. This contraction is most keenly felt near the cell edge, leading to maturation of bound integrins into FAs in this region (Fig. 5.5g-h) as VBSs become exposed as bound integrins become stretched (Fig. 5.4a-b). Consequently there is also a transient increase in the cell in the number of bound integrins (Fig. 5.5e-f). Reflecting the inhomogeneity in FA formation (Fig. 5.5g-h), spatial variations emerge in free integrin (Fig. 5.5a-b) and high-affinity integrin density (Fig. 5.5c-d), though these differences remain relatively small owing to the high-diffusivity of free integrins. As ROCK activation is significantly enhanced in response to FA formation (compared to nascent adhesions) and because ROCK (in both inactive and active forms) is assumed to be non-diffusive, significant spatial distributions

arise in activated ROCK concentration (Fig. 5.6a-b), mirroring the spatial distribution in FA density (Fig. 5.5g-h). Consequently, phosphorylation of MLCP (Fig. 5.6c-d), MLCK (Fig. 5.6e-f) and cofilin (Fig. 5.6g-h) becomes significantly enhanced, though these proteins are diffusive and so are comparatively spatially homogeneous (as would be expected based on dimensionless parameters presented in Table 5.1). These phosphorylated signaling proteins consequently lead to a significant increase in actin polymerisation (Fig. 5.7c-d) in the locality of FAs and in turn a significant decrease in actin monomer concentration (Fig. 5.7a-b). However, this reduction in monomer concentration occurs approximately uniformly, owing to the high diffusivity of actin monomers. The resultant filaments are treadmilled towards the cell nucleus and are cross-linked, in the vicinity of FAs, by activated myosin II (Fig. 5.7g-h), leading to a significant increase in VSF concentration near FAs (Fig. 5.7e-f). These VSFs exert further contractile forces on bound integrins, leading to more FA formation (Fig. 5.5g-h), strengthened signaling (Fig. 5.6) and consequently more VSF formation (Fig. 5.7e-f). This process of rapid increases in FA and VSF formation occurs over the course of around 500-2000 s after the cell is introduced to the substrate. Thereafter, redistribution of adhesions (Fig. 5.5e-h), signaling hubs (Fig. 5.6) and VSFs (Fig. 5.7e-f) dominates until a steady state is reached (after around 10000 s).

In summary Figs. 5.5-5.7 reproduce the predictions of their one-dimensional counterparts Figs. 3.9-3.11 in Ch. 3. When taken together, Figs. 5.5-5.7 demonstrate the effect of the positive feedback loop in the cell. They show how adhesion formation precipitates signaling inside the cell which, in turn, leads to the formation of actin filaments and VSFs and are able to capture how increased SF formation leads, through cell contraction (as shown in Figs. 5.3-5.4), to increased and localised FA formation.

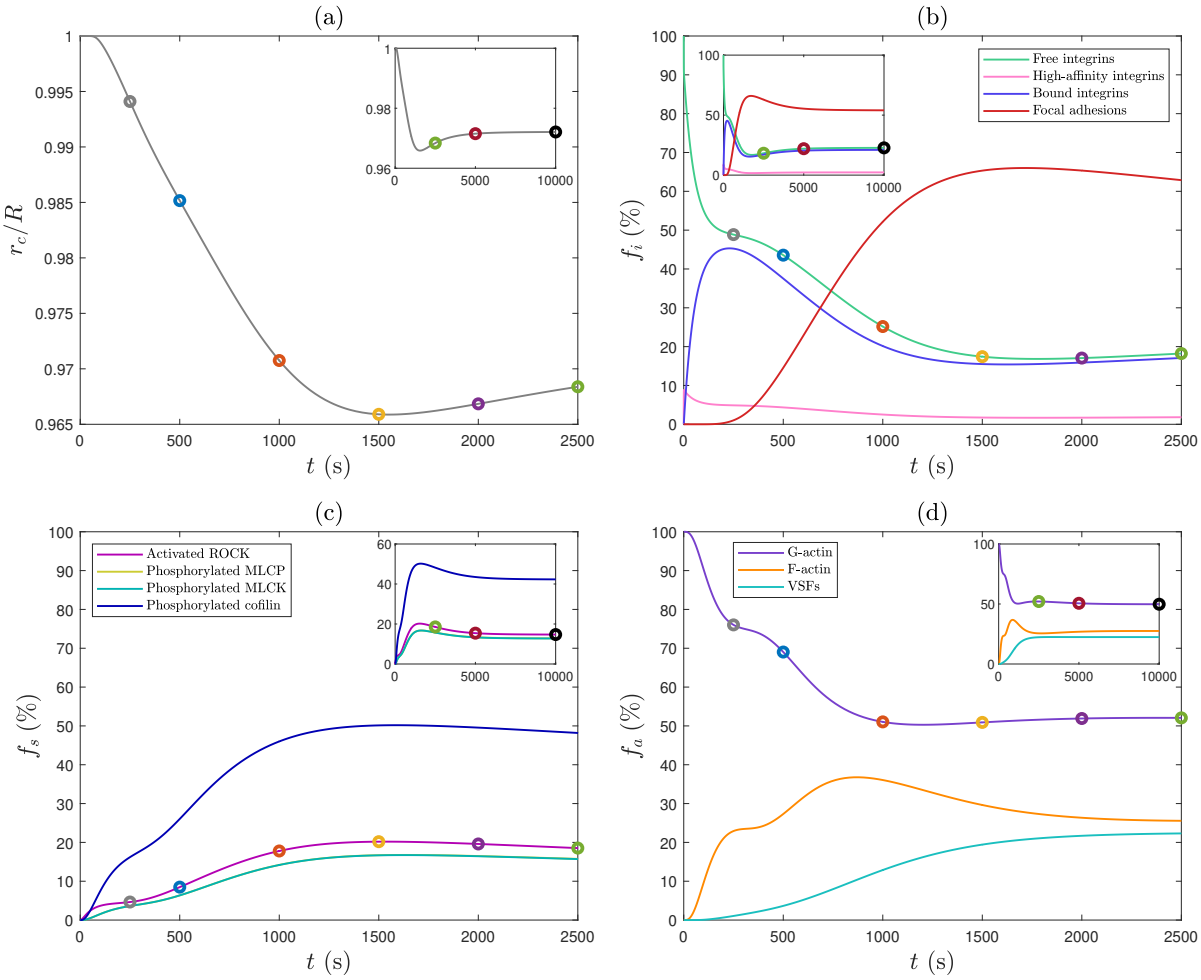

Figure 5.3: Global measures of cytoskeleton and adhesion development. (a) Evolution of dimensionless cell radius with time. Time-dependent evolution of percentage of total: (b) integrins in their various forms (free low-affinity integrins, high-affinity integrins, bound integrins and recruited into FAs), (c) ROCK activated and MLCP, MLCK and cofilin phosphorylated, (d) actin in its different forms (monomeric, polymerised into filaments or recruited into SFs). Insets show large time dynamics for each property, open circles indicate times of interest, corresponding to identically coloured lines in spatial distributions in Figs. 5.4-5.7. Parameter values are given in Table 5.1.

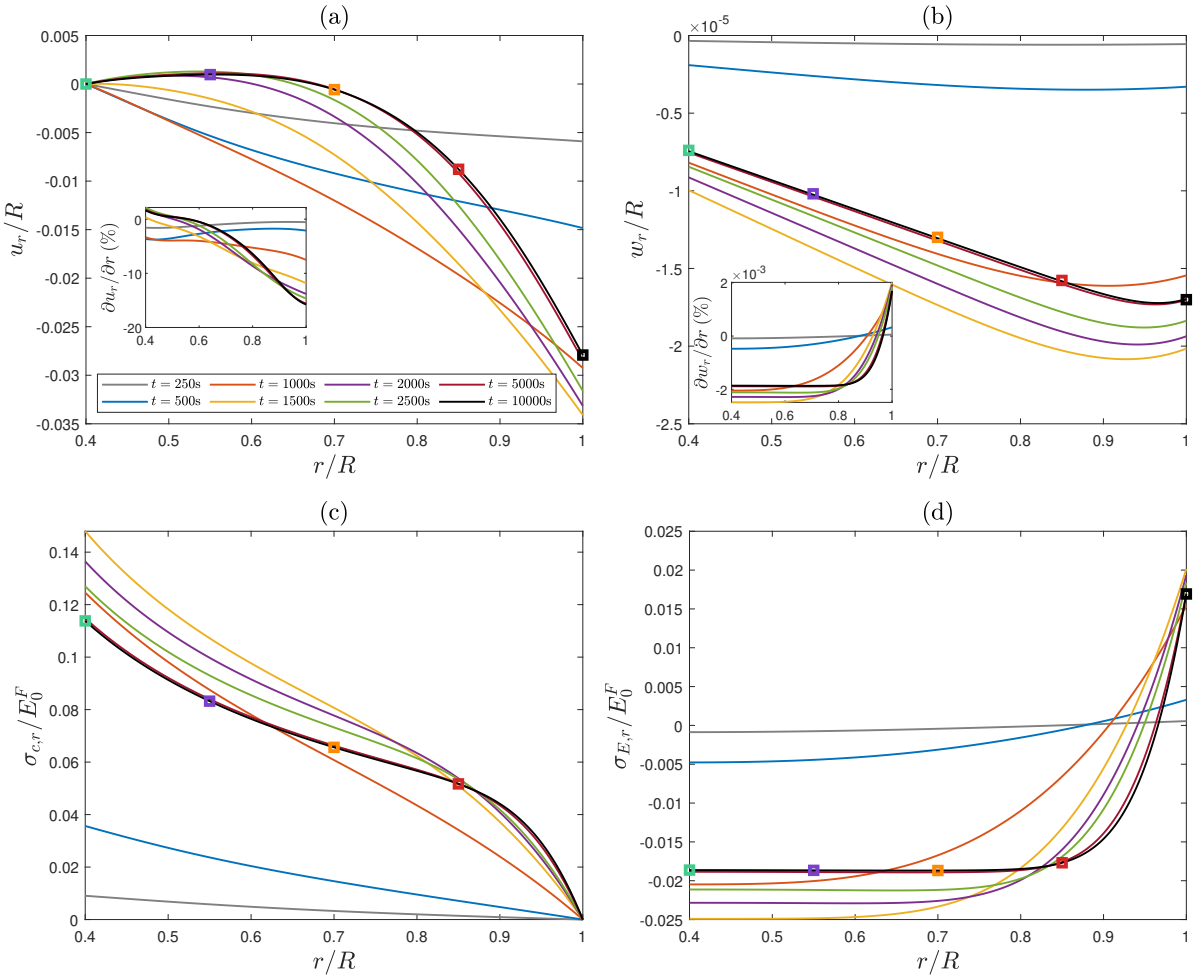

Figure 5.4: Mechanical properties of the cell and ECM. At snapshots in time, as a function of initial dimensionless radial position, dimensionless (a) radial displacement of points in cell from their initial position, (b) radial displacement of points in ECM from their initial position, (c) radial stress in cytosol, (d) radial stress in ECM. Insets in (a), (b) show radial strain, percentage stretch (positive)/compression (negative), of the cell and ECM respectively. Parameter values are given in Table 5.1.

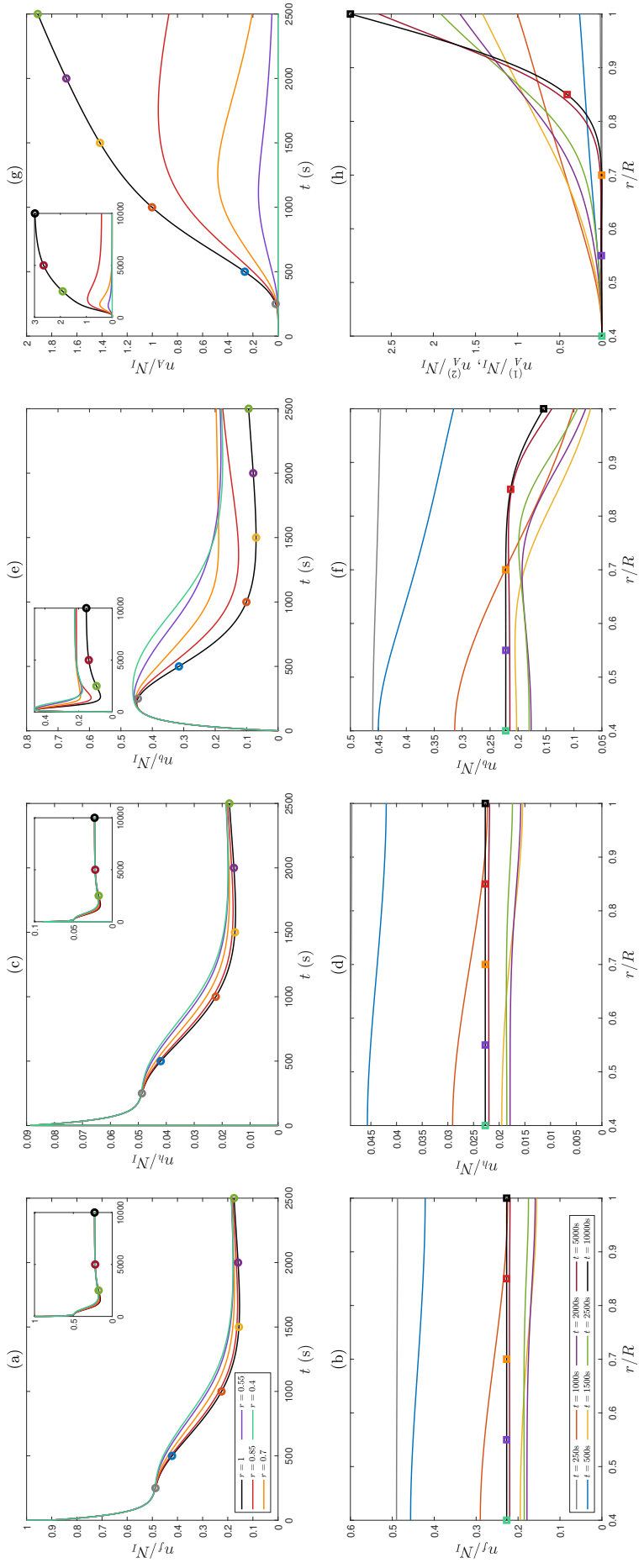

Figure 5.5: Integrin and adhesion dynamics. Spatial (radial) dynamics of integrins and adhesions where solid (dashed) lines are used to denote family one (family two) dynamics. Temporal dynamics of (a) free integrins, (c) high-affinity, (e) nascent adhesions and (g) FAs where density is dimensionless and time is dimensional (measured in seconds), insets show long time dynamics (up to $t = 10000$ s). Spatial (radial) distribution at snapshots in time of (b) free integrins, (d) high-affinity integrins, (f) nascent adhesions and (h) FAs where density and position are dimensionless. Parameter values are given in Table 5.1.

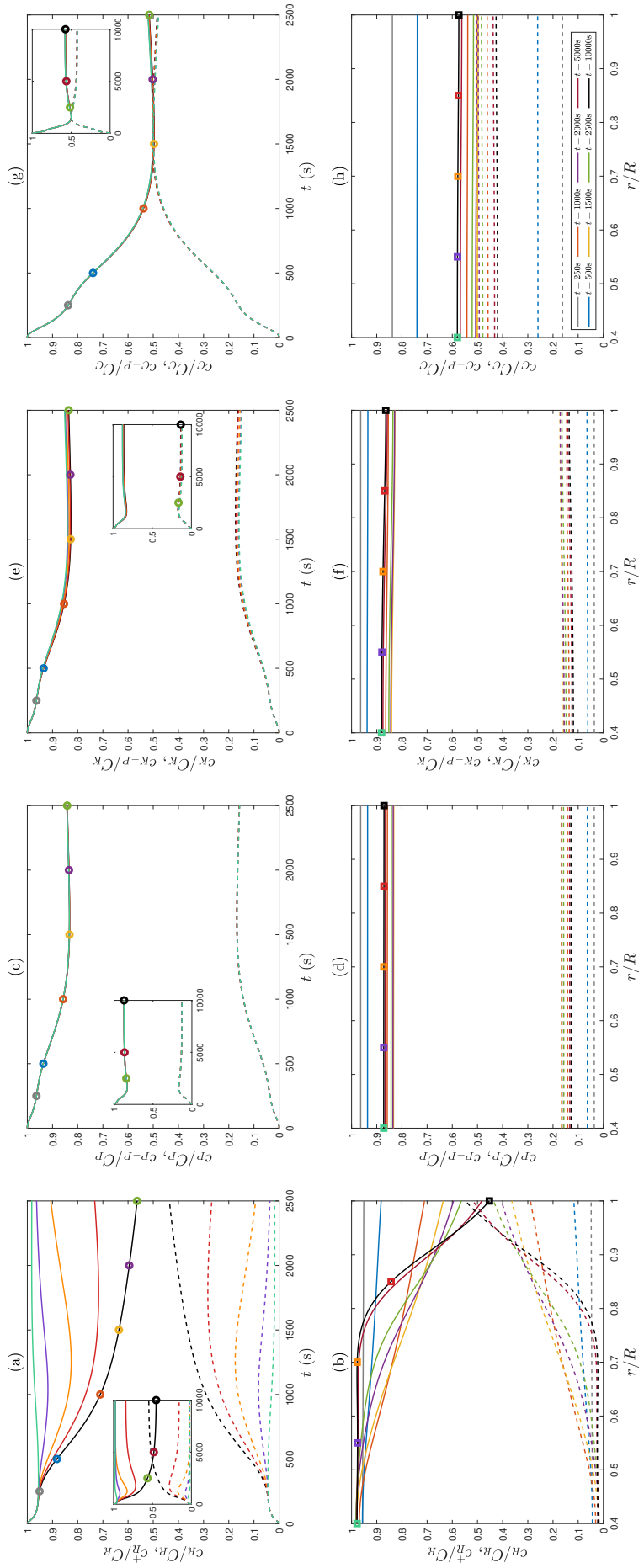

Figure 5.6: Signaling protein dynamics. Temporal and spatial (radial) dynamics of signaling proteins and downstream effectors where solid (dashed) lines are used to denote inactivated (activated) ROCK or unphosphorylated (phosphorylated) MLCP, MLCK and cofilin. Temporal dynamics of (a) ROCK, (c) MLCP, (e) MLCK and (g) cofilin where concentration is dimensionless and time is dimensional (measured in seconds), insets show long time dynamics (up to $t = 10000$ s). Spatial (radial) distribution at snapshots in time of (b) ROCK, (d) MLCP, (f) MLCK and (h) cofilin where concentration and position are dimensionless. Parameter values are given in Table 5.1.

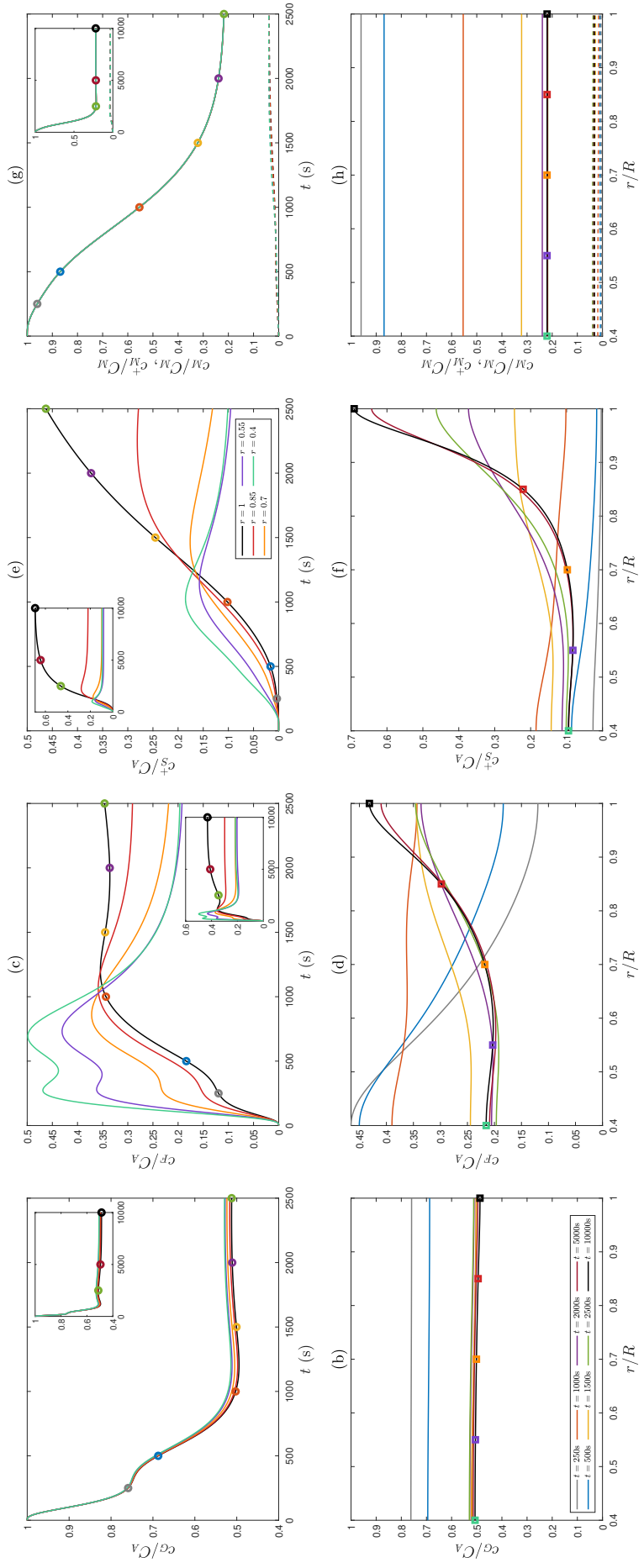

Figure 5.7: Actin and myosin dynamics. Temporal and spatial (radial) dynamics of actin families and myosin II where solid (dashed) lines are used to denote family one (family 2) actin filaments or to denote inactivated (activated) myosin II. Temporal dynamics of (a) actin monomers, (c) actin filaments, (e) actomyosin VSFs and (g) myosin II where concentration is dimensionless and time is dimensional (measured in seconds), insets show long time dynamics (up to $t = 10000$ s). Spatial (radial) distribution at snapshots in time of (b) actin monomers, (d) actin filaments, (f) actomyosin VSFs and (h) myosin II where concentration and position are dimensionless. Parameter values are given in Table 5.1.

5.7 Linearisation around the axisymmetric state

In Sec. 5.6 we found that the cell forms adhesions and develops contractile VSFs when introduced to a (stiff) substrate. We observe in Sec. 5.6.4 that, after some time (on the order of an hour), the cell will settle to a near steady axisymmetric state. In order to understand the susceptibility of the cell to non-axisymmetric deformations, we linearise the model around this axisymmetric base state. In particular, we perturb all quantities with a modal perturbation of (small) amplitude ϵ. Hence, all concentrations and densities can be written as the sum of a baseline value (denoted by a bar) and a perturbation (denoted by a hat), i.e. $c = \bar{c} + \epsilon\hat{c}$, $n = \bar{n} + \epsilon\hat{n}$. Moreover, displacements in the cell and ECM be written as $\boldsymbol{u} = \bar{\boldsymbol{u}} + \epsilon\hat{\boldsymbol{u}}$, $\boldsymbol{w} = \bar{\boldsymbol{w}} + \epsilon\hat{\boldsymbol{w}}$ and we assume all mechanical properties of the cell, ECM and adhesions can be written as the sum of a baseline axisymmetric component (denoted by a bar) and a small modal perturbation denoted by a hat. All values denoted by a bar correspond to the axisymmetric base state values extracted from our axisymmetric model, discussed in Sec. 5.6.4, and consequently have no $\theta-$dependence. Note that this linearisation is independent of the assumption of linear elasticity, which is present in the axisymmetric model also.

5.7.1 Mechanical equations

The Cauchy stress inside the cell cytoplasm can similarly be decomposed into its axisymmetric base state value plus a small perturbation, by writing $\boldsymbol{\sigma}_c = \bar{\boldsymbol{\sigma}}_c + \epsilon\hat{\boldsymbol{\sigma}}_c$ with

$$\boldsymbol{\sigma_c} = \left(\bar{E}_c + \epsilon\hat{E}_c\right)\left(\bar{\boldsymbol{\epsilon}}_c + \epsilon\hat{\boldsymbol{\epsilon}}_c\right) + \left(\bar{\mu}_c + \epsilon\hat{\mu}_c\right)\left(\frac{\partial\bar{\boldsymbol{\epsilon}}_c}{\partial t} + \epsilon\frac{\partial\hat{\boldsymbol{\epsilon}}_c}{\partial t}\right) + \left(\bar{\boldsymbol{\tau}} + \epsilon\hat{\boldsymbol{\tau}}\right) + O\left(\epsilon^2\right). \tag{5.44}$$

It follows that

$$\boldsymbol{\sigma}_c = \bar{E}_c\bar{\boldsymbol{\epsilon}}_c + \bar{\mu}_c\frac{\partial\bar{\boldsymbol{\epsilon}}_c}{\partial t} + \bar{\boldsymbol{\tau}} + \epsilon\left(\bar{E}_c\hat{\boldsymbol{\epsilon}}_c + \hat{E}_c\bar{\boldsymbol{\epsilon}}_c + \bar{\mu}_c\frac{\partial\hat{\boldsymbol{\epsilon}}_c}{\partial t} + \hat{\mu}_c\frac{\partial\bar{\boldsymbol{\epsilon}}_c}{\partial t} + \hat{\boldsymbol{\tau}}\right) + O\left(\epsilon^2\right), \tag{5.45}$$

where, noting the assumption that $\bar{u}_r$ is independent of θ and $\bar{u}_\theta = 0$ (from Sec. 5.6),

$$\bar{\boldsymbol{\epsilon}}_c = \frac{\partial\bar{u}_r}{\partial r}\boldsymbol{e}_r \otimes \boldsymbol{e}_r + \frac{\bar{u}_r}{r}\boldsymbol{e}_\theta \otimes \boldsymbol{e}_\theta, \tag{5.46a}$$

and where the perturbation infinitesimal stress tensor is given by

$$\hat{\boldsymbol{\epsilon}}_c = \frac{\partial\hat{u}_r}{\partial r}\boldsymbol{e}_r \otimes \boldsymbol{e}_r + \frac{1}{r}\left(\frac{\partial\hat{u}_\theta}{\partial\theta} + \hat{u}_r\right)\boldsymbol{e}_\theta \otimes \boldsymbol{e}_\theta + \frac{1}{2}\left(\frac{1}{r}\frac{\partial\hat{u}_r}{\partial\theta} + \frac{\partial\hat{u}_\theta}{\partial r} - \frac{\hat{u}_\theta}{r}\right)\left(\boldsymbol{e}_r \otimes \boldsymbol{e}_\theta + \boldsymbol{e}_\theta \otimes \boldsymbol{e}_r\right). \tag{5.46b}$$

From Eq. (5.4a) we have

$$\nabla \cdot \boldsymbol{\sigma}_c = \left(\bar{\beta}_I + \epsilon\hat{\beta}_I\right)\frac{\partial}{\partial t}\left(\bar{\boldsymbol{u}} + \epsilon\hat{\boldsymbol{u}} - \bar{\boldsymbol{w}} - \epsilon\hat{\boldsymbol{w}}\right) + \left(\bar{\kappa}_I + \epsilon\hat{\kappa}_I\right)\left(\bar{\boldsymbol{u}} + \epsilon\hat{\boldsymbol{u}} - \bar{\boldsymbol{w}} - \epsilon\hat{\boldsymbol{w}}\right) + O\left(\epsilon^2\right). \tag{5.47}$$

Combining Eq. (5.45) and Eq. (5.47) then at $O(\epsilon^0)$ we have

$$\nabla \cdot \left(\bar{E}_c\bar{\boldsymbol{\epsilon}}_c + \bar{\mu}_c\frac{\partial\bar{\boldsymbol{\epsilon}}_c}{\partial t} + \bar{\tau}\right) = \bar{\beta}_I\frac{\partial}{\partial t}\left(\bar{\boldsymbol{u}} - \bar{\boldsymbol{w}}\right) + \bar{\kappa}_I\left(\bar{\boldsymbol{u}} - \bar{\boldsymbol{w}}\right), \tag{5.48}$$

this is precisely the axisymmetric problem we have already solved in Sec. 5.6, with results detailed in Sec. 5.6.4. At $O(\epsilon)$ we have from Eq. (5.45) and Eq. (5.47) that

$$\begin{aligned}\nabla \cdot \left(\bar{E}_c\hat{\boldsymbol{\epsilon}}_c + \hat{E}_c\bar{\boldsymbol{\epsilon}}_c + \bar{\mu}_c\frac{\partial\hat{\boldsymbol{\epsilon}}_c}{\partial t} + \hat{\mu}_c\frac{\partial\bar{\boldsymbol{\epsilon}}_c}{\partial t} + \hat{\boldsymbol{\tau}}\right) &= \bar{\beta}_I\frac{\partial}{\partial t}\left(\hat{\boldsymbol{u}} - \hat{\boldsymbol{w}}\right) + \hat{\beta}_I\frac{\partial}{\partial t}\left(\bar{\boldsymbol{u}} - \bar{\boldsymbol{w}}\right) \\ &+\bar{\kappa}_I\left(\hat{\boldsymbol{u}} - \hat{\boldsymbol{w}}\right) + \hat{\kappa}_I\left(\bar{\boldsymbol{u}} - \bar{\boldsymbol{w}}\right).\end{aligned} \tag{5.49}$$

In an identical manner we write the Cauchy stress in the ECM as $\boldsymbol{\sigma}_E = \bar{\boldsymbol{\sigma}}_E + \epsilon\hat{\boldsymbol{\sigma}}_E$. A similar calculation demonstrates that

$$\bar{\boldsymbol{\epsilon}}_E = \frac{\partial\bar{w}_r}{\partial r}\boldsymbol{e}_r \otimes \boldsymbol{e}_r + \frac{\bar{w}_r}{r}\boldsymbol{e}_\theta \otimes \boldsymbol{e}_\theta, \tag{5.50}$$

with the infinitesimal perturbation strain tensor given by

$$\hat{\boldsymbol{\epsilon}}_E = \frac{\partial\hat{w}_r}{\partial r}\boldsymbol{e}_r \otimes \boldsymbol{e}_r + \frac{1}{r}\left(\frac{\partial\hat{w}_\theta}{\partial\theta} + \hat{w}_r\right)\boldsymbol{e}_\theta \otimes \boldsymbol{e}_\theta + \frac{1}{2}\left(\frac{1}{r}\frac{\partial\hat{w}_r}{\partial\theta} + \frac{\partial\hat{w}_\theta}{\partial r} - \frac{\hat{w}_\theta}{r}\right)\left(\boldsymbol{e}_r \otimes \boldsymbol{e}_\theta + \boldsymbol{e}_\theta \otimes \boldsymbol{e}_r\right). \tag{5.51}$$

We hence deduce, in a similar manner to the cell, the linearised ECM displacement equation

$$\begin{aligned}\nabla \cdot \left(\bar{E}_E\hat{\boldsymbol{\epsilon}}_E + \hat{E}_E\bar{\boldsymbol{\epsilon}}_E + \bar{\mu}_E\frac{\partial\hat{\boldsymbol{\epsilon}}_E}{\partial t} + \hat{\mu}_E\frac{\partial\bar{\boldsymbol{\epsilon}}_E}{\partial t}\right) &= \bar{\beta}_I\frac{\partial}{\partial t}\left(\hat{\boldsymbol{w}} - \hat{\boldsymbol{u}}\right) + \hat{\beta}_I\frac{\partial}{\partial t}\left(\bar{\boldsymbol{w}} - \bar{\boldsymbol{u}}\right) \\ &+\bar{\kappa}_I\left(\hat{\boldsymbol{w}} - \hat{\boldsymbol{u}}\right) + \hat{\kappa}_I\left(\bar{\boldsymbol{w}} - \bar{\boldsymbol{u}}\right).\end{aligned} \tag{5.52}$$

Initial and boundary conditions

We perturb our linearised system from the baseline state identified in Sec. 5.6. The form of this perturbation (i.e. the initial condition imposed) is discussed in detail in Sec. 5.9 (below).

The condition on the perturbation displacement at the boundary between the cell cytoplasm and cell nucleus is

$$\hat{\boldsymbol{u}}(R_n, \theta, t) = \boldsymbol{0}. \tag{5.53a}$$

On the edge of the cell adjacent to the cell membrane, the boundary conditions are applied in the unperturbed domain (following work in linear elasticity by Biot, 1963, Martin and Payton, 1964). It follows from Eq. (5.8c) that

$$(\hat{\boldsymbol{\sigma}}_c \boldsymbol{e}_r) \cdot \boldsymbol{e}_r = 0. \tag{5.53b}$$

At the edge of the cell connected to the cell membrane we also have from Eq. (5.8d) that

$$(\hat{\boldsymbol{\sigma}}_c \boldsymbol{e}_r) \cdot \boldsymbol{e}_\theta = 0. \tag{5.53c}$$

The perturbation boundary conditions on the ECM are given by

$$\hat{\boldsymbol{w}}(0, \theta, t) = \boldsymbol{0}, \quad \lim_{r \to \infty} \hat{\boldsymbol{w}}(r, \theta, t) = \boldsymbol{0}, \tag{5.53d}$$

whilst at the junctions between ECM regions either side of the cell cytoplasm boundary we match stress and displacement, as in Sec. 3.1.7 and Sec. 5.6.1. In particular, from Eqs. (5.12f)-(5.12i), at $O(\epsilon)$ for regions 1 and 2 we have

$$(\hat{\boldsymbol{\sigma}}_E \boldsymbol{n}_1) \cdot \boldsymbol{n}_1 = \left(\hat{\bar{\boldsymbol{\sigma}}}_{E,1} \boldsymbol{n}_1\right) \cdot \boldsymbol{n}_1, \quad (\hat{\boldsymbol{\sigma}}_E \boldsymbol{n}_1) \cdot \boldsymbol{t}_1 = \left(\hat{\bar{\boldsymbol{\sigma}}}_{E,1} \boldsymbol{n}_1\right) \cdot \boldsymbol{t}_1, \tag{5.53e}$$

$$(\hat{\boldsymbol{\sigma}}_E \boldsymbol{n}_2) \cdot \boldsymbol{n}_2 = \left(\hat{\bar{\boldsymbol{\sigma}}}_{E,2} \boldsymbol{n}_2\right) \cdot \boldsymbol{n}_2, \quad (\hat{\boldsymbol{\sigma}}_E \boldsymbol{n}_2) \cdot \boldsymbol{t}_2 = \left(\hat{\bar{\boldsymbol{\sigma}}}_{E,2} \boldsymbol{n}_2\right) \cdot \boldsymbol{t}_2, \tag{5.53f}$$

where, for $i = 1, 2$, $\check{\boldsymbol{\sigma}}_i = \bar{\bar{\boldsymbol{\sigma}}}_i + \epsilon \hat{\bar{\boldsymbol{\sigma}}}_i$, $\boldsymbol{n}_i = \pm \boldsymbol{e}_r$ and $\boldsymbol{t}_i = \pm \boldsymbol{e}_\theta$.

5.7.2 Biochemistry

We introduce small perturbations to all concentrations and densities in the biochemical equations Eqs. (5.42). The $O(\epsilon^0)$ equations are exactly those solved in Sec. 5.6.2 given by Eqs. (5.42). At $O(\epsilon)$ we have

$$\begin{aligned} \frac{\partial \hat{c}_G}{\partial t} = &- \left(\bar{k}_p^+ \bar{c}_G (\hat{n}_b + \hat{n}_A) + \hat{k}_p^+ \hat{c}_G (\bar{n}_b + \bar{n}_A) + \hat{k}_p^+ \bar{c}_G (\bar{n}_b + \bar{n}_A)\right) \\ &+ \left(\bar{k}_p^- \hat{c}_F + \hat{k}_p^- \bar{c}_F\right) + k_m^- \hat{c}_S^+ + D_G \left(\frac{\partial^2 \hat{c}_G}{\partial r^2} + \frac{1}{r}\frac{\partial \hat{c}_G}{\partial r} + \frac{1}{r^2}\frac{\partial^2 \hat{c}_G}{\partial \theta^2}\right), \end{aligned} \tag{5.54a}$$

$$\begin{aligned} \frac{\partial \hat{c}_F}{\partial t} + \frac{1}{r}\frac{\partial (r \hat{c}_F v_r)}{\partial r} = &\left(\bar{k}_p^+ \bar{c}_G (\hat{n}_b + \hat{n}_A) + \hat{k}_p^+ \hat{c}_G (\bar{n}_b + \bar{n}_A) + \hat{k}_p^+ \bar{c}_G (\bar{n}_b + \bar{n}_A)\right) - \left(\bar{k}_p^- \hat{c}_F + \hat{k}_p^- \bar{c}_F\right) \\ &- k_m^+ \left(\bar{c}_F \bar{c}_m^+ \left(\hat{c}_F + \hat{c}_S^+\right) + \bar{c}_F \hat{c}_m^+ \left(\bar{c}_F + \bar{c}_S^+\right) + \hat{c}_F \bar{c}_m^+ \left(\bar{c}_F + \bar{c}_S^+\right)\right) \\ &+ D_F \left(\frac{\partial^2 \hat{c}_F}{\partial r^2} + \frac{1}{r}\frac{\partial \hat{c}_F}{\partial r} + \frac{1}{r^2}\frac{\partial^2 \hat{c}_F}{\partial \theta^2}\right), \end{aligned} \tag{5.54b}$$

$$\frac{\partial \hat{c}_S^+}{\partial t} = k_m^+ \left(\bar{c}_F \bar{c}_m^+ \left(\hat{c}_F + \hat{c}_S^+\right) + \bar{c}_F \hat{c}_m^+ \left(\bar{c}_F + \bar{c}_S^+\right) + \hat{c}_F \bar{c}_m^+ \left(\bar{c}_F + \bar{c}_S^+\right)\right) - k_m^+ \hat{c}_S^+, \tag{5.54c}$$

$$\frac{\partial \hat{c}_m}{\partial t} = - \left(\bar{k}_a^+ \hat{c}_m + \hat{k}_a^+ \bar{c}_m\right) + \left(\bar{k}_a^- \hat{c}_m^+ + \hat{k}_a^- \bar{c}_m^+\right) + D_m \left(\frac{\partial^2 \hat{c}_m}{\partial r^2} + \frac{1}{r}\frac{\partial \hat{c}_m}{\partial r} + \frac{1}{r^2}\frac{\partial^2 \hat{c}_m}{\partial \theta^2}\right), \tag{5.54d}$$

$$\frac{\partial c_m^+}{\partial t} = \left(\bar{k}_a^+ \hat{c}_m + \hat{k}_a^+ \bar{c}_m\right) - \left(\bar{k}_a^- \hat{c}_m^+ + \hat{k}_a^- \bar{c}_m^+\right)$$
$$- k_m^+ \left(\bar{c}_F \bar{c}_m^+ \left(\hat{c}_F + \hat{c}_S^+\right) + \bar{c}_F \hat{c}_m^+ \left(\bar{c}_F + \bar{c}_S^+\right) + \hat{c}_F \bar{c}_m^+ \left(\bar{c}_F + \bar{c}_S^+\right)\right) \tag{5.54e}$$
$$+ k_m^- \hat{c}_S^+ + D_m^+ \left(\frac{\partial^2 \hat{c}_m^+}{\partial r^2} + \frac{1}{r}\frac{\partial \hat{c}_m^+}{\partial r} + \frac{1}{r^2}\frac{\partial^2 \hat{c}_m^+}{\partial \theta^2}\right),$$

$$\frac{\partial \hat{n}_f}{\partial t} = -k_h^+ \hat{n}_f + k_h^- \hat{n}_h + D_f \left(\frac{\partial^2 \hat{n}_f}{\partial r^2} + \frac{1}{r}\frac{\partial \hat{n}_f}{\partial r} + \frac{1}{r^2}\frac{\partial^2 \hat{n}_f}{\partial \theta^2}\right), \tag{5.54f}$$

$$\frac{\partial \hat{n}_h}{\partial t} = k_h^+ \hat{n}_f - k_h^- \hat{n}_h - k_b^+ \left(\bar{n}_h \hat{n}_s + \hat{n}_h \bar{n}_s\right) + k_b^- \hat{n}_b, \tag{5.54g}$$

$$\frac{\partial \hat{n}_b}{\partial t} = k_b^+ \left(\bar{n}_h \hat{n}_s + \hat{n}_h \bar{n}_s\right) - k_b^- \hat{n}_b - \left(\bar{k}_F^+ \hat{n}_b + \hat{k}_F^+ \bar{n}_b\right) + k_F^- \hat{n}_A, \tag{5.54h}$$

$$\frac{\partial \hat{n}_A}{\partial t} = \left(\bar{k}_F^+ \hat{n}_b + \hat{k}_F^+ \bar{n}_b\right) - k_F^- \hat{n}_A, \tag{5.54i}$$

$$\frac{\partial n_s}{\partial t} = -k_b^+ \left(\bar{n}_h \hat{n}_s + \hat{n}_h \bar{n}_s\right) + k_b^- \hat{n}_b, \tag{5.54j}$$

$$\frac{\partial \hat{c}_R}{\partial t} = -\left(\bar{k}_R^+ \hat{c}_R + \hat{k}_R^+ \bar{c}_R\right) + \left(\bar{k}_R^- \hat{c}_R^+ + \hat{k}_R^- \bar{c}_R^+\right), \tag{5.54k}$$

$$\frac{\partial \hat{c}_R^+}{\partial t} = \left(\bar{k}_R^+ \hat{c}_R + \hat{k}_R^+ \bar{c}_R\right) - \left(\bar{k}_R^- \hat{c}_R^+ + \hat{k}_R^- \bar{c}_R^+\right), \tag{5.54l}$$

$$\frac{\partial \hat{c}_P}{\partial t} = -\left(\bar{k}_1^+ \hat{c}_P + \hat{k}_1^+ \bar{c}_P\right) + k_1^- \hat{c}_{P-P} + D_P \left(\frac{\partial^2 \hat{c}_P}{\partial r^2} + \frac{1}{r}\frac{\partial \hat{c}_P}{\partial r} + \frac{1}{r^2}\frac{\partial^2 \hat{c}_P}{\partial \theta^2}\right), \tag{5.54m}$$

$$\frac{\partial \hat{c}_{P-P}}{\partial t} = \left(\bar{k}_1^+ \hat{c}_P + \hat{k}_1^+ \bar{c}_P\right) - k_1^- \hat{c}_{P-P} + D_{P-P} \left(\frac{\partial^2 \hat{c}_{P-P}}{\partial r^2} + \frac{1}{r}\frac{\partial \hat{c}_{P-P}}{\partial r} + \frac{1}{r^2}\frac{\partial^2 \hat{c}_{P-P}}{\partial \theta^2}\right), \tag{5.54n}$$

$$\frac{\partial \hat{c}_K}{\partial t} = -\left(\bar{k}_2^+ \hat{c}_K + \hat{k}_2^+ \bar{c}_K\right) + k_2^- \hat{c}_{K-P} + D_K \left(\frac{\partial^2 \hat{c}_K}{\partial r^2} + \frac{1}{r}\frac{\partial \hat{c}_K}{\partial r} + \frac{1}{r^2}\frac{\partial^2 \hat{c}_K}{\partial \theta^2}\right), \tag{5.54o}$$

$$\frac{\partial \hat{c}_{K-P}}{\partial t} = \left(\bar{k}_2^+ \hat{c}_K + \hat{k}_2^+ \bar{c}_K\right) - k_2^- \hat{c}_{K-P} + D_{K-P} \left(\frac{\partial^2 \hat{c}_{K-P}}{\partial r^2} + \frac{1}{r}\frac{\partial \hat{c}_{K-P}}{\partial r} + \frac{1}{r^2}\frac{\partial^2 \hat{c}_{K-P}}{\partial \theta^2}\right), \tag{5.54p}$$

$$\frac{\partial \hat{c}_C}{\partial t} = -\left(\bar{k}_3^+ \hat{c}_C + \hat{k}_3^+ \bar{c}_C\right) + k_3^- \hat{c}_{C-P} + D_C \left(\frac{\partial^2 \hat{c}_C}{\partial r^2} + \frac{1}{r}\frac{\partial \hat{c}_C}{\partial r} + \frac{1}{r^2}\frac{\partial^2 \hat{c}_C}{\partial \theta^2}\right), \tag{5.54q}$$

$$\frac{\partial \hat{c}_{C-P}}{\partial t} = \left(\bar{k}_3^+ \hat{c}_C + \hat{k}_3^+ \bar{c}_C\right) - k_3^- \hat{c}_{C-P} + D_{C-P} \left(\frac{\partial^2 \hat{c}_{C-P}}{\partial r^2} + \frac{1}{r}\frac{\partial \hat{c}_{C-P}}{\partial r} + \frac{1}{r^2}\frac{\partial^2 \hat{c}_{C-P}}{\partial \theta^2}\right), \tag{5.54r}$$

where quantities denoted with a bar represent baseline values calculated from the non-linear simulations presented in Sec. 5.6.

Perturbation to rate constants

Note that Eqs. (5.54) have also required expansion of some reaction rates (those that are non-constant). We deduce the perturbation reaction rates as follows. Let k_g denote a generic reaction rate which depends on a parameter ϕ, i.e. $k_g = k_g(\phi)$. Using Taylor series we can expand

$$k_g(\bar{\phi} + \epsilon\hat{\phi}) = k_g(\bar{\phi}) + \epsilon\hat{\phi}k_g'(\bar{\phi}) + O(\epsilon^2), \tag{5.55}$$

so that

$$\bar{k}_g = k_g\left(\bar{\phi}\right), \quad \hat{k}_g = \hat{\phi}k_g'\left(\bar{\phi}\right), \tag{5.56}$$

where the prime is used to denote differentiation. For most non-constant rates we have a linear relationship in one variable, the only exceptions are the rate of ROCK activation, which from Eq. (5.17) is assumed to depend on both bound integrin and FA density (and consequently requires application of Taylor series for functions of multiple variables), and the rate of FA maturation, which from Eq. (5.19) is assumed to have a quadratic dependence on the adhesion stretch. Hence, the baseline rate constant for each of these quantities is given by

$$\begin{gathered}\bar{k}_p^+ = K_p^+\bar{c}_R^+, \quad \bar{k}_p^- = K_p^-\bar{c}_C, \quad \bar{k}_a^+ = K_a^+\bar{c}_{K-P}, \quad \bar{k}_a^- = K_a^-\bar{c}_P, \\ \bar{k}_R^+ = K_R^+\left(\bar{n}_b + \delta\bar{n}_A\right), \quad \bar{k}_F^+ = k_F^+\bar{\lambda}_I^2,\end{gathered} \tag{5.57}$$

precisely those used in the axisymmetric baseline model. The perturbation rate is given by

$$\begin{gathered}\hat{k}_p^+ = K_p^+\hat{c}_R^+, \quad \hat{k}_p^- = K_p^-\hat{c}_C, \quad \hat{k}_a^+ = K_a^+\hat{c}_{K-P}, \quad \hat{k}_a^- = K_a^-\hat{c}_{P-P}, \\ \hat{k}_R^+ = K_R^+\left(\hat{n}_b + \delta\hat{n}_A\right), \quad \bar{k}_F^+ = 2K_F^+\bar{\lambda}_I\hat{\lambda}_I.\end{gathered} \tag{5.58}$$

From Eq. (5.20) we have

$$\lambda_I = \bar{\lambda}_I + \epsilon\hat{\lambda}_I = \sqrt{\left((\bar{u}_r + \epsilon\hat{u}_r) - (\bar{w}_r + \epsilon\hat{w}_r)\right)^2 + \left((\bar{u}_\theta + \epsilon\hat{u}_\theta) - (\bar{w}_\theta + \epsilon\hat{w}_\theta)\right)^2}. \tag{5.59}$$

Noting that $\bar{u}_\theta = 0$, $\bar{w}_\theta = 0$ and expanding we deduce that

$$\lambda_I = \sqrt{\left(\bar{u}_r - \bar{w}_r\right)^2} + \epsilon\frac{1}{\sqrt{\left(\bar{u}_r - \bar{w}_r\right)^2}}\left(\bar{u}_r - \bar{w}_r\right)\left(\hat{u}_r - \hat{w}_r\right) + O\left(\epsilon^2\right), \tag{5.60}$$

where we consider only the positive branch of the square root terms.

Initial and boundary conditions

The imposed initial condition on perturbation quantities depends on the exact form of perturbation imposed, we discuss this in Sec. 5.9 (below).

As discussed in Sec. 5.3.2, in order to preserve the mass of the various proteins in the

cell, we assume no flux boundary conditions for each protein species at the edge of the cytoplasm. At the boundary of the cell cytoplasm with the nucleus we have $\boldsymbol{n}_n = -\boldsymbol{e}_r$ whilst at the cell membrane we have $\boldsymbol{n}_m = \boldsymbol{e}_r$. The flux through the cell cytoplasm can be written $\boldsymbol{j}_\alpha = \bar{\boldsymbol{j}}_\alpha + \epsilon\hat{\boldsymbol{j}}_\alpha$. From Eq. (5.8j), the flux at the boundary between the cell cytoplasm and nucleus and at the cell membrane can be written as

$$\bar{\boldsymbol{j}}_\alpha \cdot \boldsymbol{e}_r = 0, \quad \bar{\boldsymbol{j}}_\alpha = D_\alpha \nabla \bar{c}_\alpha - \boldsymbol{v}_\alpha \bar{c}_\alpha, \tag{5.61a}$$

$$\hat{\boldsymbol{j}}_\alpha \cdot \boldsymbol{e}_r = 0, \quad \hat{\boldsymbol{j}}_\alpha = D_\alpha \nabla \hat{c}_\alpha - \boldsymbol{v}_\alpha \hat{c}_\alpha, \tag{5.61b}$$

at $O(\epsilon^0)$ (from the axisymmetric problem) and $O(\epsilon)$ respectively.

5.8 Fourier decomposition

For simple periodic solutions, we suppose that all $O(\epsilon)$ quantities, denoted by hats in Sec. 5.7, can be decomposed into a function of radial position and time, and a simple periodic function of θ, parameterised by an azimuthal wavenumber, $n \in \mathbb{N}$. In general, for any function $\hat{f}$ we set $\hat{f}(r,\theta,t) = \tilde{f}(r,t;n)e^{in\theta}$.

5.8.1 Mechanical equations

Under the assumption of periodicity, the infinitesimal stress tensors Eqs. (5.46b) and (5.51) satisfy $\hat{\boldsymbol{\epsilon}}_c = \tilde{\boldsymbol{\epsilon}}_c e^{in\theta}$, $\hat{\boldsymbol{\epsilon}}_E = \tilde{\boldsymbol{\epsilon}}_E e^{in\theta}$, where for each $n \in \mathbb{N}$ we have

$$\tilde{\boldsymbol{\epsilon}}_c = \frac{\partial \tilde{u}_r}{\partial r}\boldsymbol{e}_r \otimes \boldsymbol{e}_r + \frac{1}{r}\left(in\tilde{u}_\theta + \tilde{u}_r\right)\boldsymbol{e}_\theta \otimes \boldsymbol{e}_\theta + \frac{1}{2}\left(\frac{1}{r}in\tilde{u}_r + \frac{\partial \tilde{u}_\theta}{\partial r} - \frac{\tilde{u}_\theta}{r}\right)\left(\boldsymbol{e}_r \otimes \boldsymbol{e}_\theta + \boldsymbol{e}_\theta \otimes \boldsymbol{e}_r\right), \tag{5.62a}$$

$$\tilde{\boldsymbol{\epsilon}}_E = \frac{\partial \tilde{w}_r}{\partial r}\boldsymbol{e}_r \otimes \boldsymbol{e}_r + \frac{1}{r}\left(in\tilde{w}_\theta + \tilde{w}_r\right)\boldsymbol{e}_\theta \otimes \boldsymbol{e}_\theta + \frac{1}{2}\left(\frac{1}{r}in\tilde{w}_r + \frac{\partial \tilde{w}_\theta}{\partial r} - \frac{\tilde{w}_\theta}{r}\right)\left(\boldsymbol{e}_r \otimes \boldsymbol{e}_\theta + \boldsymbol{e}_\theta \otimes \boldsymbol{e}_r\right). \tag{5.62b}$$

The momentum balance equations Eq. (5.49) and Eq. (5.52) then become

$$\nabla \cdot \left[\left(\bar{E}_c\tilde{\boldsymbol{\epsilon}}_c + \tilde{E}_c\bar{\boldsymbol{\epsilon}}_c + \bar{\mu}_c\frac{\partial \tilde{\boldsymbol{\epsilon}}_c}{\partial t} + \tilde{\mu}_c\frac{\partial \bar{\boldsymbol{\epsilon}}_c}{\partial t} + \tilde{\boldsymbol{\tau}}\right)e^{in\theta}\right] = \bar{\beta}_I\frac{\partial}{\partial t}\left(\tilde{\boldsymbol{u}} - \tilde{\boldsymbol{w}}\right)e^{in\theta} + \tilde{\beta}_I\frac{\partial}{\partial t}\left(\bar{\boldsymbol{u}} - \bar{\boldsymbol{w}}\right)e^{in\theta}$$
$$+\bar{\kappa}_I\left(\tilde{\boldsymbol{u}} - \tilde{\boldsymbol{w}}\right)e^{in\theta} + \tilde{\kappa}_I\left(\bar{\boldsymbol{u}} - \bar{\boldsymbol{w}}\right)e^{in\theta}, \tag{5.63a}$$

$$\nabla \cdot \left[\left(\bar{E}_E\tilde{\boldsymbol{\epsilon}}_E + \tilde{E}_E\bar{\boldsymbol{\epsilon}}_E + \bar{\mu}_E\frac{\partial \tilde{\boldsymbol{\epsilon}}_E}{\partial t} + \tilde{\mu}_E\frac{\partial \bar{\boldsymbol{\epsilon}}_E}{\partial t}\right)e^{in\theta}\right] = \bar{\beta}_I\frac{\partial}{\partial t}\left(\tilde{\boldsymbol{w}} - \tilde{\boldsymbol{u}}\right)e^{in\theta} + \tilde{\beta}_I\frac{\partial}{\partial t}\left(\bar{\boldsymbol{w}} - \bar{\boldsymbol{u}}\right)e^{in\theta}$$
$$+\bar{\kappa}_I\left(\tilde{\boldsymbol{w}} - \tilde{\boldsymbol{u}}\right)e^{in\theta} + \tilde{\kappa}_I\left(\bar{\boldsymbol{w}} - \bar{\boldsymbol{u}}\right)e^{in\theta}. \tag{5.63b}$$

Writing $u_r = U_r$, $u_\theta = iU_\theta$, $w_r = W_r$, $w_\theta = iW_\theta$ with U_r, U_θ, W_r, $W_\theta \in \mathbb{R}$, then Eq. (5.63) yields

$$\begin{aligned}
&\frac{1}{2r^2}\left[-2\left(\tilde{E}_c\bar{U}_r + \tilde{\mu}_c\frac{\partial\bar{U}_r}{\partial t}\right) - \left(2+n^2\right)\left(\bar{E}_c\tilde{U}_r + \bar{\mu}_c\frac{\partial\tilde{U}_r}{\partial t}\right) + 3n\left(\bar{E}_c\tilde{U}_\theta + \bar{\mu}_c\frac{\partial\tilde{U}_\theta}{\partial t}\right)\right.\\
&+ 2r\tilde{\tau} + 2r\left(\tilde{E}_c\frac{\partial\bar{U}_r}{\partial r} + \tilde{\mu}_c\frac{\partial^2\bar{U}_r}{\partial r\partial t}\right) + 2r\left(\bar{E}_c\frac{\partial\tilde{U}_r}{\partial r} + \bar{\mu}_c\frac{\partial^2\tilde{U}_r}{\partial r\partial t}\right) - nr\left(\bar{E}_c\frac{\partial\tilde{U}_\theta}{\partial r} + \bar{\mu}_c\frac{\partial^2\tilde{U}_\theta}{\partial r\partial t}\right)\\
&+ 2r^2\frac{\partial\tilde{\tau}}{\partial r} + 2r^2\left(\frac{\partial\tilde{E}_c}{\partial r}\frac{\partial\bar{U}_r}{\partial r} + \frac{\partial\tilde{\mu}_c}{\partial r}\frac{\partial^2\bar{U}_r}{\partial r\partial t}\right) + 2r^2\left(\frac{\partial\bar{E}_c}{\partial r}\frac{\partial\tilde{U}_r}{\partial r} + \frac{\partial\bar{\mu}_c}{\partial r}\frac{\partial^2\tilde{U}_r}{\partial r\partial t}\right)\\
&\left.+ 2r^2\left(\tilde{E}_c\frac{\partial^2\bar{U}_r}{\partial r^2} + \tilde{\mu}_c\frac{\partial^3\bar{U}_r}{\partial r^2\partial t}\right) + 2r^2\left(\bar{E}_c\frac{\partial^2\tilde{U}_r}{\partial r^2} + \bar{\mu}_c\frac{\partial^3\tilde{U}_r}{\partial r^2\partial t}\right)\right] = \bar{\beta}_I\frac{\partial}{\partial t}\left(\tilde{U}_r - \tilde{W}_r\right)\\
&\quad + \tilde{\beta}_I\frac{\partial}{\partial t}\left(\bar{U}_r - \bar{W}_r\right) + \bar{\kappa}_I\left(\tilde{U}_r - \tilde{W}_r\right) + \tilde{\kappa}_I\left(\bar{U}_r - \bar{W}_r\right),
\end{aligned} \tag{5.64a}$$

$$\begin{aligned}
&\frac{1}{2r^2}\left[2n\left(\tilde{E}_c\bar{U}_r + \tilde{\mu}_c\frac{\partial\bar{U}_r}{\partial t}\right) + nr\left(\frac{\partial\bar{E}_c}{\partial r}\tilde{U}_r + \frac{\partial\bar{\mu}_c}{\partial r}\frac{\partial\tilde{U}_r}{\partial t}\right) - r\left(\frac{\partial\bar{E}_c}{\partial r}\tilde{U}_\theta + \frac{\partial\bar{\mu}_c}{\partial r}\frac{\partial\tilde{U}_\theta}{\partial t}\right)\right.\\
&+ r^2\left(\frac{\partial\bar{E}_c}{\partial r}\frac{\partial\tilde{U}_\theta}{\partial r} + \frac{\partial\bar{\mu}_c}{\partial r}\frac{\partial^2\tilde{U}_\theta}{\partial r\partial t}\right) + 3n\left(\bar{E}_c\tilde{U}_r + \bar{\mu}_c\frac{\partial\tilde{U}_r}{\partial t}\right) - \left(1+2n^2\right)\left(\bar{E}_c\tilde{U}_\theta + \bar{\mu}_c\frac{\partial\tilde{U}_\theta}{\partial t}\right)\\
&\left.+ nr\left(\bar{E}_c\frac{\partial\tilde{U}_r}{\partial r} + \bar{\mu}_c\frac{\partial^2\tilde{U}_r}{\partial r\partial t}\right) + r\left(\bar{E}_c\frac{\partial\tilde{U}_\theta}{\partial r} + \bar{\mu}_c\frac{\partial^2\tilde{U}_\theta}{\partial r\partial t}\right) + r^2\left(\bar{E}_c\frac{\partial^2\tilde{U}_\theta}{\partial r^2} + \bar{\mu}_c\frac{\partial^3\tilde{U}_\theta}{\partial r^2\partial t}\right)\right] =\\
&\quad \bar{\beta}_I\frac{\partial}{\partial t}\left(\tilde{U}_\theta - \tilde{W}_\theta\right) + \tilde{\beta}_I\frac{\partial}{\partial t}\left(\bar{U}_\theta - \bar{W}_\theta\right) + \bar{\kappa}_I\left(\tilde{U}_\theta - \tilde{W}_\theta\right) + \tilde{\kappa}_I\left(\bar{U}_\theta - \bar{W}_\theta\right),
\end{aligned} \tag{5.64b}$$

$$\begin{aligned}
&\frac{1}{2r^2}\left[-2\left(\tilde{E}_E\bar{W}_r + \tilde{\mu}_E\frac{\partial\bar{W}_r}{\partial t}\right) - \left(2+n^2\right)\left(\bar{E}_E\tilde{W}_r + \bar{\mu}_E\frac{\partial\tilde{W}_r}{\partial t}\right) + 3n\left(\bar{E}_E\tilde{W}_\theta + \bar{\mu}_E\frac{\partial\tilde{W}_\theta}{\partial t}\right)\right.\\
&+ 2r\left(\tilde{E}_E\frac{\partial\bar{W}_r}{\partial r} + \tilde{\mu}_E\frac{\partial^2\bar{W}_r}{\partial r\partial t}\right) + 2r\left(\bar{E}_E\frac{\partial\tilde{W}_r}{\partial r} + \bar{\mu}_E\frac{\partial^2\tilde{W}_r}{\partial r\partial t}\right) - nr\left(\bar{E}_E\frac{\partial\tilde{W}_\theta}{\partial r} + \bar{\mu}_E\frac{\partial^2\tilde{W}_\theta}{\partial r\partial t}\right)\\
&+ 2r^2\left(\frac{\partial\tilde{E}_E}{\partial r}\frac{\partial\bar{W}_r}{\partial r} + \frac{\partial\tilde{\mu}_E}{\partial r}\frac{\partial^2\bar{W}_r}{\partial r\partial t}\right) + 2r^2\left(\frac{\partial\bar{E}_E}{\partial r}\frac{\partial\tilde{W}_r}{\partial r} + \frac{\partial\bar{\mu}_E}{\partial r}\frac{\partial^2\tilde{W}_r}{\partial r\partial t}\right)\\
&\left.+ 2r^2\left(\tilde{E}_E\frac{\partial^2\bar{W}_r}{\partial r^2} + \tilde{\mu}_E\frac{\partial^3\bar{W}_r}{\partial r^2\partial t}\right) + 2r^2\left(\bar{E}_E\frac{\partial^2\tilde{W}_r}{\partial r^2} + \bar{\mu}_E\frac{\partial^3\tilde{W}_r}{\partial r^2\partial t}\right)\right] = \bar{\beta}_I\frac{\partial}{\partial t}\left(\tilde{W}_r - \tilde{U}_r\right)\\
&\quad + \tilde{\beta}_I\frac{\partial}{\partial t}\left(\bar{U}_r - \bar{W}_r\right) + \bar{\kappa}_I\left(\tilde{W}_r - \tilde{U}_r\right) + \tilde{\kappa}_I\left(\bar{U}_r - \bar{W}_r\right),
\end{aligned} \tag{5.64c}$$

$$\frac{1}{2r^2}\left[2n\left(\tilde{E}_E\bar{W}_r+\tilde{\mu}_E\frac{\partial\bar{W}_r}{\partial t}\right)+nr\left(\frac{\partial\bar{E}_E}{\partial r}\tilde{W}_r+\frac{\partial\bar{\mu}_E}{\partial r}\frac{\partial\tilde{W}_r}{\partial t}\right)-r\left(\frac{\partial\bar{E}_E}{\partial r}\tilde{W}_\theta+\frac{\partial\bar{\mu}_E}{\partial r}\frac{\partial\tilde{W}_\theta}{\partial t}\right)\right.$$
$$+r^2\left(\frac{\partial\bar{E}_E}{\partial r}\frac{\partial\tilde{W}_\theta}{\partial r}+\frac{\partial\bar{\mu}_E}{\partial r}\frac{\partial^2\tilde{W}_\theta}{\partial r\partial t}\right)+3n\left(\bar{E}_E\tilde{W}_r+\bar{\mu}_E\frac{\partial\tilde{W}_r}{\partial t}\right)$$
$$-\left(1+2n^2\right)\left(\bar{E}_E\tilde{W}_\theta+\bar{\mu}_E\frac{\partial\tilde{W}_\theta}{\partial t}\right)+nr\left(\bar{E}_E\frac{\partial\tilde{W}_r}{\partial r}+\bar{\mu}_E\frac{\partial^2\tilde{W}_r}{\partial r\partial t}\right)$$
$$\left.+r\left(\bar{E}_E\frac{\partial\tilde{W}_\theta}{\partial r}+\bar{\mu}_E\frac{\partial^2\tilde{W}_\theta}{\partial r\partial t}\right)+r^2\left(\bar{E}_E\frac{\partial^2\tilde{W}_\theta}{\partial r^2}+\bar{\mu}_E\frac{\partial^3\tilde{W}_\theta}{\partial r^2\partial t}\right)\right]=\bar{\beta}_I\frac{\partial}{\partial t}\left(\tilde{W}_\theta-\tilde{U}_\theta\right)$$
$$+\tilde{\beta}_I\frac{\partial}{\partial t}\left(\bar{W}_\theta-\bar{U}_\theta\right)+\bar{\kappa}_I\left(\tilde{W}_\theta-\tilde{U}_\theta\right)+\tilde{\kappa}_I\left(\bar{W}_\theta-\bar{U}_\theta\right). \tag{5.64d}$$

We note from Sec. 5.6 that $\bar{U}_\theta=0$, $\bar{W}_\theta=0$.

We assume that the mechanical properties of the ECM have not been perturbed so that $\tilde{E}_E=0$ and $\tilde{\mu}_E=0$. Consequently, from Eq. (5.64), we have for the ECM that

$$\frac{1}{2r^2}\left[-\left(2+n^2\right)\left(\bar{E}_E\tilde{W}_r+\bar{\mu}_E\frac{\partial\tilde{W}_r}{\partial t}\right)+3n\left(\bar{E}_E\tilde{W}_\theta+\bar{\mu}_E\frac{\partial\tilde{W}_\theta}{\partial t}\right)\right.$$
$$+2r\left(\bar{E}_E\frac{\partial\tilde{W}_r}{\partial r}+\bar{\mu}_E\frac{\partial^2\tilde{W}_r}{\partial r\partial t}\right)-nr\left(\bar{E}_E\frac{\partial\tilde{W}_\theta}{\partial r}+\bar{\mu}_E\frac{\partial^2\tilde{W}_\theta}{\partial r\partial t}\right) \tag{5.65a}$$
$$\left.+2r^2\left(\frac{\partial\bar{E}_E}{\partial r}\frac{\partial\tilde{W}_r}{\partial r}+\frac{\partial\bar{\mu}_E}{\partial r}\frac{\partial^2\tilde{W}_r}{\partial r\partial t}\right)+2r^2\left(\bar{E}_E\frac{\partial^2\tilde{W}_r}{\partial r^2}+\bar{\mu}_E\frac{\partial^3\tilde{W}_r}{\partial r^2\partial t}\right)\right]=$$
$$\bar{\beta}_I\frac{\partial}{\partial t}\left(\tilde{W}_r-\tilde{U}_r\right)+\bar{\kappa}_I\left(\tilde{W}_r-\tilde{U}_r\right)+\tilde{\kappa}_I\left(\bar{W}_r-\bar{U}_r\right),$$

$$\frac{1}{2r^2}\left[nr\left(\frac{\partial\bar{E}_E}{\partial r}\tilde{W}_r+\frac{\partial\bar{\mu}_E}{\partial r}\frac{\partial\tilde{W}_r}{\partial t}\right)-r\left(\frac{\partial\bar{E}_E}{\partial r}\tilde{W}_\theta+\frac{\partial\bar{\mu}_E}{\partial r}\frac{\partial\tilde{W}_\theta}{\partial t}\right)+r^2\left(\frac{\partial\bar{E}_E}{\partial r}\frac{\partial\tilde{W}_\theta}{\partial r}+\frac{\partial\bar{\mu}_E}{\partial r}\frac{\partial^2\tilde{W}_\theta}{\partial r\partial t}\right)\right.$$
$$+3n\left(\bar{E}_E\tilde{W}_r+\bar{\mu}_E\frac{\partial\tilde{W}_r}{\partial t}\right)-\left(1+2n^2\right)\left(\bar{E}_E\tilde{W}_\theta+\bar{\mu}_E\frac{\partial\tilde{W}_\theta}{\partial t}\right)+nr\left(\bar{E}_E\frac{\partial\tilde{W}_r}{\partial r}+\bar{\mu}_E\frac{\partial^2\tilde{W}_r}{\partial r\partial t}\right)$$
$$\left.+r\left(\bar{E}_E\frac{\partial\tilde{W}_\theta}{\partial r}+\bar{\mu}_E\frac{\partial^2\tilde{W}_\theta}{\partial r\partial t}\right)+r^2\left(\bar{E}_E\frac{\partial^2\tilde{W}_\theta}{\partial r^2}+\bar{\mu}_E\frac{\partial^3\tilde{W}_\theta}{\partial r^2\partial t}\right)\right]=\bar{\beta}_I\frac{\partial}{\partial t}\left(\tilde{W}_\theta-\tilde{U}_\theta\right)$$
$$+\bar{\kappa}_I\left(\tilde{W}_\theta-\tilde{U}_\theta\right). \tag{5.65b}$$

Boundary conditions

From Eq. (5.53a) we have

$$\tilde{U}_r(R_n,t)=0,\quad \tilde{U}_\theta(R_n,t)=0. \tag{5.66a}$$

From Eq. (5.53b) we have

$$(\tilde{\boldsymbol{\sigma}}_c \boldsymbol{e}_r) \cdot \boldsymbol{e}_r = 0, \tag{5.66b}$$

which gives

$$\bar{E}_c \frac{\partial \tilde{U}_r}{\partial r} + \tilde{E}_c \frac{\partial \bar{U}_r}{\partial r} + \bar{\mu}_c \frac{\partial^2 \tilde{U}_r}{\partial r \partial t} + \tilde{\mu}_c \frac{\partial^2 \bar{U}_r}{\partial r \partial t} + \tilde{\tau} = 0, \tag{5.66c}$$

on the cell membrane. From Eq. (5.53c) we have

$$(\tilde{\boldsymbol{\sigma}}_c \boldsymbol{e}_r) \cdot \boldsymbol{e}_\theta = 0, \tag{5.66d}$$

which gives on the cell membrane

$$\frac{\bar{E}_c}{2}\left(\frac{n}{R}\tilde{U}_r + \frac{\partial \tilde{U}_\theta}{\partial r} - \frac{1}{R}\tilde{U}_\theta\right) + \frac{\bar{\mu}_c}{2}\left(\frac{n}{R}\frac{\partial \tilde{U}_r}{\partial t} + \frac{\partial^2 \tilde{U}_\theta}{\partial r \partial t} - \frac{1}{R}\frac{\partial \tilde{U}_\theta}{\partial t}\right) = 0. \tag{5.66e}$$

Finally, the perturbation boundary conditions on the ECM from Eq. (5.53d) are given by

$$\tilde{W}_r(0,t) = 0, \quad \tilde{W}_\theta(0,t) = 0, \quad \lim_{r\to\infty} \tilde{W}_r(r,t) = 0, \quad \lim_{r\to\infty} \tilde{W}_\theta(r,t) = 0. \tag{5.66f}$$

At the junctions between ECM regions either side of the cell membrane boundary (i.e. underneath the cell nucleus and in the far field) we match stress and displacement, as is discussed below.

5.8.2 ECM below nucleus and in the far field

For the ECM below the nucleus and in the far field, we recall our assumption that $\bar{E}_E = \bar{E}$ and $\bar{\mu}_E = \bar{\mu}$ are spatially uniform and write

$$F(r,t) = \bar{E}\check{W}_{r,i} + \bar{\mu}\frac{\partial \check{W}_{r,i}}{\partial t}, \quad G(r,t) = \bar{E}\check{W}_{\theta,i} + \bar{\mu}\frac{\partial \check{W}_{\theta,i}}{\partial t}, \tag{5.67}$$

where $\check{W}_{r,i}$ and $\check{W}_{\theta,i}$ are the perturbation radial and azimuthal displacements respectively in region $i = 1, 2$. As there are no adhesions to the cell in these regions, employing Eq. (5.67) allows us to write the momentum balance equations for the ECM from Eq. (5.65) as

$$-\left(2+n^2\right)F + 2r\frac{\partial F}{\partial r} + 2r^2\frac{\partial^2 F}{\partial r^2} + 3nG - nr\frac{\partial G}{\partial r} = 0, \tag{5.68a}$$

$$-\left(1+2n^2\right)G + r\frac{\partial G}{\partial r} + r^2\frac{\partial^2 G}{\partial r^2} + 3nF + nr\frac{\partial F}{\partial r} = 0. \tag{5.68b}$$

We assume solutions to Eq. (5.68) take the form $F = \sum_{p=1}^{4} f_p r^{k_p}$, $G = \sum_{p=1}^{4} g_p r^{k_p}$ for f_p, g_p to be determined and where $k_p \in \mathbb{R}$. Using this ansatz we have

$$-\left(2+n^2\right) f_p + 2k_p f_p + 2k_p\left(k_p-1\right) f_p + 3n g_p - n k_p g_p = 0, \tag{5.69a}$$

$$-\left(1+2n^2\right) g_p + k_p g_p + k_p\left(k_p-1\right) g_p + 3n f_p + n k_p f_p = 0. \tag{5.69b}$$

Rearranging Eq. (5.69a), we deduce a relation between f_p and g_p of the form

$$g_p = \alpha_p f_p, \quad \alpha_p = \left(\frac{-\left(2+n^2\right)+2k_p^2}{n(k_p-3)}\right), \tag{5.70}$$

for $k_p \neq 3$, $n \neq 0$. Consequently, the case of $n = 0$ has to be dealt with separately, and this is presented in Sec. 5.6.1. Substituting Eq. (5.70) into Eq. (5.69b) yields

$$2\left(\frac{k_p^4+\left(n^2-1\right)^2-2k_p^2\left(1+n^2\right)}{n\left(k_p-3\right)}\right) f_p = 0, \tag{5.71}$$

and so the exponents, k_p, are given by the roots of the equation

$$k^4 - 2k^2\left(1+n^2\right) + \left(n^2-1\right)^2 = 0. \tag{5.72}$$

We deduce that the roots of Eq. (5.72) are given by

$$k_1 = n+1, \quad k_2 = n-1, \quad k_3 = -n+1, \quad k_4 = -n-1, \tag{5.73}$$

hence $k_p \in \mathbb{Z}$. We note however that these solutions require $k_p \neq 3$ in order to satisfy Eq. (5.71), hence we will need to consider cases with $k_p = 3$ separately. By Eq. (5.73) this will only occur when $n = 2$ or $n = 4$; we consider these special cases below. It follows from Eq. (5.73) that the solutions of Eq. (5.68) for $n \neq 2, 4$ take the form

$$F = f_1 r^{n+1} + f_2 r^{n-1} + f_3 r^{-n+1} + f_4 r^{-n-1}, \tag{5.74a}$$

$$G = g_1 r^{n+1} + g_2 r^{n-1} + g_3 r^{-n+1} + g_4 r^{-n-1}, \tag{5.74b}$$

where f_p, g_p are functions of time, related through Eq. (5.70) for $p = 1, 2, 3, 4$. It follows from Eq. (5.67) that

$$\bar{E}\check{W}_{r,i} + \bar{\mu}_E \frac{\partial \check{W}_{r,i}}{\partial t} = f_1 r^{n+1} + f_2 r^{n-1} + f_3 r^{-n+1} + f_4 r^{-n-1}, \tag{5.75a}$$

$$\bar{E}\check{W}_{\theta,i} + \bar{\mu}_E \frac{\partial \check{W}_{\theta,i}}{\partial t} = g_1 r^{n+1} + g_2 r^{n-1} + g_3 r^{-n+1} + g_4 r^{-n-1}. \tag{5.75b}$$

Special case with $n = 2$

For $n \neq 0$, Eq. (5.70) is satisfied if $k_p \neq 3$. Employing the same ansatz as above then for $n = 2$, from Eq. (5.73), we have $k_1 = 3$ whilst $k_2 \neq 3$, $k_3 \neq 3$, $k_4 \neq 3$. In particular, for $p = 2, 3, 4$ the relationship between f_p and g_p from Eq. (5.70) holds and, following the above analysis, we have

$$k_2 = 1, \quad k_3 = -1, \quad k_4 = -3. \tag{5.76}$$

Returning to Eq. (5.69) with $p = 1$, $k_p = 3$, $n = 2$, we deduce that $f_1 = 0$ and g_1 is a free variable.

It follows that solutions of Eq. (5.68) for $n = 2$ take the form

$$F = f_2 r + f_3 r^{-1} + f_4 r^{-3}, \tag{5.77a}$$

$$G = g_1 r^3 + g_2 r + g_3 r^{-1} + g_4 r^{-3}, \tag{5.77b}$$

where f_p, g_p are functions of time for $p = 1, 2, 3, 4$ and where f_p, g_p are related through Eq. (5.70) for $p = 2, 3, 4$. It follows from Eq. (5.67) that for $n = 2$ we have

$$\bar{E}\check{W}_{r,i} + \bar{\mu}_E \frac{\partial \check{W}_{r,i}}{\partial t} = f_2 r + f_3 r^{-1} + f_4 r^{-3}, \tag{5.78a}$$

$$\bar{E}\check{W}_{\theta,i} + \bar{\mu}_E \frac{\partial \check{W}_{\theta,i}}{\partial t} = g_1 r^3 + g_2 r + g_3 r^{-1} + g_4 r^{-3}. \tag{5.78b}$$

Special case with $n = 4$

For $n \neq 0$, Eq. (5.70) is satisfied if $k_p \neq 3$. In this case, our subsequent analysis shows that for $n = 4$ we have $k_2 = 3$ (see Eq. 5.73). Hence, $n = 4$ appears to require a different treatment. However, it emerges for $n = 4$ that Eq. (5.70) has a removable singularity when $k_p = 3$, which yields a simple relationship between f_p, g_p of the form

$$g_p = \gamma_p f_p, \quad \gamma_p = \frac{1}{2}(k_p + 3), \tag{5.79}$$

for $p = 1, 2, 3, 4$. Hence, for $n = 4$ we have

$$k_1 = 5, \quad k_2 = 3, \quad k_3 = -3, \quad k_4 = -5. \tag{5.80}$$

It follows from Eq. (5.67) that for $n = 4$ we have

$$\bar{E}\check{W}_{r,i} + \bar{\mu}\frac{\partial \check{W}_{r,i}}{\partial t} = f_1 r^5 + f_2 r^3 + f_3 r^{-3} + f_4 r^{-5}, \tag{5.81a}$$

$$\bar{E}\check{W}_{\theta,i} + \bar{\mu}\frac{\partial \check{W}_{\theta,i}}{\partial t} = g_1 r^5 + g_2 r^3 + g_3 r^{-3} + g_4 r^{-5}, \tag{5.81b}$$

where f_p, g_p are related through Eq. (5.79) (or equivalently Eq. 5.70). Observe that the form of general solution for $n = 4$ (given by Eq. 5.81) is identical to that for the general case (Eq. 5.75). Hence, $n = 4$ does not need a distinct treatment and we no longer distinguish it from the general case described by Eq. (5.75).

ECM below the nucleus

We illustrate fully the calculation for the displacement and stress in the region below the nucleus for $n \neq 2$ (i.e. with azimuthal wavenumbers other than two), with the calculation for $n = 2$ similar and described more briefly below. In this region we impose, from Eq. (5.66f), that $\check{W}_{r,1}(0,t) = 0$, $\partial\check{W}_{r,1}(0,t)/\partial t = 0$, $\check{W}_{\theta,1}(0,t) = 0$ and $\partial\check{W}_{\theta,1}(0,t)/\partial t = 0$. We deduce from Eq. (5.75) that $f_3 = 0$, $f_4 = 0$ and consequently, through Eq. (5.70), that $g_3 = 0$, $g_4 = 0$. It follows from Eq. (5.75) that we have

$$\bar{E}\check{W}_{r,1} + \bar{\mu}\frac{\partial\check{W}_{r,1}}{\partial t} = f_1 r^{n+1} + f_2 r^{n-1}, \tag{5.82a}$$

$$\bar{E}\check{W}_{\theta,1} + \bar{\mu}\frac{\partial\check{W}_{\theta,1}}{\partial t} = \alpha_1 f_1 r^{n+1} + \alpha_2 f_2 f^{n-1}, \tag{5.82b}$$

with α_1, α_2 given by Eq. (5.70). The remaining boundary conditions at the boundary with the ECM below the cell cytoplasm allow us to eliminate one of the unknowns. In particular, we set $\check{W}_{\theta,1}(R,t) = \tilde{W}_{\theta,0}(t)$, where $\tilde{W}_{\theta,0}(t)$ is the numerically calculated displacement of the ECM connected to (underneath) the cytoplasm at the boundary with the nucleus. We hence deduce from Eq. (5.82b) that

$$f_1 = \frac{1}{\alpha_1 R_n^{n+1}}\left(\bar{E}\tilde{W}_{\theta,0} + \bar{\mu}\frac{\partial\tilde{W}_{\theta,0}}{\partial t} - \alpha_2 f_2 R_n^{n-1}\right). \tag{5.83}$$

Hence from Eq. (5.82a) we solve

$$\bar{E}\check{W}_{r,1} + \bar{\mu}\frac{\partial\check{W}_{r,1}}{\partial t} = \frac{1}{\alpha_1 R_n^{n+1}}\left(\bar{E}\tilde{W}_{\theta,0} + \bar{\mu}\frac{\partial\tilde{W}_{\theta,0}}{\partial t} - \alpha_2 f_2 R_n^{n-1}\right) r^{n+1} + f_2 r^{n-1}. \tag{5.84}$$

By identifying an appropriate integrating factor, we deduce that

$$\check{W}_{r,1} = \frac{1}{\bar{\mu}} e^{-\frac{\bar{E}}{\bar{\mu}}t}\int_0^t e^{\frac{\bar{E}}{\bar{\mu}}T}\left[\frac{1}{\alpha_1 R_n^{n+1}}\left(\bar{E}\tilde{W}_{\theta,0} + \bar{\mu}\frac{\partial\tilde{W}_{\theta,0}}{\partial T} - \alpha_2 f_2 R_n^{n-1}\right) r^{n+1} + f_2 r^{n-1}\right] dT. \tag{5.85}$$

We can rewrite Eq. (5.85) as

$$\check{W}_{r,1} = A_{r,1}(t)\frac{r^{n+1}}{R_n^{n+1}} + \left(r^{n-1} - \frac{\alpha_2}{\alpha_1}\frac{R_n^{n-1}}{R_n^{n+1}} r^{n+1}\right) B_{r,1}(t), \tag{5.86}$$

where

$$A_{r,1}(t) = \frac{1}{\alpha_1\bar{\mu}} e^{-\frac{\bar{E}}{\bar{\mu}}t} \int_0^t e^{\frac{\bar{E}}{\bar{\mu}}T} \left(\bar{E}\tilde{W}_{\theta,0} + \bar{\mu}\frac{\partial \tilde{W}_{\theta,0}}{\partial T} \right) dT,$$
$$B_{r,1}(t) = \frac{1}{\bar{\mu}} e^{-\frac{\bar{E}}{\bar{\mu}}t} \int_0^t e^{\frac{\bar{E}}{\bar{\mu}}T} f_2 \, dT. \tag{5.87}$$

Imposing $\check{W}_{r,1}(R_n, t) = \tilde{W}_{r,0}(t)$ as a known function, then the numerically calculated radial displacement of the ECM at the boundary with the ECM below the cytoplasm is given by

$$B_{r,1}(t) = \frac{1}{R_n^{n-1}} \left(1 - \frac{\alpha_2}{\alpha_1} \right)^{-1} \left(\tilde{W}_{r,0}(t) - A_{r,1}(t) \right), \tag{5.88}$$

so that

$$\check{W}_{r,1} = A_{r,1}(t)\frac{r^{n+1}}{R_n^{n+1}} + \left(\frac{r^{n-1}}{R_n^{n-1}} - \frac{\alpha_2}{\alpha_1}\frac{r^{n+1}}{R_n^{n+1}} \right) \left(1 - \frac{\alpha_2}{\alpha_1} \right)^{-1} \left(\tilde{W}_{r,0}(t) - A_{r,1}(t) \right). \tag{5.89}$$

A similar calculation yields the azimuthal displacement underneath the nucleus as

$$\check{W}_{\theta,1} = A_{\theta,1}(t)\frac{r^{n+1}}{R_n^{n+1}} + \left(\alpha_2 \frac{r^{n-1}}{R_n^{n-1}} - \alpha_1 \frac{r^{n+1}}{R_n^{n+1}} \right) (\alpha_2 - \alpha_1)^{-1} \left(\tilde{W}_{\theta,0}(t) - A_{\theta,1}(t) \right), \tag{5.90}$$

where

$$A_{\theta,1}(t) = \frac{\alpha_1}{\bar{\mu}} e^{-\frac{\bar{E}}{\bar{\mu}}t} \int_0^t e^{\frac{\bar{E}}{\bar{\mu}}T} \left(\bar{E}\tilde{W}_{r,0} + \bar{\mu}\frac{\partial \tilde{W}_{r,0}}{\partial T} \right) dT,$$
$$B_{\theta,1}(t) = \frac{1}{\bar{\mu}} e^{-\frac{\bar{E}}{\bar{\mu}}t} \int_0^t e^{\frac{\bar{E}}{\bar{\mu}}T} f_2 \, dT. \tag{5.91}$$

Case with $n = 2$

If $n = 2$ then we calculate the radial and azimuthal displacement of points underneath the nucleus using Eq. (5.78). From Eq. (5.66f) we set $\check{W}_{r,1}(0,t) = 0$, $\partial\check{W}_{r,1}(0,t)/\partial t = 0$, $\check{W}_{\theta,1}(0,t) = 0$ and $\partial\check{W}_{\theta,1}(0,t)/\partial t = 0$. Hence, we have

$$\bar{E}\check{W}_{r,i} + \bar{\mu}\frac{\partial \check{W}_{r,i}}{\partial t} = f_2 r, \quad \bar{E}\check{W}_{\theta,i} + \bar{\mu}\frac{\partial \check{W}_{\theta,i}}{\partial t} = g_1 r^3 + g_2 r, \tag{5.92}$$

with f_2, g_2 related through Eq. (5.70). It follows that

$$\check{W}_{r,1} = \frac{r}{\bar{\mu}} e^{-\frac{\bar{E}}{\bar{\mu}}t} \int_0^t e^{\frac{\bar{E}}{\bar{\mu}}T} f_2(T) \, dT, \tag{5.93}$$

Imposing $\check{W}_{r,1}(R_n, t) = \tilde{W}_{r,0}(t)$, where $\tilde{W}_{r,0}(t)$ is a known function, yields

$$\check{W}_{r,1} = \frac{r}{R_n}\tilde{W}_{r,0}, \tag{5.94}$$

for $0 \leq r \leq R_n$. Integrating our azimuthal displacement equation from Eq. (5.92) gives

$$\check{W}_{\theta,1} = \frac{r^3}{\bar{\mu}} e^{-\frac{\bar{E}}{\bar{\mu}}t} \int_0^t e^{\frac{\bar{E}}{\bar{\mu}}T} g_1(T)\, dT + \frac{r}{\bar{\mu}} e^{-\frac{\bar{E}}{\bar{\mu}}t} \int_0^t e^{\frac{\bar{E}}{\bar{\mu}}T} g_2(T)\, dT. \tag{5.95}$$

Note that $g_2 = \alpha_2 f_2$, with α_2 defined by Eq. (5.70) for $n = 2$, $k_2 = 1$. Hence, recalling Eq. (5.93), we have

$$\check{W}_{\theta,1} = \frac{r^3}{\bar{\mu}} e^{-\frac{\bar{E}}{\bar{\mu}}t} \int_0^t e^{\frac{\bar{E}}{\bar{\mu}}T} g_1(T)\, dT + \alpha_2 \check{W}_{r,1}. \tag{5.96}$$

Imposing $\check{W}_{\theta,1}(R_n, t) = \tilde{W}_{\theta,0}(t)$, where $\tilde{W}_{\theta,0}(t)$ is a known function, we deduce that

$$\check{W}_{\theta,1} = \alpha_2 \check{W}_{r,1} + \frac{r^3}{R_n^3} \left(\tilde{W}_{\theta,0} - \alpha_2 \tilde{W}_{r,0} \right), \tag{5.97}$$

for $0 \leq r \leq R_n$.

ECM in the far field

We illustrate the calculation for the displacement and stress in the ECM far field for $n \neq 2$ (i.e. the azimuthal wavenumber is not equal to two), with the calculation for $n = 2$ identical. In this region we impose, from Eq. (5.66f), that

$$\lim_{r\to\infty} \check{W}_{r,2}(r,t) = 0, \quad \lim_{r\to\infty} \frac{\partial \check{W}_{r,2}(r,t)}{\partial t} = 0, \quad \lim_{r\to\infty} \check{W}_{\theta,2}(r,t) = 0, \quad \lim_{r\to\infty} \frac{\partial \check{W}_{\theta,2}(r,t)}{\partial t} = 0, \tag{5.98}$$

and deduce from Eq. (5.75) that $f_1 = 0$, $f_2 = 0$ and consequently, from Eq. (5.70), that $g_1 = 0$, $g_2 = 0$; hence, $n = 2$ does not need a distinct treatment in the far field and our subsequent analysis applies generally. It follows from Eq. (5.75) that we have

$$\bar{E}\check{W}_{r,2} + \bar{\mu}\frac{\partial \check{W}_{r,2}}{\partial t} = f_3 r^{-n+1} + f_4 r^{-n-1}, \tag{5.99a}$$

$$\bar{E}\check{W}_{\theta,2} + \bar{\mu}\frac{\partial \check{W}_{\theta,2}}{\partial t} = \alpha_3 f_3 r^{-n+1} + \alpha_4 f_4 f^{-n-1}, \tag{5.99b}$$

with α_3, α_4 given by Eq. (5.70). The remaining boundary conditions at the boundary with the ECM below the cell cytoplasm allow us to eliminate one of the unknowns. In particular, we set $\check{W}_{\theta,2}(R, t) = \tilde{W}_{\theta,N}(t)$, where $\tilde{W}_{\theta,N}(t)$ is the numerically calculated displacement of the ECM underneath the cell cytoplasm at the boundary with region 2. We hence deduce from Eq. (5.99b) that

$$f_3 = \frac{1}{\alpha_3 R^{-n+1}} \left(\bar{E}\tilde{W}_{\theta,N} + \bar{\mu}\frac{\partial \tilde{W}_{\theta,N}}{\partial t} - \alpha_4 f_4 R^{-n-1} \right). \tag{5.100}$$

Hence from Eq. (5.99a) we solve

$$\bar{E}\check{W}_{r,2} + \bar{\mu}_E \frac{\partial \check{W}_{r,2}}{\partial t} = \frac{1}{\alpha_3 R^{-n+1}} \left(\bar{E}\tilde{W}_{\theta,N} + \bar{\mu}\frac{\partial \tilde{W}_{\theta,N}}{\partial t} - \alpha_4 f_4 R^{-n-1} \right) r^{-n+1} + f_2 r^{-n-1}. \tag{5.101}$$

By identifying an appropriate integrating factor, we deduce that

$$\check{W}_{r,2} = \frac{1}{\bar{\mu}} e^{-\frac{\bar{E}}{\bar{\mu}}t} \int_0^t e^{\frac{\bar{E}}{\bar{\mu}}T} \left[\frac{1}{\alpha_3 R^{-n+1}} \left(\bar{E}\tilde{W}_{\theta,N} + \bar{\mu}\frac{\partial \tilde{W}_{\theta,N}}{\partial T} - \alpha_4 f_4 R^{-n-1} \right) r^{-n+1} + f_4 r^{-n-1} \right] dT, \tag{5.102}$$

which can be rewritten as

$$\check{W}_{r,2} = A_{r,2}(t)\frac{r^{-n+1}}{R^{-n-1}} + \left(r^{n-1} - \frac{\alpha_4}{\alpha_3}\frac{R^{-n-1}}{R^{-n+1}} r^{-n+1} \right) B_{r,2}(t), \tag{5.103}$$

where

$$\begin{aligned} A_{r,2}(t) &= \frac{1}{\alpha_3 \bar{\mu}} e^{-\frac{\bar{E}}{\bar{\mu}}t} \int_0^t e^{\frac{\bar{E}}{\bar{\mu}}T} \left(\bar{E}\tilde{W}_{\theta,N} + \bar{\mu}\frac{\partial \tilde{W}_{\theta,N}}{\partial T} \right) dT, \\ B_{r,2}(t) &= \frac{1}{\bar{\mu}} e^{-\frac{\bar{E}}{\bar{\mu}}t} \int_0^t e^{\frac{\bar{E}}{\bar{\mu}}T} f_4 \, dT. \end{aligned} \tag{5.104}$$

Imposing $\check{W}_{r,2}(R,t) = \tilde{W}_{r,N}(t)$, where $\tilde{W}_{r,N}(t)$ is the numerically calculated displacement of the ECM at the boundary, then

$$B_{r,2}(t) = \frac{1}{R^{-n-1}} \left(1 - \frac{\alpha_4}{\alpha_3} \right)^{-1} \left(\tilde{W}_{r,N}(t) - A_{r,2}(t) \right), \tag{5.105}$$

so that

$$\check{W}_{r,2} = A_{r,2}(t)\frac{r^{-n+1}}{R^{-n+1}} + \left(\frac{r^{-n-1}}{R^{-n-1}} - \frac{\alpha_4}{\alpha_3}\frac{r^{-n+1}}{R^{-n+1}} \right) \left(1 - \frac{\alpha_4}{\alpha_3} \right)^{-1} \left(\tilde{W}_{r,N}(t) - A_{r,2}(t) \right). \tag{5.106}$$

A similar calculation yields the azimuthal displacement underneath the nucleus as

$$\check{W}_{\theta,2} = A_{\theta,2}(t)\frac{r^{-n+1}}{R^{-n+1}} + \left(\alpha_4 \frac{r^{-n-1}}{R^{-n-1}} - \alpha_3 \frac{r^{-n+1}}{R^{-n+1}} \right) (\alpha_4 - \alpha_3)^{-1} \left(\tilde{W}_{\theta,N}(t) - A_{\theta,2}(t) \right), \tag{5.107}$$

where

$$\begin{aligned} A_{\theta,2}(t) &= \frac{\alpha_3}{\bar{\mu}} e^{-\frac{\bar{E}}{\bar{\mu}}t} \int_0^t e^{\frac{\bar{E}}{\bar{\mu}}T} \left(\bar{E}\tilde{W}_{r,N} + \bar{\mu}\frac{\partial \tilde{W}_{r,N}}{\partial T} \right) dT, \\ B_{\theta,2}(t) &= \frac{1}{\bar{\mu}} e^{-\frac{\bar{E}}{\bar{\mu}}t} \int_0^t e^{\frac{\bar{E}}{\bar{\mu}}T} f_4 \, dT. \end{aligned} \tag{5.108}$$

In this region it emerges that the solutions for $n = 2$ can be solved in an identical manner to the case where $n \neq 2$. Consequently, in the far field we can apply our solutions Eqs. (5.106)

and (5.107) for all $n \in \mathbb{N}$, $n \geq 1$.

Matching stress in each region

We match the normal and tangential stresses at the boundary between the ECM below the cytoplasm and the ECM underneath the nucleus and in the far field. We deduce from Eqs. (5.53e)-(5.53f) that

$$(\tilde{\boldsymbol{\sigma}}_E \boldsymbol{e}_r) \cdot \boldsymbol{e}_r = \left(\tilde{\tilde{\boldsymbol{\sigma}}}_{E,1} \boldsymbol{e}_r\right) \cdot \boldsymbol{e}_r, \quad (\tilde{\boldsymbol{\sigma}}_E \boldsymbol{e}_r) \cdot \boldsymbol{e}_\theta = \left(\tilde{\tilde{\boldsymbol{\sigma}}}_{E,1} \boldsymbol{e}_r\right) \cdot \boldsymbol{e}_\theta, \tag{5.109a}$$

$$(\tilde{\boldsymbol{\sigma}}_E \boldsymbol{e}_r) \cdot \boldsymbol{e}_r = \left(\tilde{\tilde{\boldsymbol{\sigma}}}_{E,2} \boldsymbol{e}_r\right) \cdot \boldsymbol{e}_r, \quad (\tilde{\boldsymbol{\sigma}}_E \boldsymbol{e}_r) \cdot \boldsymbol{e}_\theta = \left(\tilde{\tilde{\boldsymbol{\sigma}}}_{E,2} \boldsymbol{e}_r\right) \cdot \boldsymbol{e}_\theta. \tag{5.109b}$$

A simplifying assumption

We have theoretically described the calculation of displacement in the ECM and the associated matching of stress at the boundaries between different regions of the ECM. We deem this calculation to be relatively complicated. However, we have demonstrated in Chs. 3-4 that cells cultured on stiff substrates can form mature cell-substrate adhesions and cytoskeleton, aided by the negligible displacement of the ECM. Hence, to simplify our analysis, in subsequent modelling (and simulations) we neglect the perturbation deformation of the ECM and so we assume that $\tilde{W}_r = 0$, $\tilde{W}_\theta = 0$, $\check{W}_{r,1} = 0, \check{W}_{\theta,1} = 0$, $\check{W}_{r,2} = 0$ and $\check{W}_{\theta,2} = 0$. This assumption is justified by our linear stability analysis of our one-dimensional model (presented in App. A); in this case, the perturbation deformation of the ECM is much more easily incorporated but is shown to have negligible influence on the stability of the system for cells cultured on stiff substrates.

5.8.3 Biochemistry equations

Assuming the same periodic decomposition holds for all concentrations and densities we write, for a generic perturbation concentration, $\hat{c}$, that $\hat{c} = \tilde{c}e^{in\theta}$ and for a generic perturbation density, $\hat{n}$, we have $\hat{n} = \tilde{n}e^{in\theta}$. Under this assumption, Eqs. (5.54) become

$$\begin{aligned}\frac{\partial \tilde{c}_G}{\partial t} = &- \left(\bar{k}_p^+ \bar{c}_G \left(\tilde{n}_b + \tilde{n}_A\right) + \bar{k}_p^+ \tilde{c}_G \left(\bar{n}_b + \bar{n}_A\right) + \tilde{k}_p^+ \bar{c}_G \left(\bar{n}_b + \bar{n}_A\right)\right) \\ &+ \left(\bar{k}_p^- \tilde{c}_F + \tilde{k}_p^- \bar{c}_F\right) + k_m^- \tilde{c}_S^+ + D_G \left(\frac{\partial^2 \tilde{c}_G}{\partial r^2} + \frac{1}{r}\frac{\partial \tilde{c}_G}{\partial r} - \frac{n^2}{r^2}\tilde{c}_G\right),\end{aligned} \tag{5.110a}$$

$$\begin{aligned}\frac{\partial \tilde{c}_F}{\partial t} + \frac{1}{r}\frac{\partial \left(r \tilde{c}_F v_r\right)}{\partial r} = &\left(\bar{k}_p^+ \bar{c}_G \left(\tilde{n}_b + \tilde{n}_A\right) + \bar{k}_p^+ \tilde{c}_G \left(\bar{n}_b + \bar{n}_A\right) + \tilde{k}_p^+ \bar{c}_G \left(\bar{n}_b + \bar{n}_A\right)\right) - \left(\bar{k}_p^- \tilde{c}_F + \tilde{k}_p^- \bar{c}_F\right) \\ &- k_m^+ \left(\bar{c}_F \bar{c}_m^+ \left(\tilde{c}_F + \tilde{c}_S^+\right) + \bar{c}_F \tilde{c}_M^+ \left(\bar{c}_F + \bar{c}_S^+\right) + \tilde{c}_F \bar{c}_m^+ \left(\bar{c}_F + \bar{c}_S^+\right)\right) \\ &+ D_F \left(\frac{\partial^2 \tilde{c}_F}{\partial r^2} + \frac{1}{r}\frac{\partial \tilde{c}_F}{\partial r} - \frac{n^2}{r^2}\tilde{c}_F\right),\end{aligned} \tag{5.110b}$$

$$\frac{\partial \tilde{c}_S^+}{\partial t} = k_m^+ \left(\bar{c}_F \bar{c}_m^+ \left(\tilde{c}_F + \tilde{c}_S^+\right) + \bar{c}_F \tilde{c}_M^+ \left(\bar{c}_F + \bar{c}_S^+\right) + \tilde{c}_F \bar{c}_m^+ \left(\bar{c}_F + \bar{c}_S^+\right)\right) - k_m^+ \tilde{c}_S^+, \tag{5.110c}$$

$$\frac{\partial \tilde{c}_M}{\partial t} = -\left(\bar{k}_a^+ \tilde{c}_M + \tilde{k}_a^+ \bar{c}_m\right) + \left(\bar{k}_a^- \tilde{c}_M^+ + \tilde{k}_a^- \bar{c}_m^+\right) + D_m \left(\frac{\partial^2 \tilde{c}_M}{\partial r^2} + \frac{1}{r}\frac{\partial \tilde{c}_M}{\partial r} - \frac{n^2}{r^2}\tilde{c}_M\right), \tag{5.110d}$$

$$\begin{aligned}\frac{\partial \tilde{c}_M^+}{\partial t} = &\left(\bar{k}_a^+ \tilde{c}_M + \tilde{k}_a^+ \bar{c}_m\right) - \left(\bar{k}_a^- \tilde{c}_M^+ + \tilde{k}_a^- \bar{c}_m^+\right) \\ &- k_m^+ \left(\bar{c}_F \bar{c}_m^+ \left(\tilde{c}_F + \tilde{c}_S^+\right) + \bar{c}_F \tilde{c}_M^+ \left(\bar{c}_F + \bar{c}_S^+\right) + \tilde{c}_F \bar{c}_m^+ \left(\bar{c}_F + \bar{c}_S^+\right)\right) \\ &+ k_m^- \tilde{c}_S^+ + D_m^+ \left(\frac{\partial^2 \tilde{c}_M^+}{\partial r^2} + \frac{1}{r}\frac{\partial \tilde{c}_M^+}{\partial r} - \frac{n^2}{r^2}\tilde{c}_M^+\right),\end{aligned} \tag{5.110e}$$

$$\frac{\partial \tilde{n}_f}{\partial t} = -k_h^+ \tilde{n}_f + k_h^- \tilde{n}_h + D_f \left(\frac{\partial^2 \tilde{n}_f}{\partial r^2} + \frac{1}{r}\frac{\partial \tilde{n}_f}{\partial r} - \frac{n^2}{r^2}\tilde{n}_f\right), \tag{5.110f}$$

$$\frac{\partial \tilde{n}_h}{\partial t} = k_h^+ \tilde{n}_f - k_h^- \tilde{n}_h - k_b^+ \left(\bar{n}_h \tilde{n}_s + \tilde{n}_h \bar{n}_s\right) + k_b^- \tilde{n}_b, \tag{5.110g}$$

$$\frac{\partial \tilde{n}_b}{\partial t} = k_b^+ \left(\bar{n}_h \tilde{n}_s + \tilde{n}_h \bar{n}_s\right) - k_b^- \tilde{n}_b - \left(\bar{k}_F^+ \tilde{n}_b + \tilde{k}_F^+ \bar{n}_b\right) + k_F^- \tilde{n}_A, \tag{5.110h}$$

$$\frac{\partial \tilde{n}_A}{\partial t} = \left(\bar{k}_F^+ \tilde{n}_b + \tilde{k}_F^+ \bar{n}_b\right) - k_F^- \tilde{n}_A, \tag{5.110i}$$

$$\frac{\partial \tilde{n}_s}{\partial t} = -k_b^+ \left(\bar{n}_h \tilde{n}_s + \tilde{n}_h \bar{n}_s\right) + k_b^- \tilde{n}_b, \tag{5.110j}$$

$$\frac{\partial \tilde{c}_R}{\partial t} = -\left(\bar{k}_R^+ \tilde{c}_R + \tilde{k}_R^+ \bar{c}_R\right) + \left(\bar{k}_R^- \tilde{c}_R^+ + \tilde{k}_R^- \bar{c}_R^+\right), \tag{5.110k}$$

$$\frac{\partial \tilde{c}_R^+}{\partial t} = \left(\bar{k}_R^+ \tilde{c}_R + \tilde{k}_R^+ \bar{c}_R\right) - \left(\bar{k}_R^- \tilde{c}_R^+ + \tilde{k}_R^- \bar{c}_R^+\right), \tag{5.110l}$$

$$\frac{\partial \tilde{c}_P}{\partial t} = -\left(\bar{k}_1^+ \tilde{c}_P + \tilde{k}_1^+ \bar{c}_P\right) + k_1^- \tilde{c}_{P-P} + D_P \left(\frac{\partial^2 \tilde{c}_P}{\partial r^2} + \frac{1}{r}\frac{\partial \tilde{c}_P}{\partial r} - \frac{n^2}{r^2}\tilde{c}_P\right), \tag{5.110m}$$

$$\frac{\partial \tilde{c}_{P-P}}{\partial t} = \left(\bar{k}_1^+ \tilde{c}_P + \tilde{k}_1^+ \bar{c}_P\right) - k_1^- \tilde{c}_{P-P} + D_{P-P} \left(\frac{\partial^2 \tilde{c}_{P-P}}{\partial r^2} + \frac{1}{r}\frac{\partial \tilde{c}_{P-P}}{\partial r} - \frac{n^2}{r^2}\tilde{c}_{P-P}\right), \tag{5.110n}$$

$$\frac{\partial \tilde{c}_K}{\partial t} = -\left(\bar{k}_2^+ \tilde{c}_K + \tilde{k}_2^+ \bar{c}_K\right) + k_2^- \tilde{c}_{K-P} + D_K \left(\frac{\partial^2 \tilde{c}_K}{\partial r^2} + \frac{1}{r}\frac{\partial \tilde{c}_K}{\partial r} - \frac{n^2}{r^2}\tilde{c}_K\right), \tag{5.110o}$$

$$\frac{\partial \tilde{c}_{K-P}}{\partial t} = \left(\bar{k}_2^+ \tilde{c}_K + \tilde{k}_2^+ \bar{c}_K\right) \tilde{c}_{K-P} + D_{K-P} \left(\frac{\partial^2 \tilde{c}_{K-P}}{\partial r^2} + \frac{1}{r}\frac{\partial \tilde{c}_{K-P}}{\partial r} - \frac{n^2}{r^2}\tilde{c}_{K-P}\right), \tag{5.110p}$$

$$\frac{\partial \tilde{c}_C}{\partial t} = -\left(\bar{k}_3^+ \tilde{c}_C + \tilde{k}_3^+ \bar{c}_C\right) + k_3^- \tilde{c}_{C-P} + D_C \left(\frac{\partial^2 \tilde{c}_C}{\partial r^2} + \frac{1}{r}\frac{\partial \tilde{c}_C}{\partial r} - \frac{n^2}{r^2}\tilde{c}_C\right), \tag{5.110q}$$

$$\frac{\partial \tilde{c}_{C-P}}{\partial t} = \left(\bar{k}_3^+ \tilde{c}_C + \tilde{k}_3^+ \bar{c}_C\right) - k_3^- \tilde{c}_{C-P} + D_{C-P} \left(\frac{\partial^2 \tilde{c}_{C-P}}{\partial r^2} + \frac{1}{r}\frac{\partial \tilde{c}_{C-P}}{\partial r} - \frac{n^2}{r^2}\tilde{c}_{C-P}\right). \tag{5.110r}$$

Perturbation to rate constants

The perturbation reaction rates are all derived from Eq. (5.58) in the expected way. In particular, we have

$$\begin{gathered}\tilde{k}_p^+ = K_p^+ \tilde{c}_R^+, \quad \tilde{k}_p^- = K_p^- \tilde{c}_C, \quad \tilde{k}_a^+ = K_a^+ \tilde{c}_{K-P}, \quad \tilde{k}_a^- = K_a^- \tilde{c}_{P-P}, \\ \tilde{k}_R^+ = K_R^+ \left(\tilde{n}_b + \delta \tilde{n}_A\right), \quad \tilde{k}_F^+ = 2K_F^+ \bar{\lambda}_I \tilde{\lambda}_I,\end{gathered} \tag{5.111}$$

where from Eq. (5.60) we deduce that

$$\tilde{\lambda}_I = \frac{1}{\sqrt{\left(\bar{u}_r - \bar{w}_r\right)^2}} \left(\bar{u}_r - \bar{w}_r\right)\left(\tilde{u}_r - \tilde{w}_r\right), \tag{5.112}$$

where we consider only the positive branch of the square root.

Boundary conditions

To implement the no-flux boundary conditions at the boundary with the cell nucleus and at the cell membrane, we recall that $\boldsymbol{n}_n = -\boldsymbol{e}_r$ and on the cell membrane we have $\boldsymbol{n}_m = \boldsymbol{e}_r$. The flux through the cell cytoplasm can be decomposed as $\boldsymbol{j}_\alpha = \bar{\boldsymbol{j}}_\alpha + \epsilon\tilde{\boldsymbol{j}}_\alpha e^{in\theta}$. Hence, the perturbation boundary condition on the cell membrane and at the boundary with the nucleus, from Eq. (5.61), can be written

$$\tilde{\boldsymbol{j}}_\alpha \cdot \boldsymbol{e}_r = 0, \quad \tilde{\boldsymbol{j}}_\alpha e^{in\theta} = D_\alpha \nabla\left(\tilde{c}_\alpha e^{in\theta}\right) - \boldsymbol{v}_\alpha \tilde{c}_\alpha e^{in\theta}. \tag{5.113}$$

We note that

$$\tilde{\boldsymbol{j}}_\alpha = D_\alpha\left(\frac{\partial \tilde{c}_\alpha}{\partial r}\boldsymbol{e}_r + \frac{1}{r} in\tilde{c}_\alpha \boldsymbol{e}_\theta\right) - v_{\alpha,r}\tilde{c}_\alpha \boldsymbol{e}_r. \tag{5.114}$$

Hence, Eq. (5.113) gives the no-flux boundary condition on the cell membrane as

$$D_\alpha \frac{\partial \tilde{c}_\alpha}{\partial r} - v_{\alpha,r}\tilde{c}_\alpha = 0, \tag{5.115}$$

with an identical expression for the boundary with the cell nucleus.

5.9 Numerical implementation

To deduce the stability of the cell to various modes of deformation, we evolve the linear system presented in Sec. 5.8 in time. We let t_p denote the time that we perturb the time, relative to its introduction to the substrate (in non-linear simulations). At this time, the cell will have undergone an axisymmetric deformation from its initial state. In particular, all barred terms in the linearised equations presented in Sec. 5.8 are extracted from the non-linear axisymmetric simulations at time $t = t_p$ (see Sec. 5.6.4). We then initialise our linear simulations using an arbitrarily chosen perturbation which is consistent with the boundary conditions. In particular, for $R_n \leq r \leq R$ we introduce (dimensionless) perturbations of the form

$$\tilde{U}_r(r, 0) = -\epsilon\left(\frac{r - R_n}{R - R_n}\right), \tag{5.116}$$

i.e. we introduce a (negative) radial displacement throughout the cell cytoplasm that decays linearly, from a maximum displacement of $-\epsilon$ at the cell membrane, to zero at the boundary with the cell nucleus. In subsequent simulations we set $\epsilon = 0.01$. We do not perturb any other quantities, i.e. all perturbation concentrations and densities are set to zero initially with $\tilde{c}(x, 0) = 0$, $\tilde{n}(x, 0) = 0$.

Evolving the linear system in time, we solve the system of governing equations from Sec. 5.8 numerically, using a finite difference method based on the method lines (in a similar manner to Secs. 3.7, 5.6.3). We discretise the (dimensionless) spatial domain $R_n/R \leq r \leq$

1 using a uniform grid size Δr. We discretise all spatial derivatives using second-order finite difference stencils and employ the Matlab solver ode15s to solve the resulting large family of ODEs numerically. We employ the fictitious nodes procedure to apply the boundary conditions. We discretise the (dimensionless) domain with $\Delta r = 0.01(1 - R_n/R)$ and use stringent error bounds for the time-stepping.

In our analysis there is an initial transient as the initial configuration (described by Eq. 5.116) is not fully compatible with the governing equations, which passes after a (short) time of approximately t_t. We run simulations to a large time $t_s \gg t_t$. In this linear system, all quantities will eventually grow or decay exponentially with time, i.e. all quantities, described by a function $f(r,t)$, can eventually be written as $f(r,t) \approx \check{f}(r)e^{\Omega t}$, where $\Omega \in \mathbb{C}$ is the complex growth rate. The growth rate can be decomposed into $\Omega = \Omega_r + i\Omega_i$, where $\Omega_r = \mathrm{Re}(\Omega) > 0$ leads to exponential growth (instability), $\Omega_r < 0$ leads to exponential decay (stability) and $\Omega_r = 0$ represents neutral stability. Oscillations of the system are permissible, with frequency $\Omega_i = \mathrm{Im}(\Omega)$. These oscillations can be induced in response to some choices of initial perturbation, particularly if the initial configuration is far from compatible with the governing equations.

We determine the stability of the system by measuring the evolution of the perturbation deformation of the cell boundary (at the cell membrane) with time. We quantify the real part of the growth rate, $\mathrm{Re}(\Omega)$, by fitting an exponential curve to $\tilde{U}(R,t)$ for $t_t < t \leq t_s$. If the system exhibits exponentially growing or decay oscillations in this time frame, we fit an exponential curve to the envelope of local maxima/minima. We deduce the oscillation frequency, $\mathrm{Im}(\Omega)$, by calculating the inverse of the time, T, between two subsequent peaks (which is approximately independent of which two peaks are used), with $\mathrm{Im}(\Omega) \approx 2\pi/T$; if there are no oscillations by t_s, we suppose that $\mathrm{Im}(\Omega) = 0$.

5.10 Results

In this Section, using the linearised model developed in Secs. 5.7-5.8, we investigate the stability of the axisymmetric baseline state discussed in Sec. 5.6 to various normal modes of instability, parameterised by the azimuthal wavenumber, n. In particular, we examine the impact that perturbing the cell at different stages in the development and maturation of cell cytoskeleton and cell-substrate adhesion has on the growth rate of normal modes. For completeness, throughout our linear stability analyses we include the $n = 0$ (corresponding to axisymmetry) and $n = 1$ (corresponding to cell translation) modes. However, perturbations with $n = 0$ are analogous to our (linear) perturbations to the one-dimensional model (from Ch. 3) introduced in App. A. In this case, fully non-linear simulations demonstrate that perturbations briefly push the response of the system away from its preferred trajectory before it rapidly returns to this trajectory. Moreover, the

biological relevance of the translation mode $n = 1$ is questionable given that motile cells have different dominant signaling pathways (Ridley and Hall, 1992, Ridley et al., 1992). It follows that the modes of particular interest are $n \geq 2$; instabilities to these modes would indicate a mechanism for spontaneous surface patterning of binding cells *in vitro*.

In Fig. 5.8 we present baseline linear stability analyses, where we perturb the cell using the perturbation described by Eq. (5.116), at various times, t_p, after the cell has been introduced to the substrate. Particularly, we consider $t_p = 100$ s, $t_p = 250$ s, $t_p = 650$ s and $t_p = 1000$ s. Evolving the linear system in time, we consider the behaviour of the first six normal modes (i.e. $n = 0, 1, 2, 3, 4, 5$) and determine the stability of the system in the manner described in Sec. 5.9. We observe distinct behaviour of the system when perturbing at the four aforementioned times, including exponential decay (Fig. 5.8a), exponential growth (Fig. 5.8b), oscillatory growth (Fig. 5.8c) and oscillatory decay (Fig. 5.8d). Throughout our analysis, we denote the complex growth rate of the n^{th} mode by Ω_n. The initial rapid transient behaviour of the system (discussed in Sec. 5.9) is observed in Fig. 5.8 as near vertical lines close to the $y-$axis, reflecting the rapid adjustment of the perturbation described by Eq. (5.116). We are focused on the long-time behaviour of the system; however, these initial transients can subsequently induce the oscillatory behaviour observed in Figs. 5.8(c)-(d), when the system "overshoots" in returning to equilibrium from its initial perturbation.

At $t_p = 100$ s the cell is poorly adhered to the substrate in fully non-linear axisymmetric simulations (see Sec. 5.6.4). At this time, some bound integrins have formed (see Figs. 5.3b, 5.5e-f) but there are virtually no FAs (Fig. 5.5g-h) and there has been little actin polymerisation (Fig. 5.7c-d). The cell is stable to the perturbation described by Eq. (5.116) (see Fig. 5.8a) for all normal modes, i.e. $\mathrm{Re}(\Omega_n) < 0$. In particular, following initial (rapid) transient behaviour, the cell returns to its axisymmetric baseline state. There are also no oscillations, with $\mathrm{Im}(\Omega_n) = 0$. Moreover, stability at this time is hierarchical, with $n = 0$ the least stable mode, followed by $n = 1$ and so on, i.e. we have

$$0 > \mathrm{Re}(\Omega_0) > \mathrm{Re}(\Omega_1) > \mathrm{Re}(\Omega_2) > \mathrm{Re}(\Omega_3) > \mathrm{Re}(\Omega_4) > \mathrm{Re}(\Omega_5). \tag{5.117}$$

The stability of the axisymmetric configuration is due to the lack of mature structure (e.g. cytoskeleton and adhesion) in the cell at this early time. In particular, the (poorly-adhered) cell is unable to mechanosense and convert the perturbation from Eq. (5.116) into a biological response.

At $t_p = 250$ s we are in the early stages of the positive feedback loop in the fully non-linear axisymmetric simulations. Particularly, some actin has been polymerised (Fig. 5.7c-d) and cross-linked by activated myosin II to form VSFs (Fig. 5.7e-f). Consequently, the cell is in the early stages of contraction (see Figs. 5.3a, 5.4a), bound integrins are partially stretched and there has been a small amount of adhesion maturation (Figs. 5.3b, 5.5g-h).

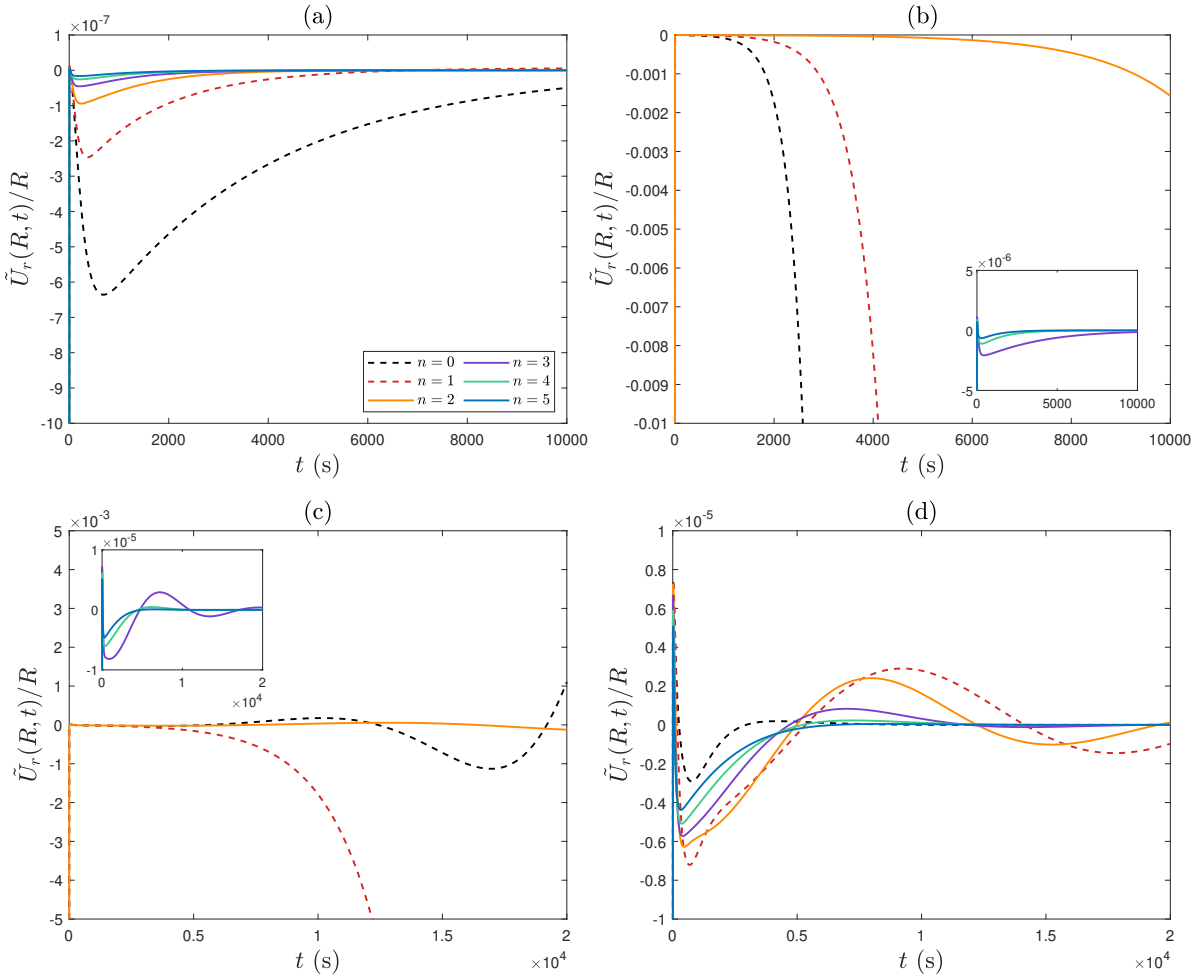

Figure 5.8: Baseline linear stability analyses. Growth or decay of the first six normal modes ($n = 0, 1, 2, 3, 4, 5$) when the cell is perturbed at (a) $t_p = 100$ s, (b) $t_p = 250$ s, (c) $t_p = 650$ s, (d) $t_p = 1000$ s. Stability is determined by considering the dimensionless radial boundary displacement of the cell, $\tilde{U}_r(R,t)/R$.

Introducing the perturbation from Eq. (5.116), the cell is unstable to modes $n = 0, 1, 2$ (see Fig. 5.8b), whilst it is stable to modes $n = 3, 4, 5$ (see inset Fig. 5.8b). The hierarchical structure in stability is maintained with

$$\mathrm{Re}(\Omega_0) > \mathrm{Re}(\Omega_1) > \mathrm{Re}(\Omega_2) > 0 > \mathrm{Re}(\Omega_3) > \mathrm{Re}(\Omega_4) > \mathrm{Re}(\Omega_5). \tag{5.118}$$

Again, there are no oscillations in the system, with $\mathrm{Im}(\Omega_n) = 0$ for each n. At this time the cell is susceptible to external influences as the cytoskeleton and adhesions are sufficiently mature so that the cell can respond to deformation, whilst a sufficient pool of free myosin II remains to further cross-link actin filaments and form more dense VSFs. Consequently, the cell contracts. Given that the $n = 0$ and $n = 1$ modes are largely redundant in our analysis (for the reasons discussed above), $\mathrm{Re}(\Omega_2) > 0$ is significant. In particular, this suggests that the cell has the ability to develop non-axisymmetric surface

patterning, in isolation, through the coupled biomechanics of cell-substrate adhesions and cell cytoskeleton, if perturbed at this stage of cell-substrate interaction. However, we would need to test this perturbation in a full two-dimensional non-linear simulation of this system to determine if mode $n = 2$ patterns are ever observable in practice.

For $t_p = 650$ s after the cell has been introduced to the substrate, the cell will be at an intermediate stage in the positive feedback loop (as discussed in Sec. 5.6.4). Particularly, there will be ongoing rapid maturation of adhesions (Figs. 5.3b, 5.5g-h), activation of ROCK and phosphorylation of its downstream effectors (Figs. 5.3c, 5.6), polymerisation of actin (Figs. 5.3d, 5.7c-d) and cross-linking of filaments by activated myosin II to form contractile VSFs (Figs. 5.3d, 5.7e-f). Perturbing the cell at this time, we lose the hierarchical behaviour exhibited at earlier perturbation times, where now $n = 1$ is the dominant mode (although biologically irrelevant). The $n = 0, 1, 2$ modes remain unstable (see Fig. 5.8c) and $n = 3, 4, 5$ modes remain stable (see inset in Fig. 5.8c). We compute

$$\mathrm{Re}(\Omega_1) > \mathrm{Re}(\Omega_0) > \mathrm{Re}(\Omega_2) > 0 > \mathrm{Re}(\Omega_3) > \mathrm{Re}(\Omega_4) > \mathrm{Re}(\Omega_5). \tag{5.119}$$

However, perturbing the cell at this time leads to oscillations (with the exception of the $n = 1$ mode). Particularly, we have $\mathrm{Im}(\Omega_1) = 0$ and $\mathrm{Im}(\Omega_0) > 0$, $\mathrm{Im}(\Omega_2) > 0$, $\mathrm{Im}(\Omega_3) > 0$, $\mathrm{Im}(\Omega_4) > 0$ and $\mathrm{Im}(\Omega_5) > 0$; there appears to be no obvious ordering to these oscillation frequencies (see Fig. 5.8c). These unstable waves form early in the evolution of the linear system, due to resistance to the imposed deformation (Eq. 5.116) by the mature adhesions and cytoskeleton. In particular, we observe in Figs. 5.8(c)-(d) that the deformation of the cell "overshoots" during the initial transient behaviour when attempting to return to its unperturbed state (due to the incompatibility of the initial condition Eq. 5.116 with the governing equations).

Finally, perturbing the cell at $t_p = 1000$ s means that the cell has formed mature adhesions and cytoskeleton and the positive feedback loop connecting the development of these structures is now subdominant in the fully non-linear axisymmetric simulations (see Sec. 5.6.4). Particularly, at this time the majority of integrins have been recruited into FAs (Fig. 5.3b), and a significant amount of myosin II has been activated (Fig. 5.7g-h) and has cross-linked actin filaments to form VSFs (Fig. 5.7e-f). At this time, the cell is stable to all perturbation modes (Fig. 5.8d), with $n = 0$ the most stable mode (of those tested), followed by a hierarchical structure with $n = 1$ the least stable mode, followed by $n = 2$ and so on. In particular, we have

$$0 > \mathrm{Re}(\Omega_1) > \mathrm{Re}(\Omega_2) > \mathrm{Re}(\Omega_3) > \mathrm{Re}(\Omega_4) > \mathrm{Re}(\Omega_5) > \mathrm{Re}(\Omega_0). \tag{5.120}$$

However, rather than pure exponential decay, we observe damped oscillatory waves for all normal modes, for exactly the same reasons as when the system is perturbed at $t_p = 650$ s.

The greatest frequency of these oscillations is for the $n = 0$ mode; thereafter a hierarchical structure in oscillation frequency is observed. In particular, we have

$$\mathrm{Im}(\Omega_0) > \mathrm{Im}(\Omega_5) > \mathrm{Im}(\Omega_4) > \mathrm{Im}(\Omega_3) > \mathrm{Im}(\Omega_2) > \mathrm{Im}(\Omega_1) > 0. \tag{5.121}$$

This switching behaviour, from an unstable response when the cell is perturbed at $t_p = 650$ s (see Fig. 5.8c), to an underdamped system (see Fig. 5.8d) when perturbed at the late stages of adhesion development, reflects the dwindling pool of myosin II available for VSF formation.

We now examine in a more systematic manner how the stage at which the cell is perturbed (governed by the parameter t_p) influences the stability of the cell to various modes of deformation, presenting two visualisations of the parameter space in Fig. 5.9. In particular, in Fig. 5.9(a) we illustrate the growth rate, $\mathrm{Re}(\Omega_n)$, of the boundary deformation, as a function of the time of perturbation (in full non-linear simulations), for various mode numbers, n. In Fig. 5.9(b) we present the growth rate, $\mathrm{Re}(\Omega_n)$, of the boundary deformation as a function of mode number for various perturbation times, t_p, in the full non-linear simulations. Regions where exponential growth (decay) will occur are shaded in light green (red). For completeness, we again include the $n = 0$ and $n = 1$ modes (as dashed lines) in our analysis. However, our primary focus remains on modes with $n \geq 2$ and so we provide no discussion of modes $n = 0$, $n = 1$. There is a degree of volatility throughout our analysis (particularly in Fig. 5.9a) but this is only due to the numerical method used to fit an exponential curve to the perturbation deformation and does not detract from our overall conclusions.

In Fig. 5.9 we observe that $\mathrm{Re}(\Omega_n) < 0$ (for $n = 0, 1, 2, 3, 4, 5$) when $t_p \lesssim 100 - 150$ s (consistent with Fig. 5.8a). In particular, the cell is stable to perturbations at these early times due to the lack of mature structure, with the cell unable to convert the applied mechanical perturbation into a biological response. With increasing time at which the perturbation is applied, we then observe a window of instability for the $n = 2$ mode. Particularly, perturbing the cell on the order of hundreds of seconds after being introduced to the substrate, we have $\mathrm{Re}(\Omega_2) > 0$. This suggests that, at these intermediate times, mechanical (and biochemical) cues can cause the cell to lose axisymmetry. Increasing the perturbation time further, the cell becomes stable to all modes of deformation, reflective of the entrenched axisymmetry due to the mature (axisymmetric) adhesions and cytoskeleton in the base state (see Sec. 5.6.4).

Our linear stability analysis suggests that for small and large perturbation times the cell remains axisymmetric. Meanwhile, non-linear simulations of the axisymmetric system demonstrate that, even though axisymmetric perturbations grow exponentially in the linear system when perturbations are applied at intermediate times (Fig. 5.9), the non-linear system adopts the same final axisymmetric state. However, for a range of intermediate

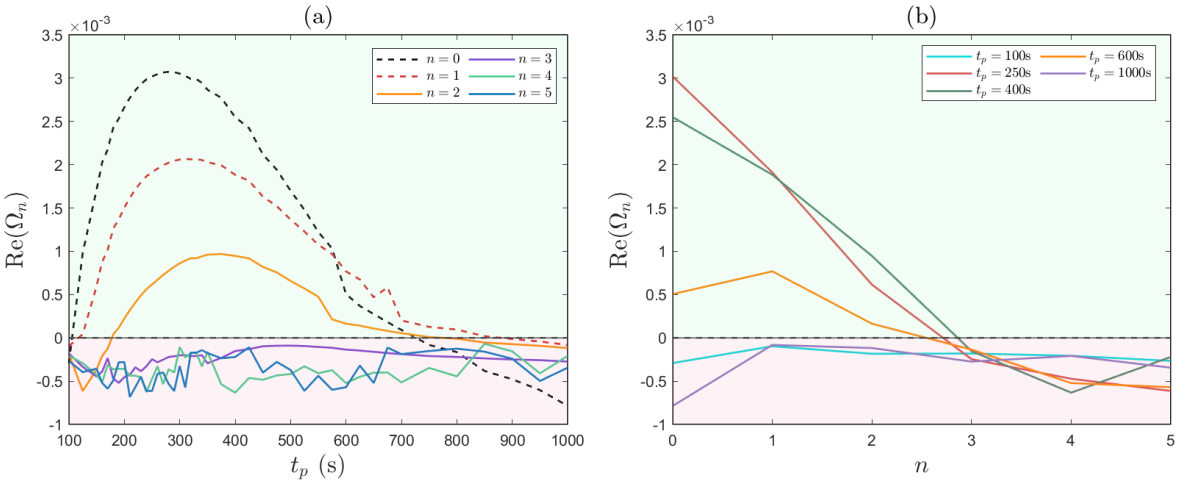

Figure 5.9: Influence of time of perturbation on cell stability. Real part of the complex growth rate as (a) a function of perturbation time, t_p, for various modes, (b) a function of mode number, for various perturbation times. Imaginary part of the complex growth rate as (c) a function of perturbation time, t_p, for various modes, (d) a function of mode number, for various perturbation times. Pale green background represents region of instability, pale red background denotes region of stability.

perturbation times the system is also unstable to higher modes of deformation (Fig. 5.9). It remains to be seen if such higher modes are ever observed in fully non-linear simulations. Nonetheless, the spontaneous transition to higher modes observed in Figs. 5.8-5.9 demonstrates the potential ability of a cell to form self-directed surface patterning *in vitro*; advancing on the prescribed forcing used in existing modelling approaches (e.g. Solowiej-Wedderburn and Dunlop, 2022).

It should be noted that the outcome from this linear stability analysis is likely highly sensitive to the prescribed form of initial perturbation and the response of the system may be enhanced using a different (optimal) perturbation. However, given the focus on mechanotransduction in this thesis, we have employed a purely mechanical perturbation (Eq. 5.116). As we prescribe only changes in displacement (and not in protein concentrations), this explains why, for $n = 0$, the system returns to the same trajectory once the perturbation washes out in fully non-linear simulations. The impact of changes to reaction kinetics in the model should also be examined (given we have to estimate several parameters in the model). However, crucially this modelling approach has demonstrated a route for the formation of surface patterning for a cell cultured in isolation *in vitro*. We are also able to demonstrate that our predictions for the growth rate of different modes are independent of the perturbation type (e.g. a biochemical rather than mechanical perturbation).

5.11 Summary

In this Chapter we have extended the one-dimensional bio-chemo-mechanical continuum model we have developed in Ch. 3 to a two-dimensional model. This extension allows for explicit incorporation of the cell nucleus, which we treat as a rigid body. It also allows for inclusion of an elastic cell membrane, the mechanical properties of which we have neglected in this current work. We have demonstrated in Sec. 5.6.4 the ability of this two-dimensional model to replicate the baseline behaviour predicted by our one-dimensional model (see Sec. 3.8). Particularly, we are able to reproduce the predicted non-uniform cell stress and striation, and localisation of FAs, VSFs and activated ROCK near to the cell edge. Moreover, the global dynamics of cell-substrate adhesion and cytoskeleton formation are shown to be consistent with predictions from both our zero-dimensional model (see Ch. 2) and our one-dimensional model (see Ch. 3).

We use the predicted axisymmetric deformation as a base state around which to conduct a linear stability analysis (Secs. 5.7-5.10) to predict the stability of the cell to various normal modes of deformation. We demonstrate that, for baseline parameter values, the cell is unstable to certain non-axisymmetric modes for an intermediate range of perturbation times, suggesting a possible mechanism for self-directed surface patterning *in vitro*. Relaxation of certain conditions imposed in our modelling (e.g. purely radial treadmilling of actin) may give access to further modes of instability. Moreover, instabilities may be enhanced through interactions of cells with their external environment (e.g. remodelling of the ECM by other cells and direct cell-cell communication), this is deferred to future work.

Chapter 6

Discussion

Motivated by an interest in controlling the differentiation of hMSCs using mechanical and biochemical cues, this thesis has focused on the development of models to describe interactions between eukaryotic cells and their microenvironment. Particularly, we have developed models to describe the formation and maturation of adhesions between a cell and substrate *in vitro*, the subsequent activation of intracellular signaling cascades and the resultant development of cell cytoskeleton due to enhanced actin polymerisation and myosin II activation. The bio-chemo-mechanical continuum models that we develop in Chs. 3-5 build particularly on models for motile cells (particularly Gracheva and Othmer, 2004, Larripa and Mogilner, 2006), a model for the contraction of SFs (by Besser and Schwarz, 2007) and to mechanical models for the deformation of a cell adhered to a substrate by (particularly Dunlop, 2019, Edwards and Schwarz, 2011). However, we provide several advancements, which we discuss in this brief Chapter, together with outlining a range of possible future research directions.

The models developed in this thesis are as minimal as possible whilst retaining the necessary biophysics. In particular, they account only for the scaffolding and signaling proteins that are key to the development of cell-substrate adhesions and cell cytoskeleton. However, despite their relative simplicity, these models are able to capture the positive feedback loop that couples cytoskeleton development to adhesion maturation, whilst crucially making no assumptions on where FAs and SFs will form and mature. Moreover, despite being motivated by modelling the interaction of hMSCs with their microenvironment, the models we have developed in Chs. 2-5 have been formulated in a general manner, lending themselves to application to a wide variety of eukaryotic cell types. A particular strength of our approach is the detailed analysis of ROCK signaling, which is known to be influential in cell function (Riento and Ridley, 2003). Moreover, by distinguishing between bound integrins (nascent adhesions) and FAs, we have been able to incorporate, empirically, the increase in ROCK signaling associated with adhesion maturation (Wozniak et al., 2004).

In addition to being able to predict the localisation of integrins, actin, myosin and signaling proteins in their various forms, our coupling to viscoelastic deformation provides insight into mechanical changes inside the cell and ECM, particularly the temporal and spatial variations in displacement, stress and strain of both structures. Crucially, deformation of the ECM due to the communication of intracellular forces via cell-substrate adhesions allows us to elucidate the mechanism by which FAs and SFs localise and provides a platform by which to later investigate biochemical remodelling (through protease secretion) of the ECM by the cell. Moreover, we rationally link nanoscale and microscale mechanical properties of the cell, ECM and adhesions through the use of discrete-to-continuum upscaling, advancing on the homogenised description of the cell provided by many existing models (see Ch. 3). Consequently, the model provides a framework for systematic investigation into how the cell biochemistry and mechanics influence cell development and facilitates prediction of internal cell measurements that are difficult to ascertain experimentally. These models are also able to replicate various experimentally observed phenomena. Indeed, our one-dimensional model predicts that increasing ligand density leads to more pronounced FA formation but has a weaker effect on nascent adhesion formation (see Sec. 4.1), consistent with experimental observations by Cavalcanti-Adam et al. (2007). Moreover, the one-dimensional model predicts a minimum ligand density (or equivalently maximum ligand spacing), below which FAs struggle to form, in line with Arnold et al. (2004). The one-dimensional model also replicates the experimental observation that cells form more FAs and VSFs when cultured on stiffer substrates (Engler et al., 2006), also elucidating the mechanism by which this occurs (see Sec. 4.3). We further demonstrate in Ch. 4 that the model developed in Ch. 3 provides a framework to predict how mechanotransductive and chemotransductive cues can be optimally applied to facilitate (or prevent) adhesion and cytoskeleton development, with potential applicability in improving experimental protocols. Particularly, we have demonstrated how probing of the cell (e.g. mimicking atomic force microscopy or magnetic tweezer experiments) can induce adhesion formation in Sec. 4.5. Further, we show in Sec. 4.6 how ROCK and myosin II inhibitors can be employed to facilitate FA and SF disassembly.

We have demonstrated in Ch. 2 that a simple ODE model to describe the cell biochemistry can successfully capture several key features of cell-substrate interaction. In particular, this spatially-averaged description of the cell is able to closely reproduce the global dynamics of the development of cell-substrate adhesions and cell cytoskeleton predicted by our one-dimensional model in Ch. 3 (compare Figs. 2.1, 3.7). The computational cost of simulating a family of ODEs that describe the average concentration of proteins in the cell is dramatically less than simulating a family of PDEs which account for spatial variations; employing the method of lines, PDEs require the solution of a time-dependent ODE at each spatial location. This simple model should be amenable to a multiple scales

analysis (Hinch, 1991, Nayfeh, 2008), which should elucidate the cause and effect of different processes. Consequently, this would allow for a systematic reduction in model complexity (through a reduction in the number of parameters and equations solved) in higher-dimensional models, improving computational efficiency.

Moving forward, the essence of our modelling approach is also applicable to motile cells. In these cells different signaling cascades (e.g. Rac) and different types of SF (e.g. dorsal fibres and transverse arcs) become important (Ridley et al., 1992, Tojkander et al., 2012) and the cell cortex becomes a crucial driver of intracellular dynamics (Cusseddu et al., 2019, Gracheva and Othmer, 2004, Mogilner and Edelstein-Keshet, 2002). This extension of the model would be complicated by the moving boundary problem that arises when considering the coupled deformation and motion of the cell. This may require, for example, application of the immersed boundary method to account for the interaction of intracellular fluid with the membrane (Mittal and Iaccarino, 2005, Peskin, 2002). However, inclusion of cell motility is necessary to describe the motion of hMSCs to maintain tissue homoeostasis and mediate repair and regeneration (de Lucas et al., 2018). Such modelling also has applications in predicting cancer metastasis (Franssen et al., 2019, Stuelten et al., 2018).

In the bio-chemo-mechanical models (presented in Chs. 3-5) we have assumed that the mechanical properties of the ECM are constant in time and have considered only mechanical remodelling of the ECM by the cell. However, the ECM is in a constant state of flux and cells continually secrete proteases which form, degrade or modify the ECM (Bonnans et al., 2014). The mechanical models we have developed should be readily adaptable to investigate how secreted proteases induce changes in cell-substrate adhesion and cell cytoskeleton through altering environmental biochemical and mechanical stimuli (e.g. through self-driven chemo- or duro-taxis). This development is a necessary step towards understanding a variety of processes including the establishment of a stem cell niche (Li and Xie, 2005, Lu et al., 2011), branching morphogenesis in the development of lungs and kidneys (Kheradmand et al., 2002, Page-McCaw et al., 2007), branching of blood vessels (Ilan et al., 2006, Mott and Werb, 2004) and wound repair (Xue and Jackson, 2015).

We have further illustrated the ability of the one-dimensional model to predict the biochemical response of the cell to distant mechanical perturbations in the ECM (e.g. mimicking ECM remodelling by another cell). Throughout this thesis we have modelled cells in isolation. However, cells rarely exist remotely and the consideration of cell-cell interactions is crucial for upscaling from cells to tissues, a necessity for applications to tissue model development (Barry et al., 2022). Cells communicate with each other through a variety of means, particularly through the formation of cadherin junctions (cell-cell adhesions) or through the release of soluble molecules (e.g. growth factors, cytokines and

chemokines). For example, the formation of cadherin junctions leads to changes in cell morphology and function through their influence on cytoskeletal tension and, consequently, on intracellular signaling (Gomez et al., 2011, Maître and Heisenberg, 2013). It is hence crucial to consider these interactions, where individual cells influence their neighbours, giving rise to collective behaviour (Brückner et al., 2021, Mishra et al., 2019, Poujade et al., 2007). Indeed, our modelling suggests these interactions may be necessary to enhance the asymmetries observed in real cells (see Ch. 5). Again, our modelling approach should be amenable to this addition, with cell-cell adhesions included through modification of the boundary conditions applied to the cell and with soluble molecules described by a set of reaction-diffusion equations.

We have modelled the cell, ECM and adhesions as Kelvin-Voigt viscoelastic materials and have assumed that deformation of each of these structures is small, allowing us to employ simple linear relations between stress and strain (in a similar manner to Besser and Schwarz, 2007, Gracheva and Othmer, 2004, Larripa and Mogilner, 2006). The assumption of linear Kelvin-Voigt viscoelasticity is appropriate for materials that behave as long-time solids. However, it would be instructive to consider other constitutive relations. For example, DiMilla et al. (1991) employ a Maxwell description (long-time fluid) for a migrating cell in the vicinity of the cell front and rear (whilst assuming Kelvin-Voigt behaviour in the cell bulk). Moreover, nanokicking of cells has been shown to induce sizeable cell deformation (Robertson et al., 2018), where the assumption of linear viscoelasticity may no longer be valid and a non-linear constitutive assumption may be required (Bonet, 2001). Furthermore, a poroelastic description of the cell may also be appropriate to describe the interaction between the cell cytosol and cytoskeleton (Copos and Guy, 2018, Moeendarbary et al., 2013, Thekkethil et al., 2024). These adaptations to the assumed rheological properties of the cell may be necessary to capture different phases of cell-substrate interaction, particularly if cell motility is incorporated.

In this thesis we have focused particularly on the mechanosensing ability of the cell cytoskeleton and cell-substrate adhesions. However, as discussed in Ch. 1, mechanosensing also occurs at the cell nucleus and stretch-activated ion channels (Enyedi and Niethammer, 2017, Isermann and Lammerding, 2013, Lammerding, 2011, Martino et al., 2018, Ridone et al., 2019). To more fully capture cellular mechanotransduction it would be useful to incorporate these effects into our model. For example, enhanced calcium signaling through activation of ion channels can lead to MLCK phosphorylation, increasing myosin II activation (Kuo and Ehrlich, 2015, Takashima, 2009). Our two-dimensional work lays the groundwork for the incorporation of nuclear mechanosensing, where we treat the nucleus as a rigid body, occupying a large volume at the centre of the cell (see Ch. 5). Signaling from this structure could be induced in our model through stress at the boundary between the cell cytoplasm and the nucleus, with a set of diffusive proteins released or activated

at this boundary. Moreover, deformation of the nucleus could be included in a relatively simple manner if we assume it has constant stiffness and viscosity. In this case, matching of stress and displacement could be employed at the boundary between the cell cytoplasm and nucleus in a similar manner to the matching employed between regions of the ECM underneath the cell and in the far field (see Chs. 3-5).

We have presented a discrete one-dimensional model to describe the mechanical properties and deformation of the cell, ECM and adhesions (see Ch. 3). By performing discrete-to-continuum upscaling we have been able to formally connect nanoscale and microscale mechanical features of the cell cytoskeleton and cell-substrate adhesions. However, we neglect a discrete description for the cell biochemistry. Discrete modelling could, for example, include molecular or Brownian dynamics simulations for the formation of cell-substrate adhesions (Bidone et al., 2019, Tong et al., 2023), signaling protein aggregation (Gabdoulline and Wade, 1998, Mereghetti et al., 2010), actin filament polymerisation (Guo et al., 2010, Lee and Liu, 2009) and myosin II cross-linking of filaments treated as discrete elastic rods (Bidone et al., 2017, Borau et al., 2012, Mak et al., 2016b). Such simulations are computationally costly, however they reduce the need for empiricism and provide significant insight into the nanoscale biochemical and mechanical properties of cell-substrate adhesion and cytoskeleton development (Erban, 2014). Hence, it would be informative to develop such a model to describe the formation and maturation of adhesions and to describe actin polymerisation and branching in two- and three-dimensions. This modelling approach may also explain the observed discrepancy in stiffness between purified actin filaments and the actin cytoskeleton (Haase and Pelling, 2015). Moreover, this approach opens up the possibility for links to the tensegrity model for mechanotransduction developed by Ingber (1997), which describes the cell as a set of compressive struts (microtubules and FAs) connected by tension cables (actin and intermediate filaments).

Another fundamental development to our modelling approach would be incorporation of intracellular fluid flows, to describe the transport of proteins, which have been neglected in the models presented in this thesis. Such modelling would allow us to elucidate the subcellular fluid mechanical processes influenced by mechanostimuli. In particular, we would be able to investigate how mechanostimuli (e.g. nanokicking) drive fluid instabilities inside the cell, generating (or enhancing) fluid flows (e.g. cytoplasmic streaming) to transport proteins and promote the polymerisation of actin filaments and maturation of adhesions to the ECM (Illukkumbura et al., 2020, Mogre et al., 2020). This would also involve considering the entrainment of the viscous cytoplasmic fluid by myosin motors (Goldstein and van de Meent, 2015, Goldstein et al., 2008).

In this thesis, we have demonstrated the ability of our modelling approach in one- and two-dimensions to investigate the influence cues from the cellular microenvironment (e.g. substrate stiffness or viscosity) have on cell-substrate adhesion and cytoskeleton develop-

ment. However, cells are fundamentally three-dimensional structures and it would be natural to extend our current bio-chemo-mechanical continuum model, firstly through depth-averaging, to a quasi-three-dimensional model, before moving to a fully three-dimensional framework, which could be implemented computationally using the finite element method. Such an extension is required, for example, for modelling the influence of fluid shear strength on cell development.

Finally, the maturation of cell-substrate adhesions and development of cell cytoskeleton is linked to intracellular signaling for changes in cell function (Geiger et al., 2009, Wozniak et al., 2004). These signaling cascades could be incorporated into our model to investigate the circumstances (e.g. substrate stiffness, fluid shear strength) where a cell will undertake a particular function. For example, future iterations of the model could incorporate the YAP/TAZ molecular pathway (previously modelled by Sun et al., 2016), which is important in the differentiation of hMSCs; or activation of FAK, and its downstream effector ERK, which regulates cell division, differentiation, and survival (Lavoie et al., 2020, Sawai et al., 2005). Consequently, the models we have developed in this thesis serve as a necessary first step to characterise the mechanotransductive cues required to direct cells to undertake a particular function.

Appendix A

Linear stability analysis of one-dimensional model

In Ch. 3 we develop a one-dimensional bio-chemo-mechanical model to describe the coupled development of cell-substrate adhesions and cell cytoskeleton, together with the deformation of the cell, ECM and adhesions. In Ch. 5 we extend this modelling approach to two spatial dimensions, where we subsequently perform a linear stability analysis (see Sec. 5.7) to predict the stability of the non-linear axisymmetric system (discussed in Sec. 5.6) to various normal modes of deformation. In a similar manner, in this Appendix we present a linear stability analysis on the one-dimensional model presented in Ch. 3.

A.1 Identification of a base state

In Sec. 3.8 we show how the cell, when introduced to a substrate, forms adhesions and develops contractile VSFs. We observe in Sec. 3.8 that, after some time (on the order of an hour), the cell will settle to a near steady state. In order to predict the stability of the cell to perturbations, we perform a linear stability analysis around the non-linear base state described in Ch. 3.

A.2 Linearisation

Linearising around the non-linear base state described in Ch. 3, we perturb all quantities by a small amount, ϵ. Hence, all concentrations and densities can be written as the sum of a baseline value (denoted by a bar) and a perturbation (denoted by a hat), i.e. $c = \bar{c} + \epsilon\hat{c}$, $n = \bar{n} + \epsilon\hat{n}$. Moreover, displacements in the cell and ECM be written as $u = \bar{u} + \epsilon\hat{u}$, $w = \bar{w} + \epsilon\hat{w}$. Additionally, we assume all mechanical properties of the cell, ECM and adhesions can be written as the sum of a baseline figure (denoted by a bar) and a small perturbation, of amplitude ϵ, denoted by a hat, in a similar manner to Sec. 5.7. All values

denoted by a bar are the base state values extracted from our full non-linear simulations (see Sec. 3.8). Note that this linearisation is independent of the assumption of linear elasticity, which is present in the non-linear model also (see Sec. 3.1). Note also that the perturbations we introduce are one-dimensional only.

A.2.1 Mechanical equations

The Cauchy stress inside the cell cytoplasm, given be Eq. (3.19c), can be decomposed into its non-linear base state value plus a small perturbation by writing $\sigma_c = \bar{\sigma}_c + \epsilon\hat{\sigma}_c$ with

$$\sigma_c = \left(\bar{E}_c + \epsilon\hat{E}_c\right)\left(\bar{\epsilon}_c + \epsilon\hat{\epsilon}_c\right) + \left(\bar{\mu}_c + \epsilon\hat{\mu}_c\right)\left(\frac{\partial\bar{\epsilon}_c}{\partial t} + \epsilon\frac{\partial\hat{\epsilon}_c}{\partial t}\right) + \left(\bar{\tau} + \epsilon\hat{\tau}\right) + O\left(\epsilon^2\right). \tag{A.1}$$

It follows that

$$\sigma_c = \bar{E}_c\bar{\epsilon}_c + \bar{\mu}_c\frac{\partial\bar{\epsilon}_c}{\partial t} + \bar{\tau} + \epsilon\left(\bar{E}_c\hat{\epsilon}_c + \hat{E}_c\bar{\epsilon}_c + \bar{\mu}_c\frac{\partial\hat{\epsilon}_c}{\partial t} + \hat{\mu}_c\frac{\partial\bar{\epsilon}_c}{\partial t} + \hat{\tau}\right) + O\left(\epsilon^2\right), \tag{A.2}$$

where

$$\bar{\epsilon}_c = \frac{\partial\bar{u}}{\partial x}, \quad \hat{\epsilon}_c = \frac{\partial\hat{u}}{\partial x}. \tag{A.3}$$

From Eq. (3.19a) we have

$$\frac{\partial\sigma_c}{\partial x} = \left(\bar{\beta}_I + \epsilon\hat{\beta}_I\right)\frac{\partial}{\partial t}\left(\bar{u} + \epsilon\hat{u} - \bar{w} - \epsilon\hat{w}\right) + \left(\bar{\kappa}_I + \epsilon\hat{\kappa}_I\right)\left(\bar{u} + \epsilon\hat{u} - \bar{w} - \epsilon\hat{w}\right) + O\left(\epsilon^2\right). \tag{A.4}$$

Combining Eq. (A.2) and Eq. (A.4) then at $O(\epsilon^0)$ we have

$$\frac{\partial}{\partial x}\left(\bar{E}_c\bar{\epsilon}_c + \bar{\mu}_c\frac{\partial\bar{\epsilon}_c}{\partial t} + \bar{\tau}\right) = \bar{\beta}_I\frac{\partial}{\partial t}\left(\bar{u} - \bar{w}\right) + \bar{\kappa}_I\left(\bar{u} - \bar{w}\right), \tag{A.5}$$

precisely the baseline non-linear problem we have solved in Ch. 3, with results detailed in Sec. 3.8. At $O(\epsilon)$ we have from Eq. (A.2) and Eq. (A.4) that

$$\begin{aligned}\frac{\partial}{\partial x}\left(\bar{E}_c\hat{\epsilon}_c + \hat{E}_c\bar{\epsilon}_c + \bar{\mu}_c\frac{\partial\hat{\epsilon}_c}{\partial t} + \hat{\mu}_c\frac{\partial\bar{\epsilon}_c}{\partial t} + \hat{\tau}\right) &= \bar{\beta}_I\frac{\partial}{\partial t}\left(\hat{u} - \hat{w}\right) + \hat{\beta}_I\frac{\partial}{\partial t}\left(\bar{u} - \bar{w}\right) \\ &\quad + \bar{\kappa}_I\left(\hat{u} - \hat{w}\right) + \hat{\kappa}_I\left(\bar{u} - \bar{w}\right).\end{aligned} \tag{A.6}$$

In an identical manner we write the Cauchy stress in the ECM, given be Eq. (3.19c), as $\sigma_E = \bar{\sigma}_E + \epsilon\hat{\sigma}_E$. A similar calculation demonstrates that

$$\bar{\epsilon}_E = \frac{\partial\bar{w}}{\partial x}, \quad \hat{\epsilon}_E = \frac{\partial\hat{w}}{\partial x}, \tag{A.7}$$

representing the baseline and perturbation infinitesimal strain tensors respectively. We

hence deduce, in a similar manner to the cell, that

$$\frac{\partial}{\partial x}\left(\bar{E}_E\hat{\epsilon}_E+\hat{E}_E\bar{\epsilon}_E+\bar{\mu}_E\frac{\partial\hat{\epsilon}_E}{\partial t}+\hat{\mu}_E\frac{\partial\bar{\epsilon}_E}{\partial t}\right)=\bar{\beta}_I\frac{\partial}{\partial t}\left(\hat{w}-\hat{u}\right)+\hat{\beta}_I\frac{\partial}{\partial t}\left(\bar{w}-\bar{u}\right)$$
$$+\bar{\kappa}_I\left(\hat{w}-\hat{u}\right)+\hat{\kappa}_I\left(\bar{w}-\bar{u}\right). \tag{A.8}$$

Boundary conditions

Following Eq. (3.31b) we impose no perturbation stress boundary conditions on the cell in the form

$$\hat{\sigma}_c\left(-L/2,t\right)=0,\quad \hat{\sigma}_c\left(L/2,t\right)=0. \tag{A.9}$$

From Eq. (3.31c) the perturbation boundary conditions on the ECM are given by

$$\hat{\bar{w}}_1(-L/2-L_1,t)=0,\quad \hat{\bar{w}}_2(L/2+L_1,t)=0, \tag{A.10a}$$

note that the barred terms here do not denote $O(\epsilon^0)$ quantities, instead these definitions follow from our setup in Sec. 3.1.7. At the junctions between ECM regions either side of the cell boundary we match stress and displacement (see Eq. 3.42), i.e.

$$\hat{\bar{w}}_1(-L/2,t)=\hat{w}(-L/2,t),\quad \hat{\bar{\sigma}}_{E,1}(-L/2,t)=\hat{\sigma}_E(-L/2,t), \tag{A.10b}$$
$$\hat{\bar{w}}_2(L/2,t)=\hat{w}(L/2,t),\quad \hat{\bar{\sigma}}_{E,2}(L/2,t)=\hat{\sigma}_E(L/2,t). \tag{A.10c}$$

A.2.2 Biochemistry

We introduce small perturbations to all concentrations and densities in the biochemical equations Eqs. (3.29)-(3.30). The $O(\epsilon^0)$ equations are exactly those presented in Ch. 3 given by Eqs. (3.29)-(3.30). At $O(\epsilon)$ we have

$$\frac{\partial\hat{c}_G}{\partial t}=-\left(\bar{k}_p^+\bar{c}_G\left(\hat{n}_b^{(1)}+\hat{n}_b^{(2)}+\hat{n}_A^{(1)}+\hat{n}_A^{(2)}\right)+\hat{k}_p^+\hat{c}_G\left(\bar{n}_b^{(1)}+\bar{n}_b^{(2)}+\bar{n}_A^{(1)}+\bar{n}_A^{(2)}\right)\right.$$
$$\left.+\hat{k}_p^+\bar{c}_G\left(\bar{n}_b^{(1)}+\bar{n}_b^{(2)}+\bar{n}_A^{(1)}+\bar{n}_A^{(2)}\right)\right)+\left(\bar{k}_p^-\left(\hat{c}_F^{(1)}+\hat{c}_F^{(2)}\right)+\hat{k}_p^-\left(\bar{c}_F^{(1)}+\bar{c}_F^{(2)}\right)\right)$$
$$+k_m^-\hat{c}_S^++D_G\frac{\partial^2\hat{c}_G}{\partial x^2}, \tag{A.11a}$$

$$\frac{\partial\hat{c}_F}{\partial t}+\frac{\partial}{\partial x}\left(\hat{c}_F^{(i)}U^{(i)}\right)=\left(\bar{k}_p^+\bar{c}_G\left(\hat{n}_b^{(i)}+\hat{n}_A^{(i)}\right)+\hat{k}_p^+\hat{c}_G\left(\bar{n}_b^{(i)}+\bar{n}_A^{(i)}\right)+\hat{k}_p^+\bar{c}_G\left(\bar{n}_b^{(i)}+\bar{n}_A^{(i)}\right)\right)$$
$$-\left(\bar{k}_p^-\hat{c}_F^{(i)}+\hat{k}_p^-\bar{c}_F^{(i)}\right)-k_m^+\left(\bar{c}_F^{(i)}\bar{c}_F^{(i)}+\bar{c}_F^{(1)}\bar{c}_F^{(2)}+\bar{c}_F^{(i)}\bar{c}_S^+\right)\hat{c}_M^+$$
$$-k_m^+\left(2\bar{c}_F^{(i)}\hat{c}_F^{(i)}+\bar{c}_F^{(1)}\hat{c}_F^{(2)}+\hat{c}_F^{(1)}\bar{c}_F^{(2)}+\bar{c}_F^{(i)}\hat{c}_S^++\hat{c}_S^+\bar{c}_F^{(i)}\right)\bar{c}_M^++D_F\frac{\partial^2\hat{c}_F^{(i)}}{\partial x^2}, \tag{A.11b}$$

$$\frac{\partial\hat{c}_S^+}{\partial t}=k_m^+\left(2\bar{c}_F^{(1)}\hat{c}_F^{(2)}+2\hat{c}_F^{(1)}\bar{c}_F^{(2)}+2\bar{c}_F^{(1)}\hat{c}_F^{(1)}+2\bar{c}_F^{(2)}\hat{c}_F^{(2)}+\bar{c}_F^{(1)}\hat{c}_S^++\hat{c}_F^{(1)}\bar{c}_S^++\bar{c}_F^{(2)}\hat{c}_S^++\hat{c}_F^{(2)}\bar{c}_S^+\right)\bar{c}_m^+$$
$$+k_m^-\left(2\bar{c}_F^{(1)}\bar{c}_F^{(2)}+\bar{c}_F^{(1)}\bar{c}_F^{(1)}+\bar{c}_F^{(2)}\bar{c}_F^{(2)}+\bar{c}_F^{(1)}\bar{c}_S^++\bar{c}_F^{(2)}\bar{c}_S^+\right)\hat{c}_m^+-k_m^+\hat{c}_S^+, \tag{A.11c}$$

$$\frac{\partial \hat{c}_M}{\partial t} = -\left(\bar{k}_a^+ \hat{c}_M + \hat{k}_a^+ \bar{c}_M\right) + \left(\bar{k}_a^- \hat{c}_M^+ + \hat{k}_a^- \bar{c}_M^+\right) + D_m \frac{\partial^2 \hat{c}_M}{\partial x^2}, \tag{A.11d}$$

$$\begin{aligned}\frac{\partial c_m^+}{\partial t} = &\left(\bar{k}_a^+ \hat{c}_M + \hat{k}_a^+ \bar{c}_M\right) - \left(\bar{k}_a^- \hat{c}_M^+ + \hat{k}_a^- \bar{c}_M^+\right) - k_m^+ \left(2\bar{c}_F^{(1)} \hat{c}_F^{(2)} + 2\hat{c}_F^{(1)} \bar{c}_F^{(2)} + 2\bar{c}_F^{(1)} \hat{c}_F^{(1)} + 2\bar{c}_F^{(2)} \hat{c}_F^{(2)}\right. \\ &\left. + \bar{c}_F^{(1)} \hat{c}_S^+ + \hat{c}_F^{(1)} \bar{c}_S^+ + \bar{c}_F^{(2)} \hat{c}_S^+ + \hat{c}_F^{(2)} \bar{c}_S^+\right) \bar{c}_m^+ - k_m^- \left(2\bar{c}_F^{(1)} \bar{c}_F^{(2)} + \bar{c}_F^{(1)} \bar{c}_F^{(1)} + \bar{c}_F^{(2)} \bar{c}_F^{(2)}\right. \\ &\left. + \bar{c}_F^{(1)} \bar{c}_S^+ + \bar{c}_F^{(2)} \bar{c}_S^+\right) \hat{c}_m^+ - k_m^+ \hat{c}_S^+ + k_m^- \hat{c}_S^+ + D_m^+ \frac{\partial^2 \hat{c}_M^+}{\partial x^2},\end{aligned} \tag{A.11e}$$

$$\frac{\partial \hat{n}_f}{\partial t} = -k_h^+ \hat{n}_f + k_h^- \hat{n}_h + D_f \frac{\partial^2 \hat{n}_f}{\partial x^2}, \tag{A.11f}$$

$$\frac{\partial \hat{n}_h}{\partial t} = k_h^+ \hat{n}_f - k_h^- \hat{n}_h - k_b^+ \left(\bar{n}_h \left(\hat{n}_s^{(1)} + n_s^{(2)}\right) + \hat{n}_h \left(\bar{n}_s^{(1)} + \bar{n}_s^{(2)}\right)\right) + k_b^- \left(\hat{n}_b^{(1)} + \hat{n}_b^{(2)}\right), \tag{A.11g}$$

$$\frac{\partial \hat{n}_b^{(i)}}{\partial t} = k_b^+ \left(\bar{n}_h \hat{n}_s^{(i)} + \hat{n}_h \bar{n}_s^{(i)}\right) - k_b^- \hat{n}_b^{(i)} - \left(\bar{k}_F^+ \hat{n}_b^{(i)} + \hat{k}_F^+ \bar{n}_b^{(i)}\right) + k_F^- \hat{n}_A^{(i)}, \tag{A.11h}$$

$$\frac{\partial \hat{n}_A^{(i)}}{\partial t} = \left(\bar{k}_F^+ \hat{n}_b^{(i)} + \hat{k}_F^+ \bar{n}_b^{(i)}\right) - k_F^- \hat{n}_A^{(i)}, \tag{A.11i}$$

$$\frac{\partial n_s^{(i)}}{\partial t} = -k_b^+ \left(\bar{n}_h \hat{n}_s^{(i)} + \hat{n}_h \bar{n}_s^{(i)}\right) + k_b^- \hat{n}_b^{(i)}, \tag{A.11j}$$

$$\frac{\partial \hat{c}_R}{\partial t} = -\left(\bar{k}_R^+ \hat{c}_R + \hat{k}_R^+ \bar{c}_R\right) + \left(\bar{k}_R^- \hat{c}_R^+ + \hat{k}_R^- \bar{c}_R^+\right), \tag{A.11k}$$

$$\frac{\partial \hat{c}_R^+}{\partial t} = \left(\bar{k}_R^+ \hat{c}_R + \hat{k}_R^+ \bar{c}_R\right) - \left(\bar{k}_R^- \hat{c}_R^+ + \hat{k}_R^- \bar{c}_R^+\right), \tag{A.11l}$$

$$\frac{\partial \hat{c}_P}{\partial t} = -\left(\bar{k}_1^+ \hat{c}_P + \hat{k}_1^+ \bar{c}_P\right) + k_1^- \hat{c}_{P-P} + D_P \frac{\partial^2 \hat{c}_P}{\partial x^2}, \tag{A.11m}$$

$$\frac{\partial \hat{c}_{P-P}}{\partial t} = \left(\bar{k}_1^+ \hat{c}_P + \hat{k}_1^+ \bar{c}_P\right) - k_1^- \hat{c}_{P-P} + D_{P-P} \frac{\partial^2 \hat{c}_{P-P}}{\partial x^2}, \tag{A.11n}$$

$$\frac{\partial \hat{c}_K}{\partial t} = -\left(\bar{k}_2^+ \hat{c}_K + \hat{k}_2^+ \bar{c}_K\right) + k_2^- \hat{c}_{K-P} + D_K \frac{\partial^2 \hat{c}_K}{\partial x^2}, \tag{A.11o}$$

$$\frac{\partial \hat{c}_{K-P}}{\partial t} = \left(\bar{k}_2^+ \hat{c}_K + \hat{k}_2^+ \bar{c}_K\right) - k_2^- \hat{c}_{K-P} + D_{K-P} \frac{\partial^2 \hat{c}_{K-P}}{\partial x^2}, \tag{A.11p}$$

$$\frac{\partial \hat{c}_C}{\partial t} = -\left(\bar{k}_3^+ \hat{c}_C + \hat{k}_3^+ \bar{c}_C\right) + k_3^- \hat{c}_{C-P} + D_C \frac{\partial^2 \hat{c}_C}{\partial x^2}, \tag{A.11q}$$

$$\frac{\partial \hat{c}_{C-P}}{\partial t} = \left(\bar{k}_3^+ \hat{c}_C + \hat{k}_3^+ \bar{c}_C\right) - k_3^- \hat{c}_{C-P} + D_{C-P} \frac{\partial^2 \hat{c}_{C-P}}{\partial x^2}, \tag{A.11r}$$

where quantities denoted with a bar represent baseline values calculated from the non-linear model presented in Ch. 3.

Perturbation to rate constants

Note that Eqs. (A.11) have also required expansion of some reaction rates (those that are non-constant). We expand these in an identical manner as in Sec. 5.7. In particular, employing Taylor series, we deduce the baseline rate constant for each of these quantities

is given by

$$\begin{gathered}\bar{k}_p^+ = K_p^+ \bar{c}_R^+, \quad \bar{k}_p^- = K_p^- \bar{c}_C, \quad \bar{k}_a^+ = K_a^+ \bar{c}_{K-P}, \quad \bar{k}_a^- = K_a^- \bar{c}_P, \\ \bar{k}_R^+ = K_R^+ \left(\bar{n}_b^{(1)} + \bar{n}^{(2)} + \delta\left(\bar{n}_A^{(1)} + \bar{n}_A^{(2)}\right)\right), \quad \bar{k}_F^+ = k_F^+ \bar{\lambda}_I^2,\end{gathered} \tag{A.12}$$

precisely those used in the baseline non-linear model presented in Ch. 3. The perturbation (i.e. $O(\epsilon)$) rates are given by

$$\begin{gathered}\hat{k}_p^+ = K_p^+ \hat{c}_R^+, \quad \hat{k}_p^- = K_p^- \hat{c}_C, \quad \hat{k}_a^+ = K_a^+ \hat{c}_{K-P}, \quad \hat{k}_a^- = K_a^- \hat{c}_{P-P}, \\ \hat{k}_R^+ = K_R^+ \left(\hat{n}_b^{(1)} + \hat{n}_b^{(2)} + \delta\left(\hat{n}_A^{(1)} + \hat{n}_A^{(2)}\right)\right), \quad \bar{k}_F^+ = 2K_F^+ \bar{\lambda}_I \hat{\lambda}_I.\end{gathered} \tag{A.13}$$

From Sec. 3.5.2 we have

$$\lambda_I = \bar{\lambda}_I + \epsilon\hat{\lambda}_I = \sqrt{\left((\bar{u} + \epsilon\hat{u}) - (\bar{w} + \epsilon\hat{w})\right)^2}. \tag{A.14}$$

We hence deduce that

$$\lambda_I = \sqrt{(\bar{u} - \bar{w})^2} + \epsilon \frac{1}{\sqrt{(\bar{u} - \bar{w})^2}} (\bar{u} - \bar{w})(\hat{u} - \hat{w}) + O\left(\epsilon^2\right), \tag{A.15}$$

where we consider only the positive branch of the square root terms.

Boundary conditions

As discussed in Sec. 3.3.2, in order to preserve the mass of the various proteins in the cell, we assume no flux boundary conditions for each protein species at the edge of the cytoplasm. The flux through the cell cytoplasm can be written $j_\alpha = \bar{j}_\alpha + \epsilon\hat{j}_\alpha$. We deduce from Eq. (3.32) that

$$U_\alpha \bar{c}_\alpha - D_\alpha \frac{\partial \bar{c}_\alpha}{\partial x} = 0, \quad U_\alpha \hat{c}_\alpha - D_\alpha \frac{\partial \hat{c}_\alpha}{\partial x} = 0, \tag{A.16}$$

representing no flux boundary conditions at $O(\epsilon^0)$ and $O(\epsilon)$ respectively.

A.3 Numerical implementation

In a similar manner to our linear stability analysis on our two-dimensional model (see Sec. 5.10), we employ the linearised one-dimensional model developed in Sec. A.2 to investigate the stability of the non-linear baseline state presented in Ch. 3. In particular, we examine the impact that perturbing the cell at different stages in the development and maturation of cell cytoskeleton and cell-substrate adhesion has on the growth rate of perturbations.

We let t_p denote the time, after the cell has been introduced the substrate, that we perturb the cell. At this time, the cell will have undergone a non-linear deformation from its initial state (see Sec. 3.8). All barred terms in the linearised equations presented in Sec. A.2 are extracted from the non-linear simulations at time t_p (see Sec. 3.8). We then initialise our linear simulations. In particular, for $-L/2 \leq x \leq L/2$ we introduce (dimensionless) perturbations of the form

$$\hat{u}(x,0) = -\epsilon\left(\frac{2x}{L}\right), \tag{A.17}$$

i.e. we introduce a (compressive) displacement throughout the cell cytoplasm that decays linearly, from a maximum displacement of $\pm\epsilon$ at the cell edge, to zero at the cell centre. In subsequent simulations we set $\epsilon = 0.01$. We do not perturb any other quantities, i.e. all other hatted terms in Sec. A.2 are set to zero initially, hence $\hat{c}(x,0) = 0$, $\hat{n}(x,0) = 0$, $\hat{w}(x,0) = 0$. To deduce the stability of the cell, we evolve the linear system presented in Sec. A.2 in time.

We solve the resulting system of governing equations from Sec. A.2 numerically, using a finite difference method based on the method lines (in a similar manner to Sec. 3.7). We discretise the dimensionless spatial domain $-1/2 \leq x \leq 1/2$ using a uniform grid size Δx. We discretise all spatial derivatives using second-order finite difference stencils and employ the Matlab solver ode15s to solve the resulting large family of ODEs numerically. We employ the fictitious nodes procedure to apply the boundary conditions. We discretise the (dimensionless) domain with $\Delta x = 0.01$ and use stringent error bounds for the time-stepping.

In our analysis there is an initial transient as the initial configuration is not fully compatible with the governing equations, which passes after a (short) time of approximately t_t. We run simulations to a large time $t_s \gg t_t$. As discussed in Sec. 5.10, all quantities in this linear system will eventually grow or decay exponentially with time, i.e. all quantities, described by a function $f(x,t)$, can be written as $f(x,t) \approx \check{f}(x)e^{\Omega t}$, where $\Omega \in \mathbb{C}$ is the complex growth rate for large t. The growth rate can be decomposed into $\Omega = \Omega_r + i\Omega_i$, where $\Omega_r = \mathrm{Re}(\Omega) > 0$ leads to exponential growth (instability), $\Omega_r < 0$ leads to exponential decay (stability) and $\Omega_r = 0$ represents neutral stability. Oscillations of the system are permissible, with frequency $\Omega_i = \mathrm{Im}(\Omega)$. These oscillations can be induced in response to some perturbations (those that are far from compatible with the governing equations).

Evolving the linear system in time, we determine the stability of the system by measuring the perturbation deformation of the cell boundary. In particular, we quantify the real part of the growth rate, $\mathrm{Re}(\Omega)$, by fitting an exponential curve to $\hat{u}(L/2,t)$ for $t_t < t \leq t_s$. If the system exhibits exponentially growing or decaying oscillations in this time interval, we fit an exponential curve to the oscillatory envelope. We deduce the oscillation

frequency, $\mathrm{Im}(\Omega)$, by calculating the inverse of the time, T, between two successive peaks (which is approximately independent of which two peaks are used), with $\mathrm{Im}(\Omega) = 2\pi/T$; if there are no oscillations by t_s, we suppose that $\mathrm{Im}(\Omega) = 0$.

A.4 Results

In Fig. A.1 we present some baseline linear stability analyses, where we perturb the cell using the perturbation described by Eq. (A.17), at various times, t_p, after the cell has been introduced to the substrate. Particularly, we consider $t_p = 100$ s, $t_p = 600$ s and $t_p = 1500$ s. We observe distinct behaviour in each of these three cases. Note the rapid initial transient behaviour (discussed above) manifests as approximately vertical lines near the $y-$axis in Fig. A.1(a); this transient reflects the introduction of the initial perturbation and its rapid decay.

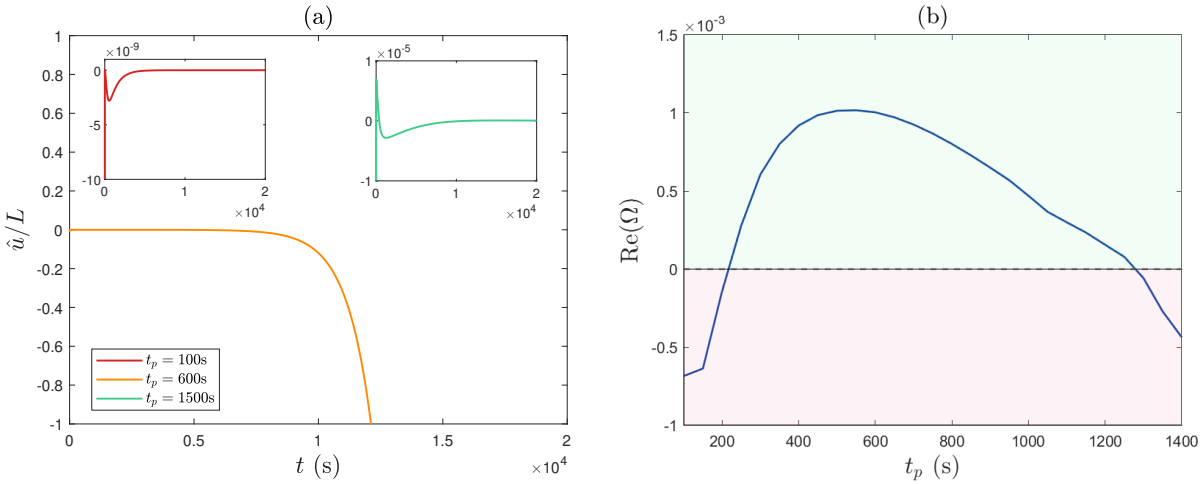

Figure A.1: Influence of time of perturbation on cell stability. (a) Baseline linear stability analyses: growth or decay of modes when the cell is perturbed at $t_p = 100$ s, $t_p = 600$ s, (d) $t_p = 1500$ s. Stability is determined by considering the dimensionless radial boundary displacement of the cell, $\hat{u}(L/2, t)/L$. (b) Real part of the complex growth rate as a function of perturbation time, t_p; pale green background represents region of instability, pale red background denotes region of stability.

At $t_p = 100$ s the cell is poorly adhered to the substrate in fully non-linear simulations (see Sec. 3.8). At this time, some bound integrins have formed (see Fig. 3.7b and Fig. 3.9e-f) but there has been little adhesion maturation (Fig. 3.9g-h) and actin polymerisation (Fig. 3.11c-d). The cell is stable to the perturbation described by Eq. (A.17) (see Fig. A.1a), i.e. $\mathrm{Re}(\Omega) < 0$. In particular, following initial (rapid) transient behaviour, the cell returns to its base state. There are also no oscillations, with $\mathrm{Im}(\Omega) = 0$. As discussed in Sec. 5.10 for the two-dimensional model, this stability is due to the lack of mature structure (e.g. cytoskeleton and adhesion) in the cell at early times. In particular,

the (poorly-adhered) cell is unable to mechanosense and convert the perturbation from Eq. (A.17) into a biological response.

At $t_p = 600$ s we are at an intermediate stage in the the positive feedback loop in the full non-linear simulations. Particularly, some actin has been polymerised (Fig. 3.11c-d) and cross-linked by activated myosin II to form VSFs (Fig. 3.11e-f). Consequently, the cell is in the process of contracting (see Figs. 3.7a, 3.8a), bound integrins are being stretched and adhesions are beginning to mature (Figs. 3.7b, 3.9g-h). The cell is unstable to the perturbation described by Eq. (A.17), with $\mathrm{Re}(\Omega) > 0$. There are no oscillations in the system, with $\mathrm{Im}(\Omega) = 0$. At this time the cell is susceptible to external influences as sufficiently mature structures (cytoskeleton and cell-substrate adhesions) have formed that can respond to deformation, whilst a sufficient pool of free myosin II remains to further cross-link actin filaments and form more dense VSFs. Consequently, the cell contracts.

Finally, perturbing the cell at $t_p = 1500$ s means that the cell has formed mature adhesions and cytoskeleton and the positive feedback loop connecting the development of these structures is becoming subdominant in fully non-linear axisymmetric simulations (see Sec. 3.8). At this time, the majority of integrins have been recruited into FAs (Fig. 3.7g-h), and a significant amount of myosin II has been activated (Fig. 3.11g-h) and has cross-linked actin filaments to form VSFs (Fig. 3.11e-f). The cell is stable to the perturbation described by Eq. (A.17), with $\mathrm{Re}(\Omega) < 0$ (Fig. A.1a). However, rather than pure exponential decay, we observe damped waves (exponentially decaying oscillations), though the system is on the precipice between exhibiting underdamping and critical damping. This underdamping (when perturbed at the late stages of adhesion development) is due to the particular form of initial perturbation (Eq. A.17) introduced to the system. In particular, we observe in Fig. A.1(a) the system "overshoots" when returning to equilibrium in its initial transient behaviour, serving as a source of oscillations.

In Fig. A.1(b) we further examine how the stage at which the cell is perturbed influences the stability of the cell to the mechanical perturbation described by Eq. (A.17). In particular, we present the growth rate $\mathrm{Re}(\Omega)$, of the boundary deformation as a function of time of perturbation (in full non-linear simulations). Regions where exponential growth (decay) will occur are shaded in light green (red). There is a slight degree of volatility throughout this analysis, owing purely to the numerical method used to fit an exponential curve to the perturbation deformation but this does not influence our conclusions. We observe that $\mathrm{Re}(\Omega) < 0$ when $t_p \lesssim 200$ s. In particular, the cell is stable at these early times due to the lack of mature structure, with the cell unable to mechanosense the applied perturbation (Eq. A.17) through cell-substrate adhesions and the cytoskeleton. With increasing time at which the perturbation is applied, owing to the development of mechanosensing structure within the cell, the cell becomes (linearly) unstable to the applied perturbation (Eq. A.17). With further increasing time ($t_p \gtrsim 1250$ s) at which the

perturbation is applied, we observe in Fig. A.1(b) that the cell redevelops linear stability to the one-dimensional mechanical perturbation (Eq. A.17), owing to the dwindling pool of myosin II available for VSF development as the cell has already developed significant amounts of mature cytoskeleton and cell-substrate adhesions in full non-linear simulations (see Sec. 3.8). These one-dimensional perturbations to the one-dimensional system are a direct analogue for the axisymmetric perturbations to the axisymmetric non-linear base state presented in Sec. 5.10, and we observe several similarities between Fig. A.1(b) and our predictions for the $n = 0$ mode (corresponding to axisymmetric deformation) in Fig. 5.9(a).

This linear stability analysis of the one-dimensional system presented in Ch. 3 provides insight to inform our approach to the analysis of the two-dimensional system presented in Ch. 5. In particular, in Sec. 5.7.1 we make the simplifying assumption that ECM deformation has little influence on the linearised dynamics of the system when the ECM is stiff. In the linear stability analysis presented in this Appendix we do not make this assumption, allowing the ECM to deform in the linearised system. We are able to demonstrate that, for a stiff ECM, the assumption of no perturbation ECM displacement has negligible influence on model predictions, hence justifying our approach in Sec. 5.7.1. Additionally, we are able to evolve the non-linear system (see Ch. 3) with perturbations akin to those introduced in the linear stability analysis (see Eq. A.17). We observe that these mechanical perturbations to the non-linear system are quickly absorbed and the cell continues to behave in exactly the way it would in the absence of perturbation (i.e. after the perturbation, the response of the system returns quickly to its preferred trajectory).

Bibliography

B. Alberts, D. Bray, K. Hopkin, A. D. Johnson, J. Lewis, M. Raff, K. Roberts, and P. Walter. *Essential cell biology*. Garland Science, 2015.

A. Y. Alexandrova, A. S. Chikina, and T. M. Svitkina. Actin cytoskeleton in mesenchymal-to-amoeboid transition of cancer cells. *Int. Rev. Cell Mol. Biol.*, 356:197–256, 2020.

M. Amano, M. Ito, K. Kimura, Y. Fukata, K. Chihara, T. Nakano, Y. Matsuura, and K. Kaibuchi. Phosphorylation and activation of myosin by rho-associated kinase (rho-kinase). *J. Biol. Chem.*, 271(34):20246–20249, 1996.

M. Amano, M. Nakayama, and K. Kaibuchi. Rho-kinase/rock: a key regulator of the cytoskeleton and cell polarity. *Cytoskeleton*, 67(9):545–554, 2010.

M. Arnold, E. A. Cavalcanti-Adam, R. Glass, J. Blümmel, W. Eck, M. Kantlehner, H. Kessler, and J. P. Spatz. Activation of integrin function by nanopatterned adhesive interfaces. *ChemPhysChem*, 5(3):383–388, 2004.

J. A. Åström, P. B. S. Kumar, I. Vattulainen, and M. Karttunen. Strain hardening, avalanches, and strain softening in dense cross-linked actin networks. *Phys. Rev. E*, 77 (5):051913, 2008.

P. Atherton, B. Stutchbury, D. Jethwa, and C. Ballestrem. Mechanosensitive components of integrin adhesions: Role of vinculin. *Exp. Cell. Res.*, 343(1):21–27, 2016.

R. A. Badley, J. R. Couchman, and D. A. Rees. Comparison of the cell cytoskeleton in migratory and stationary chick fibroblasts. *J. Muscle Res. Cell Motil.*, 1:5–14, 1980.

C. R. Bagshaw. *Muscle contraction*. Springer Science & Business Media, 1993.

N. Q. Balaban, U. S. Schwarz, D. Riveline, P. Goichberg, G. Tzur, I. Sabanay, D. Mahalu, S. Safran, A. Bershadsky, L. Addadi, et al. Force and focal adhesion assembly: a close relationship studied using elastic micropatterned substrates. *Nat. Cell Biol.*, 3(5):466–472, 2001.

J. R. Bamburg, A. McGough, and S. Ono. Putting a new twist on actin: Adf/cofilins modulate actin dynamics. *Trends Cell Biol.*, 9(9):364–370, 1999.

S. Banerjee and M. C. Marchetti. Controlling cell–matrix traction forces by extracellular geometry. *New Journal of Physics*, 15(3):035015, 2013.

R. G. Barry, N. A. Hill, and P. S. Stewart. Continuum soft tissue models from upscaling of arrays of hyperelastic cells. *Proc. R. Soc. A*, 478(2266):20220065, 2022.

L. Baumann, E. F. Bernstein, A. S. Weiss, D. Bates, S. Humphrey, M. Silberberg, and R. Daniels. Clinical relevance of elastin in the structure and function of skin. In *Aesthet. Surg. J.*, volume 3, page ojab019. Oxford University Press US, 2021.

J. L. Bays and K. A. DeMali. Vinculin in cell–cell and cell–matrix adhesions. *Cell. Mol. Life Sci.*, 74:2999–3009, 2017.

G. I. Bell. Models for the specific adhesion of cells to cells: a theoretical framework for adhesion mediated by reversible bonds between cell surface molecules. *Science*, 200 (4342):618–627, 1978.

A. Besser and U. Schwarz. Coupling biochemistry and mechanics in cell adhesion: a model for inhomogeneous stress fiber contraction. *New J. Phys.*, 9:425, 2007.

A. Besser, J. Colombelli, E. H. K. Stelzer, and U. S. Schwarz. Viscoelastic response of contractile filament bundles. *Phys. Rev. E*, 83(5):051902, 2011.

K. Bhadriraju, M. Yang, S. A. Ruiz, D. Pirone, J. Tan, and C. S. Chen. Activation of rock by rhoa is regulated by cell adhesion, shape, and cytoskeletal tension. *Exp. Cell Res.*, 313(16):3616–3623, 2007.

T. C. Bidone, W. Jung, D. Maruri, C. Borau, R. D. Kamm, and T. Kim. Morphological transformation and force generation of active cytoskeletal networks. *PLoS Comput. Biol.*, 13(1):e1005277, 2017.

T. C. Bidone, A. V. Skeeters, P. W. Oakes, and G. A. Voth. Multiscale model of integrin adhesion assembly. *PLoS Comput. Biol.*, 15(6):e1007077, 2019.

J. K. Biehl and B. Russell. Introduction to stem cell therapy. *J. Cardiovasc. Nurs.*, 24 (2):98, 2009.

T. Bihr, U. Seifert, and A. Smith. Nucleation of ligand-receptor domains in membrane adhesion. *Phys. Rev. Lett.*, 109(25):258101, 2012.

M. A. Biot. Surface instability of rubber in compression. *App. Sci. Res., Section A*, 12 (2):168–182, 1963.

A. L. Bishop and A. Hall. Rho gtpases and their effector proteins. *Biochem. J.*, 348(2): 241–255, 2000.

T. J. Bivalacqua, H. C. Champion, M. F. Usta, S. Cellek, K. Chitaley, R. C. Webb, R. L. Lewis, T. M. Mills, W. J. G. Hellstrom, and P. J. Kadowitz. Rhoa/rho-kinase suppresses endothelial nitric oxide synthase in the penis: a mechanism for diabetes-associated erectile dysfunction. *Proc. Natl. Acad. Sci. U.S.A.*, 101(24):9121–9126, 2004.

L. Blanchoin, R. Boujemaa-Paterski, C. Sykes, and J. Plastino. Actin dynamics, architecture, and mechanics in cell motility. *Physiol. Rev.*, 94(1):235–263, 2014.

J. Bonet. Large strain viscoelastic constitutive models. *Int. J. Solids Struct.*, 38(17): 2953–2968, 2001.

C. Bonnans, J. Chou, and Z. Werb. Remodelling the extracellular matrix in development and disease. *Nat. Rev. Mol. Cell Biol.*, 15(12):786–801, 2014.

C. Borau, T. Kim, T. Bidone, J. M. García-Aznar, and R. D. Kamm. Dynamic mechanisms of cell rigidity sensing: insights from a computational model of actomyosin networks. *PLOS ONE*, 7(11):e49174, 2012.

C. M. Brown, B. Hebert, D. L. Kolin, J. Zareno, L. Whitmore, A. R. Horwitz, and P. W. Wiseman. Probing the integrin-actin linkage using high-resolution protein velocity mapping. *J. Cell Sci.*, 119(24):5204–5214, 2006.

D. B. Brückner, N. Arlt, A. Fink, P. Ronceray, J. O. Rädler, and C. P. Broedersz. Learning the dynamics of cell–cell interactions in confined cell migration. *Proc. Natl. Acad. Sci. U.S.A.*, 118(7):e2016602118, 2021.

K. Burridge and C. Guilluy. Focal adhesions, stress fibers and mechanical tension. *Exp. Cell Res.*, 343(1):14–20, 2016.

K. Burridge and E. S. Wittchen. The tension mounts: stress fibers as force-generating mechanotransducers. *J. Cell Biol.*, 200(1):9–19, 2013.

K. Burridge, K. Fath, T. Kelly, G. Nuckolls, and C. Turner. Focal adhesions: transmembrane junctions between the extracellular matrix and the cytoskeleton. *Annu. Rev. Cell Dev. Biol.*, 4(1):487–525, 1988.

T. M. Butler, S. R. Narayan, S. U. Mooers, and M. J. Siegman. Rapid turnover of myosin light chain phosphate during cross-bridge cycling in smooth muscle. *Am. J. Physiol. Cell Physiol.*, 267(4):C1160–C1166, 1994.

H. M. Byrne and M. A. J. Chaplain. The importance of constitutive equations in mechanochemical models of pattern formation. *Appl. Math. Lett.*, 9(6):85–90, 1996.

D. A. Calderwood. Talin controls integrin activation. *Biochem. Soc. Trans.*, 32(3):434–437, 2004.

M. Cantini, H. Donnelly, M. J. Dalby, and M. Salmeron-Sanchez. The plot thickens: the emerging role of matrix viscosity in cell mechanotransduction. *Adv. Healthcare Mater.*, 9(8):1901259, 2020.

A. Carisey, R. Tsang, A. M. Greiner, N. Nijenhuis, N. Heath, A. Nazgiewicz, R. Kemkemer, B. Derby, J. Spatz, and C. Ballestrem. Vinculin regulates the recruitment and release of core focal adhesion proteins in a force-dependent manner. *Curr. Biol.*, 23(4):271–281, 2013.

E. A. Cavalcanti-Adam, T. Volberg, A. Micoulet, H. Kessler, B. Geiger, and J. P. Spatz. Cell spreading and focal adhesion dynamics are regulated by spacing of integrin ligands. *Biophys. J.*, 92(8):2964–2974, 2007.

T. E. Cawston and D. A. Young. Proteinases involved in matrix turnover during cartilage and bone breakdown. *Cell Tissue Res.*, 339:221–235, 2010.

M. Chalfie. Neurosensory mechanotransduction. *Nat. Rev. Mol. Cell Biol.*, 10(1):44–52, 2009.

B. Chen, B. Ji, and H. Gao. Modeling active mechanosensing in cell–matrix interactions. *Annu. Rev. Biophys.*, 44:1–32, 2015.

C. S. Chen. Mechanotransduction–a field pulling together? *J. Cell Sci.*, 121(20):3285–3292, 2008.

L. Chen, K. Painter, C. Surulescu, and A. Zhigun. Mathematical models for cell migration: a non-local perspective. *Phil. Trans. R. Soc. B*, 375(1807):20190379, 2020.

D. Choquet, D. P. Felsenfeld, and M. P. Sheetz. Extracellular matrix rigidity causes strengthening of integrin–cytoskeleton linkages. *Cell*, 88(1):39–48, 1997.

C. Ciobanasu, B. Faivre, and C. Le Clainche. Actomyosin-dependent formation of the mechanosensitive talin–vinculin complex reinforces actin anchoring. *Nat. Commun.*, 5 (1):3095, 2014.

G. Cooper and K. Adams. *The cell: a molecular approach.* Oxford University Press, 2022.

C. A. Copos and R. D. Guy. A porous viscoelastic model for the cell cytoskeleton. *ANZIAM J.*, 59(4):472–498, 2018.

S. C. Cowin. Bone poroelasticity. *J. Biomech.*, 32(3):217–238, 1999.

L. P. Cramer, M. Siebert, and T. J. Mitchison. Identification of novel graded polarity actin filament bundles in locomoting heart fibroblasts: implications for the generation of motile force. *J. Cell Biol.*, 136(6):1287–1305, 1997.

R. M. Crossley, S. Johnson, E. Tsingos, Z. Bell, M. Berardi, M. Botticelli, Q. J. S. Braat, J. Metzcar, M. Ruscone, Y. Yin, et al. Modeling the extracellular matrix in cell migration and morphogenesis: a guide for the curious biologist. *Front. Cell Dev. Biol.*, 12:1354132, 2024.

D. Cusseddu, L. Edelstein-Keshet, J. A. Mackenzie, S. Portet, and A. Madzvamuse. A coupled bulk-surface model for cell polarisation. *J. Theor. Biol.*, 481:119–135, 2019.

M. J. Dalby, N. Gadegaard, and R. O. C. Oreffo. Harnessing nanotopography and integrin–matrix interactions to influence stem cell fate. *Nat. Mater.*, 13(6):558–569, 2014.

M. J. Dalby, A. J. García, and M. Salmeron-Sanchez. Receptor control in mesenchymal stem cell engineering. *Nat. Rev. Mater.*, 3(3):1–14, 2018.

E. M. Darling, M. Topel, S. Zauscher, T. P. Vail, and F. Guilak. Viscoelastic properties of human mesenchymally-derived stem cells and primary osteoblasts, chondrocytes, and adipocytes. *J. Biomech.*, 41(2):454–464, 2008.

B. de Lucas, L. M. Pérez, and B. G. Gálvez. Importance and regulation of adult stem cell migration. *J. Cell. Mol. Med.*, 22(2):746–754, 2018.

S. Deguchi and M. Sato. Biomechanical properties of actin stress fibers of non-motile cells. *Biorheology*, 46(2):93–105, 2009.

M. Dembo, D. C. Torney, K. Saxman, and D. Hammer. The reaction-limited kinetics of membrane-to-surface adhesion and detachment. *Proc. R. Soc. B.*, 234(1274):55–83, 1988.

V. S. Deshpande, R. M. McMeeking, and A. G. Evans. A bio-chemo-mechanical model for cell contractility. *Proc. Natl. Acad. Sci. U.S.A.*, 103(38):14015–14020, 2006.

V. S. Deshpande, R. M. McMeeking, and A. G. Evans. A model for the contractility of the cytoskeleton including the effects of stress-fibre formation and dissociation. *Proc. R. Soc. A.*, 463(2079):787–815, 2007.

V. S. Deshpande, M. Mrksich, R. M. McMeeking, and A. G. Evans. A bio-mechanical model for coupling cell contractility with focal adhesion formation. *J. Mech. Phys. Solids*, 56(4):1484–1510, 2008.

S. Di Stefano, G. Florio, G. Napoli, N. M. Pugno, and G. Puglisi. On the role of elasticity in focal adhesion stability within the passive regime. *Int. J. Non-Linear Mech.*, 146: 104157, 2022.

P. A. DiMilla, K. Barbee, and D. A. Lauffenburger. Mathematical model for the effects of adhesion and mechanics on cell migration speed. *Biophys. J.*, 60(1):15–37, 1991.

D. E. Discher, P. Janmey, and Y. Wang. Tissue cells feel and respond to the stiffness of their substrate. *Science*, 310(5751):1139–1143, 2005.

M. Dogterom and B. Yurke. Measurement of the force-velocity relation for growing microtubules. *Science*, 278(5339):856–860, 1997.

R. Dominguez and K. C. Holmes. Actin structure and function. *Annu. Rev. Biophys.*, 40: 169–186, 2011.

B. L. Doss, M. Pan, M. Gupta, G. Grenci, R. Mège, C. T. Lim, M. P. Sheetz, R. Voituriez, and B. Ladoux. Cell response to substrate rigidity is regulated by active and passive cytoskeletal stress. *Proc. Natl. Acad. Sci. U.S.A.*, 117(23):12817–12825, 2020.

C. C. DuFort, M. J. Paszek, and V. M. Weaver. Balancing forces: architectural control of mechanotransduction. *Nat. Rev. Mol. Cell Biol.*, 12(5):308–319, 2011.

P. A. Dufort and C. J. Lumsden. How profilin/barbed-end synergy controls actin polymerization: A kinetic model of the atp hydrolysis circuit. *Cell Motil Cytoskeleton*, 35 (4):309–330, 1996.

C. Dunlop. Differential cellular contractility as a mechanism for stiffness sensing. *New J. Phys.*, 21(6):063005, 2019.

C. M. Edwards and U. S. Schwarz. Force localization in contracting cell layers. *Phys. Rev. Lett.*, 107(12):128101, 2011.

N. Endlich, C. A. Otey, W. Kriz, and K. Endlich. Movement of stress fibers away from focal adhesions identifies focal adhesions as sites of stress fiber assembly in stationary cells. *Cell Motil. Cytoskelet.*, 64(12):966–976, 2007.

A. J. Engler, S. Sen, and D. E. Discher. Matrix elasticity directs stem cell lineage specification. *Cell*, 126:677–689, 2006.

B. Enyedi and P. Niethammer. Nuclear membrane stretch and its role in mechanotransduction. *Nucleus*, 8(2):156–161, 2017.

R. Erban. From molecular dynamics to brownian dynamics. *Proc. R. Soc. A.*, 470(2167): 20140036, 2014.

T. Erdmann and U. S. Schwarz. Bistability of cell-matrix adhesions resulting from nonlinear receptor-ligand dynamics. *Biophys. J.*, 91(6):L60–L62, 2006.

T. Erdmann and U. S. Schwarz. Impact of receptor-ligand distance on adhesion cluster stability. *Eur. Phys. J. E*, 22:123–137, 2007.

J. Feng, M. Ito, Y. Kureishi, K. Ichikawa, M. Amano, N. Isaka, K. Okawa, A. Iwamatsu, K. Kaibuchi, D. J. Hartshorne, et al. Rho-associated kinase of chicken gizzard smooth muscle. *J. Biol. Chem.*, 274(6):3744–3752, 1999.

G. Fernandez de Grado, L. Keller, Y. Idoux-Gillet, Q. Wagner, A. Musset, N. Benkirane-Jessel, F. Bornert, and D. Offner. Bone substitutes: a review of their characteristics, clinical use, and perspectives for large bone defects management. *J. Tissue Eng.*, 9: 2041731418776819, 2018.

B. Flaherty, J. P. McGarry, and P. E. McHugh. Mathematical models of cell motility. *Cell Biochem. Biophys.*, 49:14–28, 2007.

D. A. Fletcher and R. D. Mullins. Cell mechanics and the cytoskeleton. *Nature*, 463(7280): 485–492, 2010.

R. Florencio-Silva, G. R. S. Sasso, E. Sasso-Cerri, M. J. Simões, P. S. Cerri, et al. Biology of bone tissue: structure, function, and factors that influence bone cells. *BioMed Res. Int.*, 2015, 2015.

L. C. Franssen, T. Lorenzi, A. E. F. Burgess, and M. A. J. Chaplain. A mathematical framework for modelling the metastatic spread of cancer. *Bull. Math. Biol.*, 81:1965–2010, 2019.

C. Frantz, K. M. Stewart, and V. M. Weaver. The extracellular matrix at a glance. *J. Cell Sci.*, 123(24):4195–4200, 2010.

B. M. Friedrich and S. A. Safran. How cells feel their substrate: spontaneous symmetry breaking of active surface stresses. *Soft Matter*, 8(11):3223–3230, 2012.

I. Fujiwara, D. Vavylonis, and T. D. Pollard. Polymerization kinetics of adp-and adp-pi-actin determined by fluorescence microscopy. *Proc. Natl. Acad. Sci. U.S.A.*, 104(21): 8827–8832, 2007.

R. R. Gabdoulline and R. C. Wade. Brownian dynamics simulation of protein–protein diffusional encounter. *Methods*, 14(3):329–341, 1998.

P. J. Gallagher, B. P. Herring, S. A. Griffin, and J. T. Stull. Molecular characterization of a mammalian smooth muscle myosin light chain kinase. *J. Biol. Chem.*, 266(35): 23936–23944, 1991.

H. Gao, J. Qian, and B. Chen. Probing mechanical principles of focal contacts in cell–matrix adhesion with a coupled stochastic–elastic modelling framework. *J. R. Soc. Interface.*, 8(62):1217–1232, 2011.

M. L. Gardel, K. E. Kasza, C. P. Brangwynne, J. Liu, and D. A. Weitz. Mechanical response of cytoskeletal networks. *Methods Cell Biol.*, 89:487–519, 2008.

B. Geiger, J. P. Spatz, and A. D. Bershadsky. Environmental sensing through focal adhesions. *Nat. Rev. Mol. Cell Biol.*, 10(1):21–33, 2009.

A. P. Gilmore and K. Burridge. Molecular mechanisms for focal adhesion assembly through regulation of protein–protein interactions. *Structure*, 4(6):647–651, 1996.

E. J. Goetzl, M. J. Banda, and D. Leppert. Matrix metalloproteinases in immunity. *J. Immunol.*, 156(1):1–4, 1996.

R. E. Goldstein and J. van de Meent. A physical perspective on cytoplasmic streaming. *Interface Focus*, 5(4), 2015.

R. E. Goldstein, I. Tuval, and J. van de Meent. Microfluidics of cytoplasmic streaming and its implications for intracellular transport. *Proc. Natl. Acad. Sci. U.S.A.*, 105(10): 3663–3667, 2008.

G. A. Gomez, R. W. McLachlan, et al. Productive tension: force-sensing and homeostasis of cell–cell junctions. *Trends Cell Biol.*, 21(9):499–505, 2011.

W. E. Gordon III. Immunofluorescent and ultrastructural studies of "sarcomeric" units in stress fibers of cultured non-muscle cells. *Exp. Cell Res.*, 117(2):253–260, 1978.

J. Gosline, M. Lillie, E. Carrington, P. Guerette, C. Ortlepp, and K. Savage. Elastic proteins: biological roles and mechanical properties. *Phil. Trans. R. Soc. B.*, 357(1418): 121–132, 2002.

M. E. Gracheva and H. G. Othmer. A continuum model of motility in ameboid cells. *Bull. Math. Biol.*, 66:167–193, 2004.

C. Grashoff, B. D. Hoffman, M. D. Brenner, R. Zhou, M. Parsons, M. T. Yang, M. A. McLean, S. G. Sligar, C. S. Chen, T. Ha, et al. Measuring mechanical tension across vinculin reveals regulation of focal adhesion dynamics. *Nature*, 466(7303):263–266, 2010.

H. P. Greenspan. On the growth and stability of cell cultures and solid tumors. *J. Theor. Biol.*, 56(1):229–242, 1976.

K. Guo, J. Shillcock, and R. Lipowsky. Treadmilling of actin filaments via brownian dynamics simulations. *J. Chem. Phys.*, 133(15), 2010.

W. Guo and Y. Wang. Retrograde fluxes of focal adhesion proteins in response to cell migration and mechanical signals. *Mol. Biol. Cell*, 18(11):4519–4527, 2007.

K. Haase and A. E. Pelling. Investigating cell mechanics with atomic force microscopy. *J. R. Soc. Interface*, 12(104):20140970, 2015.

C. Hahn and M. A. Schwartz. Mechanotransduction in vascular physiology and atherogenesis. *Nat. Rev. Mol. Cell Biol.*, 10(1):53–62, 2009.

K. J. Hamill, K. Kligys, S. B. Hopkinson, and J. C. R. Jones. Laminin deposition in the extracellular matrix: a complex picture emerges. *J. Cell Sci.*, 122(24):4409–4417, 2009.

D. J. Hartshorne, M. Ito, and F. Erdo¨ di. Myosin light chain phosphatase: subunit composition, interactions and regulation. *J. Muscle Res. Cell Motil.*, 19(4):325–341, 1998.

J. F. Hastings, J. N. Skhinas, D. Fey, D. R. Croucher, and T. R. Cox. The extracellular matrix as a key regulator of intracellular signalling networks. *Br. J. Pharmacol.*, 176 (1):82–92, 2019.

S. He, Y. Su, B. Ji, and H. Gao. Some basic questions on mechanosensing in cell–substrate interaction. *J. Mech. Phys. Solids*, 70:116–135, 2014.

M. Hermann and M. Saravi. A first course in ordinary differential equations. *Analytical and Numerical Methods*, 2014.

E. J. Hinch. *Perturbation Methods*. Cambridge University Press, 1991.

H. Hirata, H. Tatsumi, and M. Sokabe. Mechanical forces facilitate actin polymerization at focal adhesions in a zyxin-dependent manner. *J. Cell Sci.*, 121(17):2795–2804, 2008.

H. Hirata, K-H. Chiam, C. T. Lim, and M. Sokabe. Actin flow and talin dynamics govern rigidity sensing in actin–integrin linkage through talin extension. *J. R. Soc. Interface*, 11(99):20140734, 2014a.

H. Hirata, M. Sokabe, and C. T. Lim. Molecular mechanisms underlying the force-dependent regulation of actin-to-ecm linkage at the focal adhesions. *Prog. Mol. Biol. Transl. Sci.*, 126:135–154, 2014b.

H. Hirata, H. Tatsumi, C. T. Lim, and M. Sokabe. Force-dependent vinculin binding to talin in live cells: a crucial step in anchoring the actin cytoskeleton to focal adhesions. *Am. J. Physiol. Cell Physiol.*, 306(6):C607–C620, 2014c.

B. D. Hoffman, C. Grashoff, and M. A. Schwartz. Dynamic molecular processes mediate cellular mechanotransduction. *Nature*, 475(7356):316–323, 2011.

W. R. Holmes and L. Edelstein-Keshet. A comparison of computational models for eukaryotic cell shape and motility. *PLoS Comput. Biol.*, 8(12):e1002793, 2012.

M. Honjo, H. Tanihara, M. Inatani, N. Kido, T. Sawamura, B. Y. J. T. Yue, S. Narumiya, and Y. Honda. Effects of rho-associated protein kinase inhibitor y-27632 on intraocular pressure and outflow facility. *Investig. Ophthalmol. Vis. Sci.*, 42(1):137–144, 2001.

P. Hotulainen and P. Lappalainen. Stress fibers are generated by two distinct actin assembly mechanisms in motile cells. *J. Cell Biol.*, 173(3):383–394, 2006.

C. Hsiao, H. Cheng, C. Huang, H. Li, M. Ou, J. Huang, K. Khoo, H. Yu, Y. Chen, Y. Wang, et al. Fibronectin in cell adhesion and migration via n-glycosylation. *Oncotarget*, 8(41): 70653, 2017.

J. Hu and H. G. Othmer. A theoretical analysis of filament length fluctuations in actin and other polymers. *J. Math. Biol.*, 63:1001–1049, 2011.

J. Hu, A. Matzavinos, and H. G. Othmer. A theoretical approach to actin filament dynamics. *J. Stat. Phys.*, 128(1-2):111–138, 2007a.

J. Hu, Y. Li, Y. Hao, T. Zheng, S. K. Gupta, G. A. Parada, H. Wu, S. Lin, S. Wang, X. Zhao, et al. High stretchability, strength, and toughness of living cells enabled by hyperelastic vimentin intermediate filaments. *Proc. Natl. Acad. Sci. U.S.A.*, 116(35): 17175–17180, 2019.

K. Hu, L. Ji, K. T. Applegate, G. Danuser, and C. M. Waterman-Storer. Differential transmission of actin motion within focal adhesions. *Science*, 315(5808):111–115, 2007b.

L. Hu, C. Yin, F. Zhao, A. Ali, J. Ma, and A. Qian. Mesenchymal stem cells: cell fate decision to osteoblast or adipocyte and application in osteoporosis treatment. *Int. J. Mol. Sci.*, 19(2):360, 2018.

S. Hu, Y. Tee, A. Kabla, R. Zaidel-Bar, A. Bershadsky, and P. Hersen. Structured illumination microscopy reveals focal adhesions are composed of linear subunits. *Cytoskeleton*, 72(5):235–245, 2015.

A. F. Huxley. Muscle structure and theories of contraction. *Prog. Biophys. Mol. Biol.*, 7: 255–318, 1957.

D. Iber and I. D. Campbell. Integrin activation—the importance of a positive feedback. *Bull. Math. Biol.*, 68:945–956, 2006.

N. Ilan, M. Elkin, and I. Vlodavsky. Regulation, function and clinical significance of heparanase in cancer metastasis and angiogenesis. *Int. J. Biochem. Cell Biol.*, 38(12): 2018–2039, 2006.

R. Illukkumbura, T. Bland, and N. W. Goehring. Patterning and polarization of cells by intracellular flows. *Curr. Opin. Cell Biol.*, 62:123–134, 2020.

D. E. Ingber. Tensegrity: the architectural basis of cellular mechanotransduction. *Annu. Rev. Physiol.*, 59(1):575–599, 1997.

R. H. Insall and L. M. Machesky. Actin dynamics at the leading edge: from simple machinery to complex networks. *Dev. Cell*, 17(3):310–322, 2009.

P. Isermann and J. Lammerding. Nuclear mechanics and mechanotransduction in health and disease. *Curr. Biol.*, 23(24):R1113–R1121, 2013.

D. E. Jaalouk and J. Lammerding. Mechanotransduction gone awry. *Nat. Rev. Mol. Cell Biol.*, 10(1):63–73, 2009.

E. A. Jaffe and D. F. Mosher. Synthesis of fibronectin by cultured human endothelial cells. *J. Exp. Med.*, 147(6):1779–1791, 1978.

Y. Jamali, M. Azimi, and M. R. K. Mofrad. A sub-cellular viscoelastic model for cell population mechanics. *PLoS One*, 5(8):e12097, 2010.

G. Jiang, G. Giannone, D. R. Critchley, E. Fukumoto, and M. P. Sheetz. Two-piconewton slip bond between fibronectin and the cytoskeleton depends on talin. *Nature*, 424(6946): 334–337, 2003.

B. M. Jockusch, P. Bubeck, K. Giehl, M. Kroemker, J. Moschner, M. Rothkegel, M. Rudiger, K. Schluter, G. Stanke, and J. Winkler. The molecular architecture of focal adhesions. *Annu. Rev. Cell Dev. Biol.*, 11(1):379–416, 1995.

L. R. Johnson. *Physiology of the gastrointestinal tract*. Elsevier, 2006.

Z. Kabaeva, M. Zhao, and D. E. Michele. Blebbistatin extends culture life of adult mouse cardiac myocytes and allows efficient and stable transgene expression. *Am. J. Physiol. - Heart Circ. Physiol.*, 294(4):H1667–H1674, 2008.

K. E. Kamm and J. T. Stull. The function of myosin and myosin light chain kinase phosphorylation in smooth muscle. *Annu. Rev. Pharmacol. Toxicol.*, 25(1):593–620, 1985.

K. E. Kamm and J. T. Stull. Regulation of smooth muscle contractile elements by second messengers. *Annu. Rev. Physiol.*, 51(1):299–313, 1989.

N. K. Karamanos, A. D. Theocharis, Z. Piperigkou, D. Manou, A. Passi, S. S. Skandalis, D. H. Vynios, V. Orian-Rousseau, S. Ricard-Blum, C. E. H. Schmelzer, et al. A guide to

the composition and functions of the extracellular matrix. *FEBS J.*, 288(24):6850–6912, 2021.

E. Kassianidou and S. Kumar. A biomechanical perspective on stress fiber structure and function. *Biochim. Biophys. Acta, Mol. Cell Res.*, 1853(11):3065–3074, 2015.

K. Katoh, Y. Kano, M. Amano, H. Onishi, K. Kaibuchi, and K. Fujiwara. Rho-kinase–mediated contraction of isolated stress fibers. *J. Cell Biol.*, 153(3):569–584, 2001.

A. Katsumi, A. W. Orr, E. Tzima, and M. A. Schwartz. Integrins in mechanotransduction. *J. Biol. Chem.*, 279(13):12001–12004, 2004.

R. Kaunas, P. Nguyen, S. Usami, and S. Chien. Cooperative effects of rho and mechanical stretch on stress fiber organization. *Proc. Natl. Acad. Sci. U.S.A.*, 102(44):15895–15900, 2005.

J. F. Kelleher, S. J. Atkinson, and T. D. Pollard. Sequences, structural models, and cellular localization of the actin-related proteins arp2 and arp3 from acanthamoeba. *J. Cell Biol.*, 131(2):385–397, 1995.

J. P. Kemp and W. M. Brieher. The actin filament bundling protein α-actinin-4 actually suppresses actin stress fibers by permitting actin turnover. *J. Biol. Chem.*, 293(37): 14520–14533, 2018.

P. Keshavanarayana, M. Ruess, and R. de Borst. A feedback-loop extended stress fiber growth model with focal adhesion formation. *Int. J. Solids Struct.*, 128:160–173, 2017.

P. Keshavanarayana, M. Ruess, and R. de Borst. On the monolithic and staggered solution of cell contractility and focal adhesion growth. *Int. J. Numer. Methods Biomed. Eng.*, 34(11):e3138, 2018.

S. B. Khatau, C. M. Hale, P. J. Stewart-Hutchinson, M. S. Patel, C. L. Stewart, P. C. Searson, D. Hodzic, and D. Wirtz. A perinuclear actin cap regulates nuclear shape. *Proc. Natl. Acad. Sci. U.S.A.*, 106(45):19017–19022, 2009.

F. Kheradmand, K. Rishi, and Z. Werb. Signaling through the egf receptor controls lung morphogenesis in part by regulating mt1-mmp-mediated activation of gelatinase a/mmp2. *J. Cell Sci.*, 115(4):839–848, 2002.

K. A. Kilian, B. Bugarija, B. T. Lahn, and M. Mrksich. Geometric cues for directing the differentiation of mesenchymal stem cells. *Proc. Natl. Acad. Sci. U.S.A.*, 107(11): 4872–4877, 2010.

D. Kim and D. Wirtz. Tight coupling between nucleus and cell migration through the perinuclear actin cap. *Biophys. J.*, 106(2):43a, 2014.

K. M. Kim, Y. J. Choi, J. Hwang, A. R. Kim, H. J. Cho, E. S. Hwang, J. Y. Park, S. Lee, and J. Hong. Shear stress induced by an interstitial level of slow flow increases the osteogenic differentiation of mesenchymal stem cells through taz activation. *PLoS One*, 9(3), 2014.

T. Kim, W. Hwang, and R. D. Kamm. Computational analysis of a cross-linked actin-like network. *Exp. Mech.*, 49:91–104, 2009a.

T. Kim, W. Hwang, H. Lee, and R. D. Kamm. Computational analysis of viscoelastic properties of crosslinked actin networks. *PLoS Comput. Biol.*, 5(7):e1000439, 2009b.

T. Kitazawa, M. Eto, T. P. Woodsome, and M. D. Khalequzzaman. Phosphorylation of the myosin phosphatase targeting subunit and cpi-17 during ca2+ sensitization in rabbit smooth muscle. *J. Physiol.*, 546(3):879–889, 2003.

T. Kiuchi, T. Nagai, K. Ohashi, and K. Mizuno. Measurements of spatiotemporal changes in g-actin concentration reveal its effect on stimulus-induced actin assembly and lamellipodium extension. *J. Cell Biol.*, 193(2):365–380, 2011.

B. Klapholz and N. H. Brown. Talin–the master of integrin adhesions. *J. Cell Sci.*, 130 (15):2435–2446, 2017.

J. Kolega. The role of myosin ii motor activity in distributing myosin asymmetrically and coupling protrusive activity to cell translocation. *Mol. Biol. Cell*, 17(10):4435–4445, 2006.

D. Kong, B. Ji, and L. Dai. Stability of adhesion clusters and cell reorientation under lateral cyclic tension. *Biophys. J.*, 95(8):4034–4044, 2008.

D. Kong, B. Ji, and L. Dai. Stabilizing to disruptive transition of focal adhesion response to mechanical forces. *J. Biomech.*, 43(13):2524–2529, 2010.

F. Kong, A. J. García, A. P. Mould, M. J. Humphries, and C. Zhu. Demonstration of catch bonds between an integrin and its ligand. *J. Cell Biol.*, 185(7):1275–1284, 2009.

T. E. G. Krueger, D. L. J. Thorek, S. R. Denmeade, J. T. Isaacs, and W. N. Brennen. Concise review: mesenchymal stem cell-based drug delivery: the good, the bad, the ugly, and the promise. *Stem Cells Transl. Med.*, 7(9):651–663, 2018.

I. Y. Kuo and B. E. Ehrlich. Signaling in muscle contraction. *Cold Spring Harb. Perspect. Biol.*, 7(2):a006023, 2015.

J. S. Lai, K. Onaran, and W. N. Findley. *Creep and Relaxation of Nonlinear Viscoelastic Materials: With an Introduction to Linear Viscoelasticity*. North-Holland, 1976.

J. Lammerding. Mechanics of the nucleus. *Compr. Physiol.*, 1(2):783, 2011.

K. Larripa and A. Mogilner. Transport of a 1d viscoelastic actin–myosin strip of gel as a model of a crawling cell. *Physica A*, 372(1):113–123, 2006.

C. M. Laukaitis, D. J. Webb, K. Donais, and A. F. Horwitz. Differential dynamics of $\alpha 5$ integrin, paxillin, and α-actinin during formation and disassembly of adhesions in migrating cells. *J. Cell Biol.*, 153(7):1427–1440, 2001.

H. Lavoie, J. Gagnon, and M. Therrien. Erk signalling: a master regulator of cell behaviour, life and fate. *Nat. Rev. Mol. Cell Biol.*, 21(10):607–632, 2020.

E. J. Lawrence, E. Boucher, and C. A. Mandato. Mitochondria-cytoskeleton associations in mammalian cytokinesis. *Cell Div.*, 11:1–16, 2016.

C. P. Leblond. Synthesis and secretion of collagen by cells of connective tissue, bone, and dentin. *Anat. Rec.*, 224(2):123–138, 1989.

K. Lee and A. J. Liu. Force-velocity relation for actin-polymerization-driven motility from brownian dynamics simulations. *Biophys. J.*, 97(5):1295–1304, 2009.

S. H. Lee and R. Dominguez. Regulation of actin cytoskeleton dynamics in cells. *Molecules and cells*, 29(4):311–326, 2010.

K. Legerstee and A. B. Houtsmuller. A layered view on focal adhesions. *Biology*, 10(11): 1189, 2021.

K. Legerstee, B. Geverts, J. A. Slotman, and A. B. Houtsmuller. Dynamics and distribution of paxillin, vinculin, zyxin and vasp depend on focal adhesion location and orientation. *Sci. Rep.*, 9(1):10460, 2019.

D. Li and B. Ji. Predicted rupture force of a single molecular bond becomes rate independent at ultralow loading rates. *Phys. Rev. Lett.*, 112(7):078302, 2014.

L. Li and T. Xie. Stem cell niche: structure and function. *Annu. Rev. Cell Dev. Biol.*, 21: 605–631, 2005.

Y. J. Li, J. H. Haga, and S. Chien. Molecular basis of the effects of shear stress on vascular endothelial cells. *J. Biomech.*, 38(10):1949–1971, 2005.

J. K. Liao, M. Seto, and K. Noma. Rho kinase (rock) inhibitors. *J. Cardiovasc. Pharmacol.*, 50(1):17–24, 2007.

H. H. Lipowsky, D. T. Bowers, B. L. Banik, and J. L. Brown. Mesenchymal stem cell deformability and implications for microvascular sequestration. *Ann. Biomed. Eng.*, 46: 640–654, 2018.

J. Lippincott-Schwartz, E. Snapp, and A. Kenworthy. Studying protein dynamics in living cells. *Nat. Rev. Mol. Cell Biol.*, 2(6):444–456, 2001.

J. Liu, H. Gao, and X. Wang. The role of the rho/rock signaling pathway in inhibiting axonal regeneration in the central nervous system. *Neural Regen. Res.*, 10(11):1892–1896, 2015.

A. Livne and B. Geiger. The inner workings of stress fibers- from contractile machinery to focal adhesions and back. *J. Cell Sci.*, 129(7):1293–1304, 2016.

P. Lu, K. Takai, V. M. Weaver, and Z. Werb. Extracellular matrix degradation and remodeling in development and disease. *Cold Spring Harbor Perspect. Biol.*, 3(12), 2011.

M. E. Lukashev and Z. Werb. Ecm signalling: orchestrating cell behaviour and misbehaviour. *Trends Cell Biol.*, 8(11):437–441, 1998.

G. W. G. Luxton, E. R. Gomes, E. S. Folker, E. Vintinner, and G. G. Gundersen. Linear arrays of nuclear envelope proteins harness retrograde actin flow for nuclear movement. *Science*, 329(5994):956–959, 2010.

M. Maekawa, T. Ishizaki, S. Boku, N. Watanabe, A. Fujita, A. Iwamatsu, T. Obinata, K. Ohashi, K. Mizuno, and S. Narumiya. Signaling from rho to the actin cytoskeleton through protein kinases rock and lim-kinase. *Science*, 285(5429):895–898, 1999.

J. Maître and C. Heisenberg. Three functions of cadherins in cell adhesion. *Curr. Biol.*, 23(14):R626–R633, 2013.

M. Mak, F. Spill, R. D. Kamm, and M. H. Zaman. Single-cell migration in complex microenvironments: mechanics and signaling dynamics. *J. Biomech. Eng.*, 138(2):021004, 2016a.

M. Mak, M. H. Zaman, R. D. Kamm, and T. Kim. Interplay of active processes modulates tension and drives phase transition in self-renewing, motor-driven cytoskeletal networks. *Nat. Commun.*, 7(1):10323, 2016b.

Y. Mao and J. E. Schwarzbauer. Fibronectin fibrillogenesis, a cell-mediated matrix assembly process. *Matrix Biol.*, 24(6):389–399, 2005.

C. J. Martin and R. G. Payton. Thermoelastic stresses in a slab. *J. Math. Mech.*, pages 1–30, 1964.

F. Martino, A. R. Perestrelo, V. Vinarskỳ, S. Pagliari, and G. Forte. Cellular mechanotransduction: from tension to function. *Front. Physiol.*, 9:824, 2018.

P. S. Mathieu and E. G. Loboa. Cytoskeletal and focal adhesion influences on mesenchymal stem cell shape, mechanical properties, and differentiation down osteogenic, adipogenic, and chondrogenic pathways. *Tissue Eng. Part B Rev.*, 18(6):436–444, 2012.

A. Matzavinos and H. G. Othmer. A stochastic analysis of actin polymerization in the presence of twinfilin and gelsolin. *J. Theor. Biol.*, 249(4):723–736, 2007.

M. Mavrakis and M. A. Juanes. The compass to follow: Focal adhesion turnover. *Curr. Opin. Cell Biol.*, 80:102152, 2023.

R. C. May and L. M. Machesky. Phagocytosis and the actin cytoskeleton. *J. Cell Sci.*, 114(6):1061–1077, 2001.

M. Maziveyi and S. K. Alahari. Cell matrix adhesions in cancer: The proteins that form the glue. *Oncotarget*, 8(29):48471, 2017.

R. M. McMeeking and V. S. Deshpande. A bio-chemo-mechanical model for cell contractility, adhesion, signaling, and stress-fiber remodeling. *Biomech. Model. Mechanobiol.*, pages 53–81, 2017.

P. Mereghetti, R. R. Gabdoulline, and R. C. Wade. Brownian dynamics simulation of protein solutions: structural and dynamical properties. *Biophys. J.*, 99(11):3782–3791, 2010.

R. Merkel, N. Kirchgeßner, C. M. Cesa, and B. Hoffmann. Cell force microscopy on elastic layers of finite thickness. *Biophys. J.*, 93(9):3314–3323, 2007.

A. K. Mishra, J. P. Campanale, J. A. Mondo, and D. J. Montell. Cell interactions in collective cell migration. *Development*, 146(23):dev172056, 2019.

R. Mittal and G. Iaccarino. Immersed boundary methods. *Annu. Rev. Fluid Mech.*, 37: 239–261, 2005.

E. Moeendarbary, L. Valon, M. Fritzsche, A. R. Harris, D. A. Moulding, A. J. Thrasher, E. Stride, L. Mahadevan, and G. T. Charras. The cytoplasm of living cells behaves as a poroelastic material. *Nat. Mater.*, 12(3):253–261, 2013.

A. Mogilner. Mathematics of cell motility: have we got its number? *J. Math. Biol.*, 58: 105–134, 2009.

A. Mogilner and L. Edelstein-Keshet. Regulation of actin dynamics in rapidly moving cells: a quantitative analysis. *Biophys. J.*, 83(3):1237–1258, 2002.

S. S. Mogre, A. I. Brown, and E. F. Koslover. Getting around the cell: physical transport in the intracellular world. *Phys. Biol.*, 17(6):061003, 2020.

J. Monod, J. Wyman, and J. Changeux. On the nature of allosteric transitions: a plausible model. *J. Mol. Biol.*, 12(1):88–118, 1965.

D. F. Mosher, P. E. Schad, et al. Cross-linking of fibronectin to collagen by blood coagulation factor xiiia. *J. Clin. Investig.*, 64(3):781–787, 1979.

J. D. Mott and Z. Werb. Regulation of matrix biology by matrix metalloproteinases. *Curr. Opin. Cell. Biol.*, 16(5):558–564, 2004.

J. K. Mouw, G. Ou, and V. M. Weaver. Extracellular matrix assembly: a multiscale deconstruction. *Nat. Rev. Mol. Cell Biol.*, 15(12):771–785, 2014.

L. D. Muiznieks and F. W. Keeley. Molecular assembly and mechanical properties of the extracellular matrix: A fibrous protein perspective. *Biochim. Biophys. Acta, Mol. Basis Dis.*, 1832(7):866–875, 2013.

J. M. Muncie and V. M. Weaver. The physical and biochemical properties of the extracellular matrix regulate cell fate. *Current. Top. Mol. Biol.*, 130:1–37, 2018.

E. Muneyuki, E. Nishida, K. Sutoh, and H. Sakai. Purification of cofilin, a 21,000 molecular weight actin-binding protein, from porcine kidney and identification of the cofilin-binding site in the actin sequence. *J. Biochem.*, 97(2):563–568, 1985.

J. D. Murray, P. K. Maini, and R. T. Tranquillo. Mechanochemical models for generating biological pattern and form in development. *hys. Rep.*, 171(2):59–84, 1988.

H. Nagamoto and K. Yagi. Properties of myosin light chain kinase prepared from rabbit skeletal muscle by an improved method. *J. Biochem.*, 95(4):1119–1130, 1984.

A. H. Nayfeh. *Perturbation methods*. John Wiley & Sons, 2008.

P. Nigro, J. Abe, and B. C. Berk. Flow shear stress and atherosclerosis: a matter of site specificity. *Antioxid. Redox Signaling*, 15(5):1405–1414, 2011.

H. Nikukar, S. Reid, P. M. Tsimbouri, M. O. Riehle, A. S. G. Curtis, and M. J. Dalby. Osteogenesis of mesenchymal stem cells by nanoscale mechanotransduction. *ACS Nano*, 7(3):2758–2767, 2013.

P. W. Oakes, T. C. Bidone, Y. Beckham, A. V. Skeeters, G. R. Ramirez-San Juan, S. P. Winter, G. A. Voth, and M. L. Gardel. Lamellipodium is a myosin-independent mechanosensor. *Proc. Natl. Acad. Sci. U.S.A.*, 115(11):2646–2651, 2018.

A. W. Orr, B. P. Helmke, B. R. Blackman, and M. A. Schwartz. Mechanisms of mechanotransduction. *Dev. Cell*, 10(1):11–20, 2006.

A. Page-McCaw, A. J. Ewald, and Z. Werb. Matrix metalloproteinases and the regulation of tissue remodelling. *Nat. Rev. Mol. Cell Biol.*, 8(3):221–233, 2007.

J. T. Parsons, A. R. Horwitz, and M. A. Schwartz. Cell adhesion: integrating cytoskeletal dynamics and cellular tension. *Nat. Rev. Mol. Cell Biol.*, 11(9):633–643, 2010.

S. L. Parsons, S. A. Watson, P. D. Brown, H. M. Collins, and R. J. C. Steele. Matrix metalloproteinases. *Br. J. Surg.*, 84(2):160–166, 1997.

M. J. Paszek, N. Zahir, K. R. Johnson, J. N. Lakins, G. I. Rozenberg, A. Gefen, C. A. Reinhart-King, S. S. Margulies, M. Dembo, D. Boettiger, et al. Tensional homeostasis and the malignant phenotype. *Cancer cell*, 8(3):241–254, 2005.

M. J. Paszek, D. Boettiger, V. M. Weaver, and D. A. Hammer. Integrin clustering is driven by mechanical resistance from the glycocalyx and the substrate. *PLoS Comput. Biol.*, 5(12):e1000604, 2009.

A. Pathak, V. S. Deshpande, R. M. McMeeking, and A. G Evans. The simulation of stress fibre and focal adhesion development in cells on patterned substrates. *J. R. Soc. Interface*, 5(22):507–524, 2008.

I. Patla, T. Volberg, N. Elad, V. Hirschfeld-Warneken, C. Grashoff, R. Fässler, J. P. Spatz, B. Geiger, and O. Medalia. Dissecting the molecular architecture of integrin adhesion sites by cryo-electron tomography. *Nat. Cell Biol.*, 12(9):909–915, 2010.

S. Pellegrin and H. Mellor. Actin stress fibres. *J. Cell Sci.*, 120(20):3491–3499, 2007.

X. Peng, J. Huang, C. Xiong, and J. Fang. Cell adhesion nucleation regulated by substrate stiffness: a monte carlo study. *J. Biomech.*, 45(1):116–122, 2012.

Y. V. Pereverzev, O. V. Prezhdo, M. Forero, E. V. Sokurenko, and W. E. Thomas. The two-pathway model for the catch-slip transition in biological adhesion. *Biophys. J.*, 89 (3):1446–1454, 2005.

C. S. Peskin. The immersed boundary method. *Acta Numer.*, 11:479–517, 2002.

L. J. Peterson, Z. Rajfur, A. S. Maddox, C. D. Freel, Y. Chen, M. Edlund, C. Otey, and K. Burridge. Simultaneous stretching and contraction of stress fibers in vivo. *Mol. Biol. Cell*, 15(7):3497–3508, 2004.

T. D. Pollard. Actin and actin-binding proteins. *Cold Spring Harb. Perspect. Biol.*, 8(8): a018226, 2016.

T. D. Pollard and G. G. Borisy. Cellular motility driven by assembly and disassembly of actin filaments. *Cell*, 112(4):453–465, 2003.

T. D. Pollard, L. Blanchoin, and R. D. Mullins. Molecular mechanisms controlling actin filament dynamics in nonmuscle cells. *Annu. Rev. Biophys. Biom.*, 29(1):545–576, 2000.

M. Poujade, E. Grasland-Mongrain, A. Hertzog, J. Jouanneau, P. Chavrier, B. Ladoux, A. Buguin, and P. Silberzan. Collective migration of an epithelial monolayer in response to a model wound. *Proc. Natl. Acad. Sci. U.S.A.*, 104(41):15988–15993, 2007.

M. Prager-Khoutorsky, A. Lichtenstein, R. Krishnan, K. Rajendran, A. Mayo, Z. Kam, B. Geiger, and A. D. Bershadsky. Fibroblast polarization is a matrix-rigidity-dependent process controlled by focal adhesion mechanosensing. *Nat. Cell Biol.*, 13(12):1457–1465, 2011.

M. Prass, K. Jacobson, A. Mogilner, and M. Radmacher. Direct measurement of the lamellipodial protrusive force in a migrating cell. *J. Cell Biol*, 174(6):767–772, 2006.

P. P. Provenzano and P. J. Keely. Mechanical signaling through the cytoskeleton regulates cell proliferation by coordinated focal adhesion and rho gtpase signaling. *J. Cell Sci.*, 124(8):1195–1205, 2011.

R. Prudent, N. Demoncheaux, H. Diemer, V. Collin-Faure, R. Kapur, F. Paublant, L. Lafanechère, S. Cianferani, and T. Rabilloud. A quantitative proteomic analysis of cofilin phosphorylation in myeloid cells and its modulation using the lim kinase inhibitor pyr1. *PLoS One*, 13(12):e0208979, 2018.

J. Qian, J. Wang, and H. Gao. Lifetime and strength of adhesive molecular bond clusters between elastic media. *Langmuir*, 24(4):1262–1270, 2008.

J. Qian, J. Wang, Y. Lin, and H. Gao. Lifetime and strength of periodic bond clusters between elastic media under inclined loading. *Biophys. J.*, 97(9):2438–2445, 2009.

B. Rappaz, A. Barbul, A. Hoffmann, D. Boss, R. Korenstein, C. Depeursinge, P. J. Magistretti, and P. Marquet. Spatial analysis of erythrocyte membrane fluctuations by digital holographic microscopy. *Blood Cells Mol. Dis.*, 42(3):228–232, 2009.

E. G. Rens and R. M. H. Merks. Cell shape and durotaxis explained from cell-extracellular matrix forces and focal adhesion dynamics. *iScience*, 23(9), 2020.

S. Ricard-Blum. The collagen family. *Cold Spring Harb. Perspect. Biol.*, 3(1):a004978, 2011.

A. J. Ridley and A. Hall. The small gtp-binding protein rho regulates the assembly of focal adhesions and actin stress fibers in response to growth factors. *Cell*, 70(3):389–399, 1992.

A. J. Ridley, H. F. Paterson, C. L. Johnston, D. Diekmann, and A. Hall. The small gtp-binding protein rac regulates growth factor-induced membrane ruffling. *Cell*, 70(3): 401–410, 1992.

P. Ridone, M. Vassalli, and B. Martinac. Piezo1 mechanosensitive channels: what are they and why are they important. *Biophys. Rev.*, 11(5):795–805, 2019.

K. Riento and A. J. Ridley. Rocks: multifunctional kinases in cell behaviour. *Nat. Rev. Mol. Cell Biol.*, 4(6):446–456, 2003.

A. Rigort, D. Günther, R. Hegerl, D. Baum, B. Weber, S. Prohaska, O. Medalia, W. Baumeister, and H. Hege. Automated segmentation of electron tomograms for a quantitative description of actin filament networks. *J. Struct. Biol.*, 177(1):135–144, 2012.

D. Riveline, E. Zamir, N. Q. Balaban, U. S. Schwarz, T. Ishizaki, S. Narumiya, Z. Kam, B. Geiger, and A. D. Bershadsky. Focal contacts as mechanosensors: externally applied local mechanical force induces growth of focal contacts by an mdia1-dependent and rock-independent mechanism. *J. Cell Biol.*, 153(6):1175–1186, 2001.

S. N. Robertson, P. Campsie, P. G. Childs, F. Madsen, H. Donnelly, F. L. Henriquez, W. G. Mackay, M. Salmerón-Sánchez, M. P. Tsimbouri, C. Williams, et al. Control of cell behaviour through nanovibrational stimulation: nanokicking. *Phil. Trans. R. Soc. A*, 376(2120), 2018.

W. Ronan, V. S. Deshpande, R. M. McMeeking, and J. P. McGarry. Numerical investigation of the active role of the actin cytoskeleton in the compression resistance of cells. *. Mech. Behav. Biomed. Mater.*, 14:143–157, 2012.

W. Ronan, V. S. Deshpande, R. M. McMeeking, and J. P. McGarry. Cellular contractility and substrate elasticity: a numerical investigation of the actin cytoskeleton and cell adhesion. *Biomech. Model. Mechanobiol.*, 13:417–435, 2014.

O. Rossier, V. Octeau, J. Sibarita, C. Leduc, B. Tessier, D. Nair, V. Gatterdam, O. Destaing, C. Albiges-Rizo, R. Tampé, et al. Integrins $\beta 1$ and $\beta 3$ exhibit distinct dynamic nanoscale organizations inside focal adhesions. *Nat. Cell Biol.*, 14(10):1057–1067, 2012.

R. Ruimerman, P. Hilbers, B. Van Rietbergen, and R. Huiskes. A theoretical framework for strain-related trabecular bone maintenance and adaptation. *J. Biomech.*, 38(4): 931–941, 2005.

L. T. Saldin, M. C. Cramer, S. S. Velankar, L. J. White, and S. F. Badylak. Extracellular matrix hydrogels from decellularized tissues: Structure and function. *Acta Biomater.*, 49:1–15, 2017.

L. J. Sandell and T. Aigner. Articular cartilage and changes in arthritis: cell biology of osteoarthritis. *Arthritis Res. Ther.*, 3:1–7, 2001.

S. Satoh and T. Tominaga. mdia-interacting protein acts downstream of rho-mdia and modifies src activation and stress fiber formation. *J. Biol. Chem.*, 276(42):39290–39294, 2001.

H. Sawai, Y. Okada, H. Funahashi, Y. Matsuo, H. Takahashi, H. Takeyama, and T. Manabe. Activation of focal adhesion kinase enhances the adhesion and invasion of pancreatic cancer cells via extracellular signal-regulated kinase-1/2 signaling pathway activation. *Mol. Cancer*, 4:1–12, 2005.

U. S. Schwarz and M. L. Gardel. United we stand–integrating the actin cytoskeleton and cell–matrix adhesions in cellular mechanotransduction. *J. Cell Sci.*, 125(13):3051–3060, 2012.

U. S. Schwarz and S. A. Safran. Physics of adherent cells. *Rev. Mod. Phys.*, 85(3):1327–1381, 2013.

E. Schwob and R. P. Martin. New yeast actin-like gene required late in the cell cycle. *Nature*, 355(6356):179–182, 1992.

T. Shemesh, B. Geiger, A. D. Bershadsky, and M. M. Kozlov. Focal adhesions as mechanosensors: a physical mechanism. *Proc. Natl. Acad. Sci. U.S.A.*, 102(35):12383–12388, 2005.

M. D. Shoulders and R. T. Raines. Collagen structure and stability. *Annu. Rev. Biochem.*, 78:929–958, 2009.

P. Singh and J. E. Schwarzbauer. Fibronectin and stem cell differentiation–lessons from chondrogenesis. *J. Cell. Sci.*, 125(16):3703–3712, 2012.

P. Singh, C. Carraher, and J. E. Schwarzbauer. Assembly of fibronectin extracellular matrix. *Annu. Rev. Cell Dev. Biol.*, 26:397–419, 2010.

J. V. Small, K. Rottner, I. Kaverina, and K. I. Anderson. Assembling an actin cytoskeleton for cell attachment and movement. *Biochim. Biophys. Acta, Mol. Cell Res.*, 1404(3): 271–281, 1998.

J. Solowiej-Wedderburn and C. M. Dunlop. Sticking around: Cell adhesion patterning for energy minimization and substrate mechanosensing. *Biophys. J.*, 121(9):1777–1786, 2022.

J. Solowiej-Wedderburn and C. M. Dunlop. Cell-strain-energy costs of active control of contractility. *Physical review E*, 107(6):L062401, 2023.

A. P. Somlyo and A. V. Somlyo. Signal transduction and regulation in smooth muscle. *Nature*, 372(6503):231–236, 1994.

A. P. Somlyo and A. V. Somlyo. Ca2+ sensitivity of smooth muscle and nonmuscle myosin ii: modulated by g proteins, kinases, and myosin phosphatase. *Physiol. Rev.*, 83 (4):1325–1358, 2003.

J. M. Squire. Muscle contraction: Sliding filament history, sarcomere dynamics and the two huxleys. *Glob. Cardiol. Sci.*, 2016(2), 2016.

C. H. Stuelten, C. A. Parent, and D. J. Montell. Cell motility in cancer invasion and metastasis: insights from simple model organisms. *Nat. Rev. Cancer*, 18(5):296–312, 2018.

T. Sumi, K. Matsumoto, Y. Takai, and T. Nakamura. Cofilin phosphorylation and actin cytoskeletal dynamics regulated by rho-and cdc42-activated lim-kinase 2. *J. Cell Biol.*, 147(7):1519–1532, 1999.

M. Sun, F. Spill, and M. H. Zaman. A computational model of yap/taz mechanosensing. *Biophys. J.*, 110(11):2540–2550, 2016.

M. Sun, G. Chi, P. Li, S. Lv, J. Xu, Z. Xu, Y. Xia, Y. Tan, J. Xu, L. Li, et al. Effects of matrix stiffness on the morphology, adhesion, proliferation and osteogenic differentiation of mesenchymal stem cells. *Int. J. Med. Sci.*, 15(3):257, 2018.

T. Svitkina. The actin cytoskeleton and actin-based motility. *Cold Spring Harbor Perspect. Biol.*, 10(1):a018267, 2018.

T. M. Svitkina, A. B. Verkhovsky, K. M. McQuade, and G. G. Borisy. Analysis of the actin–myosin ii system in fish epidermal keratocytes: mechanism of cell body translocation. *J. Cell Biol.*, 139(2):397–415, 1997.

A. G. Szent-Györgyi. Calcium regulation of muscle contraction. *Biophys. J.*, 15(7):707–723, 1975.

S. Tadokoro, S. J. Shattil, K. Eto, V. Tai, R. C. Liddington, J. M. de Pereda, M. H. Ginsberg, and D. A. Calderwood. Talin binding to integrin ß tails: a final common step in integrin activation. *Science*, 302(5642):103–106, 2003.

M. Taffetani, M. Griebel, D. Gastaldi, S. M. Klisch, and P. Vena. Poroviscoelastic finite element model including continuous fiber distribution for the simulation of nanoindentation tests on articular cartilage. *J. Mech. Behav. Biomed. Mater.*, 32:17–30, 2014.

S. Takashima. Phosphorylation of myosin regulatory light chain by myosin light chain kinase, and muscle contraction. *Circ. J.*, 73(2):208–213, 2009.

M. G. Tansey, R. A. Word, H. Hidaka, H. A. Singer, C. M. Schworer, K. E. Kamm, and J. T. Stull. Phosphorylation of myosin light chain kinase by the multifunctional calmodulin-dependent protein kinase ii in smooth muscle cells. *J. Biol. Chem.*, 267(18): 12511–12516, 1992.

M. G. Tansey, K. Luby-Phelps, K. E. Kamm, and J. T. Stull. Ca (2+)-dependent phosphorylation of myosin light chain kinase decreases the ca2+ sensitivity of light chain phosphorylation within smooth muscle cells. *J. Biol. Chem.*, 269(13):9912–9920, 1994.

Y. H. Tee, T. Shemesh, V. Thiagarajan, R. F. Hariadi, K. L. Anderson, C. Page, N. Volkmann, D. Hanein, S. Sivaramakrishnan, M. M. Kozlov, et al. Cellular chirality arising from the self-organization of the actin cytoskeleton. *Nat. Cell Biol.*, 17(4):445–457, 2015.

N. Thekkethil, J. Köry, M. Guo, P. S. Stewart, N. A. Hill, and X. Luo. Modelling the rheology of living cell cytoplasm: Poroviscoelasticity and fluid-to-solid transition. *Biomech. Model. Mechanobiol.*, 2024.

W. Thomas. Catch bonds in adhesion. *Annu. Rev. Biomed. Eng.*, 10:39–57, 2008.

W. Thomas, M. Forero, O. Yakovenko, L. Nilsson, P. Vicini, E. Sokurenko, and V. Vogel. Catch-bond model derived from allostery explains force-activated bacterial adhesion. *Biophys. J.*, 90(3):753–764, 2006.

T. Thoresen, M. Lenz, and M. L. Gardel. Thick filament length and isoform composition determine self-organized contractile units in actomyosin bundles. *Biophys. J.*, 104(3): 655–665, 2013.

I. A. Titushkin and M. R. Cho. Controlling cellular biomechanics of human mesenchymal stem cells. In *Annu. Int. Conf. IEEE Eng. Med. Biol. Soc.*, pages 2090–2093. IEEE, 2009.

S. Tojkander, G. Gateva, G. Schevzov, P. Hotulainen, P. Naumanen, C. Martin, P. W. Gunning, and P. Lappalainen. A molecular pathway for myosin ii recruitment to stress fibers. *Curr. Biol.*, 21(7):539–550, 2011.

S. Tojkander, G. Gateva, and P. Lappalainen. Actin stress fibers–assembly, dynamics and biological roles. *J. Cell Sci.*, 125(8):1855–1864, 2012.

S. Tojkander, G. Gateva, A. Husain, R. Krishnan, and P. Lappalainen. Generation of contractile actomyosin bundles depends on mechanosensitive actin filament assembly and disassembly. *Elife*, 4:e06126, 2015.

D. Tong, N. Soley, R. Kolasangiani, M. A. Schwartz, and T. C. Bidone. Integrin αiibβ3 intermediates: From molecular dynamics to adhesion assembly. *Biophys. J.*, 122(3): 533–543, 2023.

G. Totsukawa, Y. Yamakita, S. Yamashiro, D. J. Hartshorne, Y. Sasaki, and F. Matsumura. Distinct roles of rock (rho-kinase) and mlck in spatial regulation of mlc phosphorylation for assembly of stress fibers and focal adhesions in 3t3 fibroblasts. *J. Cell Biol.*, 150(4):797–806, 2000.

G. Totsukawa, Y. Wu, Y. Sasaki, D. J. Hartshorne, Y. Yamakita, S. Yamashiro, and F. Matsumura. Distinct roles of mlck and rock in the regulation of membrane protrusions and focal adhesion dynamics during cell migration of fibroblasts. *J. Cell Biol.*, 164(3): 427–439, 2004.

J. J. Tyson, K. C. Chen, and B. Novak. Sniffers, buzzers, toggles and blinkers: dynamics of regulatory and signaling pathways in the cell. *Curr. Opin. Cell Biol.*, 15(2):221–231, 2003.

R. Uehara, G. Goshima, I. Mabuchi, R. D. Vale, J. A. Spudich, and E. R. Griffis. Determinants of myosin ii cortical localization during cytokinesis. *Curr. Biol.*, 20(12): 1080–1085, 2010.

I. Ullah, R. B. Subbarao, and G. J. Rho. Human mesenchymal stem cells-current trends and future prospective. *Biosci. Rep.*, 35(2):e00191, 2015.

M. Urbanczyk, S. L. Layland, and K. Schenke-Layland. The role of extracellular matrix in biomechanics and its impact on bioengineering of cells and 3d tissues. *Matrix Biol.*, 85:1–14, 2020.

F. J. Vernerey and M. Farsad. A mathematical model of the coupled mechanisms of cell adhesion, contraction and spreading. *J. Math. Biol.*, 68:989–1022, 2014.

M. Vicente-Manzanares, X. Ma, R. S. Adelstein, and A. R. Horwitz. Non-muscle myosin ii takes centre stage in cell adhesion and migration. *Nat. Rev. Mol. Cell Biol.*, 10(11): 778–790, 2009.

S. Walcott and S. X. Sun. A mechanical model of actin stress fiber formation and substrate elasticity sensing in adherent cells. *Biophys. J.*, 98(3):365a, 2010.

Y. Wang, X. R. Zheng, N. Riddick, M. Bryden, W. Baur, X. Zhang, and H. K. Surks. Rock isoform regulation of myosin phosphatase and contractility in vascular smooth muscle cells. *Circ. Res.*, 104(4):531–540, 2009.

S. Wasserman. Fh proteins as cytoskeletal organizers. *Trends Cell Biol.*, 8(3):111–115, 1998.

N. Watanabe, T. Kato, A. Fujita, T. Ishizaki, and S. Narumiya. Cooperation between mdia1 and rock in rho-induced actin reorganization. *Nat. Cell Biol.*, 1(3):136–143, 1999.

R. C. Webb. Smooth muscle contraction and relaxation. *Adv. Physiol. Educ.*, 27(4): 201–206, 2003.

K. L. Wegener, A. W. Partridge, J. Han, A. R. Pickford, R. C. Liddington, M. H. Ginsberg, and I. D. Campbell. Structural basis of integrin activation by talin. *Cell*, 128(1):171–182, 2007.

Z. Wei, V. S. Deshpande, R. M. McMeeking, and A. G. Evans. Analysis and interpretation of stress fiber organization in cells subject to cyclic stretch. *J. Biomech. Eng.*, 130(3): 031009, 04 2008.

E. S. Welf, U. P. Naik, and B. A. Ogunnaike. A spatial model for integrin clustering as a result of feedback between integrin activation and integrin binding. *Biophys. J.*, 103 (6):1379–1389, 2012.

C. A. Wilson, M. A. Tsuchida, G. M. Allen, E. L. Barnhart, K. T. Applegate, P. T. Yam, L. Ji, K. Keren, G. Danuser, and J. A. Theriot. Myosin ii contributes to cell-scale actin network treadmilling through network disassembly. *Nature*, 465(7296):373–377, 2010.

S. J. Winder and K. R. Ayscough. Actin-binding proteins. *J. Cell Sci.*, 118(4):651–654, 2005.

M. A. Wozniak, K. Modzelewska, L. Kwong, and P. J. Keely. Focal adhesion regulation of cell behavior. *Biochim. Biophys. Acta, Mol. Cell Res.*, 1692(2-3):103–119, 2004.

M. Xue and C. J. Jackson. Extracellular matrix reorganization during wound healing and its impact on abnormal scarring. *Adv. Wound Care*, 4(3):119–136, 2015.

K. M. Yamada, J. W. Collins, D. A. Cruz Walma, A. D. Doyle, S. G. Morales, J. Lu, K. Matsumoto, S. S. Nazari, R. Sekiguchi, Y. Shinsato, et al. Extracellular matrix dynamics in cell migration, invasion and tissue morphogenesis. *Int. J. Exp. Pathol.*, 100 (3):144–152, 2019.

N. Yamana, Y. Arakawa, T. Nishino, K. Kurokawa, M. Tanji, R. E. Itoh, J. Monypenny, T. Ishizaki, H. Bito, K. Nozaki, et al. The rho-mdia1 pathway regulates cell polarity and focal adhesion turnover in migrating cells through mobilizing apc and c-src. *Mol. Cell. Biol.*, 26(18):6844–6858, 2006.

G. Yourek, S. M. McCormick, J. J. Mao, and G. C. Reilly. Shear stress induces osteogenic differentiation of human mesenchymal stem cells. *Regen. Med.*, 5(5):713–724, 2010.

B. Yue. Biology of the extracellular matrix: an overview. *J. Glaucoma*, 23:S20–S23, 2014.

W. Zakrzewski, M. Dobrzyński, M. Szymonowicz, and Z. Rybak. Stem cells: past, present, and future. *Stem Cell Res. Ther.*, 10(1):1–22, 2019.

J. Zang, G. Cavet, J. H. Sabry, P. Wagner, S. L. Moores, and J. A. Spudich. On the role of myosin-ii in cytokinesis: division of dictyostelium cells under adhesive and nonadhesive conditions. *Mol. Biol. Cell*, 8(12):2617–2629, 1997.

E. Zelzer and B. R. Olsen. The genetic basis for skeletal diseases. *Nature*, 423(6937): 343–348, 2003.

C. Zhu, J. Lou, and R. P. McEver. Catch bonds: physical models, structural bases, biological function and rheological relevance. *Biorheology*, 42(6):443–462, 2005.